Femtosecond pulsed enhancement cavity for mutli-photon entanglement studies

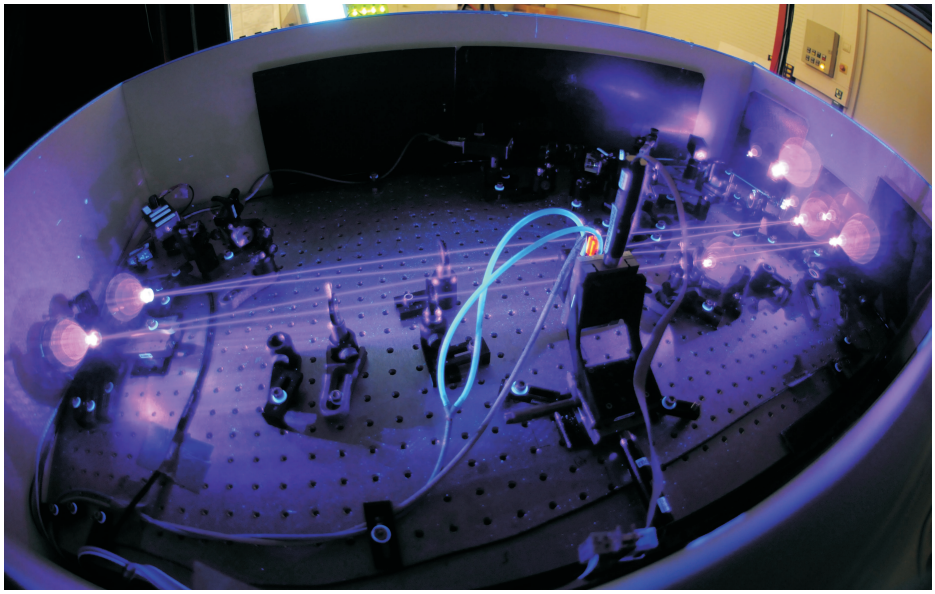

Diplomarbeit an der Fakultät für Physik
der Technischen Universität München
durchgeführt am
Max-Planck-Institut für Quantenoptik

Author:
Patrick Steffen Michelberger

München

02.12.2009

Für meine Mutter.

Contents

Chapter 1

Introduction

At the beginning of the 20$^{\text{th}}$ century, a new era in the history of natural sciences commenced. With the ground breaking work of Max Planck and Albert Einstein on the radiation law ([1]) and the photoelectric effect ([2]), the road towards the formulation of quantum mechanics had been stated. Subsequently, the mathematical formulation of quantum mechanics as a theory had been mainly performed by Werner Heisenberg and Erwin Schrödinger. Ever since its introduction, probably no other physical theory has changed mankind's understanding of nature so tremendously as quantum mechanics did. Already in its early days, the inherent probabilistic characteristics of it led to intense argumentations about the implications this new theory has on the fundamental structure of physics, which culminated in the famous Einstein phrase[1] *"Gott würfelt nicht"* . In order to challenge the aforementioned feature, Albert Einstein, Boris Podolski and Nathan Rosen devised a Gedankenexperiment in their seminal EPR paper ([3]), which pointed out yet another important property of quantum mechanics, namely the possibility of non-classical correlations between different quantum mechanical objects; a phenomenon termed entanglement by Erwin Schrödinger ([4]). John Bell later took on the ideas of EPR and formulated a mathematical inequality, the so-called Bell inequality ([5], [6]), in order to test the predictions from quantum mechanics. Experiments conducted with respect to these fundamental questions ([7]-[9]) have shown agreement with the expectations derived from quantum mechanical theory[2]. Although having otherwise not been considered of practical interest to begin with, entanglement has been realised to promise enormous potential for improvements in communication technology and computing within the recent past ([10]), opening up the entire new field of quantum information processing. In contrast to classical information processing, classical two-valued bits are commonly replaced by quantum mechanical two-level systems, called quantum bits or qubits ([11]), which allow for superposition and entangled states.
The advantages that quantum mechanics introduces into communication techniques can for instance be found in cryptography, whereby it, in principle, permits secure communication between different parties, by exchanging a secret quantum key ([12], [13]). Also the teleportation of information between two different parties is enabled ([14]). Since photons are the information carriers of choice within this area of research, due to their little susceptibility to decoherence, most initial experiments involving entangled states have been performed by utilisation of bipartite photonic systems ([15], [16]). However utilising multiqubit entangled states offers the possibility on the one hand to use novel quantum error correction codes for communication protocols ([17]) and on the other hand to apply communication schemes between multiple parties ([18]-[20]), and to perform telecloning of quantum information to multiple recipients ([21]-[23]).
In terms of computational tasks, quantum mechanics allows to yield a considerable speed-up in certain operations, like search algorithms and prime number factorisations ([29], [24], [25]), compared to entirely classical computing. Research hereupon has been undertaken by preferably incorporating atomic based systems in the first place, as the interactions between atoms and ions in traps are easier to control than the ones of photons. Realisation of quantum gates for the latter particles have initially be though to require non-linear optical effects ([142]), which are very weak, consequently leading to low efficiencies in the gate operations. However in the following it has been shown that non-deterministic computation is also possible by relying on linear optics only ([26], [27]), which fuelled the research on photonic based quantum logic ([28]-[31]). Therein, multi-photon entangled states form a required resource. While quantum computing has been in first instance based on the circuit model ([34]), it has later been realised that alternative computing methods are possible ([33], [34]). One of these is the one-way quantum computer,

[1] *"God does not gamble."*

[2] Although there are still potential loopholes and no experiment has so far been succeeded in closing all of them simultaneously.

which hinges on initially multi-partite entangled states, called cluster states, to perform quantum computation. This has been a completely new approach and demonstrated that multi-partite entanglement can be of utmost importance.
Thus multiqubit entangled quantum states based on photons represent a valuable ingredient in the future development of quantum information technology, for which studying their characteristic properties is a subject of general interest for further progress in both fields of research outlined above. Such states entail in general a much richer structure regarding their entanglement than their bipartite counterparts do, for example states with more than 3 qubits can be divided up into different families ([89], [146]-[148]), each exhibiting different entanglement properties, like the aforementioned cluster states. Another particular example of such states is the family of Dicke states, which have been discovered by R. H. Dicke the spin operators for describing "superradiant gases" ([150], [35]). Symmetric Dicke states exhibit the specific feature of having a high persistency against decoherence ([36]) and can be regarded to be rather persistent in terms of their entanglement, which is e.g. useful in communicational tasks.
In order to observe multipartite photonic states in the laboratory, the non-linear process of spontaneous parametric down conversion (SPDC) can be employed. SPDC was first studied theoretically as early as 1967 ([37]), and was experimentally investigated in 1970 ([38]). Since the correlations in the output photons of the down conversion process became apparent ([126]), SPDC has been realised to constitute a suitable tool for production of the desired entangled states, as it is for instance reviewed in reference ([40]). For this reason it became the workhorse for photon sources in most experiments dealing with photon-based quantum states and quantum information processing. In combination with a linear optical set-up and conditional detection ([87]), multi-photon entanglement can be observed and characterised. Since contemporary experiments are focussing on the entanglement in states with photon numbers as high as six ([23], [43]-[46]), ultrashort laser pulses are required to pump the SPDC process([141]).
Within this work, a novel photon source of the aforementioned type, designed to enable the observation of the six-photon Dicke state with three excitations ([43], [47]), will be introduced. Since the six-photon count rates, achievable with contemporary, commercially available laser systems ([44]) are very low, thus requiring long measurement times, the pumping source presented in this work utilises a recent enhancement mechanism for ultrashort laser pulses. Therewith high six photon count rates become readily available. The enhancement scheme utilises the coherent addition of ultrashort, mode-locked laser pulses in passive, narrowband optical resonators[3] ([41], [42]). Furthermore this cavity represents the first enhancement resonator for femtosecond laser pulses in the ultra-violet (UV) wavelength range.
In the following text, all necessary design parameters are first laid out theoretically, followed by an experimental investigation of these. We will start in chapter 2 by calculating the properties of the optical components, required to build the resonator system, also assessing the expected power enhancement of the pumping pulses for the SPDC process. In chapter 3 the experimental set-up will be described. Chapter 4 deals with the characterisation of the cavity in terms of the pumping beam quality, the experimentally achievable power enhancement and the finesse of the resonator. Afterwards chapter 5 will focus on the temporal properties of the UV pumping pulses inside the cavity. Here we describe what is to our knowledge the first intra-cavity autocorrelation experiment, which also uses SPDC as the required non-linear process. Finally, a characterisation of the device as a source for multiphoton states will be undertaken in chapter 6, in which additionally the entanglement, observable in the output states, will be discussed in terms of the pump pulses' spectral properties.

[3]The bandwidth of the resonator is narrow with respect to the spectral width of its individual resonances.

Chapter 2

Cavity design

In this work the extension of recent designs regarding enhancement cavities for ultra-short laser pulses to the ultra-violet (UV) regime will be explored. Previous experiments have utilised resonators particularly for the purpose of second-harmonic and even higher harmonic generation (see e.g. [169], [170], [51], [52], [53]). Commonly all these devices are based on infra-red (IR) pumping beams. For applications in quantum information science based on photonic qubits, spontaneous parameteric down-conversion (SPDC) has however become the workhorse most contemporary experiments deal with, particularly every set-up interested in multi-qubit states relies on this type of interaction. Since SPDC works the other way around than SHG, the two photons, referred to as signal and idler, of approximately half the energy and double the wavelength of the incoming photon are generated[1]. So UV light is used to drive the non-linear process, yielding IR outputs for which state of the art single photon avalanche photodiodes achieve efficiencies as high as $\eta_{\text{det}} \approx 50\%$. Hence for our experiment, which is devised to generate multi-qubit entangled quantum states with high count rates, an enhancement resonator operating in the UV is required. We will thus take up previous considerations for femtosecond IR resonators (e.g. [54], [55]) in combination with the idea of enhancing UV light inside a cavity, already shown in the picosecond regime ([56]) and merge them together to this, yet unexplored, combination.
One of the basic ideas that cavities for ultra-short pulse lasers are founded on, is the coherent addition of subsequently emitted pulses. The most simplistic and hand-waving view on this is to consider the optical pulse already situated inside the resonator to precisely meet up with an external one after every round-trip as drawn in fig. 2.1. If the electric fields of both now interfere constructively with each other, the intensity inside the cavity builds up successively and is only limited by losses occurring during each round-trip. In such a way, enough pump power can be generated to enable simultaneous emission of several signal and idler photon pairs in SPDC, allowing in turn the observation of multi-qubit quantum states with high count rates.
Of course reality is not exactly as easy as that and a detailed examination of all important parameters of the cavity and its application as a high flux photon source will be provided in the course of this work. Nonetheless the aforementioned short summary is sufficient to get the general idea and allows to start the discussion by consideration of a suitable resonator design serving the described needs.
A free space set-up will be mandatory, since operation with ultra-short UV light is a prerequisite and any fibre based device would come along with great loss and dispersion. Desiring furthermore to have pulses propagating on round-trips in order to avoid to great an amount of dispersion and loss, directly implies the construction of a ring cavity. The non-linear optical crystal to be placed inside requires some necessary focussing optics, which is taken care of by the cavity mirrors in order to include as little dispersive material as possible. We decide to build a bow-tie shaped cavity, (see fig. 2.1) allowing the potential insertion of an additional second crystal for future experiments[2]. The most important boundary condition is yet to be set by the repetition rate of the applied pumping laser source. We use a titanium sapphire (Ti:Sa) laser source[3] with a pulse repetition rate of $f_{rep} \approx 80.79\,MHz$. Therefore we have to have a round-trip time of pulses corresponding to $\Delta t_{RT} = \frac{1}{f_{rep}}$ and in turn a cavity length of $L_{cav} = \Delta t_{RT} \cdot c \approx 3.71\,m$. Working with UV-pulses will also require dispersion considerations, whereby particularly for ultra-short laser pulses these kind of effects are important. The cavity will thus only consist of the four indispensable end mirrors ($M1$-$M4$ in fig. 2.1) and just contain the non-linear crystal, which here will be beta-barium borate, $\beta - BaB_2O_4$ (BBO), of $L_{\text{BBO}} = 1\,mm$ length, and air.

[1] See subsec. 6.1.1 for details.
[2] Such as e.g. quantum telecloning ([16], [21], [22]).
[3] working at a central wavelength of $\lambda_{\text{laser}} = 780\,nm$, subsequently frequency doubled to $\lambda_p = 390\,nm$, required for pumping, prior to cavity coupling

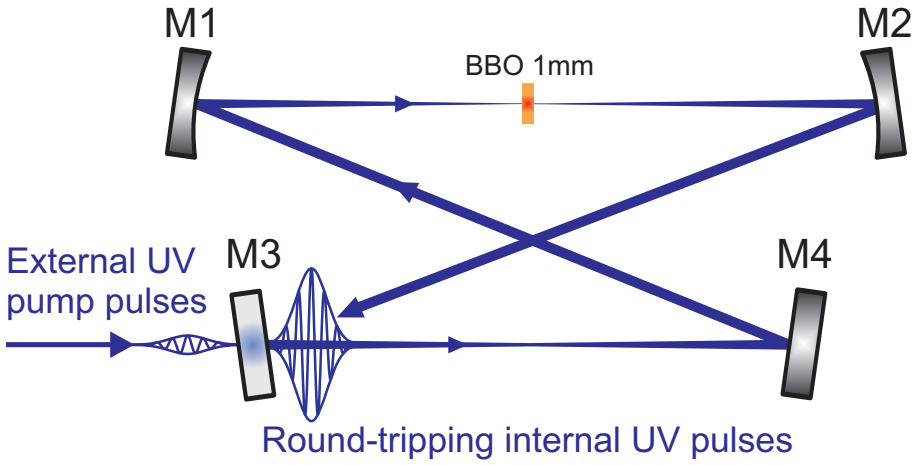

Figure 2.1: Schematic drawing of a bow-tie shaped ring cavity for ultra-short laser pulses. The intra-cavity pulse adds up constructively with the external one at the input coupler after every round-trip. In that way the intensity is enhanced inside the resonator to a level sufficient to allow for considerable multi-photon pair emission rates in SPDC.

Altogether we are going to design, build and characterise the first femto-second, UV bow-tie enhancement resonator of approximately 81 MHz repetition rate, comprising a BBO crystal, air and four end mirrors. In order to get going, all design parameters for building and properly operating the cavity have to be worked out in the first place, which is done in this chapter. The discussion starts with the cavity mirrors, their radii of curvature and reflectance/ transmittance properties. It will turn out, that the latter directly depend on the losses internal pulses are subject to, which are also connected to the cavity finesse. Subsequently dispersive effects will be examined, their influences on the free spectral range (FSR) of the longitudinal modes will be explained and an expectation for the power enhancement within the cavity will be derived. Finally the process of cavity input coupling and pulse addition, already roughly conceptualised in fig. 2.1, will be explored in thorough detail. As the last point in this context, the considerations regarding the $f_{rep} = 80\,MHz$ cavity will be taken further to the even higher repetition rate[4] of $n \cdot f_{rep}$ and consequently resonators of shorter lengths L_{cav}/n.

2.1 Choice of cavity mirrors

2.1.1 Cavity mirror radii of curvature

Knowing the desired length, the radii of curvature for all mirrors involved have to be calculated as the initial step towards every resonator design. These kind of discussions offer the great advantage of being equal for pulsed and continuous wave situations, because they only depend on spatial and not temporal light properties. So, in the following, we can conveniently neglect any pulsed structure and just, simplistically spoken, do the analysis for one single frequency within the pump spectrum as it will be the same for all the others. All time dependencies in the electric fields will consequently be neglected. Furthermore the proper wave nature of light will be accounted for straight away. A brief summary of it will be given before moving on to the actual stability criteria and mirror radii of the cavity[5].

Basics on intra-cavity mode characteristics Coherent laser light is generally known to follow the wave equation extracted from Maxwell's equations ([59])

$$\vec{\nabla}^2\Psi + \vec{k}^2\Psi = 0, \tag{2.1}$$

whereby Ψ represents the light field and $\vec{k}$ is the propagation vector with $|\vec{k}| = \frac{2\pi n}{\lambda}$. For a single frequency it is commonly solved in paraxial approximation ([58]) and a solution is e.g. given by a plane wave along the propagation direction, here defined as the z-axis, with a simple transverse Gaussian profile ([61]),

[4] The resonator design will be considered for the cases $n = 2, 3, 4$, whereas an expression for the power enhancement valid for arbitrary n is derived.

[5] If the reader is thus not familiar with the extension of simple ray tracing to the framework of Gaussian beams, explanations about either of both and their connection to one another can e.g. be found in ([57]) or ([58]).

referred to as $TEM_{0,0}$ mode:

$$\Psi = \Psi_0 \frac{w_0}{w} \exp\left(-i\left(\frac{kr^2}{2q} + \zeta\right)\right) \exp\left(-ik(z - z_0)\right) \tag{2.2}$$

$r = \sqrt{x^2 + y^2}$ labels the coordinate in the transverse direction, the amplitude factor $\frac{w_0}{w}$ accounts for the intensity decrease on axis due to the diffraction of the beam away from its waist position $z = z_0$, ζ is the Gouy phase and q the complex beam parameter. While the Gouy phase

$$\zeta = \arctan\left(\frac{\lambda(z - z_0)}{\pi w_0^2}\right)$$

causes a rapid phase change of the electric field by propagating through the beam waist ([62]), it is the complex beam parameter q which does really concern us here. It is defined by

$$\frac{1}{q(z)} = \frac{1}{R(z)} - \frac{i\lambda}{\pi w(z)^2}, \tag{2.3}$$

with $R(z)$ standing for the radius of curvature of the electric field wavefronts and $w(z)$ for the beam radius at a certain position z. Both quantities depend on the aforementioned coordinate in the following way ([61])

$$w^2(z) = w_0^2\left(1 + \left(\frac{(z - z_0)}{z_R}\right)^2\right) \tag{2.4}$$

$$R(z) = (z - z_0) \cdot \left(1 + \left(\frac{z_R}{(z - z_0)}\right)^2\right) \tag{2.5}$$

with the Rayleigh range $z_R = \frac{\pi w_0^2}{\lambda}$, in which the constant w_0, called beam waist, is the minimal beam radius at the focus, where the radius of curvature $R(z)$ equals ∞ and the wavefronts are plane waves. We hence recognise the optical beam to diverge away from the minimum spot size position z_0 (with $w(z_0) = w_0$ and $R(z_0) = \infty$) and to deviate considerably from the plane wave approach, $\Psi = \Psi_0 \exp(ikz)$, at greater distances $\Delta z = z - z_0$. The Rayleigh range assigns the positions along the optical axis ($z = \pm z_R$), where the beam waists are $w(\pm z_R) = \sqrt{2} w_0$ and the radii of curvature $R(\pm z_R) = \pm 2 z_R$, being the location of greatest overall wavefront curvature. For larger distances from the waist position, the divergence angle can be obtained by linear approximation of eq. (2.4) to ([63]) $\theta = \frac{\lambda}{\pi w_0}$. We can therefrom infer the diffraction of the optical beam to be the smaller the larger its waist w_0 is and vice versa. Hence tightly focussed laser beams, e.g. applied for trapping single atoms ([64]), show tremendous diffraction and tiny Rayleigh ranges z_R, requiring very accurate positioning of objects into their focal points.
It shall also be noted here, that this work follows the common convention regarding the signs of radii of curvature ([58]). These are taken to be positive, if position coordinates are to the right of the focal spots at $\{z_0, z_1\}$ (see fig. 2.2), i.e. for $z > \{z_0, z_1\}$, with optical beam wavefronts diverging away from $\{z_0, z_1\}$, and respectively negative if locations are to the left of the aforementioned minimum diameter points, i.e. $z < \{z_0, z_1\}$, with wavefronts converging towards $z = \{z_0, z_1\}$. Please acknowledge the inequalities to be well defined only within each individual sector in fig. 2.2.

Higher order modes and M^2 factor Eq. (2.2) is not the only possibility in the solution space of the differential equation (2.1). Depending on the boundary conditions, higher order transverse modes can be obtained as well. For circular symmetric systems, such as our cavity, these are constituted by the generalised Laguerre polynomials L_p^l ([63]), whereby p stands for the radial and l for the angular mode number. The expression eq. (2.2) consequently modifies to:

$$\Psi = \Psi_0 \frac{w_0}{w} \left(\sqrt{2}\frac{r}{w(z)}\right)^l \cdot L_p^l\left(2\frac{r^2}{w^2}\right) \cdot \exp\left(-i\left(\frac{kr^2}{2q} + \zeta_{p,l}\right)\right) \exp\left(-ikz\right) \tag{2.6}$$

Since the polynomial of lowest order is:

$$L_0^l(x) = 1 \tag{2.7}$$

one can retain the $TEM_{0,0}$ mode for a parameter choice of $p = 0$, $l = 0$. The intensity distributions of the first couple of modes can e.g. be found depicted in reference ([58]). For these higher order modes, the Gouy phase gets changed as well to:

$$\zeta_{p,l} = (2p + l + 1) \cdot \arctan\left(\frac{\lambda z}{\pi w_0^2}\right)$$

In terms of the down-conversion process it is very advantageous to have pumping with the fundamental $TEM_{0,0}$ mode in order to guarantee for a well-defined phase-matching situation and spatial distribution of the down-conversion photons (see [101] for details), yielding also a good coupling efficiency into a single mode (SM) optical fibre applied for transfer of the photons to the linear optical set-up analysing them[6]. Therefore the resonator is supposed to operate on the aforementioned mode only, which is experimentally realised by proper mirror adjustment and input-coupling alignment. The obtained transversal intensity distribution within the cavity is discussed in section 4.1 (see fig. 4.1).
However real laser beams in resonators are hardly ever describable solely by a Gaussian beam and some multimode structure is normally present on top, influencing the values for divergence and waist as stated in eq. (2.4). The quality of these is expressed in terms of parameters expected for purely Gaussian beams by introduction of an additional factor, called the M^2 ([65]). The beam waist expression for such a multimode situation can be rewritten to ([66]):

$$\tilde{w}(z) = w_0^2 \left(1 + \left(\frac{\lambda \cdot M^2 \cdot (z - z_0)}{\pi w_0^2}\right)^2\right) \tag{2.8}$$

The Gaussian formulae are obtained for $M^2 = 1$, while for deviation thereof an $M^2 > 1$ will be observed. It shall be particularly noted here, that the M^2-factor connects to both, the waist and divergence of the beam, and it is therefore not sufficient to measure just one of these for proper beam analysis ([66]). We will come back to that later on in course of the experimental determination of the cavity parameters[7]. For the moment, only the modification of the complex beam parameter by multimode effects is important:

$$\frac{1}{\tilde{q(z)}} = \frac{1}{R(z)} - \frac{i\lambda}{\pi\tilde{w}(z)^2} = \frac{1}{R(z)} - \frac{iM^2\lambda}{\pi w(z)^2} \tag{2.9}$$

which should in principle be accounted for in the following calculations. Nevertheless taking up later results from eq. (4.1), the measured quality factors for our intra-cavity beams are close to one, wherefore the computations concerning cavity stability and mirror radii of curvature are just performed for the pure Gaussian situation.

Propagation of Gaussian beams and resonator stability Gaussian beams can be propagated through linear optical elements by the aid of ray transfer matrices known from ray tracing ([57]). Since all relevant parameters necessary for the description of a Gaussian beam's spatial propagation are contained within the complex beam parameter q (namely radius of curvature, beam waist and wavelength), it is sufficient to only focus on this quantity. Tracing a light beam can be executed by application of matrices having a dimensionality of 2 × 2, which accounts for the two aforementioned free parameters within q. The various matrices comprise particular structures for specific elements, whereby for us just lenses and bulk media of refractive indices n are important[8]. The respective expressions are ([63]):

$$A_{\text{material}} = \begin{pmatrix} 1 & \frac{d}{n} \\ 0 & 1 \end{pmatrix}; \quad A_{\text{free-space}} = \begin{pmatrix} 1 & d \\ 0 & 1 \end{pmatrix}; \quad A_{\text{lens}} = \begin{pmatrix} 1 & 0 \\ -\frac{1}{f} & 1 \end{pmatrix} \tag{2.10}$$

Since no real lenses are inserted into the resonator for dispersion reasons, the mirrors $M1$ and $M2$ in figs. 2.1 and 2.2 take over this job and their focal length is connected to their radii of cuvature by $f = \frac{R}{2}$. Beam propagation through a combined system of the above mentioned elements can now be done by firstly computing the transfer matrix of the entire conglomerate A_{sys}, by successive multiplication of the appropriate element matrices. Secondly the complex beam parameter at the exit of the optical arrangement, q_f, can be determined from the one at the entrance, q_i, by a functional dependence known as the ABCD law ([58], [57], [60], [86]). With a general transfer matrix

$$A_{sys} = \begin{pmatrix} A & B \\ C & D \end{pmatrix}, \tag{2.11}$$

it is denoted by ([58], [63]):

[6] Refer to section 3.3 for details.
[7] see section 4.1
[8] Others can e.g. by found in reference ([63]).

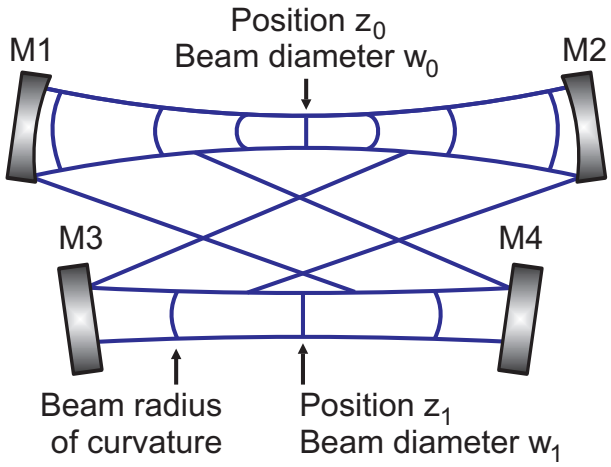

Figure 2.2: Our stable bow-tie cavity with a schematically conceptualised Gaussian beam. Two waists w_0, w_1 are obtained at positions z_0, z_1 in the middle of the distance between mirrors $M1$ and $M2$, or $M3$ and $M4$, respectively.

$$q_f = \frac{A \cdot q_i + B}{C \cdot q_i + D} \tag{2.12}$$

Within optical cavities one would like to store light without leakage, i.e. on the one hand optical ray-paths should be closed after a number of n round-trips in order to avoid rays to miss one of the cavity mirrors and thereby escape. On the other hand the beam diameter should not grow infinitely large after multiple round-trips, as otherwise it would exceed the mirror dimensions and light intensity is lost. The former can be translated into a requirement regarding the ray transfer matrix for a single round-trip, which should, after n round-trips, equalise itself after a single one, or more formally spoken:

$$A_{sys}^n \stackrel{!}{=} A_{sys} \Longleftrightarrow \begin{pmatrix} A & B \\ C & D \end{pmatrix}^n \stackrel{!}{=} \begin{pmatrix} A & B \\ C & D \end{pmatrix} \tag{2.13}$$

This expression can be evaluated ([58]) to yield an inequality for the diagonal entries in A_{sys}, the cavity stability criterion ([63]):

$$-1 < \frac{1}{2}(A + D) < +1 \tag{2.14}$$

Whenever A and D fulfill eq. (2.14) the underlying optical resonator can be regarded as stable, whereas otherwise it is unstable and light is lost after some period of time.
For properly designing our system we however must also have some information about the beam shape, which can be gained from the latter of the above stated conditions for light storage. Transforming it into a quantitative argument implies the complex beam parameter being forced to resemble itself after an arbitrary number of round-trips $\tilde{n}$. That means, the beam shape at the starting position $z_0 =$ is recovered after $\tilde{n}$ round-trips of stored light, whereby of course no light can in the meantime leak out of the system if it is stable. For our particular set-up, we would constantly like to have the same shape of the pumping beam impinging onto the BBO crystal. Thus the complex beam parameter has to be the same after every pulse circulation, restricting the requirement even further to $\tilde{n} = 1$:

$$A_{sys} \cdot q \stackrel{!}{=} q \tag{2.15}$$

A Gaussian beam obeying the consequences from the above stated conditions has also been drawn schematically in fig. 2.2.

Cavity radii of curvature As a first step towards the computation of the radii of curvature for the four cavity mirrors, referred to as R_{M1} to R_{M4}, depicted in fig. 2.2, the simplification of constructing a symmetric cavity is undertaken, whereby the axis of symmetry shall be located at exactly half the distance between mirrors $M1$ and $M2$ respectively $M3$ and $M4$, corresponding in turn to $R_{M1} = R_{M2}$ and $R_{M3} = R_{M4}$. Another constraint arises from the pumping geometry of the down-conversion process. It has been recognised within our group, that the SPDC process tends to work best, if the pumping beam diameter is on the order of $d_0^{\text{pump}} = 2w_0^{\text{pump}} = 200\,\mu m$ for a collinear type-II arrangement, as applied

here[9]. Additionally the phase fronts of the waves should be flat, i.e. $R_{\text{pump}} \to \infty$, wherefore the crystal is to be positioned at the focal plane of the pump. We furthermore intend to construct a set-up primarily devised for a single crystal to be accommodated between mirrors $M1$ and $M2$, thus only one focal spot of $d_0^{\text{pump}} \approx 200\,\mu m$ is needed. Therefrom the opportunity to go for yet another great simplification is enabled by choosing flat mirrors for the pair $M3$ and $M4$ with $R_{M3} = R_{M4} = \infty$. The focal length of these items will accordingly be $f_{M3} = f_{M4} = \infty$ as well. By consequently having all the off-diagonal elements in the mirror transfer matrices eq. (2.10) vanishing, we can ignore both mirrors in the context of the entire systems matrix A_{sys} and only account for the combined distance between mirror $M2$ and $M1$, named $d_{M2,M1} = d_{M2,M3} + d_{M3,M4} + d_{M4,M1}$ (see fig. 2.2), in the following. Since the entire length of the resonator is due to be $L_{cav} = 3.71\,m$, set by the measured laser repetition rate, the optical path within the denser BBO crystal[10] of just $L_{\text{BBO}} = 1\,mm$ thickness is negligible compared to the remainder in air[11] and will hence also be ignored. Such a simplification shall be noted to only be valid outside the regime of tight focussing, which would correspond to a waist sizes for the focussed laser beam of about $w_0 \leq 10\,\mu m$, therefore being fulfilled here. After these preconsiderations we can now evaluate the cavity's transfer matrix, which will be regarded in dependence of the two decisive parameters R_{M1} and $d_{M1,M2}$ by the replacement $d_{M2,M1} = L_{cav} - d_{M1,M2}$:

$$\begin{aligned}
A_{sys} &= \begin{pmatrix} 1 & 0 \\ -\frac{2}{R_{M1}} & 1 \end{pmatrix} \cdot \begin{pmatrix} d_{M2,M1} & \\ 0 & 1 \end{pmatrix} \cdot \begin{pmatrix} 1 & 0 \\ -\frac{2}{R_{M2}} & \end{pmatrix} \cdot \begin{pmatrix} 1 & d_{M1,M2} \\ 0 & 1 \end{pmatrix} \\
&= \begin{pmatrix} 1 & d_{M2,M1} \\ -\frac{2}{R_{M1}} & 1 - \frac{2d_{M2,M1}}{R_{M1}} \end{pmatrix} \cdot \begin{pmatrix} 1 & d_{M1,M2} \\ -\frac{2}{R_{M2}} & 1 - \frac{2d_{M1,M2}}{R_{M2}} \end{pmatrix} \\
&= \begin{pmatrix} 1 - \frac{2d_{M2,M1}}{R_{M2}} & d_{M1,M2} + d_{M2,M1} - \frac{2d_{M1,M2}d_{M2,M1}}{R_{M2}} \\ \frac{4d_{M2,M1}}{R_{M1}R_{M2}} - \frac{2}{R_{M1}} - \frac{2}{R_{M2}} & 1 - \frac{2d_{M1,M2}}{R_{M2}} - \frac{2d_{M1,M2}}{R_{M1}} - \frac{2d_{M2,M1}}{R_{M1}} + \frac{4d_{M1,M2}d_{M2,M1}}{R_{M1}R_{M2}} \end{pmatrix} \\
&= \begin{pmatrix} 1 - \frac{2L_{cav} - 2d_{M1,M2}}{R_{M1}} & L_{cav} - \frac{2d_{M1,M2}L_{cav} - 2d_{M1,M2}^2}{R_{M1}} \\ \frac{4L_{cav} - 4d_{M1,M2}}{R_{M1}^2} & 1 - \frac{2d_{M1,M2} + 2L_{cav}}{R_{M1}} + \frac{4L_{cav}d_{M1,M2} - 4d_{M1,M2}^2}{R_{M1}^2} \end{pmatrix}
\end{aligned} \tag{2.16}$$

There are still the two variables $\{R_{M1},\, d_{M1,M2}\}$ to be determined by the single condition (2.14) (eq. (2.15) does not contribute any additional restrictions), so some freedom in choice is available. We decide to start from a confocal scenario and assume some sensible radii of curvature for the mirrors $M1$ and $M2$. Subsequently, the distance between mirrors $M1$ and $M2$ is varied in such a way, to still satisfy the stability requirement (2.14) but to simultaneously yield a beam waist at the focus of the desired $w_0 = 100\,\mu m$ by the aid of eq. (2.15). This deviation in mirror spacing is hence the free parameter to be optimised for. A confocal arrangement implies $d_{M1,M2} = f_{M1} + f_{M2} = \frac{R_{M1}}{2} + \frac{R_{M2}}{2} = R_{M1}$: For reasons to be stated later, it is however far from being the best choice, since it is first not easy to align properly and second very sensitive to any external influences[12]. In other words, every slight deviation from perfect mirror orientation in combination with slight longitudinal mirror displacement can in principle render such a cavity unstable. Hence the introduction of an excess distance referred to as parameter a. The reason why a not a certain mirror distance is assumed and the radii of curvature are then optimised accordingly is as follows: The pursued approach stems from the very practical requirement to spot a decent manufacturer for qualitative high-reflective laser mirrors suitable for femto-second (fs) UV-laser pulses (i.e. low dispersion), which are able to sustain the enormous peak powers we are compelled to achieve inside the resonator. In their standardised versions, these mirrors come along with certain radii of curvature only[13]. Under these circumstances, the variation of the mirror separation, which can in principle be set to arbitrary and in practice to at least finer-than-a-cm-scale values, is sensible.
For the matrix in eq. (2.16) our approach means substitution of $d_{M1,M2}$ by $d_{M1,M2} = R_{M1} + a$. As it turns out, a rather useful choice is $R_{M1} = 0.8\,m$, which is a readily purchasable standard radius and furthermore satisfies all required needs as will be shown now: Insertion into eq. (2.14) leaves us with a possible excess distance range of

$$0\,m \leq a \leq 0.3673\,m \tag{2.17}$$

[9] Whereby $d_0^{\text{pump}} = 2w_0^{\text{pump}} = 400\,\mu m$ tend to work best for a non-collinear type-II set-up. For an explanation regarding both scenarios, see subsec. 6.1.1 later in the text.
[10] Extraordinary refractive index $n_{ext}^{\text{BBO}}(\lambda = 390\,nm) = 1.6683$, ordinary refractive index $n_{ord}^{\text{BBO}}(\lambda = 390\,nm) = 1.6953$
[11] Refractive index of air here take as $n_{\text{air}} = 1$, with a speed of light $c = 299709984.5\,\frac{m}{s}$. accounting for it
[12] thus also the difficulty in alignment
[13] Manufacturer: Layertec GmbH; Ernst-Abbe-Weg 1; 99441 Memmingen; Germany

within which the cavity is stable. We can furthermore evaluate the condition for the complex beam parameter, eq. (2.15). For an arbitrary cavity, symbolised by a propagation matrix (2.13), q can be evaluated, under the constraints set by eq. (2.15) and $AD - BC = 1$, to receive the general solution ([60]):

$$\frac{1}{q_{M1}} = -\frac{A-D}{2B} - i \cdot \frac{\sqrt{1 - \left(\frac{A+D}{2}\right)^2}}{B}, \tag{2.18}$$

which reduces for the appropriate system matrix, stated in eq. (2.16), to:

$$\begin{aligned}\frac{1}{q_{M1}} = &-\frac{2d_{M1,M2}^2 + 2d_{M1,M2}\left(R_{M1} - L_{cav}\right)}{2d_{M1,M2}^2 R_{M1} - 2L_{cav}d_{M1,M2}R_{M1} + L_{cav}R_{M1}^2} \\ &+\frac{i \cdot R_{M1}^2 \sqrt{\frac{(R_{M1}-d_{M1,M2})(d_{M1,M2}-L_{cav}+R_{M1})\left(d_{M1,M2}^2 - d_{M1,M2}L_{cav} + L_{cav}R_{M1}\right)}{R_{M1}^4}}}{2d_{M1,M2}^2 R_{M1} - 2L_{cav}d_{M1,M2}R_{M1} + L_{cav}R_{M1}^2}\end{aligned} \tag{2.19}$$

Insertion of the relevant numbers and inversion yields the final functional dependence of $q_{M1}(a)$ on the excess distance parameter a, given by[14]:

$$q_{M1}(a) = \frac{1}{2} \cdot \frac{2.40 + 1.43 \cdot \sqrt{-2.1099 + a} \cdot \sqrt{-1.74 + a} \cdot \sqrt{-0.37 + a} \cdot \sqrt{a}}{-3.01 + 1.43 \cdot a} + \frac{1}{2} \cdot \frac{1.87 \cdot a - 1.43 \cdot a}{-3.01 + 1.43 \cdot a} \tag{2.20}$$

Considering the beam waist to be retrievable from the complex beam parameter via

$$w(z) = \sqrt{\frac{-\lambda_p}{\pi \cdot \mathrm{Im}\left(1/q(z)\right)}} \tag{2.21}$$

provides the opportunity to examine the minimal beam waist in the symmetry point between mirrors $M1$ and $M2$. To do so, another propagation of the beam has to be implemented, since eq. (2.16) returns q_{M1} at the position of mirror $M1$. A convenient measure for the necessary distance is provided by the wavefront curvature of $q_{M1}(a)$ in eq. (2.20), given by

$$R_{z=z_{M1}}(a) = \left(\mathrm{Re}\left(\frac{1}{q_{M1}(a)}\right)\right)^{-1}, \tag{2.22}$$

since it provides the distance the point comprising plane wavefronts (i.e. the beam waist) is apart from the position of mirror $M1$ ($z = z_{M1}$). The relevant transfer matrix is thus given by:

$$A_{M1 \to z_{w_0}} = \begin{pmatrix} 1 & -R_{z=z_{M1}}(a) \\ 0 & 1 \end{pmatrix} \tag{2.23}$$

It shall be noted that $R_{z=z_{M1}}(a)$ has to be taken negatively according to the applied sign convention, since the laser beam is converging at $z = z_{M1}$. Calculation of the new complex beam parameter by the ABCD law (2.12) and subsequent extraction of the beam waist yields

$$w_{0,z=z_0}(a) = \sqrt{\frac{39}{100\pi}} \sqrt{-\left[\mathrm{Im}\left(\left[f(a) - \frac{1}{2}\mathrm{Re}\left(g(a)\right)\right]^{-1}\right)\right]^{-1}}, \tag{2.24}$$

with

$$\begin{aligned} f(a) &= \frac{2.41 + 1.42\sqrt{-2.11 + a} \cdot \sqrt{-1.74 + a} \cdot \sqrt{-0.37 + a} \cdot \sqrt{a} + a \cdot 1.87 - a^2 \cdot 1.42}{2a \cdot 1.43 - 2 \cdot 3.01} \\ g(a) &= \frac{2.41 + 1.43 \cdot \sqrt{-2.11 + a} \cdot \sqrt{-1.74 + a} \cdot \sqrt{-0.37 + a} \cdot \sqrt{a} + a \cdot 1.87 - a^2 \cdot 1.43}{a^2 \cdot 1.43 - 3.01} \end{aligned}$$

The above expression is plotted as a function of the excess distance a in fig. 2.3. We can infer the minimum beam waist $w_0(a)$ to reach the desired value of roughly $100\,\mu m$ within a range of approximately $0.15\,m \leq a \leq 0.23\,m$, which offers the property of having a shallow gradient. Such a behaviour is very

[14] This equation shall be noted to contain a non-vanishing imaginary part since $a < 0.37$.

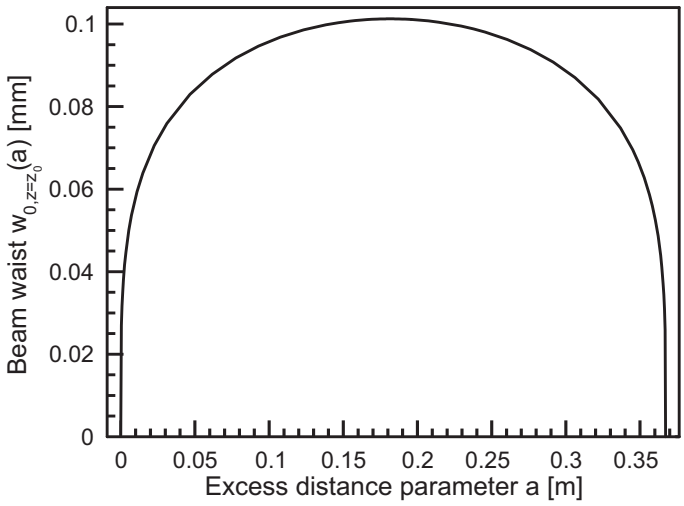

Figure 2.3: Minimum beam waist $w_{0,z=z_0}(a)$, eq. (2.24), as a function of the excess distance a. A region of shallow gradient and thus insensitivity to distance changes is apparent for $0.15\,m \leq a \leq 0.23\,m$, offering stability in the SPDC pump geometry.

much favourable, since it allows for small misadjustments of the mirror separation without spoiling the beam size and therefore influencing the down-conversion process remarkably. In other words the beam waist does not change much if a is varied within the aforementioned region, in contrast to the situation at the proximities of the stable cavity interval ($a \approx 0\,m$ and $a \approx 0.3673\,m$) where $w_0(a)$ is strongly susceptible to any changes in a. Especially since such deviations are not only created by systematic alignment errors, but also by thermal fluctuations of the resonator system, it is very pleasant to have a range of approximately $8\,cm$ available over which the beam waist is roughly not altered.
To gain greatest advantage out of the insensitivity region, the point with a gradient $\frac{dw_0(a)}{da} = 0$ will be chosen as excess distance, corresponding obviously to the maximum in fig. 2.3 at $a = 0.182\,m$. Hence the beam waist at the BBO crystal, as well as the distances between the mirrors $M1 \leftrightarrow M2$ and $M3 \leftrightarrow M4$ reach values of:

$$w_0 = 101\,\mu m \quad ; \quad d_{M1,M2} = 0.982\,m \quad ; \quad d_{M2,M1} = 2.728\,m \tag{2.25}$$

We acknowledge our initial assumption of having $R_{M1} = R_{M2} = 0.8\,m$ to be justified, fulfilling all requirements for stability and mode geometry. With the particular choice of distances, the cavity set-up is determined completely as is the optical mode within it. The wavefront curvature and beam waist of the latter can hence be analysed as a function of position along the cavity's optical axis (z-axis). Appropriate calculations are once again performed with the transfer matrices, whereby a variable propagation distance z has to be inserted. For the part of the resonator between mirrors $M1$ and $M2$, referred to as sector 1, the corresponding matrix is given by:

$$A_{\text{sec.1}}(z) = \begin{pmatrix} 1 & z \\ 0 & 1 \end{pmatrix}, \tag{2.26}$$

in contrast to sector 2, with the beam going back from $M2$ to $M1$ via $M3$ and $M4$, in which case $A_{\text{sec.1}}(R + a)$ and the mirror matrix for $M2$ have to be applied prior to another propagation matrix of variable distance z:

$$\begin{aligned} A_{\text{sec.2}}(z) &= \begin{pmatrix} 1 & z \\ 0 & 1 \end{pmatrix} \cdot \begin{pmatrix} 1 & 0 \\ -\frac{2}{R_{M2}} & 1 \end{pmatrix} \cdot \begin{pmatrix} 1 & d_{M1,M2} \\ 0 & 1 \end{pmatrix} \\ &= \begin{pmatrix} 1 - \frac{2z}{R_{M2}} & d_{M1,M2} + z - \frac{2z d_{M1,M2}}{R_{M2}} \\ -\frac{2}{R_{M2}} & 1 - \frac{2 d_{M1,M2}}{R_{M2}} \end{pmatrix} \end{aligned} \tag{2.27}$$

If we apply both matrices to the complex beam parameter at $M1$, $\frac{1}{q_{M1}} = \frac{1}{R_{M1}} - i\frac{\lambda}{\pi w_{M1}^2}$, the beam radii $w(z)$ and wavefront curvatures $R(z)$ can be extracted by eqs. (2.21) and (2.22) at any position $z \in [0, L_{cav}]$. Results have been plotted in fig. 2.4 for $w(z)$ on the left and $R(z)$ on the right hand side. There are not surprisingly two focal spots apparent, whereby the second one w_1 is located at the

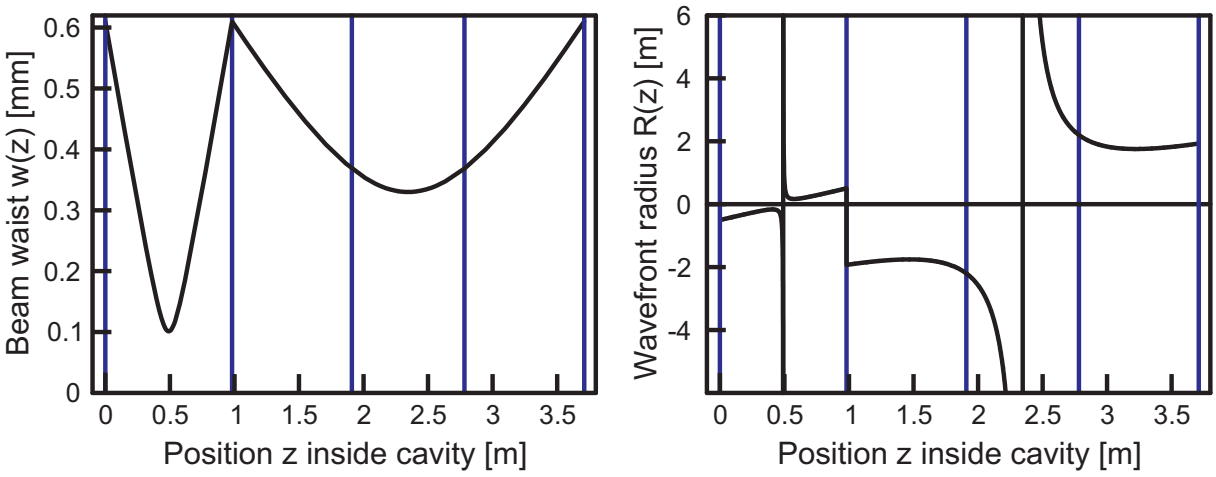

Figure 2.4: Beam waist $w(z)$ (left) and wavefront radius of curvature $R(z)$ (right) over entire length of the cavity $z \in [0, L_{cav}]$. Two focal points are present, where $R(z)$ diverges to infinity and $w(z)$ adopts its minimal values of $w_0 = 101\,\mu m$ and $w_1 = 330\,\mu m$. Into the former focal point, the BBO crystal will be placed.

symmetry point z_1 in the middle of the distance between mirrors $M3$ and $M4$, i.e. $\Delta z = 1.364\,m$ away from either mirror, exhibiting a waist size of $w_1 = 330\,\mu m$. So positioning a second non-linear crystal here would offer the opportunity to implement two photon pair sources within a single cavity. Certain types of experiments, like quantum telecloning ([16], [21], [22]), needing one multiphoton entangled state and one single qubit, commonly generated by heralding a SPDC source ([49]), would consequently become feasible with our apparatus as well. Furthermore a second crystal would also negatively influence the dispersion properties of the resonator, thus changing the pump spectrum and the amount of generated SPDC photons per time, as we shall see throughout the remainder of this text[15]. So an implementation of such a quantum information protocol would require some further calculations regarding expected count rates.
The singularities of the wavefront curvature in fig. 2.4 correspond to focus positions since plane waves with $R(z = \{z_0, z_1\}) \rightarrow \pm\infty$ are expected there. The uncontinuous jumps at the positions of mirror $M1$ and $M2$ account for the change in wavefront radius of curvature imparted by mirror lensing effects that follow the well known thin lens equation ([63]), $\frac{1}{R_{\text{final}}} = \frac{1}{R_{\text{initial}}} - \frac{2}{R_{\text{mirror}}}$, embedded in the transfer matrix method. Clearly $M3$ and $M4$ do not cause such modifications because of their flatness $R_{M3} = R_{M4} = \infty \rightarrow \frac{2}{R_{\text{mirror}}} = 0 \rightarrow \frac{1}{R_{\text{final}}} = \frac{1}{R_{\text{initial}}}$. The saddle points in the $R(z)$ function occur at the Rayleigh range $z = z_{\{1,2\}} \pm z_{R_{\{1,2\}}}$ of each focus as the wavefront has its greatest values there. One final word about the wavefront curvatures at the locations of $M1$ and $M2$, being $R(z_{M1}) = -0.5047\,m$ and $R_{z_{M2}} = 0.5047\,m$. These are obviously unequal to the mirror curvatures of $R_{i\in\{M1,M2\}} = \mp 0.8\,m$. Such a behaviour might seem counterintuitive to the commonly known situation of a two mirror cavity, whose mirror curvatures must match those of the beam wavefronts. However for ring cavities this requirement is not valid anymore as the beam would otherwise be reflected back into itself again, i.e. within both sectors 1 and 2 the complex beam parameter $q(z)$ would have to be exactly the same at equal distances z say to either side of mirror $M2$. Clearly that is impossible already by the mere fact of having different lengths in both sectors ($d_{M1,M2} < d_{M2,M1}$).

Resonator stability diagram What is still pending now is to assess the stability of a cavity implemented with the above set of parameters. The insensitivity against small changes in the excess parameter a and consequently in the mirror separations $d_{M1,M2}$, $d_{M2,M1}$ has already been mentioned (see fig. 2.3). Deviations in the proper mirror positioning or orientation, affecting the values for the radii of curvature, in combination with distance alteration have not yet been discussed. However there is a very convenient scheme available to do so, which is known as the stability diagram (see e.g. [57], [58], [63]). Although the aforementioned method is normally only applicable for two mirror resonators, it is extendable to our situation under the assumption of symmetry around z_0, i.e. $R_{M1} = R_{M2} = \bar{R}$. We can rewrite the stability criterion, eq. (2.14), to:

[15] Particularly outlined in subsec. 2.1.4, 2.1.5 and 6.3.2

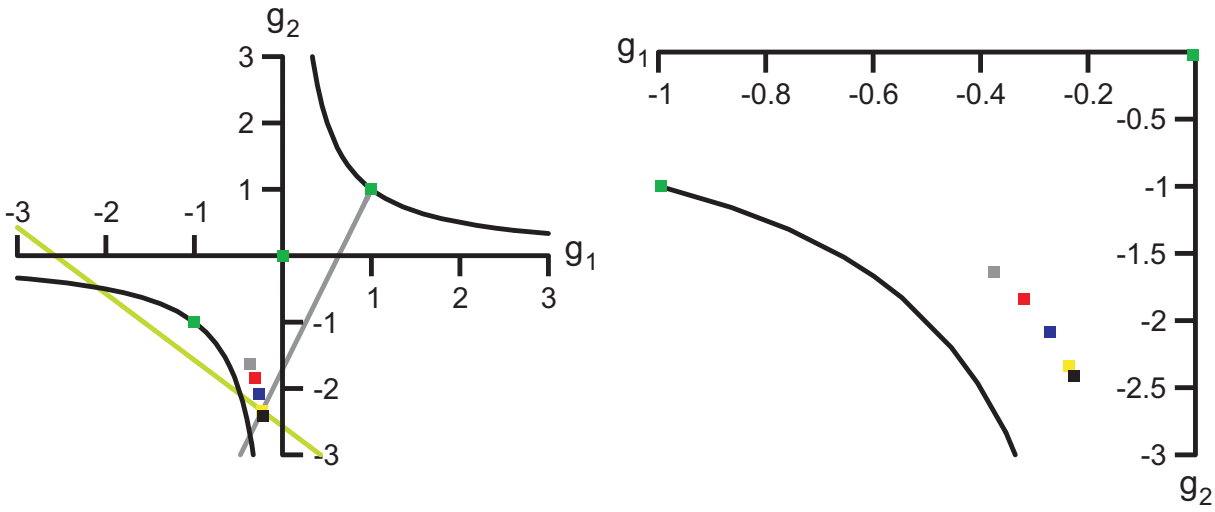

Figure 2.5: Stability diagram for cavity. The black point indicates the positioning of the full length cavity with $L_{cav} \approx 3.71\,m$. The gray, red, blue and yellow boxes are the locations of a cavity with half length $L'_{cav} \approx 1.83\,m$, as described further in subsec. 2.2.1. Ultimately the green symbols represent commonly known symmetric two mirror arrangements, namely confocal cavities with $d = R$ and $\{g_1 = 0, g_2 = 0\}$, concentric cavities with $d = 2R$ and $\{g_1 = -1, g_2 = -1\}$ as well as planar cavities with $R = \infty$ and $\{g_1 = 1, g_2 = 1\}$. Since all three of these are lying at the stability boundaries in the diagram, they are very susceptible to negative influences and potentially quickly loose their stability under such slight disturbances. The straight grey line accounts for the change in the stability parameters, starting from a cavity of $f_{rep} \approx 160\,MHz$ repetition rate and mirror radii of curvatures of $R_{M1,M2} = 0.4\,m$, by variation of the values for $R_{M1,M2}$, while keeping $d_{M1,M2}$ and $d_{M2,M1}$ fixed, whereby the green line shows a treatment of the opposite variational scenario; both are discussed in subsec. 2.2.1.

$$-1 < \frac{1}{2} Tr\left(A_{sys}\right) < +1 \Longleftrightarrow 0 < \frac{1}{4} Tr\left(A_{sys}\right) + \frac{1}{2} < +1 \tag{2.28}$$

Using the transfer matrix for our system (eq. (2.16)), we get:

$$\begin{aligned}
0 < & \frac{1}{4}\left(1 - \frac{2d_{M2,M1}}{R_{M2}} + 1 - \frac{2d_{M1,M2}}{R_{M2}} - \frac{2d_{M1,M2}}{R_{M1}} - \frac{2d_{M2,M1}}{R_{M1}}\right) \\
& + \frac{1}{4}\left(\frac{4d_{M1,M2}d_{M2,M1}}{R_{M1}R_{M2}}\right) + \frac{1}{2} < 1 \\
\Leftrightarrow 0 < & 1 - \frac{d_{M2,M1}}{2\bar{R}} - \frac{d_{M1,M2}}{2\bar{R}} - \frac{d_{M1,M2}}{2\bar{R}} - \frac{d_{M2,M1}}{2\bar{R}} + \frac{d_{M1,M2}d_{M2,M1}}{\bar{R}^2} < 1 \\
\Leftrightarrow 0 < & 1 - \frac{d_{M1,M2}}{\bar{R}} - \frac{d_{M2,M1}}{\bar{R}} + \frac{d_{M1,M2}d_{M2,M1}}{\bar{R}^2} < 1 \\
\Leftrightarrow 0 < & \underbrace{\left(1 - \frac{d_{M1,M2}}{\bar{R}}\right)}_{=:g_1}\underbrace{\left(1 - \frac{d_{M2,M1}}{\bar{R}}\right)}_{=:g_2} < 1 \\
\Leftrightarrow 0 < & \, g_1 \cdot g_2 < 1
\end{aligned} \tag{2.29}$$

For our set of cavity parameters, the g_1 and g_2 factors yield $g_1 = -0.23$ and $g_2 = -2.41$. The point $\{g_1, g_2\}$ can now be plotted in a graphic, showing g_2 over g_1, which is called the stability diagram. The boundaries of the inequality (2.29) can be inserted therein as well, defined by $g_2 = \frac{1}{g_1}$, $g_1 = 0$ and $g_2 = 0$. Such a representation is provided in fig. 2.5, whereby all parameter sets $\{g_1, g_2\}$ that lie within the area enclosed by the coordinate axes and the black hyperbulae represent stable resonator systems, according to eq. (2.29). The left figure shows an overview of the entire stability diagram, whereas the right figure focusses onto the interesting part for our particular situation. The green points in the former represent common, symmetric two-mirror cavity systems, whose properties are discussed thoroughly in references ([57], [58], [86]). The diagram 2.5 offers now the intriguing possibility to estimate what happens if either the mirror separations $d_{M1,M2}$, $d_{M2,M1}$ or the mirror radii of curvature R_{M1}, R_{M2} are slightly changed[16]. Such an

[16] The latter e.g. by changing the angular orientation of the mirror.

alteration would consequently modify the respective parameter $g_1 \to g_1 + \Delta g_1$ or $g_2 \to g_2 + \Delta g_2$ leading to a displacement of the cavity position in the diagram. If one of the above mentioned stability boundaries is crossed thereby, the resonator becomes unstable and no intensity build-up is possible anymore. Hence a sophisticated arrangement should stay as far off these boundaries as possible. Comparing the location of our cavity to the confocal two-mirror scenario at $g_{1,2} = 0$, explains the reason for including the excess distance a in order to specifically not have a confocal arrangement which is most sensitive in its stability to disturbances. Therefore also the highest gradients of the beam waist $w_0(a)$ are located around $a = 0$ in fig. 2.3. Fig. 2.5 implies that our particular choice of parameters allows for some errors, i.e. the datapoint symbolising the cavity has some additional stable space around it, however it is still far off the ideal position, located around the parameter set $\{g_1, g_2\} = \{\pm\frac{1}{2}, \pm\frac{1}{2}\}$. Nevertheless it will turn out to be sufficient for our needs. Stable locking conditions, depending also on some other frequency related parameters examined later on, can be preserved over time scales of days, which is indeed quite good for pulsed optical resonators. The positioning of the device within the stability diagram is hence convenient. In addition to the just stated analysis an approximation made shall be mentioned: In deriving eq. (2.29), a symmetric cavity arrangement has been assumed, i.e. R_{M1} has been set equal to R_{M2}. However if e.g. a deviation is introduced in only one of both radii, say $M1$[17], this implies, generally speaking, $R_{M1} = x \cdot R_{M2}$, causing eq. (2.28) not to factorise anymore like in eq. (2.29). The non-factorisability is also the reason why the stability diagram is only applicable for two mirror cavities or symmetric ring cavities, which in fact resemble a two mirror system. Nevertheless if deviations from the symmetric situations are small, i.e. $R_{M1} \to R_{M1} + \Delta R_{M1}$ with $\Delta R_{M1} \ll R_{M1}$, as expected for slight misadjustments, mismanufacturing, thermal drifts etc., the parameter g_1 can be Taylor expanded according to:

$$g_1^{\text{dev}} = 1 - \frac{d_{M1,M2}}{R_{M1}} + \Delta R_{M1} \approx 1 - \frac{d_{M1,M2}}{R_{M1}} + \frac{d_{M1,M2}}{R_{M1}^2} \cdot \Delta R_{M1} + ...$$

Insertion into eq. (2.29) returns:

$$\begin{aligned} g_1^{\text{dev}} \cdot g_2 &= \left(1 - \frac{d_{M1,M2}}{R_{M1} + \Delta R_{M1}}\right) \cdot \left(1 - \frac{d_{M2,M1}}{R_{M2}}\right) \\ &= \left(1 - \frac{d_{M1,M2}}{R_{M1}} + \frac{d_{M1,M2}}{R_{M1}^2} \cdot \Delta R_{M1}\right) \cdot \left(1 - \frac{d_{M2,M1}}{R_{M2}}\right) \\ &\overset{(*)}{=} \underbrace{1 - \frac{d_{M1,M2}}{R_{M1}} - \frac{d_{M2,M1}}{R_{M2}} + \frac{d_{M1,M2} d_{M2,M1}}{R_{M1} R_{M2}}}_{= g_1 \cdot g_2} + \underbrace{\frac{d_{M1,M2}}{R_{M1}^2} \Delta R_{M1}}_{\to 0} - \underbrace{\frac{d_{M1,M2} d_{M2,M1}}{R_{M2} R_{M1}^2} \Delta R_{M1}}_{\to 0} \\ &\approx g_1 \cdot g_2 \end{aligned} \tag{2.30}$$

Step $(*)$ is justified since $\Delta R_{M1} \ll R_{M1} \vee R_{M2}$. Of course this is just a crude simplification, but it proves the factorisability of eq. (2.29) not to be influenced too tremendously by considering the system's behaviour under stability estimation.
There is also a counterintuitive point to be gathered from fig. 2.5: While all symmetric two mirror resonator are positioned on the straight line connecting the three green points, ring cavities, symmetric in their mirror radii but comprising unequal mirror separations, do not show this feature for the simple reasons that $d_{M1,M2} \neq d_{M2,M1}$ directly leads to $g_1 \neq g_2$ and consequently to a growing separation from this line for increasing differences between $d_{M1,M2}$ and $d_{M2,M1}$.

Summary All important geometrical design parameters for the enhancement resonator of $f \approx 80\,MHz$ repetition rate have now been derived and are summarised in appendix A.1. Since beam diameters at the four mirrors are small enough, half-inch optics can be employed and an even smaller component for one mirror, used for the later introduced cavity stabilisation, is possible allowing for fast enough regulation frequencies (see subsec. 3.2.1). The next step in the design process is now to determine the mirror reflectivities and transmittivities, whose values are connected to the cavity loss and the desired future applications.

2.1.2 Loss inside cavity and cavity Finesse

To allow for best enhancement properties, the losses in the resonator should obviously be as low as possible. From this perspective it is demanded to use coatings for mirrors $M1$, $M2$ and $M4$ (fig. 2.2)

[17] or alternatively a different one for either of both

with high reflectances R. Since the mirror $M2$ shall furthermore be employed as an output coupler for the infra-red photons, generated by the SPDC process, a high transmittance T within their wavelength range is desired for this particular constituent. A central wavelength of $\lambda_{SPDC} \approx 780\,nm$ and a full width half maximum (FWHM) spectral width on the order of $\Delta\lambda \approx 9\,nm$ are to be expected for the down converted light, as we will see in subsec. 5.3.3. Suitable components, meeting these requirements, have been purchased from the company Layertec[18].
For the moment, we are only concerned by the properties regarding UV power storage. For the mirrors $M1$, $M2$, $M4$ a transmission of $T_i = 0.0002\hat{=}0.02\,\%$ is obtained, corresponding to a reflectance of $R_i = 1 - T_i = 0.9998\hat{=}99.98\,\%$, with $i \in \{M1, M2, M3\}$. For a combination of all three mirrors the reflectance accumultes to

$$R_{M1,M2,M3} = R_{M1} \cdot R_{M2} \cdot R_{M3} = (0.9998)^3 = 0.9994\hat{=}99.94\,\% \tag{2.31}$$

Besides these reflectors, we also have air and a $1\,mm$ thick BBO crystal[19] incorporated into the set-up, which also contribute to the overall losses. For the latter an averaged absorption specification at $\lambda = 266\,nm$ of $\alpha_{\mathrm{BBO}} \approx 0.1\,\frac{1}{cm}$ can be found ([67]), which is anticipated to be similar for our wavelength range. So a transmittance of $T^{abs.}_{\mathrm{BBO}} = 1 - \exp(-0.01) = 0.99005\hat{=}99.01\,\%$ can be expected. The crystal is anti-reflection (AR) coated at around $390\,nm$, adding an extra reflection loss of $R^{refl.1}_{\mathrm{BBO}} \approx 0.4\,\%$ at the incidence surface and $R^{refl.2}_{\mathrm{BBO}} = 0.1\,\%$ at the exit surface. So ultimately the non-linear medium has a transmittance of

$$T^{theo}_{\mathrm{BBO}} = T^{abs.}_{\mathrm{BBO}} \cdot (1 - R^{refl.1}_{\mathrm{BBO}}) \cdot (1 - R^{refl.2}_{\mathrm{BBO}}) = 0.9851\hat{=}98.51\,\%. \tag{2.32}$$

The direct measurement of this quantity, yielding

$$T^{exp}_{\mathrm{BBO}} = 0.975\hat{=}97.5\,\%, \tag{2.33}$$

reveals acceptable agreement with these supplier specifications and shall be used for the further analysis. Air contributes by an absorption coefficient of $\alpha_{\mathrm{air}} = 0.27\,\frac{1}{km}$ ([68]), averaged between $337\,nm$ and $488\,nm$, with a transmittivity of $T_{\mathrm{air}} = 0.999\hat{=}99.9\,\%$, loosing $0.1\,\%$ of the pulse intensity during one round-trip in the resonator. Altogeher the accumulated transmission T^{noIC}_{cav}, neglecting mirror $M3$, and the associated loss, R^{noIC}_{cav}, can be computed to

$$T^{\mathrm{noIC,\ BBO}}_{cav} = T^{exp}_{\mathrm{BBO}} \cdot T_{\mathrm{air}} \cdot (1 - R_{M1,M2,M3}) = 0.9734\hat{=}97.34\,\% \tag{2.34}$$

$$R^{\mathrm{noIC,\ BBO}}_{cav} = 1 - T^{\mathrm{noIC,\ BBO}}_{cav} = 0.0266\hat{=}2.66\,\% \tag{2.35}$$

and without the non-linear crystal

$$T^{\mathrm{noIC,\ noBBO}}_{cav} = T_{\mathrm{air}} \cdot (1 - R_{M1,M2,M3}) = 0.9984\hat{=}99.84\,\% \tag{2.36}$$

$$R^{\mathrm{noIC,\ noBBO}}_{cav} = 1 - T^{\mathrm{noIC,\ noBBO}}_{cav} = 0.0016\hat{=}0.16\,\% \tag{2.37}$$

are obtained. Following the customary approach for cw cavities, the remaining input coupler $M3$ has now to be chosen in such a way to reach a steady state field inside the resonator ([57]). That is to say, the intensity transmission through $M3$ has to cancel the losses experience by light already stored inside the resonator. Disregarding absorption by the input coupler, its transmission should hence equal the numbers in eqs. (2.34) and (2.36) yielding theoretical[20] reflectances of

$$R^{\mathrm{IC,\ BBO,\ theo}}_{cav} = 0.9734\hat{=}97.34\,\% \tag{2.38}$$

$$R^{\mathrm{IC,\ noBBO,\ theo}}_{cav} = 0.9984\hat{=}99.84\,\% \tag{2.39}$$

For ultra-fast optical enhancement resonators, the criterion for input coupler selection is somewhat more subtle though and the frequency comb structure of the mode-locked pulses has to be considered as well ([58], [73]). This will be done now, by consideration of the power enhancement inside the cavity, which also permits to understand the influences of loss and associated finesse changes.
The derivation will start within the time domain and looking at pulse propagation inside an arbitrary

[18] Layertec GmbH, Ernst-Abbe-Weg 1, 99441 Mellingen, Germany
[19] Newlight Photonics, 264 Westmoreland Avenue, Toronto, ON M6H 3A5, Canada
[20] Theoretical in terms of not every arbitrary relectance to be producible.

resonator system, as shown in fig. 2.1. However for simplicity we will still stick to regarding only a single frequency component ω within our pulse spectrum for the moment and subsequently extend the expression to the full picture later. Observing fig. 2.1, an electric field of E_0 is present in front of the input coupler, here denoted as $M1$, and the intra-cavity field just after propagation through this device is $t_{IC} \cdot E_0$. During one round-trip, the field is reflected off mirror $M2$, with a reflectivity of r_{M2}, and suffers losses inside the resonator, described by a lowered transmittivity $t_{loss}(\omega) < 1$. Furthermore there are also additional phase shifts occuring due to dispersion, which add a factor of $\exp(-i\Phi(\omega))$, so the entire field after one circulation inside the cavity is $E = t_{IC}t_{loss}r_{M2}r_{IC}E_0 \exp\left(i\left(\frac{\omega}{c}L_{cav} + \Phi(\omega)\right)\right)$. If the repetition rate of the resonator now matches the pumping laser, the electric fields are superimposed after every round-trip with light just coupled in, leading, in the steady state limit, to an overall field within the resonator, which resembles the geometric progression

$$\begin{aligned} E_{cav} &= t_{IC}E_0 + t_{IC}E_0 t_{loss} r_{M2} r_{IC} e^{\left(i\left(\frac{\omega}{c}L_{cav}+\Phi(\omega)\right)\right)} + t_{IC}E_0 \left(t_{loss} r_{M2} r_{IC} e^{\left(i\left(\frac{\omega}{c}L_{cav}+\Phi(\omega)\right)\right)}\right)^2 + ... \\ &= t_{IC}E_0 \sum_{n=0}^{\infty} \underbrace{t_{loss} r_{M2} r_{IC} e^{\left(i\left(\frac{\omega}{c}L_{cav}+\Phi(\omega)\right)\right)}}_{=:G(\omega)} = \frac{t_{IC}E_0}{1-G(\omega)}, \end{aligned} \tag{2.40}$$

whereby the quantity $G(\omega)$ is called the net round-trip gain[21]. This picture is readily extended to our situation by substituting $t_{loss}(\omega) = \sqrt{T^{exp}_{\mathrm{BBO}}(\omega) \cdot T_{\mathrm{air}}(\omega)}$ and $r_{M2}(\omega) = \sqrt{R_{M1,M2,M3}(\omega)}$. The effects of losses and all mirrors but the input coupler can be accumulated to yet another constant $r^{\mathrm{noIC}}(\omega) = \sqrt{T^{exp}_{\mathrm{BBO}}(\omega) T_{\mathrm{air}}(\omega) R_{M1,M2,M3}(\omega)}$ and additional inclusion of r_{IC} gives the quantitiy $r(\omega) = r_{IC}(\omega) r^{\mathrm{noIC}}(\omega)$. Computing the power enhancement PE, which will be defined for the purposes stated in this thesis as power inside the resonator with respect to power in front of the input coupler, the following expression is achieved ([51], [52]):

$$PE(\omega) = \frac{|E_{cav}|^2}{|E_0|^2} = \frac{|t_{IC}(\omega)|}{1 + r(\omega) - 2r(\omega)\cos\left(\frac{\omega}{c}L + \Phi(\omega)\right)} = \frac{|t_{IC}(\omega)|}{1 + r(\omega) - 2r(\omega)\cos\left(\phi(\omega)\right)} \tag{2.41}$$

and the electric field E_{cav} will acquire a phase shift of ([51])

$$\Psi(\omega) = \arctan\left(\frac{r(\omega)\sin\left(\frac{\omega}{c}L + \Phi(\omega)\right)}{1 - r(\omega)\cos\left(\frac{\omega}{c}L_{cav} + \Phi(\omega)\right)}\right) + \arg\left(t_{IC}(\omega)\right) \tag{2.42}$$

The power enhancement comprises resonances whenever the argument of the cosine in eq. (2.41) equals an integer multiple of 2π. Anticipating the additional phase shift Φ to be constant[22], the resonance condition for the pumping light frequency translates into $\omega \stackrel{!}{=} n \cdot \frac{2\pi c}{L_{cav}} = n \cdot \omega_{FSR}$, with the free-spectral range (FSR) of the cavity denoted by $\omega_{FSR} = \frac{2\pi c}{L_{cav}} = 2\pi f_{rep}$, which corresponds to the pulse repetition rate of the resonator. An intriguing visualisation of aforementioned requirement is shown in fig. 2.6 b), simplifying the system by a two mirror arrangement once more. Intensity built-up is possible, whenever the pumping wavelength is chosen to match the length of the resonator in such a way to show anti-nodes at both mirror positions and a complete oscillation period of the electric field in between. The separation between two of these suitable wavelengths is expressed by the free spectral range $\lambda_{FSR} = \frac{2\pi c}{\omega_{FSR}}$. Please also note the difference between a two mirror arrangement and a ring cavity in this context: While the former allows for half wavelengths as well, thereby exhibiting a FSR of $\omega^{2\,\mathrm{mirror\ cav.}}_{FSR} = \frac{c}{2L_{cav}}$, a ring-shaped arrangement permits complete wavelengths only, consequently a FSR of $\omega^{\mathrm{ring\ cav.}}_{FSR} = \frac{c}{L_{cav}}$ twice as big (as plotted in fig. 2.6 b)). The power enhancement of a individual resonance is displayed in fig. 2.6 a), whereby the full width at half maximum (FWHM) of the peak is given for low loss cavity, i.e. $1 - r \approx 1$ by ([51])

$$\Delta\omega_{FWHM} = \frac{1-r}{\pi\sqrt{r}} =: \frac{\omega_{FSR}}{F} \tag{2.43}$$

The quantity $F = \frac{\pi\sqrt{r}}{1-r}$ is named the finesse of the cavity and constitutes a measure for the resonance widths, as can be inferred from the above definition. It is also connected to the losses inside the system, by being proportional to $r(\omega) \sim t^{exp}_{\mathrm{BBO}}(\omega) t_{\mathrm{air}}(\omega) r_{M1,M2,M3}(\omega) r_{IC}(\omega)$, and frequency dependent. If the losses increase, i.e. $r \searrow$, the finesse decreases ($F \searrow$) and the resonance widths rise ($\Delta\omega_{FWHM} \nearrow$). Accordingly the number of round-trips of the stored, circulating electric field shrink as well; so the finesse

[21] The progression converges because $t_{loss}, r_{M2}, r_{IC} < 1$.

[22] This is not the case in reality, since dispersion in the resonator is wavelength dependent, as we will shortly see.

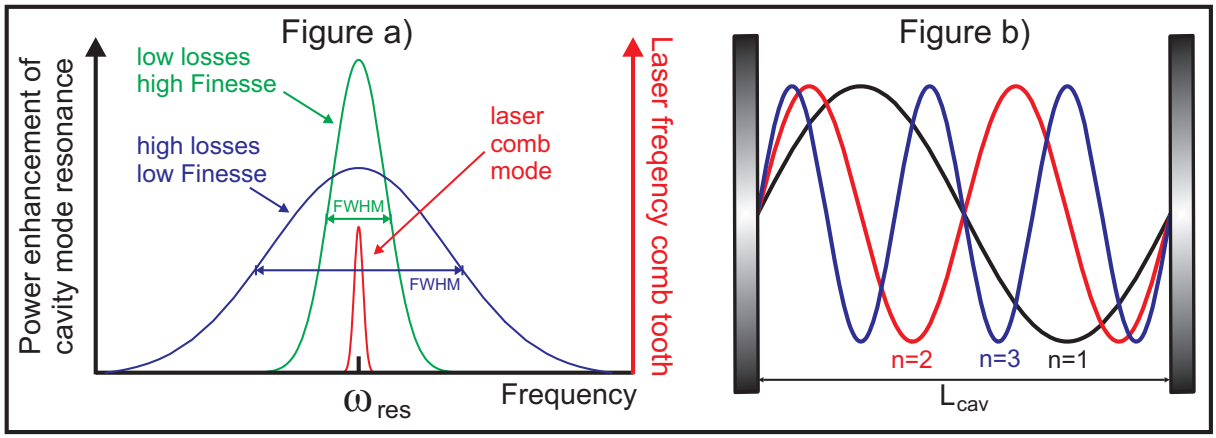

Figure 2.6: Cavity resonances. Fig. a): Schematic power enhancement of cavity resonance as function of frequency. The resonance has a width proportional to the intra-cavity loss and thereby to the finesse F. To achieve coupling, the red laser frequency comb tooth has to overlap with the resonance, which is easier to fulfil for systems of lower finesse. However these have lower enhancement as indicated by the height of the cavity resonance. Fig. b): Schematic representation of resonance condition, simplified by a two mirror arrangement. Intensity build-up is achieved, whenever the wavelength matches the cavity length in terms of having an anti-node at the locations of the end mirrors, containing a full oscillation period in between. The character n denotes the number of the resonance.

is furthermore a representative for this property as well. It will be evaluated experimentally later on in section 4.3. An important observation to be made from fig. 2.6 a) are narrowed peak widths for higher finesse values. This implies for our set-up, that the BBO crystal will lower the achievable enhancement of stored UV pulses due to higher losses, however simultaneously broadens the individual cavity resonances, rendering it therefore easier to hit these by the external pumping frequencies[23], as we will see shortly in subsec. 2.1.4.
For the initial question concerning input coupler choice for pulsed resonator system, the above discussion suggests to utilise a mirror reflectivity r_{IC}, which maximises the power enhancement or alternatively the intra-cavity pulse power. However in order to do so, the full frequency spectrum of the pumping pulses has to be considered due to the proportionality of PE to ω in eq. (2.41). So we will also have to include the wavelength dependence of the refractive indices of air and the BBO crystal into the investigations, as they influence $\phi(\omega)$ in eq. (2.41). The mirror reflectivities and losses in the cavity remain to be assumed wavelength independent.

2.1.3 Power-enhancement and input coupler choice

Cavity mirror influences As a first step towards phase estimations inside the resonator, the influences of the cavity mirrors shall be neglected. These only add dispersion contributions to the phase, which are minor compared to the numbers the BBO crystal and air impart on the UV pulses. From the group-velocity dispersion (GVD) graph for the actually implemented mirrors, provided by the manufacturer, values within the spectral region of the pumping pulse ($\lambda_{UV} \in \{389.45\,nm, 390.55\,nm\}$) on the order of approximately $10\,fs^2$ are obtained. Mirror effects can thus be disregarded for the remainder of all dispersion examinations, since having only air inside the resonator already causes a $GVD_{\text{air}}(\lambda = 390\,nm) \approx 191\,fs^2$ and with the additional non-linear crystal the entire resonator filling distorts the pulse by a $GVD_{\text{air+BBO}}(\lambda = 390\,nm) \approx 378\,fs^2$. The GVD and the figures just mentioned will be analysed more closely in subsec. 2.1.5.

Refractive index of air and BBO What is left is to evaluate the contributions made by the BBO crystal and air. Both influence the round-trip phase $\phi(\omega) \Longleftrightarrow \phi(\lambda)$ by the wavelength dependence of their refractive indices. This is commonly described by the Sellmeier equation ([69], [72], [101]), given in its most general form by:

[23] These shall be noted to have much smaller linewidths than $\Delta\omega_{FWHM}$ of the resonator, so there is some frequency interval which they can be displaced over, while still yielding approximately equal overlap with the cavity resonances.

$$n(\lambda)^2 = A + \frac{B}{C - \frac{1}{\lambda^2}} + \frac{D}{E - \frac{1}{\lambda^2}} \tag{2.44}$$

with A, B, C, D and E being material specific constants. For air the necessary parameters can be found in reference ([70], [71]), providing an index function of:

$$n^{\text{air}}(\lambda) = 1 + \frac{8342.54 + \frac{15998\,\mu m^2}{38.9\,\mu m^2 - \frac{1}{\lambda^2}} + \frac{2406147\,\mu m^2}{130\,\mu m^2 - \frac{1}{\lambda^2}}}{100000000} \tag{2.45}$$

with λ in units of μm. The constants are evaluated at a temperature of $T = 15^\circ\,C$ and pressure of $p = 101325\,Pa$ with a carbon dioxide content of 0.045 %, which is acceptable for the experimental environment at hand.
For BBO, two different refractive indices exist for light polarisation along the ordinary or extraordinary crystal direction, respectively. A more detailed discussion of the latter two directions in terms of birefrigent crystals can e.g. be found in subsec. 6.1.1 or in references ([72], [84], [101]). The appropriate formula for ordinarily polarised light is given by:

$$n_{ord}^{\text{BBO}}(\lambda) = \sqrt{2.7359 - 0.01354 \cdot \lambda^2 \frac{1}{\mu m^2} + \frac{0.01878}{\lambda^2 - 0.01822\,\frac{1}{\mu m^2}}} \tag{2.46}$$

Its extraordinary counterpart is furthermore dependent on the angle of crystal orientation, which equals here the phase matching angle for type-II collinear spontaneous parametric down-conversion[24] of $\theta_{SPDC} = 43.52^\circ$, and is given by:

$$n_{ext}^{\text{BBO}} = \frac{\sqrt{\frac{3.11\cdot10^{-14} - 2.74\,\frac{1}{\mu m^2}\cdot\lambda^2 + 1.35\cdot10^{10}\,\frac{1}{\mu m^4}\lambda^4}{1.82\cdot10^{-14} - \lambda^2}}\sqrt{\frac{2.74\cdot10^{-14} - 2.38\,\frac{1}{\mu m^2}\cdot\lambda^2 + 1.52\cdot10^{10}\,\frac{1}{\mu m^4}\lambda^4}{1.67\cdot10^{-14} - \lambda^2}}}{\sqrt{\frac{5.07\cdot10^{-28} - 7.35\cdot10^{-14}\,\frac{1}{\mu m^2}\cdot\lambda^2 + 2.55\,\frac{1}{\mu m^4}\cdot\lambda^4 - 1.44\cdot10^{10}\,\frac{1}{\mu m^6}\cdot\lambda^6}{3.04\cdot10^{-28} - 3.49\cdot10^{-14}\,\frac{1}{\mu m^2}\cdot\lambda^2 + \lambda^4}}} \tag{2.47}$$

The necessary parameters for both expressions can be found in reference ([72]), considered at a temperature of $T = 20^\circ\,C$ with wavelengths again in units of μm.

Phase after round-trip The phase shift ϕ imparted onto the intra-cavity pulses after one round-trip can now be evaluated by considering a polarisation direction along the extraordinary axis in the BBO crystal. The reason for that originates from the phase matching condition of the down-conversion process[25]. With a cavity length of $L_{cav} = 3.71\,m$ and a crystal thickness of $L_{\text{BBO}} = 1\,mm$, the phase ϕ turns out to be

$$\phi(\omega) = \frac{\omega}{c \cdot n_{ext}^{\text{BBO}}(\frac{2\pi c}{\omega})} L_{\text{BBO}} + \frac{\omega}{c \cdot n^{\text{air}}(\frac{2\pi c}{\omega})}(L_{cav} - L_{\text{BBO}}) \tag{2.48}$$

for a resonator arrangement include the non-linearity and

$$\phi(\omega) = \frac{\omega}{c \cdot n^{\text{air}}(\frac{2\pi c}{\omega})} L_{cav} \tag{2.49}$$

for its absence. A graphical representation for both scenarios is provided in fig. 2.7 for a wavelength range of $\lambda_{UV} \in \{386\,nm, 394\,nm\}$, well containing our UV pumping spectrum.

Spectrally resolved power enhancement With these preliminary considerations, the power enhancement as a function of the pumping frequency ω can now be calculated by application of eqs. (2.41) and (2.45)-(2.49). For this purpose the overall cavity reflectivity $r(\omega)$ will be split up again into $r(\omega) = r_{IC}(\omega) \cdot r_{noIC}(\omega)$. While the latter reflectivity is determined by the cavity losses stated in subsec. 2.1.2, the former quantity will be the variable to optimise for. Calculations yield, for the situation with the BBO, power enhancement curves as they are exemplarily represented in fig. 2.8 a). We can see that the enhancement factor for each wavelength component within the pulse varies quite a lot for different input coupler reflectivities. The vertical lines at $\lambda_1 = 389.5\,nm$ and $\lambda_2 = 390.5\,nm$ represent the spectral region, over which the dispersion compensation and accordingly the input coupling condition is optimised for, as will be explained shortly in subsec. 2.1.4. Within this interval, the external frequency modes should best match cavity resonances, i.e. optimally couple into resonator, and thus experience

[24] See subsec. 6.1.1 for more details.
[25] See the discussion in subsec. 6.1.1.

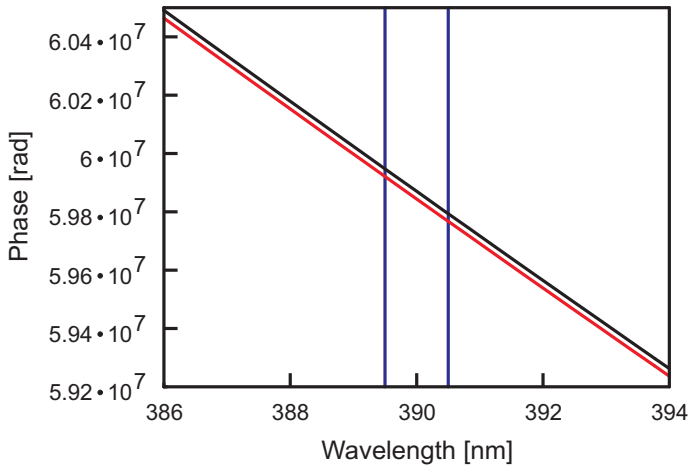

Figure 2.7: Phase shift $\phi(\lambda)$ of UV pulses after one round-trip inside the enhancement resonator. Black curve: cavity with air and a $1\,mm$ thick BBO crystal. Red curve: Cavity just containing air. The blue vertical lines indicate the spectral region over which dispersion compensation will be optimised.

the highest power enhancement. If the overlap between external frequencies ω and cavity resonances, positioned at $\omega_{cav} = n \cdot \omega_{FSR}$ was perfect within the entire range $\omega \in \{\frac{2\pi c}{\lambda_2}, \frac{2\pi c}{\lambda_1}\}$, the power enhancement would have a flat roof top over this region. The examined M-shaped structure is however due to deviations from perfect matching for some frequencies (see subsec. 2.1.4), whereby the best coincidence is achieved at the positions λ_k at which the power enhancement is maximal ($PE(\lambda_k) = PE_{max}$). For continuously changing the input coupler reflectivity[26] $T_{IC} = 1 - r_{IC}^2$, these maximal power enhancements are depicted in fig. 2.8 b), and an overall maximal power enhancement

$$PE_{max}^{\mathrm{BBO}} \approx 37.7 \quad \text{at a mirror transmittivity of: } T_{IC}^{\mathrm{BBO}} \approx 2.66\,\% \tag{2.50}$$

is achieved. The analogue curves are plotted in fig. 2.9 for a situation without the non-linear crystal. A maximal power enhancement of

$$PE_{max}^{\mathrm{noBBO}} \approx 625 \quad \text{at a mirror transmittivity of: } T_{IC}^{\mathrm{noBBO}} \approx 0.16\,\% \tag{2.51}$$

is yielded. These values coincide with those calculated previously in eqs. (2.34) and (2.36). For best power enhancement, we do however not necessarily want to maximise the spectral power enhancement at a certain pumping frequency, which is analogue to a cw case and thereby not surprisingly resembles numbers derived exactly for such a situation. Instead we do have to maximise the intra-cavity enhancement over all frequencies or wavelengths, included in our pumping spectrum, simultaneously. In order to do so, a suitable pumping spectrum has to be considered in the first place. Subsequently, the spectrally resolved power enhancement $PE(\lambda)$ from fig. 2.8 and 2.9 will be multiplied with this normalised external reference spectrum to gain its amplified internal counterpart, as it is expected for the dispersion relations and losses of the incorporated optical components. Ultimately it is the energy content yielded by integration over the spectral intensities of these pulses, which has to be maximised as a function of the input coupler transmittance.
For an external UV pumping spectrum our choice falls onto the mean UV spectrum for datasets originating from the power enhancement measurement used in subsec. 4.2.2 and plotted in fig. 4.5 b). According to the results we will obtain in subsec. 5.3.4, a Sech-pulse profile appears to be more appropriate for the laser pulses involved. The experimental data, normalised to its maximum value, will for the following calculations thus be fitted with a Sech-intenstiy profile, defined as

$$I_{Sech}(\lambda) = \mathrm{sech}^2\left(\frac{\lambda - \lambda_0}{\Delta\lambda}\right) \tag{2.52}$$

with a centre wavelength of $\lambda_0 \approx 390.188 \pm 0.001\,nm$ and a width parameter $\Delta\lambda \approx 0.653 \pm 0.002\,nm$. The resulting fitted function, together with the underlying averaged, measured spectrum, is presented

[26] Losses in the input coupler during propagation have been completely neglected for this calculation. However in reality they are not negligible, especially not in the UV regime. So the real values for the input coupler coating parameters are always slightly different in experimental optimisation than in this theoretical estimation, besides that not any arbitrary reflectivity is readily avaiblable commercially anyway.

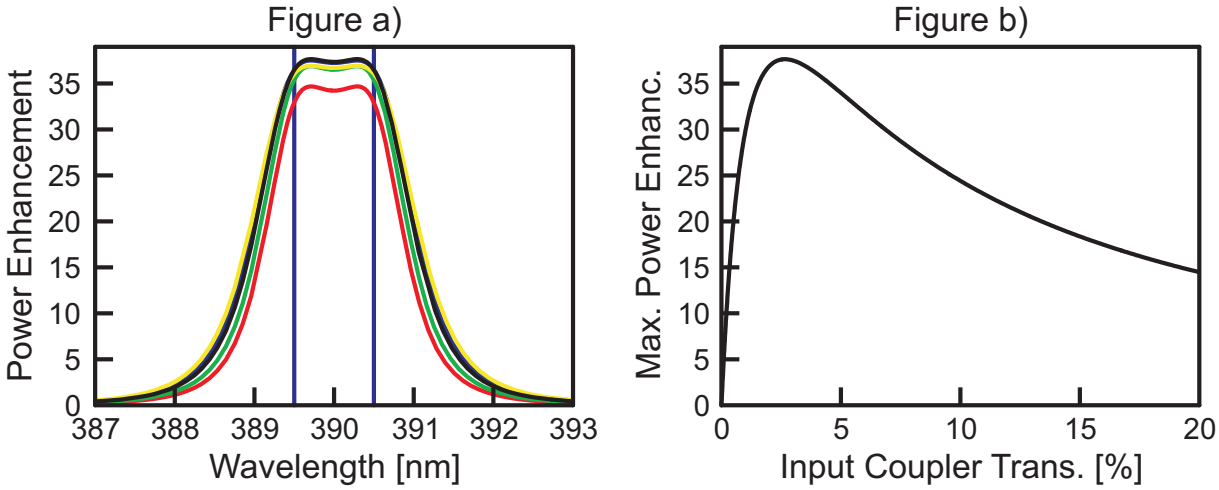

Figure 2.8: Spectrally resolved power enhancement $PE(\omega)$ as a function of the input coupler transmittance $T_{IC}(\omega)$ for a resonator arrangement comprising the BBO crystal. Fig. a): Examples of spectral power enhancement functions received for various input coupler choices. The colour coding of the lines is as follows: Red $\Leftrightarrow T_{IC} = 1.5\,\%$, green $\Leftrightarrow T_{IC} = 2.0\,\%$, black $\Leftrightarrow T_{IC} = 2.66\,\%$, blue $\Leftrightarrow T_{IC} = 3.0\,\%$, yellow $\Leftrightarrow T_{IC} = 3.5\,\%$. The blue vertical lines correspond again to the wavelength range, dispersion compensation is optimised for. Fig. b): Maximum power enhancement $PE_{max}^{\mathrm{BBO}}(\lambda_k)$ achievable for varying the input coupler transmittance.

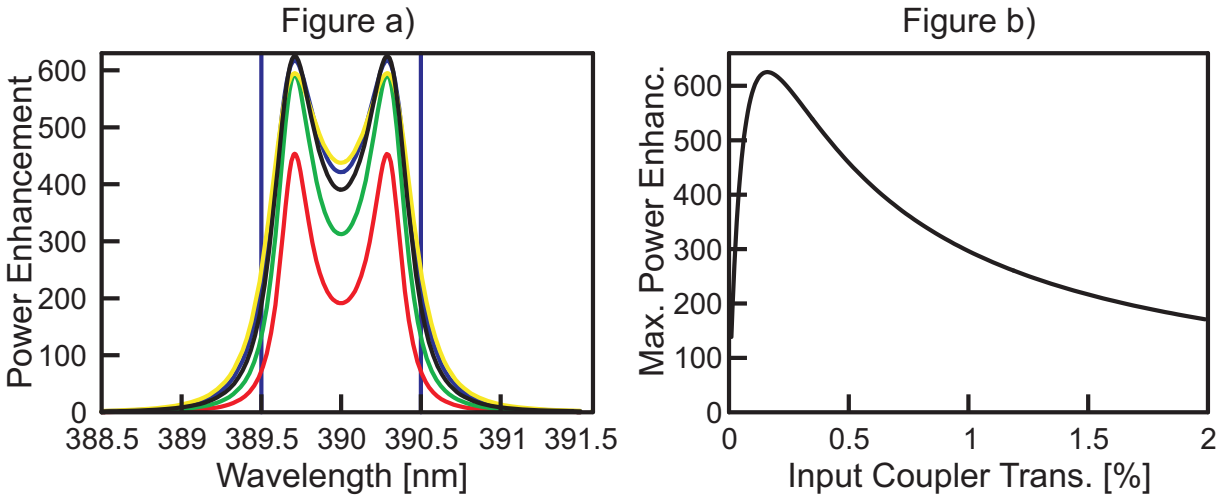

Figure 2.9: Spectrally resolved power enhancement $PE(\omega)$ as a function of the input coupler transmittance $T_{IC}(\omega)$ for an empty cavity. Fig. a): Examples of spectral power enhancement functions received for various input coupler choices. The colour coding of the lines is as follows: Red $\Leftrightarrow T_{IC} = 0.05\,\%$, green $\Leftrightarrow T_{IC} = 0.1\,\%$, black $\Leftrightarrow T_{IC} = 0.16\,\%$, blue $\Leftrightarrow T_{IC} = 0.2\,\%$, yellow $\Leftrightarrow T_{IC} = 0.25\,\%$. The blue vertical lines correspond again to the wavelength range, dispersion compensation is optimised for. Fig. b): Maximum power enhancement $PE_{max}^{\mathrm{noBBO}}(\lambda_k)$ achievable for varying the input coupler transmittance.

in fig. 2.10. This function is furthermore normalised to its integrated areal coverage, constituting a value of $A_{Sech} = \int I_{Sech}(\lambda)d\lambda \approx 1.305$, to allow for simple retrieval of the overall power enhancement, also integrated over all wavelength within the pulse: i.e. $I'_{Sech}(\lambda) = \frac{I_{Sech}(\lambda)}{A_{Sech}}$. Subsequently, it is now multiplied by the spectrally resolved power enhancement function, as plotted in figs. 2.8, 2.9 and stated generally in eq. (2.41) together with the crystal's and air's dispersion properties (eqs. (2.45), (2.47)) to provide the pulse spectrum as it is expected to establish inside the resonator system. For an arrangement with BBO, the obtained internal spectra are plotted in fig. 2.11 a), the ones for an empty resonator can be seen in fig. 2.12 a).

Since it is the overall power enhancement $\bar{PE}$, which is of interest here, integration over the internal spectra has to be pursued. The normalisation of the external spectrum I'_{Sech} permits to directly read out the desired value from this operation. The resulting enhancement factors are shown as a function of

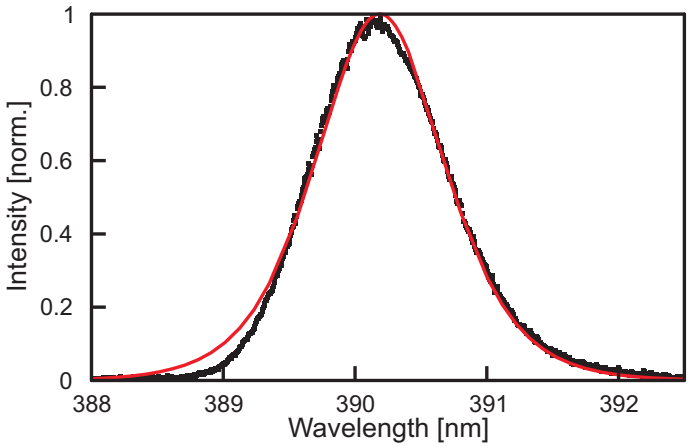

Figure 2.10: Mean spectrum averaged over the individual external UV spectra measured for power enhancement determination, as also shown in fig. 4.5. The black boxes represent the experimental data and the red line denotes the Sech fit according to eq. (2.52).

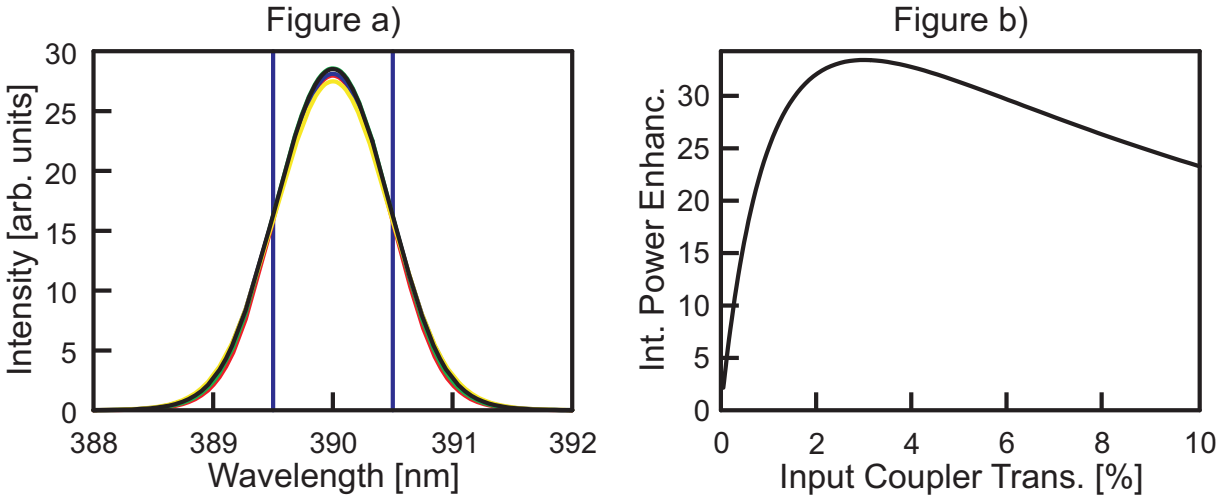

Figure 2.11: Expected internal UV spectrum for the cavity including the BBO crystal. Fig a) shows the internal pulse spectra, whereby the colour coding represents different input coupler transmittances T_{IC} as follows: Red $\Leftrightarrow T_{IC} = 2\,\%$, green $\Leftrightarrow T_{IC} = 2.5\,\%$, black $\Leftrightarrow T_{IC} = 3.03\,\%$, blue $\Leftrightarrow T_{IC} = 3.5\,\%$, yellow $\Leftrightarrow T_{IC} = 4\,\%$.Fig. b) gives the areal coverage, or in other words the integrated power enhancement, of the internal pulses as a function of the input coupler transmittance.

input coupler transmission in figs 2.11 b) and 2.12 b) for the respective resonator scenarios. With respect to this more appropriate quantity to optimise for, the best mirror transmittances deviate from the cw results (2.38), (2.39) and magnifications of

$$\bar{PE}_{max}^{\mathrm{BBO}} \approx 33 \quad \text{with an input coupler transmittances } T_{IC}^{\mathrm{BBO}} \approx 3.03\,\% \tag{2.53}$$

$$\bar{PE}_{max}^{\mathrm{noBBO}} = 341 \quad \text{with an input coupler transmittances } T_{IC}^{\mathrm{noBBO}} = 0.26\,\% \tag{2.54}$$

are expected. It shall be strongly stressed here, especially if comparing these theoretical values with the experimental results in subsec. 4.2.2 (eqs. (4.5) and (4.6)), that perfect transverse mode matching during input coupling has been assumed throughout the entire calculation. That is to say, if external frequencies match with cavity resonances, all the intensity of the impinging beam is coupled into the resonator. For our experimental situation, yet about 50 % get reflected off the input coupler, even for having all frequency related affairs well adjusted and the input coupling condition (see subsec. 2.1.4) fulfilled. Hence, the power, that really gets enhanced, is of only half the magnitude incorporated here for multiplication with $PE(\lambda)$. For a comparison with the experiment, this means in turn that the enhancement numbers in eqs. (2.53) and (2.54) have to be devided by an additional factor of 2 in order to account for the degraded coupling, yielding $\bar{PE}_{max}^{\mathrm{BBO},\,1/2} \approx 17$ and $\bar{PE}_{max}^{\mathrm{noBBO},\,1/2} \approx 171$.

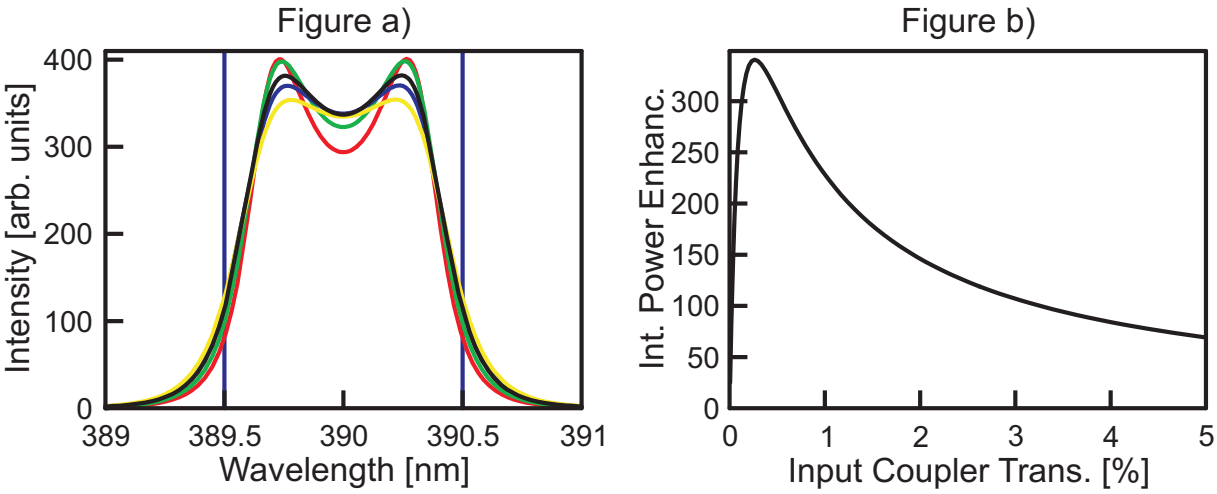

Figure 2.12: Expected internal UV spectrum for the cavity without the BBO. Fig a) shows the internal pulse spectra, whereby the colour coding represents different input coupler transmittances T_{IC} as follows: Red $\Leftrightarrow$ $T_{IC} = 0.15\,\%$, green $\Leftrightarrow$ $T_{IC} = 0.2\,\%$, black $\Leftrightarrow$ $T_{IC} = 0.26\,\%$, blue $\Leftrightarrow$ $T_{IC} = 0.3\,\%$, yellow $\Leftrightarrow$ $T_{IC} = 0.35\,\%$. Fig. b) gives the areal coverage, or in other words the integrated power enhancement, of the internal pulses as a function of the input coupler transmittance.

So altogether the input coupler transmittance should be positioned somewhere around 3 % with BBO. For experimental optimisation, several components have been purchased[27]. Slightly contrary to the theoretical predicition, the components with[28]

$$R_{IC}^{\mathrm{BBO}} = 97.36\,\% \quad \text{and consequently: } T_{IC}^{\mathrm{BBO}} = 2.64\,\% \tag{2.55}$$

$$R_{IC}^{\mathrm{noBBO}} = 98.72\,\% \quad \text{and consequently: } T_{IC}^{\mathrm{noBBO}} = 1.28\,\% \tag{2.56}$$

$$\tag{2.57}$$

have shown the highest intra-cavity power levels achievable. Therefore we will apply these mirrors as input couplers for the respective arrangement with and without the BBO crystal.

2.1.4 Coupling conditions into cavity by frequency comb matching

In the following, the coupling conditions necessary to operate the enhancement resonator will be explained. There are in general three fundamental requirements ([51], [52]) to accomplish pulse amplification, which extend the crude picture given in the introduction to this chapter. First the intra-cavity pulses' envelope has to be maintained during round-tripping. Second the repetition rates of the incoming external pulses have to match the round-trip time of the pulses inside cavity and finally, third, the electric fields of the individual frequencies, comprised by stored pulses, have to stay in phase with their external counterparts. All these requirements share two common constraints. On the one hand, the absence of dispersion inside the resonator, or at least a distortion low enough to still enable coherent electric field overlap, is necessary. On the other hand, the entire procedure is founded on pulses consisting of a coherent superposition of modes, or in other words mode-locked laser pulses described by a frequency comb ([73]). For alternative sources of laser pulses with no coherence between different mode contributions, enhancement inside pulsed optical resonators is not feasible, as explained in ([51]). Despite the statement of the aforementioned conditions in the time domain, a comprehensible analysis is conveniently undertaken in the frequency domain. Therefore the discussion about input coupling will start from the frequency comb structure of the external pumping laser, which can be stated ([73]) as

$$\omega_n = n \cdot \omega_{rep} + \omega_{CEO} \tag{2.58}$$

with a pulse repetition rate of ω_{rep} and a constant carrier-envelope-phase offset frequency[29] ω_{CEO}. This comb is drawn schematically in the lower half of fig. 2.13, which indicates ω_{CEO} to define the offset and

[27] with nominal values of $T_{IC} \in \{0.1\,\%, 1\,\%, 2\,\%, 3\,\%, 5\,\%\}$

[28] The numbers represent measured values and therefore slightly deviate from the nominal specifications.

[29] The carrier envelope offset is not really steady over time. However it varies on much longer time scales than fluctuations on the cavity length occur. Therefore it can be assumed as a constant for deriving the coupling condition.

hence the positioning of the comb teeth, separated by ω_{rep}, along the frequency axis. We have already deduced the condition for external frequency modes to match cavity resonances from fig. 2.6. To achieve perfect input coupling, every comb tooth, present within the pulse, must coincide with a cavity resonance. Those have been fixed by the power enhancement $PE(\lambda)$, eq. (2.41), as the internal cavity frequencies, for which the following condition applies ([51]):

$$2\pi\tilde{n} = \phi(\omega'_{\tilde{n}}) \Longleftrightarrow 2\pi\tilde{n} = \frac{\omega'_{\tilde{n}}}{c}L_{cav} + \Phi(\omega'_{\tilde{n}}) \Longleftrightarrow \omega'_{\tilde{n}} = \tilde{n}\frac{2\pi c}{L_{cav}} - \frac{c\cdot\Phi(\omega'_{\tilde{n}})}{L_{cav}} \tag{2.59}$$

The modes $\omega'_{\tilde{n}}$ nearly represent a frequency comb like structure themselves, similar to eq. (2.58), but unfortunately the second term still comprises a frequency dependence, due to the dispersive phase shift $\Phi(\omega'_{\tilde{n}})$, see e.g. eq. (2.48). A customary approach to deal with this problem is to execute a Taylor expansion in terms of ω' according to ([51])

$$\Phi(\omega') = -\Phi_0 + \tau\omega' + \psi(\omega') \tag{2.60}$$

whereby a constant phase offset Φ_0, the group round-trip time inside the cavity τ and higher order dispersion term $\psi(\omega')$ appear. The latter includes all wavelength dependent effects, which tend to deform the pulse shape initially coupled into the resonator. It will be subject of further investigations in subsec. 2.1.5. For the moment however, we acknowledge eq. (2.59) to change into

$$\omega'_{\tilde{n}} = \tilde{n}\frac{2\pi}{\frac{L_{cav}}{c}+\tau} + \underbrace{\frac{\Phi_0}{\frac{L_{cav}}{c}+\tau}}_{=:\omega'_{CEO}} + \underbrace{\frac{\psi(\omega')}{\frac{L_{cav}}{c}+\tau}}_{=:\omega''_{CEO}} = \tilde{n}\underbrace{\frac{2\pi}{\frac{L_{cav}}{c}+\tau}}_{=:\omega'_{rep}} + \underbrace{\omega'_{CEO}+\omega''CEO}_{=:\tilde{\omega}_{CEO}} = \tilde{n}\cdot\omega'_{rep} + \tilde{\omega}_{CEO}, \tag{2.61}$$

which now resembles our external frequency comb structure (eq. (2.59)) up to the, still frequency dependent, factor ω''_{CEO}. Although this does not look to offer great advantage at first sight, it is intriguing to anticipate absence of all dispersion within the resonator for a moment. In such a scenario, the internal pulse circulation frequency ω'_{rep} as well as the constant phase shift Φ_0, accumulated during one round-trip, can be made to perfectly agree with those of the external pumping comb (eq. (2.59)). In our experiment, the accessible parameters to control both combs with respect to one another are the carrier-envelope offset of the external comb and the central wavelength λ_c of its spectrum, as well as the cavity length.

The former set of parameters offers free adjustment of the external mode locations, which can be understood by examination of fig. 2.13. Choosing λ_c determines the position of the comb centre and therefore simultaneously the location of all other modes along the frequency axis[30]. Subsequently modifying ω_{CEO} yields an alteration of the teeth spacings and hence of ω_{rep} of the comb. This is due to the fixation of the central mode, which prevents any dislocation of the entire spectrum along the wavelength axis. So, if the offset of the lowest constituent is changed, only the separations between adjacent teeth can vary[31]. Thereby the offset frequencies of the external comb and the cavity resonances can be adjusted to coincide. Furthermore, the spacing between cavity modes and external comb teeth is set to concur by modifying the denominator $\frac{2\pi}{\frac{L_{cav}}{c}+\tau}$ directly via L_{cav} and indirectly by changing the pulse round-tip time τ for variations in[32] L_{cav}.

In the time domain, matching the comb spacings corresponds to the equalisation of the pulse round-trip time inside the cavity and the time between two successive laser pulses (condition 2 from above), whereby adjusting the offset frequencies enables coherent addition of the coupled to the circulating pulse by having the frequency teeth overlap with the cavity resonances (condition 3 from above, see also fig. 2.6). In other words, what can be influenced and optimised experimentally accords to the fitting of a straight line in a phase-over-frequency diagram, given by the laser frequency comb with an ordinate offset determined by the carrier envelope phase ([73]) ϕ^{ext}_{CEO}, given by

$$\phi(\omega) = n\frac{\omega_n L_{cav}}{c} + \phi^{\text{ext}}_{CEO} = n\frac{\omega_n L_{cav}}{c} + \frac{\omega_{CEO}L_{cav}}{c} \tag{2.62}$$

to the entire intra-cavity phase function

[30] reciprocal to the wavelength axis shown in fig. 2.13

[31] An intriguing analogue for such a behaviour is to imagine a rubber band fixed at its middle by a nail and somebody pulling with equal forces at either ends.

[32] Of course an alteration of L_{cav} also changes ω'_{CEO} and the carrier-envelope-offset of the external pump beam would technically have to be readjusted again by the aforementioned method. Yet, cavity modes are much broader than their external counterparts, allowing for some mismatch. Nevertheless achieving mode overlap is an optimisation process between both degrees of freedom, whose experimental access is coupled.

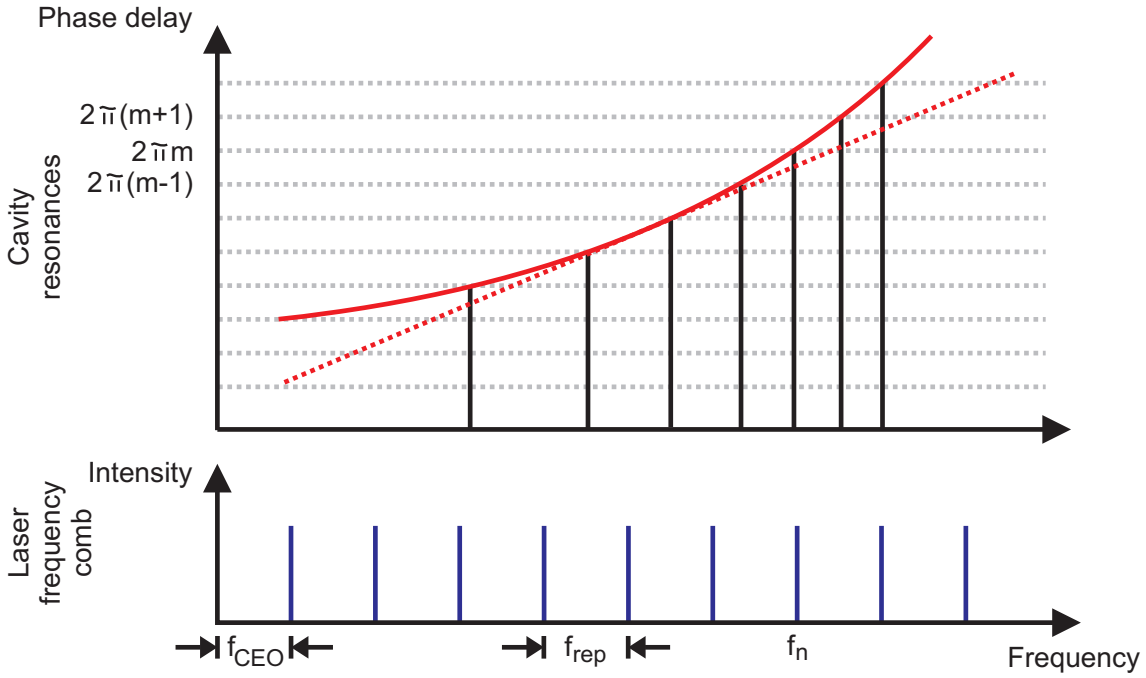

Figure 2.13: Schematic drawing of the frequency comb matching condition for cavity input coupling. For explanations see main text. Source: ([52]).

$$\phi(\omega') = \tilde{n}\omega'_{rep}\frac{L_{cav}}{c} + \tilde{\omega}_{CEO}\frac{L_{cav}}{c} \tag{2.63}$$

stated in eqs. (2.61) or (2.59), respectively. The latter is a straight line for the absence of higher order dispersion ($\psi(\omega') = 0$) as well, allowing to achieve perfect resemblance between eqs (2.62) and (2.63), thus enabling coupling of the entirety of the external pulses into the resonator. The enhancement would accordingly solely be determined by the frequency dependence of the cavity losses $r(\omega_{\tilde{n}}) = r_{IC}(\omega_n)r_{noIC}(\omega_{\tilde{n}})$. However the real apparatus shows a non-vanishing $\psi(\omega')$, as can be inferred from fig. 2.7 already. For the overall phase $\phi(\omega')$, this translates into a deviation from the straight line situation, whose shape is subject to the particular frequency dependence of $\psi(\omega')$. Group velocity dispersion (GVD), which is of second order in ω' and discussed further in subsec. 2.1.5, contributes the most to $\psi(\omega')$ in our situation, wherefore a parabolic behaviour of the intra-cavity phase

$$\phi(\omega') \approx -\Phi_0 + \left(\frac{L_{cav}}{c} + \tau\right)\omega'_{\tilde{n}} + \mathrm{GVD}\cdot(\omega'_{\tilde{n}})^2 + ... \tag{2.64}$$

is obtained as shown in the top part of fig. 2.13. It is clear, that the above mentioned external fitting parameters are now not sufficient anymore to achieve proper phase compensation over the entire external spectrum. Only at the positions of coincidence between the straight line eq. (2.62) and the intra-cavity function (2.64) perfect phase compensation can be obtained. So some residual phase $\Delta\phi(\omega, \omega')$, which accords to

$$\Delta\phi(\omega,\omega') = \phi(\omega') - \phi(\omega) = \left(\tilde{n}\frac{2\pi}{\frac{L_{cav}}{c}+\tau} + \frac{\Phi_0}{\frac{L_{cav}}{c}+\tau} + \frac{\psi(\omega_{\tilde{n}})}{\frac{L_{cav}}{c}+\tau}\right)\frac{L_{cav}}{c} - n\frac{\omega_n L_{cav}}{c} - \frac{\omega_{CEO}L_{cav}}{c} \tag{2.65}$$

will be retained in the denominator of the power enhancement, eq. (2.41), causing an amplification of the external mode ω_n lower than the maximally accomplishable enhancement on resonance (i.e. for $\Delta\phi(\omega, \omega') = 0$). In terms of the frequency combs, the dispersion results in a displacement of the intra-cavity comb teeth away from the locations apparent without the addiational term $\psi(\omega')$. Their shifts in position are also nicely conceivable from the top part of fig. 2.13 and can be understood by the constraint for the resonance frequencies to meet the phase requirement set by eq. (2.59). So any additional dispersion $\psi(\omega')$ will modify the cavity resonances by ω''_{CEO}, hence diminishing the overlap with certain external frequency comb modes and causing a smaller fraction of the external pulse spectrum to be coupled into the resonator. We will see later within section 5.3, that the shortening in the spectrum will translate

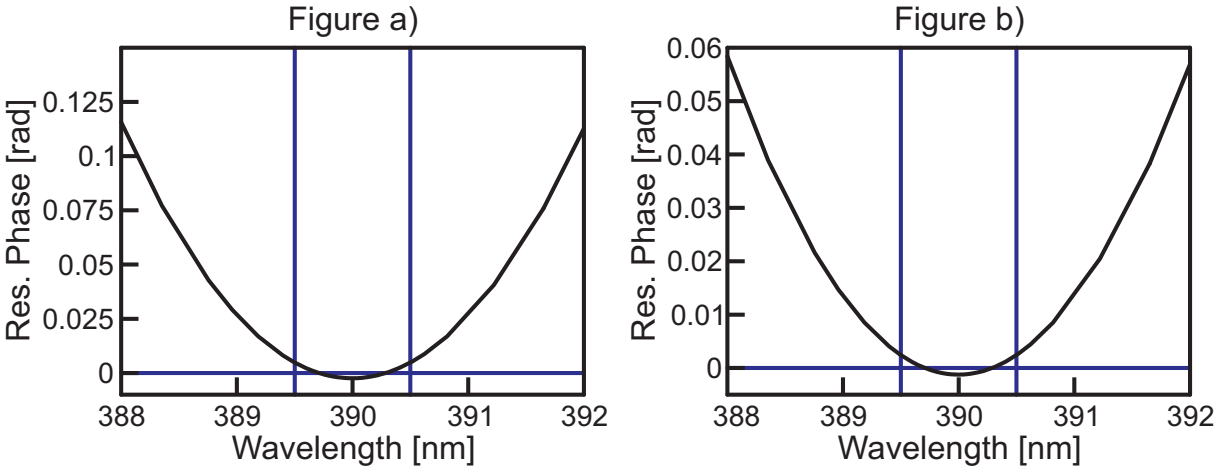

Figure 2.14: Residual phase $\Delta\phi(\omega,\omega')$ after phase compensation and thus input coupling optimisation by fitting eq. (2.65) with eq. (2.62). Figure a) shows the scenario with the BBO crystal inside the resonator, whereas for fig. b) the crystal is absent.

into an elongation in the pulse duration. At the same time it becomes also reasonable, that a smaller cavity finesse eases this frequency comb matching condition for input coupling. Since resonances are broader for such a higher loss scenario, the dislocation of internal comb teeth, depicted in fig. 2.13, could partially be compensated by the increase in $\Delta\omega'_{FWHM}$ (see eq. (2.43)). Phase compensation is executed experimentally by regulating $\omega_n = \omega_{rep}^{\text{pump}}$, ω_{CEO} and L_{cav} in such away to maximise the overall power enhancement $\bar{PE}$ (see eqs. (2.53) and (2.54)), details about the actual implementation can be found in subsec. 3.2.2. For the theoretical calculations of $PE(\lambda)$, as stated in figs. 2.8 a) and 2.9 a), the best fit for the straight line in eq. (2.62) to the intra-cavity phase function, eq. (2.64), within the wavelength interval $\lambda \in \{\lambda_{min}^{opt}, \lambda_{max}^{opt}\}$ is utilised, which causes an intersection in two points[33]. The boundaries of the optimisation region, $\lambda_{min}^{opt} = 389.5\,nm$ and $\lambda_{max}^{opt} = 390.5\,nm$, are indicated in all graphs showing theoretical calculations[34] by the straight vertical lines. Due to perfect dispersion compensation, the two comb frequencies, whose residual phase $\Delta\phi(\omega,\omega') = 0$ in fig. 2.14, experience the maximal power enhancement $PE(\lambda)$, consequently causing the M-shaped structure of the spectrally resolved power enhancement curves in figs. 2.8 and 2.9. The difference in $PE(\lambda)$ for these optimally coupled points to the spectral range between them obviously relates to the amount of losses and thereby to the finesse. Since higher losses allow more of the aforementioned intermediate frequencies to penetrate into the resonator as well, the power enhancement results in having a flatter top structure. Although a predominantly parabolic dispersive phase contribution $\psi(\omega')$ is obtained theoretically (see fig. 2.14) the experimental situation does not necessarily have to resemble this behaviour, wherefore also third order terms could in principle contribute, allowing our straight line fit (eq. (2.62)) to intersect the cavity phase (eq. (2.64)) in more than two points, which would correspond to three or more modes experiencing perfect dispersion compensation and maximum coupling efficiency.
Finally it is also clear now, that the first condition, mentioned at the beginning, corresponds to the absence of dispersion or at least its smallness over the wavelength range of interest, since changes within the spectrum and accordingly, in the time domain, within the pulse form are provoked by it. In the following the dispersion shall in be stated for the situation at hand.

2.1.5 Higher order dispersion in resonator

In order to investigate the higher order dispersion inside the resonator, we can in a first step look at the remainder of the phase function (2.65) after phase compensation by the externally accessible parameters, i.e. after fitting with the straight line in eq. (2.62) having ω_n and ω_{CEO} as the optimisation parameters. Thereby the residual phase $\Delta\phi(\omega,\omega')$, as defined by eq. (2.65), is calculated and the results are shown in fig. 2.14 for the situation with the BBO crystal inside the resonator and in fig. 2.15 for its absence.
If the compensation parameters are chosen such, that all linear parameters in eq. (2.65) cancel each other, i.e. $\frac{\Phi_0}{\tau+L_{cav}/c} = \omega_{CEO}$ and $\frac{2\pi\tilde{n}}{\tau+L_{cav}/c} = n\cdot\omega_n$, the contributions to $\Delta\phi(\omega,\omega')$ are solely due to the

[33] While for $\psi(\omega')$ is predominantly $\sim\omega'^2$, there is a second option of a tangential fit with coincidence in one point for a mainly parabolic dispersion $\phi(\omega')$.
[34] These are: figs. 2.7-2.9, 2.11, 2.12, 2.14, 2.67, 2.20, 2.21, 2.22-2.25

dispersion $\psi(\omega'_{\tilde{n}})$. Anticipating this situation for the following analysis, the curves in figs. 2.14 and 2.15 can be understood by writing out the further Taylor expansion terms, contained in $\psi(\omega')$ (see also eq. (2.60))

$$\Delta\phi(\omega'_{\tilde{n}}) = \psi(\omega'_{\tilde{n}}) = \left(\frac{d^2\phi(\omega')}{d\omega'^2}\,|_{\tilde{n}}\right)\cdot(\omega'_{\tilde{n}})^2 + \left(\frac{d^3\phi(\omega')}{d\omega'^3}\,|_{\tilde{n}}\right)\cdot(\omega'_{\tilde{n}})^3 + ... = \mathrm{GVD}\cdot(\omega'_{\tilde{n}})^2 + \mathrm{TOD}\cdot(\omega'_{\tilde{n}})^3 + ..., \tag{2.66}$$

whereby the second derivative of the phase with respect to the intra-cavity light's frequency has been named group velocity dispersion[35], GVD, and respectively the next higher derivative third order dispersion, TOD.
The former effect causes the individual frequency components within the laser pulses to propagate with different velocities. For normal dispersive media, i.e. GVD > 0, bluer light with modes of shorter wavelengths travels slower than its red counterpart made up of larger wavelengths. All naturally occurring materials behave like that and abnormal dispersion (GVD < 0) is commonly achieved by either incorporating prism pairs ([111]), or alternatively including chirped mirrors into the set-up ([74]). Accordingly all optical components within our apparatus have GVD > 0, causing their individual contributions to accumulate during round-tripping. The varying propagation speeds influence the overall pulse shape by firstly elongating it in its time duration and secondly by introducing a chirp on the carrier frequency. That is to say, the oscillation period of the pulse's electric field becomes longer towards the leading edge and shorter towards the trailing edge of the pulse.
The latter of the two relevant terms in eq. (2.66) is even more lethal to the maintenance of the pulse shape. It causes a previously well defined single pulse to split up into one mother pulse of greater intensity and some daughter pulses successively decreasing in their electric field amplitude. The positioning of these additional pulses in front of or beyond the mother pulse depends on the sign of the third order dispersion. Very nice and intriguing graphical explanations about both contributions can also be found in reference ([111]) and shall therefore not be repeated here.
From the residual phase behaviour, as it is represented in fig. 2.14, the dominance of group velocity dispersion is clearly visible, since both graphs show parabolic shapes and must thus be mainly determined by distortions of second order proportional to ω'^2. These results are quite pleasant in terms of the measurements to be done in this thesis. As we will frequently rely on a full-width-half-maximum (FWHM) definition of the pulse duration, particularly in the course of chapter 5, it is important to know, that such a convention makes sense for the description of the actually apparent pulses[36]. Also for the SPDC process and its emission structure it is important to a single, undistorted pump pulse: Multiple copies of lower energy would in this respect not only decrease the conversion efficiency, but also cause an emission split-up into bunches of photon pairs according to the split-up pulse shape. Due to the requirement of temporal photon pair indistinguishibility, a subsequent creation-time window-filtering of the emitted SPDC photons is pursued, outlined in subsec. 6.2.2. The bunched emission characteristics, obtained by TOD influences, would in turn substantially exceed the aforementioned time window, which would impart an additional suppression of the desired high photon state production rates[37].
We can finally evaluate the GVD directly, by considering its definition ([51])

$$\mathrm{GVD} = \frac{d^2\phi(\omega')}{d\omega'^2} = \frac{d^2}{d\omega'^2}k(\omega')L_{cav} = \frac{d^2}{d\omega'^2}\frac{n(\omega')\omega'}{c}L_{cav} = \frac{2\frac{dn(\omega')}{d\omega'} + \omega'\frac{d^2n(\omega')}{d\omega'^2}}{c} \tag{2.67}$$

in combination with the intra-cavity phase function, stated in eqs. (2.48) and (2.49). The resulting values are shown graphically in fig. 2.15 a) for a cavity with BBO and in fig. 2.15 b) without the crystal.
We acknowledge the group velocity dispersion for the former scenario to be situated between $376.8\,fs^2 \leq \mathrm{GVD}^{\mathrm{BBO}} \leq 378.4\,fs^2$ and for the latter to amount to $190.2\,fs^2 \leq \mathrm{GVD}^{\mathrm{noBBO}} \leq 190.94\,fs^2$. It thus comprises some very slight wavelength dependence, however the more important fact concerns the difference between both arrangements: With respect to dispersion, the effects of the air filling of the resonator are non-negligible and contribute to the entire second order dispersion by as much as the $1\,mm$ thick BBO crystal. So even for applications only incorporating the cavity as a high repetition rate resonator, dispersion compensation will potentially become an issue[38].

[35] Sometimes also referred to as group delay dispersion, GDD.
[36] The reader should realise that ambiguities appear for the presence of TOD, due to the splitting of the pulse into several copies, which all have their own FWHM pulse duration.
[37] See subsec. 6.3.2.
[38] It shall further be noted, that these values exceed by far the contributions expected from the cavity mirrors, which should be $\mathrm{GVD}_{mirrors} \leq 20\,fs^2$ according to the manufacturer's specifications. Neglecting them in the course of the previous discussion is therefore justified.

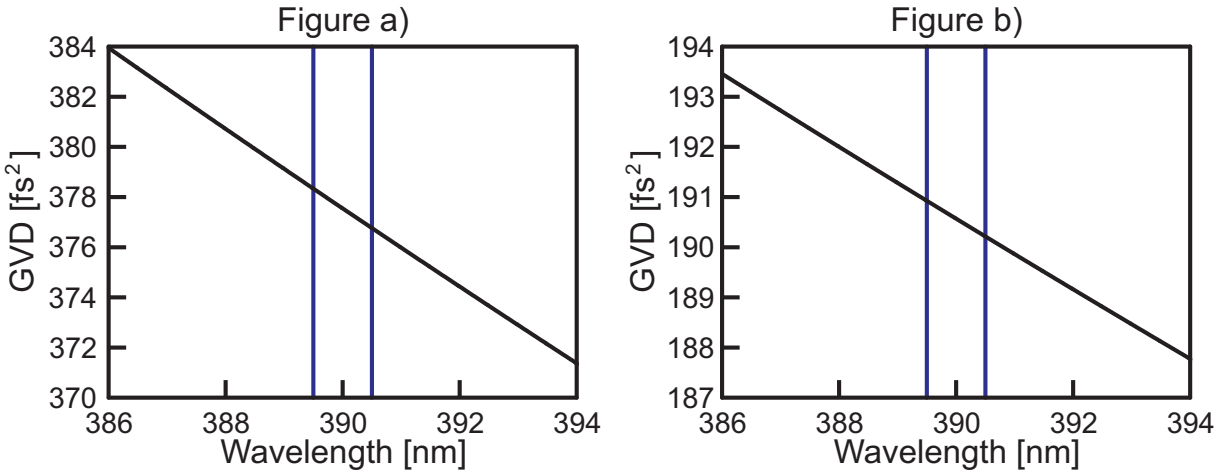

Figure 2.15: Group velocity dispersion GVD as calculated by eq. (2.67). Fig. a) shows the cavity with the BBO and fig. b) without it.

Thinking about best pumping conditions and least pulse distortion possible, GVD numbers as high as our $\mathrm{GVD}^{\mathrm{BBO}} \approx 377.6\, fs^2$ could be compensated for by substituting one of the cavity mirrors for a chirped version ([74]). However in order to keep things as simple as possible, the first step to operate the system has been pursued without introducing negative dispersion. Since the obtained outcomes for all relevant cavity parameters, which are discussed in detail throughout the remainder of this dissertation, have satisfied our requirements, any attempts regarding cancellation of GVD have not been undertaken yet. Before we will go through the aforementioned characteristics of the enhancement device, we will beforehand also consider cavities of shorter lengths associated with higher repetition rates.

2.2 Cavity of doubled repetition rate

2.2.1 Cavity mirror radii of curvature

The steps towards a cavity of $L'_{cav} = 1.829\, m$ length is absolutely analogous to the previous discussion of the $f_{rep} = 80.79\, MHz$ system. Starting ground is thus once again the calculation of the appropriate mirror curvatures and the associated optical beam characterisation as well as the stability analysis. Since all the required theoretical background together with the implemented methology for concluding onto these quantities has already been thoroughly explained in the course of subsec. 2.2.1, they shall not be repeated here and the following text will be restricted to merely stating the results of the calculations and discussing those.
Opposite to the full length cavity considerations, several initial mirror curvatures will be considered. This is because fulfilling the restrictions on the beam waist of $w_0 \stackrel{!}{=} 100\, \mu m$, imparted by the SPDC process, cannot be completely achieved for the half length version, at least not if the symmetric bow-tie type design is to be kept up. We have decided to stick to the arrangement and rather live with a slightly deviating waist. Beginning the computation with the background knowledge from subsec. 2.2.1, a sensible choice for the radii of curvature of mirrors $M1$ and $M2$ appears to be $R_{M1} = R_{M2} = 0.4\, m$, for which the excess parameter range, showing cavity stability, is calculated applying eq. (2.14). Suitable values for a are situated within the interval

$$0\, m < a < 0.190831\, m$$

The functional dependence of the beam waist $w_0(a)$ at the focus in sector 1 on the excess parameter is evaluated as well, resulting in a curve depicted in fig. 2.16 by the yellow line. Therefrom we can infer already the insufficiency of the assumed mirror radii in terms of achieving an appropriate beam waist value. The maximal number for w_0, with least susceptibility to changes in a, is realised at $a = 0.094\, m$ causing the length of sector 1 to be $d_{M1,M2} = 49.4\, cm$ and leaving for sector 2 $d_{M2,M1} = 1.335\, m$ long. A minimum beam waist w_0 with a number as low as $w_0 = 72,69\, \mu m$ is retained in this situation. Since this is approximately 25% less than the required magnitude, greater readii for R_{M1} and R_{M2} will have to be implemented. Prior to that, the beam waist $w(z)$ and the wavefront radii of curvature $R(z)$ are computed over the entire length of the cavity for later comparison. The computation follows exactly

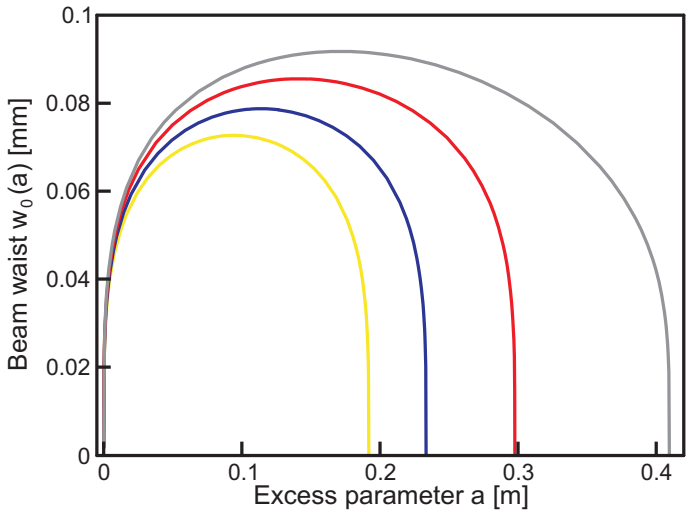

Figure 2.16: Minimal beam waist $w_0(a)$ as a function of the excess parameter for a stable cavity situation. The yellow curve represents the situation for mirror curvatures $R_{M1} = R_{M2} = 0.4\,m$, the blue curve the one for $R_{M1} = R_{M2} = 0.42\,m$, the red curve the one for $R_{M1} = R_{M2} = 0.44\,m$ and the grey curve the one for $R_{M1} = R_{M2} = 0.456\,m$, which is the largest radius possible to still yield a stable symmetric cavity.

the eqs. (2.26) and (2.27) by substituting the respective distances. Results are indicated by the yellow curves in fig. 2.16 with the beam waist $w(z)$ on the left hand side and the wavefront radius of curvature $R(z)$ on the right hand side. In terms of their behaviour, the analog of what has been said in context of the $L_{cav} = 3.71\,m$ investigations applies here as well. These two quantities are also stated explicitely in the table below for the four most prominent locations in the resonator[39], which are the positions of mirrors $M1$, $M2$ and the minimal beam waists w_0, w_1:

z position	Beam waist $w(z)$	Wavefront radius of curvature $R(z)$
z_{M1}	$428\,\mu m$	$-25\,cm$
z_{M2}	$428\,\mu m$	$25\,cm$
z_0	$73\,\mu m$	∞
z_1	$299\,\mu m$	∞

In order to figure out possible mirror radii, the previous assumption about R_{M1}, R_{M2} is now successively increased and all relevant parameters are read out for each new mirror curvature setting. A suitable increment to use here is $\Delta R_{M1,M2} = 2\,cm$, which is large enough to still be manufactured properly during mirror production. In the following the results are stated in a summary version, since they do not show remarkable new insights. However it turns out, that the maximal possible mirror radius is limited by[40] $R_{M1} = 0.456\,m$ for a symmetric resonator design and all radii beyond result in an unstable system.

1. For the situation with mirror radii of curvature $R_{M1} = R_{M2} = 0.42\,m$ we obtain:

   - Excess parameter range: $0\,m < a < 0.233\,m$ with a maximum at $a = 0.114\,m$.
   - Minimum beam waist dependence $w_0(a)$ in this interval as displayed by the blue curve in fig. 2.16.
   - Length for sector 1 of $d_{M1,M2} = 0.534\,m$ and for sector 2 of $d_{M2,M1} = 1.295\,m$.
   - Beam waists $w(z)$ and wavefront radii $R(z)$ within the resonator ($0\,m < z < L'_{cav}$) as indicated by the blue lines in fig. 2.17.
   - Numerical values at the locations of mirrors $M1$, $M2$ and beam waists w_0, w_1 (i.e. z_0, z_1):

z position	Beam waist $w(z)$	Wavefront radius of curvature $R(z)$
z_{M1}	$428\,\mu m$	$-27.6\,cm$
z_{M2}	$428\,\mu m$	$27.6\,cm$
z_0	$79\,\mu m$	∞
z_1	$218\,\mu m$	∞

[39] Please note: Positions for mirrors $M3$ and $M4$ have not been included as they can be set arbitrarily within sector 2.

[40] The precision of this value is higher than what can actually be guaranteed by the supplier, nevertheless it has been evaluated in order to get a more thorough feeling for the boundary.

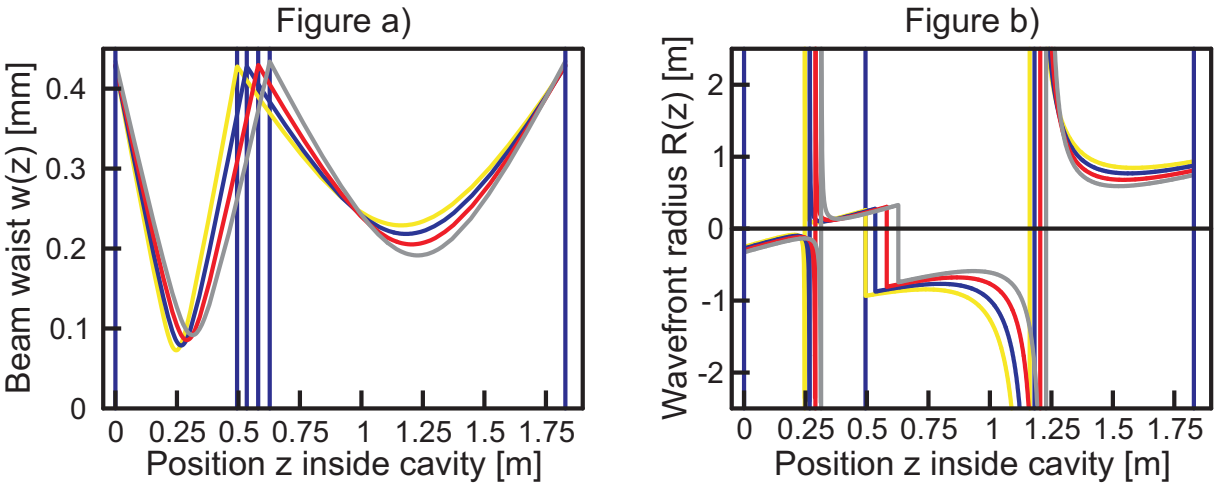

Figure 2.17: a): Beam waist $w(z)$ as a function of the position $0 < z < L'_{cav}$ within the resonator. b): Wavefront curvature $R(z)$ of the optical beam inside the cavity over the same range $0\,m < z < L'_{cav}$. Yellow curves represent the situation for mirror curvatures $R_{M1} = R_{M2} = 0.4\,m$, blue curves the ones for $R_{M1} = R_{M2} = 0.42\,m$, red curves the ones for $R_{M1} = R_{M2} = 0.44\,m$ and gray curves the ones for $R_{M1} = R_{M2} = 0.456\,m$, which is the largest radius possible to still yield a stable symmetric cavity.

- Consequently still too small a minimal beam waist within sector 1 of $w_0 = 79\,\mu m$.

2. For the situation with mirror radii of curvature $R_{M1} = R_{M2} = 0.44\,m$ we obtain:

   - Excess parameter range: $0\,m < a < 0.297\,m$ with a maximum at $a = 0.141\,m$.
   - Minimum beam waist dependence $w_0(a)$ in this interval as displayed by the red curve in fig. 2.16.
   - Length for sector 1 of $d_{M1,M2} = 0.581\,m$ and for sector 2 of $d_{M2,M1} = 1.249\,m$.
   - Beam waists $w(z)$ and wavefront radii $R(z)$ within the resonator ($0\,m < z < L'_{cav}$) as indicated by the red lines in fig. 2.17.
   - Numerical values at the locations of mirrors $M1$, $M2$ and beam waists w_0, w_1 (i.e. z_0, z_1):

z position	Beam waist $w(z)$	Wavefront radius of curvature $R(z)$
z_{M1}	$430\,\mu m$	$-30.2\,cm$
z_{M2}	$430\,\mu m$	$30.2\,cm$
z_0	$86\,\mu m$	∞
z_1	$205\,\mu m$	∞

   - Consequently a minimal beam waist within sector 1 of $w_0 = 86\,\mu m$, which comes closer to the desired value.

3. For the situation with mirror radii of curvature $R_{M1} = R_{M2} = 0.456\,m$ we obtain:

   - Excess parameter range: $0\,m < a < 0.4096\,m$ with a maximum at $a = 0.171\,m$.
   - Minimum beam waist dependence $w_0(a)$ in this interval as displayed by the black curve in fig. 2.16.
   - Length for sector 1 of $d_{M1,M2} = 0.627\,m$ and for sector 2 of $d_{M2,M1} = 1.202\,m$.
   - Beam waists $w(z)$ and wavefront radii $R(z)$ within the resonator ($0\,m < z < L'_{cav}$) as indicated by the black lines in fig. 2.17.
   - Numerical values at the locations of mirrors $M1$, $M2$ and beam waists w_0, w_1 (i.e. z_0, z_1):

z position	Beam waist $w(z)$	Wavefront radius of curvature $R(z)$
z_{M1}	$434\,\mu m$	$-32.8\,cm$
z_{M2}	$434\,\mu m$	$32.8\,cm$
z_0	$92\,\mu m$	∞
z_1	$191\,\mu m$	∞

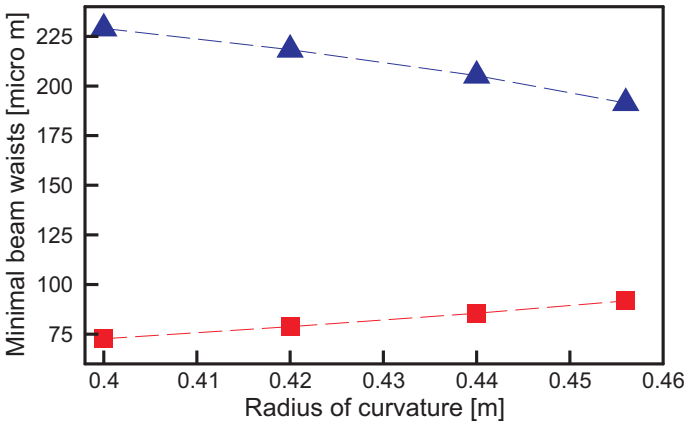

Figure 2.18: Minimum beam waist changes by variation of the mirror curvatures R_{M1} and R_{M2}. The red boxes and line account for the minimal beam waist w_0 in sector 1 while the blue triangles and line stand for w_1 in sector 2. Both symbol types represent calculated values and the dashed lines are just interpolated straight lines between the data points.

The maximum possible waist for the symmetric ring cavity system is hence given by $w_0^{\max} = 92\,\mu m$, which is rather close to the desired $w_0^{pump} = 100\,\mu m$. Since the latter represents just a guideline number, based on experience, the obtained value can be regarded to closely enough fulfill the needs imparted by down-conversion pumping. So our cavity design is scalable up to the doubled repetition rate in terms of its stability. To better allow for spotting the changes of both minimal beam waists w_0 and w_1, they have been plotted as a function of the mirror radii in fig. 2.18. The beam waist w_1 in sector 2 decreases while its counterpart w_0 in sector 1 increases, the gradients of both quantities are different though and comprise a sightly non-linear dependence on the mirror radius.
Interestingly, from fig. 2.16 it can be seen that the dependence of the minimal beam waist $w_0(a)$ on the excess parameter a looses its symmetry around its maximum for mirror radii close to the edge of stable cavity arrangements (represented by $R_{M1} = R_{M2} = 0.456\,m$). These curves show steeper gradients in beam diameter changes towards the side of a confocal system, i.e. $a < a_{max}$ with $\frac{dw_0(a)}{da} \mid_{a=a_{max}} = 0$.
Observing furthermore the behaviour of the wavefront radii of curvature and the beam waists, as shown in fig. 2.17, together with the lengths $d_{M1,M2}$ for all four calculated situations, the connection expected for a two mirror cavity can be revealed for the symmetric ring case as well: That is to say, the larger the radius of curvature, the longer the focal length of each mirror ($f = \frac{R}{2}$) and the greater the wavefront radii. If the focal length of the mirrors increases, the divergence angle of the beam decreases and consequently the minimal spot size at the focus becomes greater. Also, in order to obtain a mirror distance between $M1$ and $M2$, exceeding the confocal case, $d_{M1,M2} = R$, $d_{M1,M2}$ has to increase if R_{M1} is incremented. Additionally the excess parameter a also rises in its value, which corresponds to a growing deviation from the confocal arrangement and should translate into an enhanced positioning of the respective resonator arrangement in the stability diagram.
Thus an assessment of the stabilities[41] of each individual resonator design is undertaken using the above stated values and eq. (2.29). The results are presented in fig. 2.5 with each mirror curvature drawn in the already familiar colour coding ($R_{M1} = R_{M2} = 0.4\,m$ in yellow, $R_{M1} = R_{M2} = 0.42\,m$ in blue, $R_{M1} = R_{M2} = 0.44\,m$ in red and $R_{M1} = R_{M2} = 0.456\,m$ in grey). Indeed we can infer growing mirror curvatures and mirror separations $d_{M1,M2}$ to result in a system's location moving away from the boundary line $g_1 = 0$, gaining more stability space around it. The symmetric situations $R_{M1} = R_{M2} = 0.44\,m$, $R_{M1} = R_{M2} = 0.456\,m$, sensible for SPDC pumping, are also more centred in their location than our actual device of full length ($L_{cav} = 3.71\,m$), thus promising even greater stability against negative influences, such as misalignment and drifts. Furthermore it shall be pointed out, that the positions of the calculated points are located on a hyperbola parallel to the boundary line $g_2 = \frac{1}{g_1}$. This behaviour opposes the expectation gained from symmetric two-mirror resonators, which are found on the diagonal through quadrants 4 and 1 (see fig. 2.5, intersection line of the green points). However for the computed points the optimum excess distance with zero gradient in waist deviation has always been chosen, hence altering the length of sector 1. In other words, both the radii of curvature R_i in $g_1 = 1 - \frac{d_{M1,M2}}{R_{M1}}$ and $g_2 = 1 - \frac{d_{M2,M1}}{R_{M2}}$ as well as the distances d_j are modified simultaneously. If only the mirror curvatures in both quantities are changed, while still preserving a symmetric condition and keeping the distances

[41] which is again justified solely by talking about a symmetric situation

$d_{M1,M2}$, $d_{M2,M1}$ fixed, point movement along a straight line of gradient $\frac{dg_2}{dg_1} > 0$ is obtained. Similarly if only the distances $d_{M1,M2}$, $d_{M2,M1}$ are altered with the R_i fixed, motion along a straight line of gradient $\frac{dg_2}{dg_1} < 0$ results. For starting values given by the $R_{M1} = R_{M2} = 0.4$ situation, both of these cases have been included into fig. 2.5, whereby the former is indicated by a grey line and the latter by a yellow one.

Higher repetition rate systems In the course of these cavity mirror investigations, even higher repetition rates have been given a thought. Explicit calculations have been done for a three times higher repetition rate of $f_{rep} = 246\,MHz$, resulting in a cavity length of $L'_{cav} = 1.22\,m$, and a fourfold one of $f_{rep} = 328\,MHz$, leaving us with a length of $L'_{cav} = 0.915\,m$. Both cases have only been considered under the assumption of a symmetric cavity and the detailed calculation results can be found in the appendix (see section A.2). They provide mirror radii of curvature with corresponding maximal beam waists w_0 and minimal beam waists w_1 of:

	Radii of curvature R_{M1}, R_{M2}	Max. waist w_0	Min. waist w_1
$L'_{cav} = 1.22\,m$	$0.305\,m$	$75\,\mu m$	$155\,\mu m$
$L'_{cav} = 0.915\,m$	$0.229\,m$	$65\,\mu m$	$134\,\mu m$

Obviously the waists w_0 are lower than $w_0^{SPDC} = 100\,\mu m$ and their counterparts w_1 are larger than that number. To utilise such higher repetition rates one option could consequently be to drop the symmetry in radii of curvature between $M1$ and $M2$ and introduce a certain ratio between both, $R_{M1} = x \cdot R_{M2}$. Of course in assessing these systems, the stability diagram is not applicable as the approximation in eq. (2.30) does not hold anymore. However it turns out, that high repetition rate enhancement resonators inherently carry a major drawback in terms of the available count rates from the SPDC process, preventing an actual implementation for our purposes[42]. The arguments leading towards this conclusion will now be discussed in the context of the intra-cavity pulse structure and the power enhancement.

2.2.2 Power enhancement, implication on available pumping powers and expected count rates

The main reason behind the considerations regarding a resonator of higher repetition rate for our experiment has been biased by the wish for less noise on top of the desired photonic quantum state[43] ([43]). Unfortunately, as one can inferred e.g. from reference ([75]) and as we will also see in chapter 5, just scaling up the pumping power of the down-conversion process is not a sensible option to achieve this goal. Instead it can indeed worsen the entire situation, due to the emission characteristics of SPDC, which lead to a steeper increase in production rates for higher photon pair numbers with increasing electric field strengths of the pump. So employing to high a pump power can cause the photon state, which shall be produced by the SPDC source, to drown in noise stemming from the aforementioned higher orders. While the relevant details enabling a more thorough understanding are laid out in chapter 5, for the moment it is just important to note, that a photon source operating at twice the repetition rate was thought to cure this problem simply by having a lower enhancement factor for the intra-cavity pulses at higher repetition rates. The initial idea was to keep the count rates of the desired pair number up by having a higher repetition rate of the SPDC process, but simultaneously suppress unwanted higher order terms by their greater sensitivity to pumping power decrease. As we will see in course of chapter 6, the noise contributions at the highest achievable pumping power levels are at the edge of what is bearable to still retain sensible results. For this reason it would have been nice to maintain the high count rate levels achieved, while having a tool to get rid of some noise. The following argumentation will now consider the amplification properties of shorter cavities and evaluate its implications on expected count rates for an arbitrary shortening fraction. Subsequently the analog theoretical expectations for power enhancement and dispersion, as stated in subsec. 2.1.3 and 2.1.5, will be shown for the particular scenario of a resonator $L'_{cav} = 1.829\,m$ in length.

Frequency domain picture Probably the most simple way to think about any changes introduced into the pulse structure and its related parameters by shortening the cavity can be obtained by investigation of the frequency combs again. The separation of the cavity frequency comb modes (eq. (2.59)) has been show in subsec. 2.1.2 to be set by $\omega_{rep} = \frac{2\pi}{\tau + L_{cav}/c}$. Evaluating the coupling condition for a cavity

[42] At least with our current laser system, as will be shown in subsec. 2.2.2.

[43] Please note that the following discussion incorporates scaling behaviour of the SPDC process on the pumping power as well as some results for photon numbers achieved by our set-up. These are all to be provided in chapter 5. The reader not familiar with down-conversion might thus want to visit the theoretical introduction in subsec. 6.1.2, before going through the remainder of the present chapter.

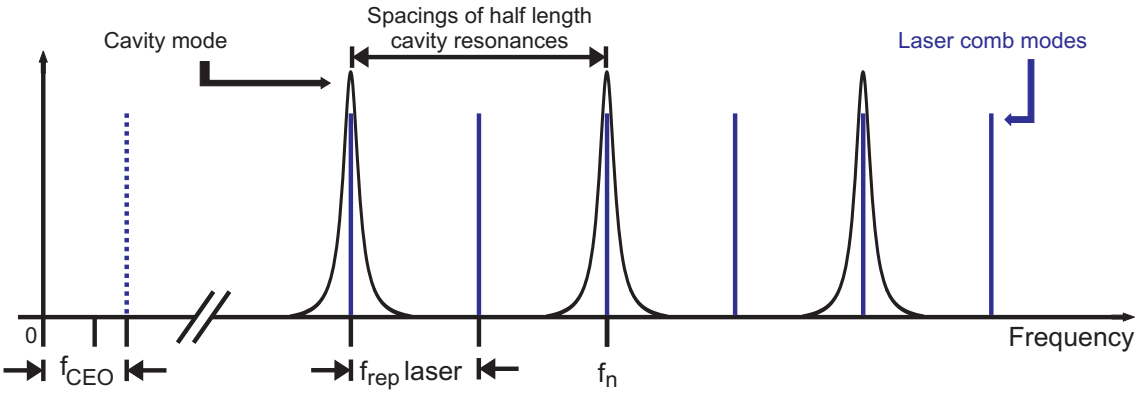

Figure 2.19: External and internal frequency combs for cavity of half lengths. For simplicity, dispersion effects shifting the cavity resonances have been ignored in the drawing.

shortened by an arbitrary integer number n, therefore substituting L_{cav} by $L'_{cav} = L_{cav}/n$ and $\tau' = \tau/n$, gives $\omega'_{rep} = n\frac{2\pi}{\tau + L_{cav}/c} = n \cdot \omega_{rep}$. This means that the separation between resonances is magnified by a factor n and only every n^{th} external frequency mode can penetrate into the cavity, even if higher order dispersion is completely absent. The situation is depicted in fig. 2.19 for $n = 2$ and we will assume dispersion to be negligible for the estimation that is to follow.
The entire electric field inside the resonator of length L_{cav}, $E_{tot}^{L_{cav}}(\omega')$, is established by the summation over all frequency contributions $E_i(\omega'_i)$, i.e.

$$E_{tot}^{L_{cav}}(\omega') = \sum_{i=0}^{N} E_i(\omega'_i) \approx N \cdot E_i(\omega'_i), \tag{2.68}$$

whereby N is the number of all comb modes present in the pumping beam and the electric fields have been anticipated to be vaguely equal for all[44] $i \in N$. Since only $N' = \frac{N}{n}$ external comb teeth can be transmitted into the cavity, due to the matching conditions introduced in subsec. 2.1.4, the internal electric field for the shorter resonator of length L'_{cav} diminishes to

$$E_{tot}^{L'_{cav}}(\omega') = \sum_{i=0}^{N'} E_i(\omega'_i) \approx N' \cdot E_i(\omega'_i) = \frac{1}{n} E_{tot}^{L_{cav}}(\omega'). \tag{2.69}$$

Obeying furthermore the intensity and thus also the optical power to scale with E_{tot}^2, we obtain

$$PE'^{L'_{cav}} = \frac{1}{n^2} PE^{L_{cav}}. \tag{2.70}$$

It is also important to make oneself aware of the n times higher number of pumping beam penetrations through the BBO crystal, caused by the n times higher circulation frequency of pulses inside the apparatus. On time average, the SPDC process will therefore see the pumping light n times instead of only once as for the length L_{cav}. Altogether this implies the down-conversion to be pumped by a power $\frac{1}{n^2}$ times lower, but the generated photon pair number to appear n times more often during an averaging time interval. The main result from the detailed calculations, which is to follow, can thus already be retrieved by aid of this very easy picture. Due to the non-linearity in photon pair generation rates with respect to the pumping power, which approximately scale for a pair number l proportional to[45] $(P_{UV})^l$, the expected number of $\tilde{n}_l$ simultaneously emitted photon pairs, produced in one time bin, reduces by (eq. (6.18))

$$\tilde{n}_l \sim P_{UV}^l = \left(\frac{P^{L_{cav}}}{n^2}\right)^l \cdot n. \tag{2.71}$$

So for a cavity of half length ($n = 2$) we obtain a six-photon count rate, originating from a three pair emission ($l = 3$), reduced by a factor of $\frac{1}{32}$, which would clearly be far too low, if the count-rates available with our set-up are observed (please see fig. 6.7 in chapter 6), detailed numbers are given later in table

[44] This is clearly an oversimplification, however it is sufficient for the estimation obtainable from frequency space. An exact calculation is to follow in the time domain.

[45] The proportionality is only valid in the small pump power limit, which is still fulfilled here. See subsec. 6.1.2 and 6.3.2 or respectively ([161]) for details.

2.1. To cut a long story short, such higher repetition rate resonators would for this very reason not provide the advantages we have expected to gain initially, wherefore they have not been considered for actual implementation either. Since upon now, the argument provided by eq. (2.71) is still just a crude approximation, a proper derivation will be considered in the following, which allows to calculate the expected spectrally resolved power enhancement as well.

Time domain consideration and power enhancement To exemplify the modifications happening in the time domain, we will in a first step take up the reasoning applied in the derivation of the $PE(\lambda)$ (eq. (2.41)) in subsec. 2.1.2. Referring to fig. 2.1, the modifications for n round-trips of the stored electric field between two pumping pulses are based on an analogous sum as in eq. (2.41) only that each operation due to optical components, i.e. t_{loss}, r_{M2}, r_{IC}, $\phi(\omega)$, acts n-times on the transmitted field $t_{IC}E_0$. So the electric field inside the resonator can easily be written down as

$$\begin{aligned} E'_{cav} &= t_{IC}E_0 + t_{IC}E_0\left(t_{loss}r_{M2}r_{IC}\right)^n e^{\left(i\left(\frac{\omega}{c}nL'_{cav}+n\phi(\omega)\right)\right)} \\ &\quad + t_{IC}E_0\left(\left(t_{loss}r_{M2}r_{IC}\right)^n e^{\left(i\left(\frac{\omega}{c}nL'_{cav}+n\phi(\omega)\right)\right)}\right)^2 + ... \\ &= t_{IC}E_0\sum_{i=0}^{\infty}\left(t_{loss}r_{M2}r_{IC}\right)^n e^{\left(i\left(\frac{\omega}{c}nL'_{cav}+n\phi(\omega)\right)\right)} = \frac{t_{IC}E_0}{1-G(\omega)^n}, \end{aligned} \tag{2.72}$$

whereby all quantities maintain their meanings from subsec. 2.1.2. $G(\omega)$ is accordingly the round-trip gain for one single circulation inside the new resonator. If the power enhancement $PE'(\lambda)$ is calculated and furthermore an apparatus of low loss is assumed, which is justified by the previous considerations in subsec. 2.1.2, allowing to expand ([76]) $1-\left(t_{loss}r_{M2}r_{IC}\right)^n \approx n\cdot\left(1-t_{loss}r_{M2}r_{IC}\right)$, a scaling of

$$PE'^{L_{cav}}(\lambda) = \frac{T_{IC}}{\left(1-\left(t_{loss}r_{M2}r_{IC}\right)^n\right)^2} \approx \frac{T_{IC}}{n^2\cdot\left(1-t_{loss}r_{M2}r_{IC}\right)^2} = \frac{1}{n^2}\cdot PE^{L_{cav}}(\lambda) \tag{2.73}$$

is obtained, which yields the same result as eq. (2.71). However, the considerations eq. (2.72) are based on only observe intra-cavity fields after n round-trips, when they coincide with the external pump again. Though for the higher repetition rate scenarios discussed here, there are $n-1$ intermediate pulse enhancements apparent as well. That is to say, once the field is inside, it looses a fraction of its field amplitude and gets distorted by dispersion during every round-trip. Therefore after the first round-trip, the intra-cavity field looks different to the one after the second round-trip, which does itself appear different to the one after the third circulation, etc. In terms of power enhancement for SPDC pumping, there are hence in principle multiple different power enhancements apparent, namely exactly as many as there are round-trips of the intra-cavity field between two successive pumping pulses. What we are interested in here is the power and pulse shape seen by the BBO crystal, which determines the SPDC photon yield. This power consequently changes after every round-trip, since the pulses on the one hand experience losses and dispersion during every circulation, but on the other hand are only enhanced after every n circulations. So there has to be another method devised, which offers the possibility to investigate the changes on the pulses after every single time they have propagated around the resonator.
In order to keep things simple and easy to grasp, we will for the moment restrict n to 2 and allow for shorter lengths later on again. A convenient way to start is to anticipate a pseudo-steady state situation: We know already about the differences in pulse appearances, let us thus denote the field after one round-trip by $E'^{1\,rt}_{cav}$ and the one after the second round-trip by $E'^{2\,rt}_{cav}$. The latter has completed two circulations, i.e. experienced the $G(\omega)$ twice and is superposed with the external pump, whereas the former represents this field after yet another round-trip, with $G(\omega)$ having operated on it once more. Mathematically spoken a coupled equation system is obtained ([77]):

$$E'^{1\,rt}_{cav} = G(\omega)\cdot E'^{2\,rt}_{cav} \tag{2.74}$$

$$E'^{2\,rt}_{cav} = G(\omega)\cdot E'^{1\,rt}_{cav} + t_{IC}E_0 \tag{2.75}$$

Solving it for each electric field $E'^{i\,rt}_{cav}$, with $i\in\{1,2\}$, provides

$$E'^{1\,rt}_{cav} = \frac{G(\omega)\cdot t_{IC}E_0}{1-G(\omega)^2} = G(\omega)\cdot E'^{2\,rt}_{cav} \tag{2.76}$$

$$E'^{2\,rt}_{cav} = \frac{t_{IC}E_0}{1-G(\omega)^2}, \tag{2.77}$$

which corresponds to two round-trips with the real steady state situation in eq. (2.72), but contains an additional gain factor $G(\omega)$ in the numerator for pulses after a single circulation. In terms of power enhancements

$$PE'^{1\,rt}(\lambda) = \frac{G^2(\omega) \cdot T_{IC}}{\left(1 - G(\omega)^2\right)^2} \tag{2.78}$$

$$PE'^{2\,rt}(\lambda) = \frac{T_{IC}}{\left(1 - G(\omega)^2\right)^2}, \tag{2.79}$$

this difference suppresses the amplification of pulses, examined after one round-trip, with respect to those after two. The last point is clear, since after propagating around the resonator once, the pulse has only experienced losses but no additional amplification by the external source yet.
Generalisation of the results (2.76)-(2.79) is absolutely straight forwardly achieved by

$$\begin{aligned} E'^{1\,rt}_{cav} &= G(\omega) \cdot E'^{2\,rt}_{cav} \\ E'^{2\,rt}_{cav} &= G(\omega) \cdot E'^{1\,rt}_{cav} \\ &\vdots \\ E'^{n-1\,rt}_{cav} &= G(\omega) \cdot E'^{n-2\,rt}_{cav} \\ E'^{n\,rt}_{cav} &= G(\omega) \cdot E'^{n-1\,rt}_{cav} + t_{IC} E_0, \end{aligned} \tag{2.80}$$

leaving us with the expected n different expressions for the power enhancement, depending on the number of round-trips j, according to

$$PE'^{j\,rt}(\lambda) = \frac{G^{2j}(\omega) \cdot T_{IC}}{\left(1 - G(\omega)^n\right)^2} \quad \text{if } j \neq n \tag{2.81}$$

$$PE'^{j\,rt}(\lambda) = \frac{T_{IC}}{\left(1 - G(\omega)^n\right)^2} \quad \text{if } j = n \tag{2.82}$$

So we can infer the intra-cavity pulses to decrease in their intensity successively until they are re-amplified by the next external pumping pulse[46].
To investigate the scaling of the count rates, the already introduced simplification of a low loss cavity with $G(\omega) \approx 1$ shall now be used again. From eq. (2.81) one can infer this assumption to overestimate the SPDC pumping power and thus also the number producible photon-pairs. Furthermore it becomes arbitrarily bad for going continuously to shorter cavity lengths, since $\lim_{n\to\infty} G(\omega)^n \to 0$, even if $G(\omega) < 1 \wedge G(\omega) \approx 1$. Nevertheless it is still sufficient for $n = 2$, the example we are most interested in. Execution reduces eq. (2.81) to eq. (2.82) and subsequent expansion of the latter's denominator returns,

$$PE'^{j\,rt}(\lambda) \approx \frac{T_{IC}}{\left(1 - G(\omega)^n\right)^2} \approx \frac{T_{IC}}{n^2 \cdot \left(1 - G(\omega)\right)^2} = \frac{1}{n^2} PE^{L_{cav}}(\lambda), \tag{2.83}$$

which once more reproduces the result in eq. (2.71) from the simple frequency comb estimations. Considering the scaling behaviour of the down-conversion process as stated in subsec. 6.1.2, the dependence of the production rate $\tilde{n}_l$ of l simultaneously generated photon pairs on the pumping power $P^{cav}_{UV} = \int PE(\lambda) P^{ext}_{UV} d\lambda$ is described like $\tilde{n}_l \sim (P^{cav}_{UV})^l$, see eq. (2.71). Therewith one can compute the expected count rates at maximum power enhancement with respect to the data observed for our cavity of full length L_{cav} at an intra-cavity UV power of $P^{L_{cav}}_{UV} \approx 7.2\,W$, which shall be called $\tilde{n}_{l,L_{cav}}$. With desired photon count rates[47] and disturbing higher order emissions[48], as they are extractable from fig. 6.7, for a $f_{rep} = 80.79\,MHz$ resonator

Observed number of photons	Desired coincidences ($\frac{l}{2}\cdot$ H, $\frac{l}{2}\cdot$ V)	Higher order contributions
2	$2.25 \cdot 10^7 \frac{\text{counts}}{min}$	$2 \cdot 10^7 \frac{\text{counts}}{min}$
4	$66000 \frac{\text{counts}}{min}$	$17000 \frac{\text{counts}}{min}$
6	$150 \frac{\text{counts}}{min}$	$62 \frac{\text{counts}}{min}$

[46] The results so far shall be noted to be strict, i.e. no approximations have been made yet, besides the absence of loss in the input coupler.
[47] These are coincidences comprising an equal number of horizontally (H) and vertically (V) polarised photons.
[48] Those represent coincidences with an unequal number of H and V polarised photons.

the functional dependence of the interesting two-, four-, and six-photon events[49] are for the shorter cavities:

$$\tilde{n}^{HV}_{1,L'_{cav}} = \frac{1}{n}\cdot\tilde{n}^{HV}_{1,L_{cav}} \quad \tilde{n}^{HHVV}_{2,L'_{cav}} = \frac{1}{n^3}\cdot\tilde{n}^{HHVV}_{2,L_{cav}} \quad \tilde{n}^{HHHVVV}_{3,L'_{cav}} = \frac{1}{n^5}\cdot\tilde{n}^{HHHVVV}_{3,L_{cav}} \tag{2.84}$$

Higher order noise behaves as:

$$\tilde{n}^{notHV}_{1,L'_{cav}} = \frac{1}{n^3}\cdot\tilde{n}^{notHV}_{1,L_{cav}} \quad \tilde{n}^{notHHVV}_{2,L'_{cav}} = \frac{1}{n^5}\cdot\tilde{n}^{notHHVV}_{2,L_{cav}} \quad \tilde{n}^{notHHHVVV}_{3,L'_{cav}} = \frac{1}{n^7}\cdot\tilde{n}^{notHHHVVV}_{3,L_{cav}} \tag{2.85}$$

Observed number of photons	Desired coincidences ($\frac{l}{2}\cdot$ H, $\frac{l}{2}\cdot$ V)	Higher order contributions
2	$1.125\cdot10^7\,\frac{\text{counts}}{\text{min}}$	$2.5\cdot10^6\,\frac{\text{counts}}{\text{min}}$
4	$8250\,\frac{\text{counts}}{\text{min}}$	$531.25\,\frac{\text{counts}}{\text{min}}$
6	$4.69\,\frac{\text{counts}}{\text{min}}$	$0.48\,\frac{\text{counts}}{\text{min}}$

Table 2.1: Expected count rates for a shorter cavity of $f_{rep}\approx 160\,MHz$ repetition rate, derived from the measurement outcomes stated in fig. 6.7 for $P_{UV}=7.2\,W$ average pumping power.

For the resonator system of twice the repetition rate ($n=2$), the actual count rates to be expected are listed in table 2.1. Considering these, a shorter cavity clearly reduces the six-photon count rates by an amount exceeding what is tolerable in order to end up with half way sensible measurement times. To underpin that with numbers, the characterisation of the genuine six-qubit entangled[50] Dicke $|D^3_6\rangle$-quantum state, see references ([43])-([47]) for further explanations, a measurement time of approximately 2 weeks has been necessary. The HHHVVV count rate level in this experiment has been $3.6\frac{\text{counts}}{\text{min}}$. For the cavity of half length, we would expect only $0.11\frac{\text{counts}}{\text{min}}$ and an approximate measurement time of 64 weeks, i.e. more than 1 year would be required in order to collect an equal number of events. Such a measurement duration is obviously completely illusionary, as even if one was determined enough to attempt this kind of long term measurement, the experimental apparatus would neither be stable over these time scales nor maintain its initial alignment. Hence for quantum state preparation, comprising six or more qubits, shortening of the resonator is not a sensible means for noise reduction. In terms of four photon count rates, the numbers in table 2.1 are still sufficiently high to allow for convenient measurement durations. However they come into the region of rates, which are achievable by non-enhanced UV pumping beams, i.e. just having frequency doubled ultra-short laser pulses directly impinging onto the non-linear medium without intermediate amplification. Such an experiment is for instance described in reference ([50]).
Ultimately the higher repetition rate enhancement resonator does not provide advantages for our purposes as long as the laser pulse repetition rate, pumping the cavity, is not scaled up as well. The only way to achieve shorter measurement times while high maintaining count rate levels and sufficient quantum state fidelity[51] is hence to purchase a new laser system with e.g. high MHz to GHz duty cycle rates[52].

2.2.3 Power enhancement and dispersion for a cavity of half length

Although the shorter cavity approach has just been proven not to enable the achievement of our initial goals, for completeness the expected characteristic parameters for a system of half length ($L'_{cav}=1.829\,m$) shall nevertheless still be stated. The derivation of the individual quantities is absolutely analogous, up to the substitution of L'_{cav} for L_{cav}, to the statements already given in subsec. 2.1.2, 2.1.5 and the one for the power enhancement in 2.2.2 with $n=2$. Thus only results will be presented in the following and the reader is pointed out the previous text where appropriate.

Losses In terms of losses the only alteration concerns the contributions imparted by the air inside the resonator, as the BBO thickness is kept constant. With an absorption coefficient of ([68]) $\alpha_{\text{air}}=0.27\,\frac{1}{km}$ a transmission of $T'_{\text{air}}=99.95\,\%$ is obtained, which is sensible since half the propagation distance within the medium should result in half the losses due to this medium. With the transmittivity through the BBO of $T^{exp}_{\text{BBO}}=97.5\,\%$ (eq. (2.33)) and a reflectance of the cavity mirrors $R_{M1,M2,M4}=99.94\,\%$ (eq. (2.31)), cw input coupler recommendations of

[49] i.e. one, two-and three photon-pair emissions
[50] see reference ([35]) for descriptions of the term genuine multi-qubit entangled.
[51] Please refer to reference ([35]) for a definition of fidelity.
[52] For instance available from: Msquared lasers, 1 Technology Terrace, Todd Campus, West of Scotland Science Park, Maryhill Road, Glasgow, G20 0XA, United Kingdom

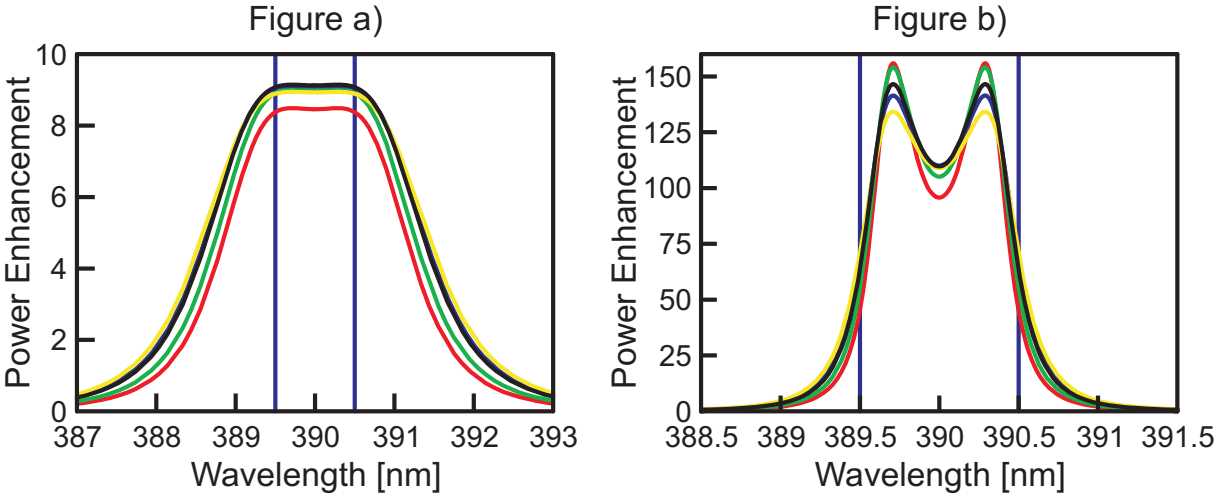

Figure 2.20: Power enhancement curves for the first possible pulse shape inside the shortened cavity, appearing between two successive pumping pulses when the intra-cavity pulse has completed an additional round-trip and considering different input coupler transmittances T_{IC}. Fig. a) shows the scenario with BBO. The colour coding is: Red $\Leftrightarrow T_{IC} = 1.5\,\%$, green $\Leftrightarrow T_{IC} = 2\,\%$, black $\Leftrightarrow T_{IC} = 2.71\,\%$ (best choice), blue $\Leftrightarrow T_{IC} = 3\,\%$, yellow $\Leftrightarrow T_{IC} = 3.5\,\%$. Fig. b) represents an empty resonator, with a colour coding of: Red $\Leftrightarrow T_{IC} = 0.05\,\%$, green $\Leftrightarrow T_{IC} = 0.1\,\%$, black $\Leftrightarrow T_{IC} = 0.15\,\%$ (best choice), blue $\Leftrightarrow T_{IC} = 0.2\,\%$, yellow $\Leftrightarrow T_{IC} = 0.25\,\%$.

$$R_{cav/2}^{\text{IC, BBO, theo.}} = 97.39\,\% \tag{2.86}$$

$$R_{cav/2}^{\text{noIC, BBO, theo.}} = 99.89\,\% \tag{2.87}$$

are obtained, calculated analogously to eqs. (2.38) and (2.39). These numbers are very similar to the ones obtained previously, as the influence of air on the total intra-cavity loss is minor compared to the non-linear crystal's share.

Power enhancement In order to derive the spectrally resolved power enhancement $PE(\lambda)$, both possible intra-cavity pulse shapes have to be considered separately. Inserting the new cavity length L'_{cav} into the function for the phase $\phi(\omega)$, eq. (2.48), and subsequent utilisation of eq. (2.78) allows to determine the power enhancement after one round-trip with the BBO crystal inside the resonator. Similarly applying the phase function from eq. (2.49) together with eq. (2.78) gives the situation without crystal. Exemplary curves for both arrangements are shown in fig. 2.20 for the former in plot a) and the latter in plot b).
Equally, the power enhancement for the appearing pulse shape after two round-trips can be yielded from $PE'^{2\,rt}(\lambda)$ in eq. (2.79) and the respective spectrally resolved power enhancements, for the apparatus with and without the BBO crystal, based on some different input coupler transmittances are drawn in fig. 2.21.
One can infer from figs. 2.20 and 2.21 in comparison with figs. 2.8 and 2.9 for the $80.79\,MHz$ resonator an approximate constancy in the power enhancement achieved for the BBO presence, whereas for its absence the magnification factors $PE(\lambda)$ roughly doubles. This is not surprising, since the achievable maximal enhancement at a particular wavelength is just determined by the losses inside the cavity. While these are dominated by the BBO and thus do not considerably change in the first case, they half in the second case, so the power enhancement for individual wavelengths can roughly double.
In order to evaluate the overall power enhancement achieved, as well as the optimal choice for an input coupler, we will proceed in the same way as described in subsec. 2.1.3. For an external spectrum, the dataset shown in fig. 2.10 will be applied again. The intra-cavity spectrum will accordingly be computed by multiplying the appropriately normlised external UV spectrum with the spectrally resolved power enhancement. Subsequently the overall amplification $\bar{PE}$ can be received from integration over the expected internal pulse spectrum. Internal pulse spectra have been evaluated by incorporating the power enhancements shown in figs. 2.20 and 2.21, whose curves are shown in fig. 2.22 a)-2.25 a) for both possible pulse shapes and both experimental arrangements, respectively.

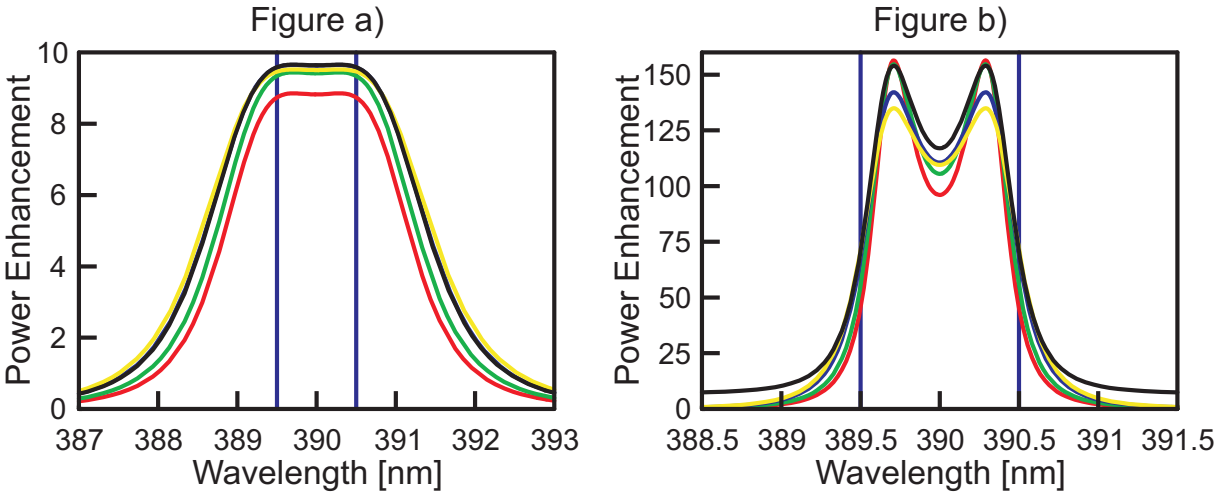

Figure 2.21: Power enhancement curves for the second possible pulse shape inside the shortened cavity, appearing after completion of two round-trips. Fig. a) shows the scenario with BBO by a colour coding of: Red $\Leftrightarrow T_{IC} = 1.5\,\%$, green $\Leftrightarrow T_{IC} = 2\,\%$, black $\Leftrightarrow T_{IC} = 2.82\,\%$ (best choice), blue $\Leftrightarrow T_{IC} = 3\,\%$, yellow $\Leftrightarrow T_{IC} = 3.5\,\%$. Fig. b) represents an empty resonator, with a colour coding of: Red $\Leftrightarrow T_{IC} = 0.05\,\%$, green $\Leftrightarrow T_{IC} = 0.1\,\%$, black $\Leftrightarrow T_{IC} = 0.15\,\%$ (best choice), blue $\Leftrightarrow T_{IC} = 0.2\,\%$, yellow $\Leftrightarrow T_{IC} = 0.25\,\%$.

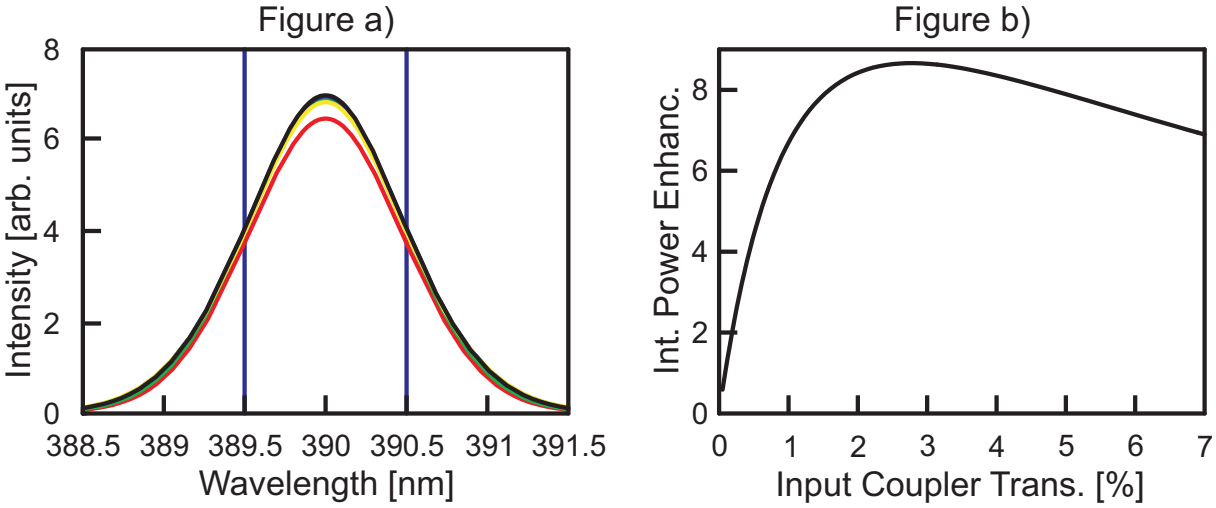

Figure 2.22: Internal pulse spectrum and integrated power enhancement for intra-cavity pulses between two external pumping pulses (described by eq. (2.78)) for a resonator with a BBO crystal. Fig. a) shows the expected internal pulse spectra, with a colour coding of: Red $\Leftrightarrow T_{IC} = 1.5\,\%$, green $\Leftrightarrow T_{IC} = 2\,\%$, black $\Leftrightarrow T_{IC} = 2.92\,\%$ (best choice), blue $\Leftrightarrow T_{IC} = 3\,\%$, yellow $\Leftrightarrow T_{IC} = 3.5\,\%$. Fig. b) states the overall power enhancement as a function of input coupler transmittance. The best amplification of a factor 8.7 is achieved for $T_{IC}^{1\,rt,\,\mathrm{BBO}} = 2.92\,\%$.

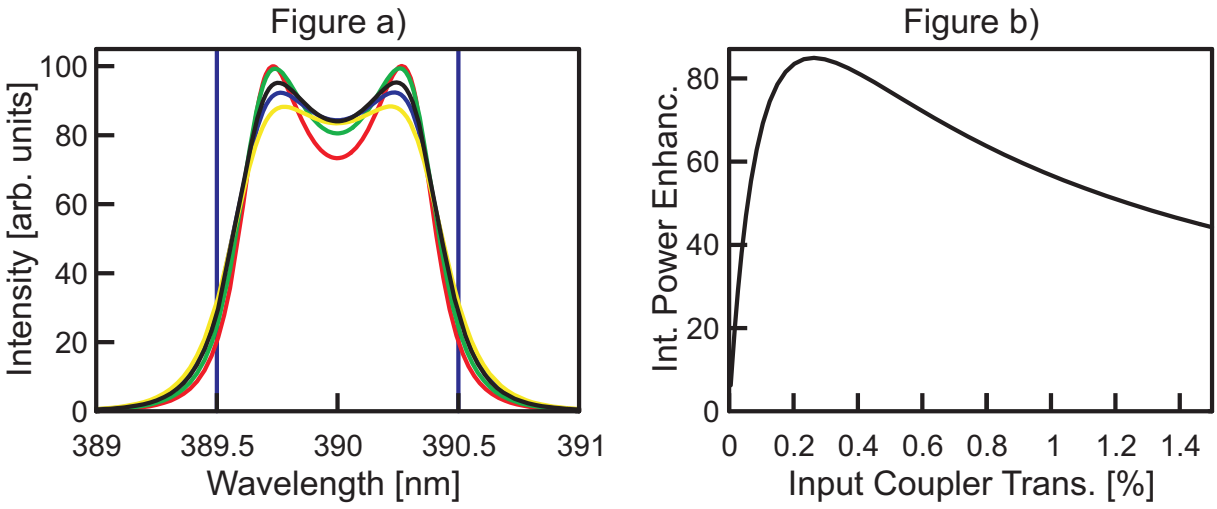

Figure 2.23: Internal pulse spectrum and integrated power enhancement for intra-cavity pulses between two external pumping pulses (described by eq. (2.78)) for a resonator without a BBO crystal. Fig. a) shows the expected internal pulse spectra, with a colour coding of: Red $\Leftrightarrow T_{IC} = 0.15\,\%$, green $\Leftrightarrow T_{IC} = 0.2\,\%$, black $\Leftrightarrow T_{IC} = 0.26\,\%$ (best choice), blue $\Leftrightarrow T_{IC} = 0.3\,\%$, yellow $\Leftrightarrow T_{IC} = 0.35\,\%$. Fig. b) states the overall power enhancement as a function of input coupler transmittance. The best amplification of a factor 85 is achieved for $T_{IC}^{1\,rt,\ \mathrm{noBBO}} = 0.26\,\%$.

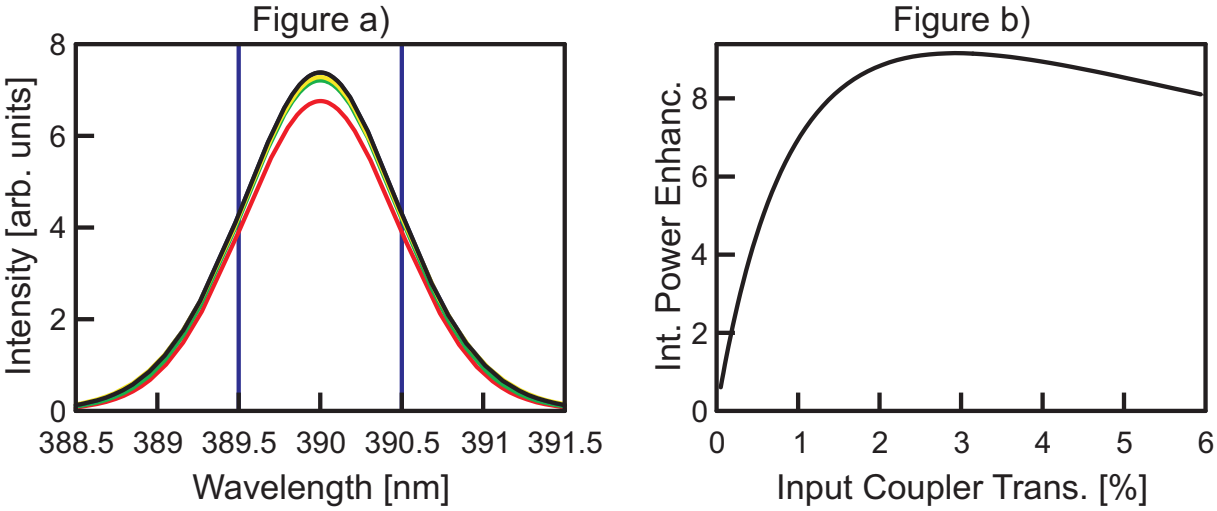

Figure 2.24: Internal pulse spectrum and integrated power enhancement for intra-cavity pulses coinciding with the external pumping pulses (described by eq. (2.79)) for a resonator with a BBO crystal. Fig. a) shows the expected internal pulse spectra, with a colour coding of: Red $\Leftrightarrow T_{IC} = 1.5\,\%$, green $\Leftrightarrow T_{IC} = 2\,\%$, black $\Leftrightarrow T_{IC} = 2.92\,\%$ (best choice), blue $\Leftrightarrow T_{IC} = 3\,\%$, yellow $\Leftrightarrow T_{IC} = 3.5\,\%$. Fig. b) states the overall power enhancement as a function of input coupler transmittance. The best amplification of a factor 9.2 is achieved for $T_{IC}^{2\,rt,\ \mathrm{BBO}} = 2.92\,\%$.

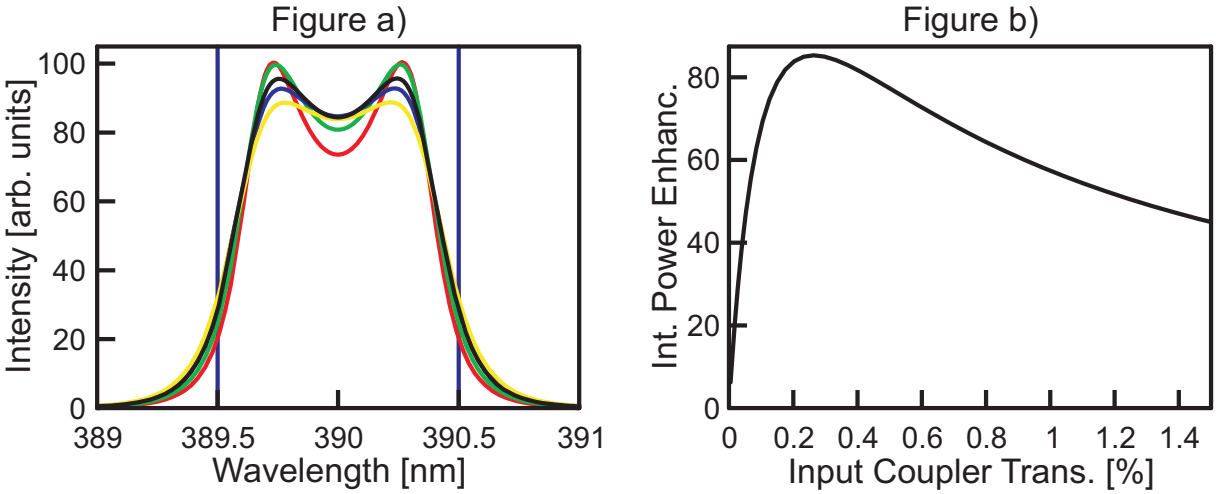

Figure 2.25: Internal pulse spectrum and integrated power enhancement for intra-cavity pulses coinciding with the external pumping pulses (described by (eq. 2.79)) for a resonator without a BBO crystal. Fig. a) shows the expected internal pulse spectra, with a colour coding of: Red $\Leftrightarrow T_{IC} = 0.15\,\%$, green $\Leftrightarrow T_{IC} = 0.2\,\%$, black $\Leftrightarrow T_{IC} = 0.26\,\%$ (best choice), blue $\Leftrightarrow T_{IC} = 0.3\,\%$, yellow $\Leftrightarrow T_{IC} = 0.35\,\%$. Fig. b) states the overall power enhancement as a function of input coupler transmittance. The best amplification of a factor 85 is achieved for $T_{IC}^{2\,rt,\ \mathrm{noBBO}} = 0.26\,\%$.

Optimisation of the input coupler transmittivity is once more implemented by repeating the aforementioned procedure for continuously changing the T_{IC} values and searching for the maximally achievable overall power enhancement. The dependences of PE on T_{IC} for all four occurring situations are plotted in fig. 2.22 b)-2.25 b). Optimal input coupler reflectivities and the associated expected maximal overall power enhancements are listed in table 2.2 below, whereby the number of round-trips after the last amplification by the external source is referred to as i, with $i \in \{1, 2\}$:

i	BBO crystal inserted:	R_{IC}	Maximal PE
1	yes	97.18 %	8.7
2	yes	97.08 %	9.2
1	no	99.74 %	85
2	no	99.74 %	85

Table 2.2: Theoretical prediction of input coupler reflectance for highest integrated power enhancement.

The amplifications in both experimental arrangements is slightly lower for the pulses after one round-trip, since they have not yet been amplified by the external pump again and are thus subject to higher losses as explained in subsec. 2.2.2. The same reasoning also applies to the required input coupler reflectances for the situation with BBO. In contrast the equality in R_{IC} for both round-trip numbers in an arrangement with no crystal can be explained by the low losses once again. With only air and cavity mirrors $(G(\omega))^2 = R_{IC}^{\mathrm{noBBO}} = 0.9985 \approx 1$ (see eq. 2.87), wherefore the numerator in eq. (2.78) $(G(\omega))^2 T_{IC} \approx T_{IC}$ resembles the one in eq. (2.79), leading to identical reflectances.

Chapter 3

Cavity operation

In the following chapter the experimental set-up shall be described. In order to do so, three main parts are to be focussed on: The first concerns preparation of the pumping beam prior to its coupling into the enhancement resonator. The second deals with the stabilisation mechanism of the cavity. Ultimately also the linear optical set-up employed to observe an entangled multi-qubit state from the output of the intra-cavity spontaneous parametric down-conversion (SPDC) process is going to be introduced.

3.1 Pumping-beam preparation

3.1.1 Laser system and frequency conversion

We will step into the discussion by considering our initial laser light source, which is a commercially available titanium sapphire (Ti:Sa) laser system[1] pumped in the green by a $10\,W$ solid state laser[2]. Utilising this device, mode-locked ultra-short laser pulses with an average output power of $2\,W$, centred around $\lambda_{\text{Ti:Sa}} = 780\,nm$ at a repetition rate of $f_{rep} \approx 80\,MHz$ are obtained. An autocorrelation measurement of these indicates a pulse duration of $\tau_{\text{Ti:Sa}} = 130\,fs$, assuming Sech-shaped pulses (see chapter 5 for details on this). Observation of the Ti:Sa output with a spectrometer resulted in a spectral bandwidth of $\Delta\lambda_{\text{Ti:Sa}} \approx 5.5\,nm$, so a time-bandwidth product of $\Delta\nu_{\text{Ti:Sa}} \cdot \tau_{\text{Ti:Sa}} = 0.379$ is received (for more details on this quantity, see subsec. 5.2.2). The IR output pulses can be modified in terms of their central wavelength and the amount of negative GVD, they experience inside the laser cavity, by propagation through four prisms. Both degrees of freedom are externally accessible and are used for preserving the input coupling condition into the resonator as outlined later in subsec. 3.2.2. Here it shall just be mentioned, that in order to keep the central wavelength of the Ti:Sa spectrum constant, a small fraction of its output is split-off and continuously monitored by a spectrometer[3]. A computer controlled motor connected to the central-wavelength-adjust screw of the laser, processes these recorded spectra and takes care of the cancellation of small wavelength drifts by appropriately moving the motor. The rate of this stabilisation procedure is approximately on the order of $1\,Hz$.
In order to enter the necessary wavelength range required for the SPDC process, a frequency conversion of the IR pulses has to be undertaken. Therefore, a non-linear lithium triborate (LBO) crystal[4] is inserted for sum-frequency generation of the aforementioned pulses[5]. An in depth discussion of the underlying physical mechanisms is skipped here, as it is not important and can be found in the literature, e.g. reference ([79]). What is important for this work is the outcome of the frequency doubling process, which leave us with a pumping pulse centred at a wavelength in the UV of $\lambda_{p,0} = 390\,nm$ with an average power of $\bar{P}_{UV} = 0.54\,W$. Its spectral width is on the order of $\Delta\lambda_p = 1.1\,nm$ and its pulse duration is about $\tau_p = 150\,fs$; the origin of both values will be discussed in detail in chapter 5. The up-conversion set-up is depicted schematically in fig. 3.1 and its real world implementation can be seen in fig. 3.2. In order to get rid of the remaining IR light not converted in the LBO crystal, the resulting output beam is subject to multiple reflections off mirrors, which are highly reflective in the UV but transmittive in the IR.

[1] Model: Spectra Physics Tsunami
[2] Model: Spectra Physics Millennia
[3] Model: Ocean Optics HR 4000
[4] See ([72]) and ([78]) for material properties.
[5] It should be noted, that although such a process is commonly referred to as second-harmonic generation (SHG), in reality comb modes of different frequencies within the pumping pulse can mix with one another as well, causing cross terms.

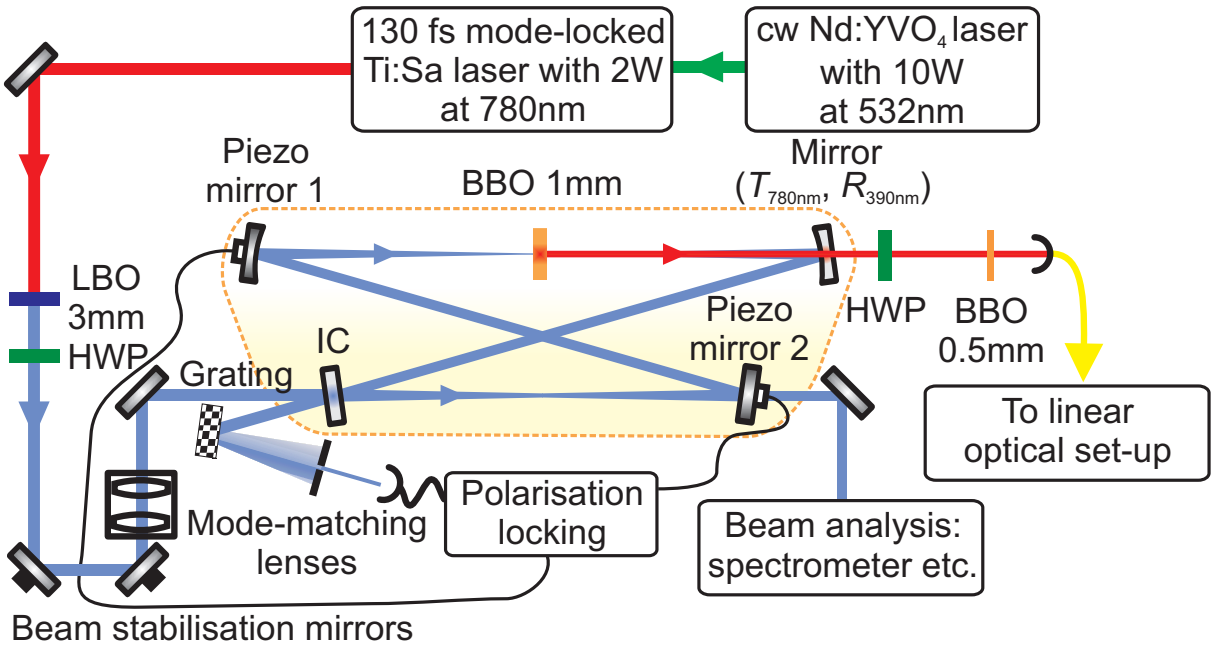

Figure 3.1: Schematic drawing of the enhancement cavity set-up. The output of a mode-locked laser source in the IR is frequency doubled by an LBO crystal into the UV and subsequently coupled into the resonator after propagation through some lenses to match the transverse cavity mode. Stabilisation of the resonator length is achieved by polarisation locking according to the Hänsch-Coulliaud method, utilising two mirrors mounted onto piezo electric transducers. The field inside the resonator is monitored by a spectrometer and a photodiode, which observe the leakage through one of the cavity mirrors. SPDC photons, generated within the non-linear BBO crystal inside the resonator, are coupled out through another mirror, rotated in their polarisation with a half-wave plate and subsequently impinging onto another BBO crystal of half length, cancelling temporal and spatial walk-off effects between both photons in the created pair, imparted by the first BBO (see subsec. 6.2.2). Thereafter the SPDC photons are coupled into an AR-coated single mode (SM) optical fibre, guiding them to the linear optical set-up explained in more detail in section 3.3.

3.1.2 Transverse mode matching of pump and cavity

In order to achieve good input coupling into the resonator, not only the frequency comb modes of the external pulses have to match the cavity's longitudinal modes, but also the transverse spatial modes of both have to coincide. There is a two-fold requirement on the external pumping beam in that respect: On the one hand, the transverse Gaussian mode has to fit the Laguerre-Gaussian mode profile of the intra-cavity beam (eq. (2.6)), which is intended to be $TEM_{0,0}$. On the other hand, also the transverse location of the pump has to be such that is fits to the one of the cavity mode, whose positioning is solely determined by the tilting angles of the four cavity mirrors.
Achievement of the former condition is obtained by shaping the frequency-doubled output pulse of the LBO crystal by cylindrical lenses, as depicted in fig. 3.2. These minimise the astigmatism resulting from the frequency doubling of the Ti:Sa pulses. To achieve furthermore equal Gaussian mode sizes at the position of minimal beam waist inside the cavity, a telescope is applied in front of the input coupling mirror (schematically incorporated in fig. 3.1). Thereby we are able to achieve a reasonable high input-coupling ratio of approximately 50 % of the external beam. Although there is also some frequency comb[6] and polarisation[7] mismatch included in this figure, the main contribution presumably results nonetheless from insufficient mode quality of the external UV beam. Such a degradation is tolarable for our experimental purposes[8], however it should be improved, if the resonator is sought to yield the maximal enhancement.
The latter of the initially stated requirements stems once from the occurrence of drifts in the positioning and the angle of the pumping beam on the face of the cavity input coupler. The main contributor to those are changes in the emission direction of the Ti:Sa output beam. This is due to the cavity mirrors within

[6] see chapter 5
[7] see subsec. 3.2.1 below
[8] see discussion about count rates and noise in chapter 6

the laser system having to be occasionally realigned to achieve the maximum IR output of $2\,W$, which also requires resetting of the tilting angle orientation of the LBO crystal to achieve phase matching and thus the highest available UV power. Such a manipulation changes the orientation of the mode within the laser oscillator and also the positioning plus the angle of the laser output with respect to the optical axis of the system. Keeping the last mentioned two parameters constant at the cavity input coupler, can yet be achieved by a compensation scheme for such alterations, employing two reflecting mirrors with automated angular adjust, as visible in fig. 3.2 and schematically included in fig. 3.1 as well. Both mirrors are mounted on piezo-electric transducers (PTZ), which are capable of performing the required angular displacement. They are driven by an error signal derived from two quadrant photodiods, onto which some minor portion of the beam is incident in after having been reflected off both mirrors. The error signal is set in such a way, that the mirrors always keep the position and the incidence angle of the pump at the input coupler in resemblance with the analogue parameters of the intra-cavity beam.

3.2 Cavity stabilisation scheme

In the previous chapter, the requirements for external pumping pulse enhancement by the cavity have been explained in terms of the frequency comb matching condition in subsec. 2.1.4. Fulfilment of this condition requires adjustment of both frequency combs involved, whereby their parameters ω_{rep} and ω_{CEO} have to be matched. In recalling again the expression for the cavity comb ω'_n from eq. (2.61), we can infer the distance of the intra-cavity frequency comb teeth[9]

$$\omega'_{rep} = \frac{2\pi}{\tau + L_{cav}/c},$$

comprising the group round trip time τ and the experimentally accessible parameter of the cavity length L_{cav}. In contrast the offset frequency (eq. (2.61))

$$\tilde{\omega}_{CEO} = \frac{\Phi_0}{\frac{L_{cav}}{c} + \tau} + \frac{\Psi(\omega')}{\frac{L_{cav}}{c} + \tau}$$

can only be changed together with, but cannot varied independently of ω'_{rep}, as all other parameters entering are fixed dispersion features of the resonator. In other words, we can pin the cavity comb by keeping the FSR of the resonator constant, which simultaneously also sets $\tilde{\omega}_{CEO}$, since the dispersion of the cavity is assumed to be steady. However we have no means of additionally altering $\tilde{\omega}_{CEO}$ to our liking, so the correct positioning of both combs with respect to one another is executed by manipulating the external one. The following explanations will now focus firstly on a method to achieve stabilisation and subsequently take care about the mechanisms to adjust the offset frequency of the external comb, defined in eq. (2.58), in an appropriate way to satisfy the input coupling constraint.

3.2.1 Implementation of the Hänsch-Coulliaud locking scheme

In principle there are several ways to stabilise the length of an optical resonator, among which possibly the most prominent examples[10] are the Pound-Drever-Hall ([80], [81]) and the Hänsch-Coulliaud ([82], [83]) locking scheme. The first one operates by imparting modulated side-bands onto the frequencies within the signal, whereby the second is based on the polarisation of the light and shall be used for our purposes.
Its basic implementation is very well explained in reference ([82]) and shall thus not be repeated here. However the actual working principle of this technique is slightly more elaborate in our set-up, as we utilise a birefringent crystal as polarisation selective intra-cavity element ([83]) and have an incoming beam consisting of an entire frequency spectrum, in contrast to the single mode scenario considered in reference ([82]). The applied polarisation geometry is set as follows: The preferred polarisation direction of the cavity is orientated along the vertical direction[11], referred to as $|V\rangle$. The incoming beam has some slight diagonal component, i.e. $E_p \sim \alpha|V\rangle + \beta|H\rangle$ with $\alpha \gg \beta$, whereby $|H\rangle$ assigns horizontal polarisation. However only $|V\rangle$-polarisation can couple into the resonator, due to the birefringence in the BBO crystal. For the optimum phase matching angle of the collinear type-II SPDC, given by $\theta = 43.53°$, the refractive indices for the extraordinary and ordinary polarised rays[12] are $n_{ext} = 1.632$ and $n_{ord} = 1.695$ respectively,

[9] The modifications of the denominator with regard to the expression for the free spectral range $FSR = \frac{2\pi c}{L_{cav}}$ shall be inferred to stem from the rewriting the intra-cavity mode structure into a frequency comb in eq. (2.61).
[10] Unless an additional stabilised frequency comb is considered.
[11] This is due to the phase-matching requirement of the SPDC process, which requires pumping light polarised along the direction of the extraordinary refractive index in the BBO crystal, here vertical, as outlined in subsec. 6.1.1.
[12] See reference ([84]) or the discussion in subsec. 6.1.1 later on for an explanation of these terms

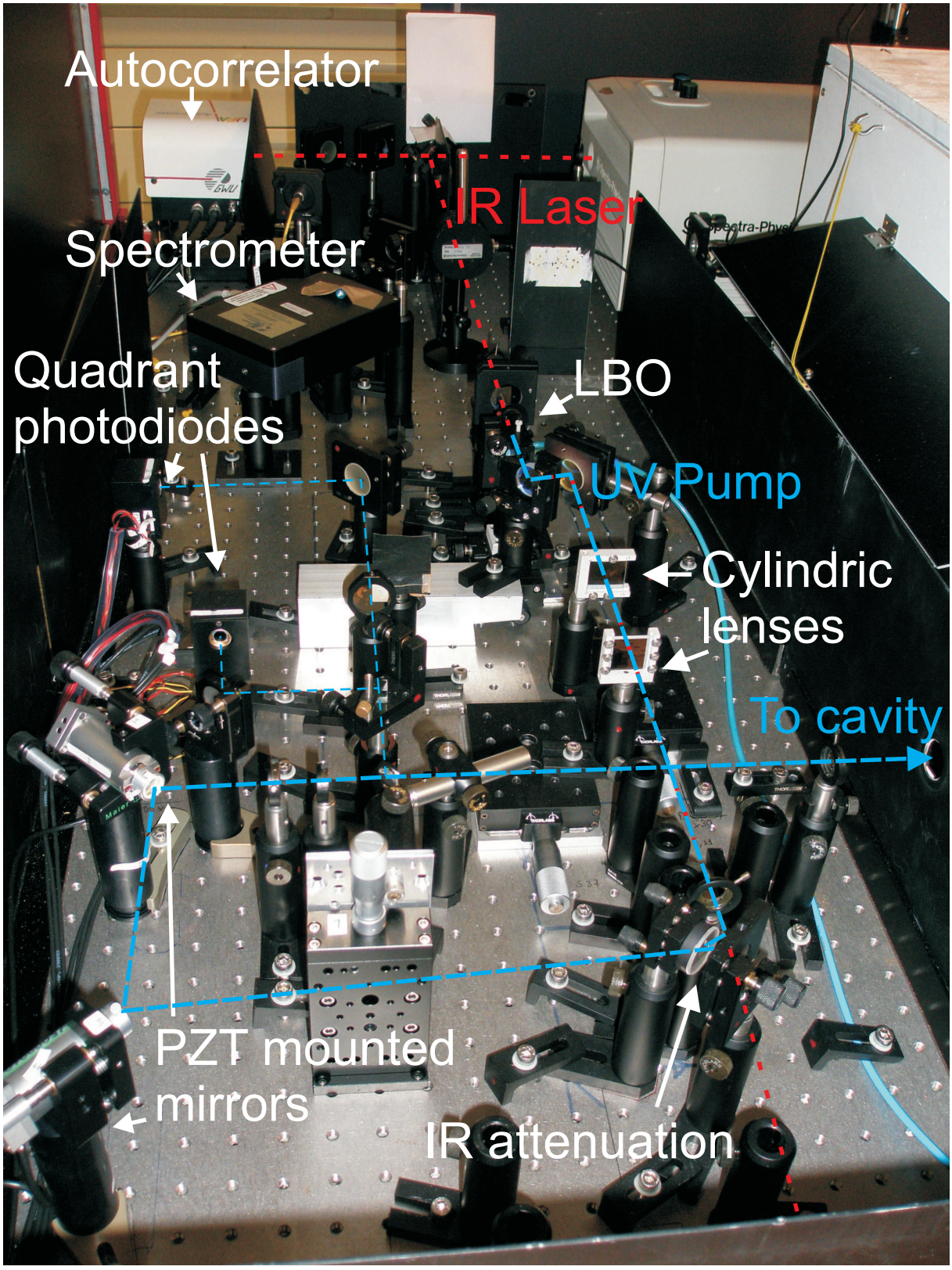

Figure 3.2: Experimental implementation of the optics required for the pumping beam generation of the cavity. One can infer from this photograph the autocorrelator, used to measure the output pulse duration $\tau_{\mathrm{Ti:Sa}}$, the spectrometer for observing the spectral width $\Delta\lambda_{\mathrm{Ti:Sa}}$ and its central wavelength $\lambda_{\mathrm{Ti:Sa}}$, as well as the LBO crystal used for frequency doubling, followed by the transverse positioning and pointing angle stabilisation scheme with its two PZT mounted mirrors and quadrant photodiodes.

at a wavelength of $\lambda = 390\,nm$. In the case of resonance at $\lambda = 390\,nm$ for the extraordinary light, which in our case corresponds to $|V\rangle$ polarisation, a wavelength of $\lambda_{ord} = 390.007\,nm$ would be resonant for the ordinary, $|H\rangle$-polarised part. This results in a frequency difference of $\Delta\nu_{biref} = 19\,GHz$ between both resonance frequencies. Furthermore the widths of the cavity resonances are governed by the finesse of the cavity, which we will infer in subsec. 4.3.2 to be $F \approx 72$. The FWHM linewidth $\Delta\nu$ of a resonance is connected to this value and the FSR $\nu_{FSR} \approx 80\,MHz$ according to ([85])

$$F = \frac{\nu_{FSR}}{\Delta\nu}, \tag{3.1}$$

which results in $\Delta\nu \approx 1.1\,MHz$ bandwidth per resonance. Hence the two resonances for $|V\rangle$ polarisation at $\lambda_{|V\rangle} = 390\,nm$ and for $|H\rangle$ polarisation at $\lambda_{|H\rangle} = 390.007\,nm$ are well separated. Also the laser frequency comb modes of the mode-locked oscillator are much narrower than the $\Delta\nu_{biref} = 19\,GHz$, preventing any overlap between the small component of the external $|H\rangle$ polarised light and the cavity resonance at $\lambda_{|H\rangle}$. So if we were just considering one comb mode at $390\,nm$, only the $|V\rangle$ polarisation would be resonant with the cavity, leading to reflection of the $|H\rangle$ component. However, even if considering the presence of the entire external frequency comb with a mode separation of $\omega_{rep} = 2\pi \cdot 80\,MHz$, the $|H\rangle$-polarised resonance of the cavity would be positioned at $19\,GHz = 237.5 \cdot \omega_{rep}$ towards the red of the resonant $|V\rangle$-polarised tooth, which lies exactly between two external comb teeth. Since the cavity's spectral acceptance bandwidth of $1.1\,MHz$ for $|H\rangle$ polarisation is much narrower than the separation between two external comb teeth, the $|H\rangle$-polarised light is off-resonant, when the cavity is stabilised onto its $|V\rangle$-polarised counterpart. The cavity length is actually set by a pair of PZTs, onto which the cavity mirrors $M1$ and $M3$ in fig. 2.2 are mounted on (see 3.1). The first PZT operates at a maximal bandwidth of $10\,kHz$ with a travel range of $2.2\,\mu m$, taking care of rapidly occurring length fluctuations, whereby the second one has a greater range of $12\,\mu m$, with a bandwidth of about $3\,Hz$ and cancelling long term drifts of the cavity length.
Regarding the generation of an error signal, one has to be aware of the multiple frequency nature of the laser light impinging onto the beam splitter in the polarisation analysis part of the locking set-up (see fig. 3.1). We know from subsec. 2.1.4 that cavity resonances get slightly displaced from their original position by the influence of higher order dispersion. Therefore the optimal cavity comb repetition rate ω'_{rep} in eq. (2.61) for achieving best comb tooth overlap varies for different parts of the pulse spectrum. If the entire spectrum was to impinge onto the beam splitter, the locking process could just pick a certain part in the frequency spectrum and choose an appropriate cavity length to stabilise the input coupling for this region. However after some time it could just hop on to utilise another part of the spectrum and set L_{cav} to optimise for that. So an inherent element of instability would be introduced by utilising the entire spectrum. Hence we select only a small fraction in the centre of the spectrum, by reflecting the beam off a grating and choosing the relevant frequency interval by two razor blades, working as a Fourier filter and dismissing unwanted components. The chosen fraction is subsequently used for the error signal generation by polarisation analysis like it is described in reference ([82]). All actually implemented components within the Hänsch-Coullioud lock apparatus can be seen in fig. 3.1. For the selected frequency part, the best input coupling conditions can be obtained, since dispersion compensation, according to the scheme introduced in subsec. 2.1.4, is optimal there. Experimentally this spectral region can be inferred by comparison of the appropriately scaled internal cavity spectrum with the normalised one of the external pump. Such an examination is conducted later in subsec. 4.2.4.

3.2.2 Maintenance of pump pulse coupling into the cavity

By fixation of the cavity length, the internal comb is set in all of its degrees of freedom according to eq. (2.61). To fulfil the input coupling condition, outlined in subsec. 2.1.4, the external laser comb has to be tweaked in its parameters ω_{rep} and ω_{CEO} to achieve best comb mode overlap. We achieve this, by changing the dispersion, the pulses inside the laser oscillator experience, via the optical path length of the light within the four prisms positioned in the laser cavity[13]. In this way, the frequency comb tooth separation of the laser beam, ω_{rep}, and also the carrier-envelope phase offset, ω_{CEO}, are changed simultaneously. However, as we have already mentioned, the central wavelength of the IR pulses is fixed in its frequency positioning. Considering an idealised picture, in which this fixation operates always the same comb tooth, a modification in both aforementioned quantities can thus only displace comb modes along the frequency axis with respect to the central mode, symmetrically to either side of it[14]. Thereby the separation between teeth and the offset frequency are changed in a controlled way,

[13] A more thorough explanation of their operational principle can be found in reference ([111]).

[14] In reality the central wavelength adjustment will pick different teeth at a time, due to its limited sensitivity. Therefore the entire comb will also be displaced along the frequency axis, when modifying the prism position. However one can still

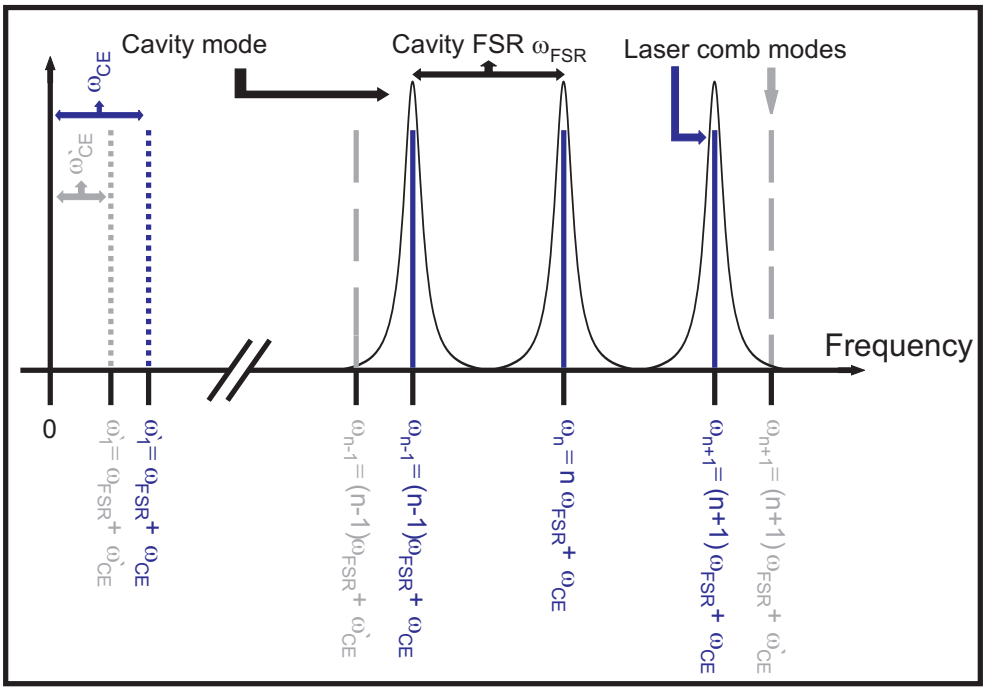

Figure 3.3: Schematic, idealised representation of changes introduced on the external frequency comb (blue) by changing the dispersion compensation inside the laser oscillation. Moving the prisms therein in and out of the beam, while keeping the central wavelength of the comb constant, results in displacements with respect to the initial comb modes (grey dashed lines). The new offset and separation between teeth can bring the external comb (solid lines) into resonance with the longitudinal modes of the enhancement resonator (solid black curves).

while keeping the envelope of the comb in place during the process, as it is also shown schematically in fig. 3.3. Since the frequency comb structure is maintained throughout the sum frequency generation process ([79]), the UV pumping pulses inherit any modifications carried out in the Ti:Sa output. For a correct choice of the prism positioning, coupling into the resonator can be achieved for most parts of the external spectrum, as will be experimentally examined further in subsec. 4.2.4. Once set, the input coupling condition can be maintained over a time scale of hours up to days without considerable changes. In the event of termination of the comb matching, an automated routine scans possible prism positions in dependence of the obtained cavity level, while continuously keeping the central wavelength of the IR laser constant. It subsequently chooses the position of the highest obtainable power inside the resonator and can thereby almost always restore the coupling into the resonator. The downside of the method is, that it does not apply a feedback loop and the exact restoration of the cavity level before termination of the input-coupling cannot be guaranteed.

3.3 Linear optical set-up

In the last part of this chapter, focus shall be placed on the further processing of the photons generated in the SPDC process. To do so, the experimental implementation of our linear optical set-up is introduced, as it is commonly applied in photon based quantum entanglement experiments utilising the polarisation degree of freedom.

Experimental implementation As shown in fig. 3.1, the infra-red SPDC photons are coupled out of the resonator through mirror $M2$ and subsequently rotated by a $\lambda/2$ wave-plate in their polarisation, swapping around $|H\rangle$ and $|V\rangle$. Such a rotation is necessary for erasing the "welcher Weg" information imparted onto the two photons in a down-conversion pair by the birefringence of the BBO crystal. Thus another BBO of half length is placed behind the wave-plate, reversing the formers influences on the photon distinguishability. More information hereupon is provided later in subsec. 6.2.2. Yet the aforementioned

achieve frequency comb input coupling in the described manner. Yet the described simplification makes the fundamental principle more intelligible.

exchange of polarisations must be kept in mind, when comparing calculated SPDC spectra, generated inside the resonator, with the ones measured after the SM fibre, conducted in subsec. 5.3.3 (i.e. $|V\rangle$ inside the resonator corresponds to $|H\rangle$ detected in the linear optical set-up). After transmission through the BBO, the photons are coupled into an anti-reflection (AR) coated single mode (SM) optical fibre, whose numerical aperture also defines the selected part of the spatial distribution of the down-conversion (see [101] for details) and which simultaneously works as a transverse mode filter. Maintenance of the $|H/V\rangle$-polarisation coordinate system after propagation through the fibre with respect to the optical axes of the BBO crystal is guaranteed by a polarisation controller, usually referred to as paddle polariser. Beyond the fibre, the photons are incident into a linear optical set-up, whose layout is presented in fig. 3.4. First of all, photons are spectrally filtered by an interference filter of $\Delta\lambda = 2.8\,nm$ spectral width, centred symmetrically around $780\,nm$. The spectral narrowing results in an extension of the photons' coherence lengths, thereby erasing temporal distinguishability between successively emitted SPDC photon pairs (see subsec. 6.2.2). Subsequently, the photons are distributed into six spatial modes by the aid of five non-polarising beam splitters (BS) particularly aligned for complete polarisation independences in reflectances R_i and transmittances T_i, whose values are $R_{\mathrm{BS}_1-\mathrm{BS}_4} = 0.42$, $T_{\mathrm{BS}_1-\mathrm{BS}_4} = 0.58$ for the beam splitters BS_1 till BS_4 and $R_{\mathrm{BS}_5} = 0.48$, $T_{\mathrm{BS}_5} = 0.52$ for the beam splitter BS_5 in fig. 3.4, respectively. Such a mode arrangement allows to identify the desired six-photon entangled state by simultaneous detection of a single photon within each arm. At the front end of each spatial mode, a pair of birefringent yttrium-vanadate (YVO_4) crystals is placed. These compensate for phase shifts imposed onto the photons by the birefringence within the beam splitters $\mathrm{BS}_1 - \mathrm{BS}_5$. Exact compensation of such excess phases can be achieved first by rotating the crystals around the optical axis in order to conserve the $|H\rangle$ and $|V\rangle$ polarisation direction, followed by changing the angle of the YVO_4-crystals' face plane with respect to the optical axis to maintain the correct phase of any initial state, which is a superposition of $|H\rangle$ and $|V\rangle$ components. Finally a polarisation analysis unit is terminating each arm. Contained therein are a $\lambda/2$ followed by a $\lambda/4$ wave-plate, behind which a polarising beam splitter (PBS) is mounted, splitting the incoming light up into two output modes that are observed by a single photon avalanche photodiode (SPAPD)[15] with quantum efficiencies of:

PBS output	Arm 1	Arm 2	Arm 3	Arm 4	Arm 5	Arm 6
$\|H\rangle$	$\eta_1^H \approx 52.3\,\%$	$\eta_2^H \approx 51\,\%$	$\eta_3^H \approx 41\,\%$	$\eta_4^H \approx 51.2\,\%$	$\eta_5^H \approx 50.8\,\%$	$\eta_6^H \approx 45.6\,\%$
$\|V\rangle$	$\eta_1^V \approx 52.5\,\%$	$\eta_2^V \approx 49.9\,\%$	$\eta_3^V \approx 44.8\,\%$	$\eta_4^V \approx 43.3\,\%$	$\eta_5^V \approx 54.7\,\%$	$\eta_6^V \approx 52.1\,\%$

These detectors are non photon number resolving, operating in the Geiger mode. With this scheme, it is clear that besides the desired six-photon states, also emissions of even higher qubit numbers, referred to as higher order noise, can contribute to the measured six-fold coincidence clicks. Since two photons of equal polarisation within such states can penetrate into the same arm of the analysis set-up, they exactly resemble the signature of a six-qubit quantum state. A more in depth consideration of these processes can be found in reference ([139]). Nevertheless, as it shall be seen later in subsec. 6.3.2 and reference ([43]), the higher order contributions are low enough to still allow for the observation of the states we are aiming for.

Regarding the utilisation of the linear optical set-up to infer information about photonic quantum states and its application in the course of the measurement of photonic qubits, the reader shall be pointed out to references ([87], [88], [89]), which provide nice explanations hereupon. Therefore an in depth discussion is skipped here and we will move on to the examine the parameters of the cavity.

[15] Manufacturer: Perkin Elmer

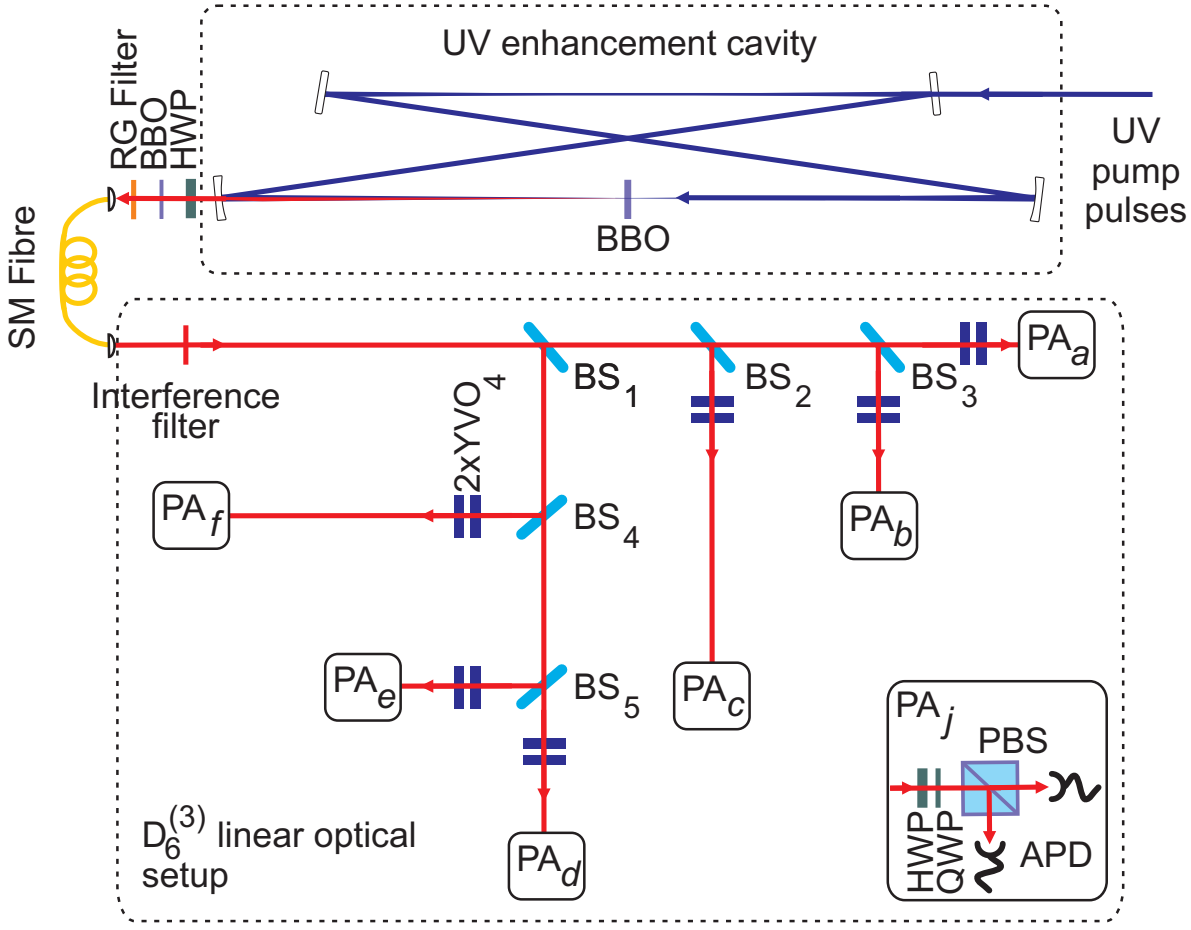

Figure 3.4: Schematic drawing of the linear optical set-up. The output of the SM fibre is propagated through an interference filter and subsequently split-up into six spatial modes with five non-polarising beam splitters (BS). Additionally each arm contains two YVO_4-crystals for phase compensation. The polarisation of photons within each arm is analysed by an arrangement consisting of a $\lambda/2$ and a $\lambda/4$ plate, followed by a PBS and two single photon avalanche photodiodes (SPAPD) positioned in each output arm of the PBS.

Chapter 4

Characterisation of cavity parameters

After all necessary design parameters have successfully been determined and the set-up of our enhancement cavity apparatus has been laid out, it is time to characterise the experimentally implemented device. There are two different aspects that have to be dealt with: On the one hand, the intrinsic properties of the resonator itself are to be examined. These concern the excited transverse optical mode, the stability of the intra-cavity power over time, the achievable power enhancement and the finesse of the cavity. On the other hand, the influences by the resonator on the temporal characteristics of pulses stored therein have to be taken care of as well. The latter are forwarded to the next chapter, whereas we will be analysing the former in the following.

4.1 Transverse mode

Transverse optical mode To infer the transverse mode, excited inside the resonator, there are two features of the stored light to be looked at. One is obviously the transverse intensity distribution in a plane perpendicular to the optical axis of the cavity. In terms of what has been said about higher order Laguerre-Gaussian contributions, see eq. (2.6) and reference ([58]), the requirement of having a Gaussian-like intensity, without additional humps to the side of the global maximum, in order to resemble the $TEM_{0,0}$ mode scenario, is fairly obvious. We measure this spatial light distribution inside the cavity by aid of the signal leaking through cavity mirror $M4$, see fig. 2.2, since an internal picturing is not possible because of the unavoidable cavity mode blocking associated with it. It has also been checked, that transmission through the optical component does not change the beam profile, allowing for such an observation method. Data taking is performed by application of a standard beam profiler with the leakage signal directly impinging onto the device, after some attenuation with neutral density filters. The resulting image of the intensity distribution is shown in fig. 4.1 a) and proves to be a nice, circular-symmetric mode with an intensity level increase, approximately given by a Gaussian distribution. Hence our expectations, stemming from the desired $TEM_{0,0}$ situation, are fulfilled by the experimental findings.

M^2-factor However, only looking at the intensity distribution of light in the transverse plane does not yet prove the resonator to maintain just a single Gaussian mode. This is because the description of optical systems by Gaussian beams is a simplification and real world devices never actually operate on the fundamental $TEM_{0,0}$ mode only, but always have at least some minor additional multi-transverse-mode contributions participating as well. These might still enable one to receive a transverse mode, closely resembling the desired $TEM_{0,0}$ shape[1], however they change the longitudinal propagation features of the entire beam ([57]). Assessment of the multi-mode characteristics of an optical beam is commonly undertaken by measuring its M-factor, as indicated in subsec. 2.2.1 and references ([66], [63], [57]). Therefore the deviations in the relationship between diffraction angle and beam waist from the pure Gaussian case, eq. (2.4), are utilised for a growing multimode fraction and thus a larger M. The factor is evaluated by measuring the beam radius of an initially converging beam at several different positions in front and beyond its focus. The procedure is more thoroughly laid out in reference ([66]) and is referred to as four-cuts method, since the authors suggested to determine the beam diameter in two planes at either side of the focus. For our particular case, we will once more employ cavity leakage, this time

[1] at certain positions along the beam path at least

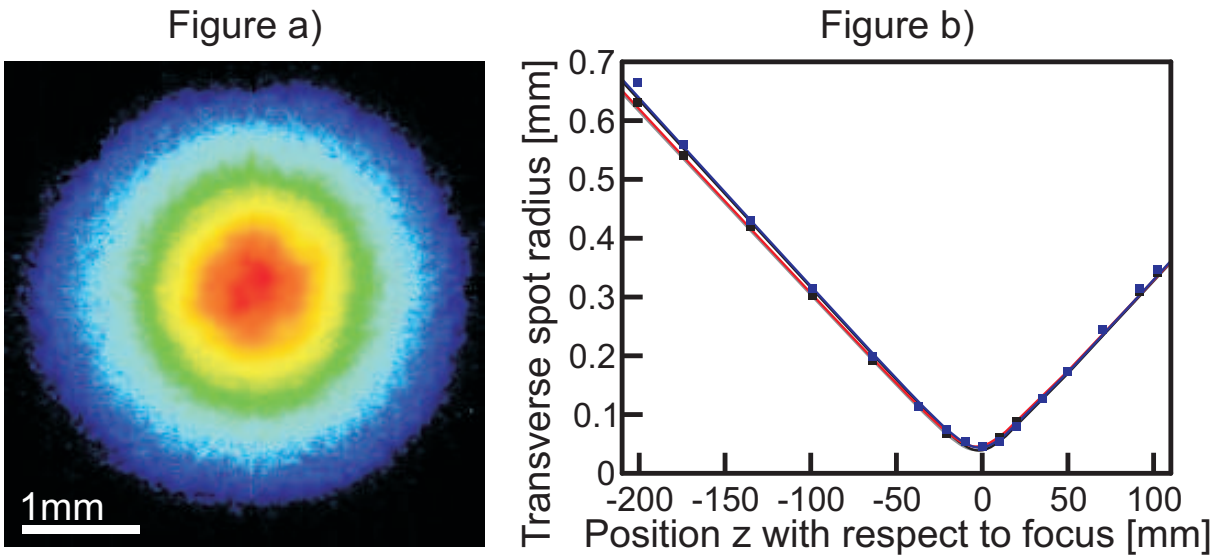

Figure 4.1: Plot a): Experimentally determined intensity profile of the UV cavity mode as transmitted through mirror $M4$. Red areas correspond to high intensity regions, whereas a degradation of intensity is obtained the bluer the colour gets. Black indicates the absence of a considerable UV light level. One can infer a Gaussian profile, expected for a mode close to the $TEM_{0,0}$ situation as also implied by the measured M^2 factors. Plot b): Measured beam widths of transmitted UV signal through mirror $M2$ in the proximity of its focal position. The black boxes are beam radii in the x-direction and the blue boxes correspond to radii in the y-direction. Fitted beam radius behaviours for ideal Gaussian beams, according to eq (2.4), are drawn in grey and black for the x- and y-direction, respectively. Taking the multimode nature into account yields fitted functions, given by eq. (2.8), displayed in red for the x-direction with an $M_x = 1.07 \pm 0.01$ and in blue for the y-direction with an $M_y = 1.07 \pm 0.02$.

through mirror $M2$, which is subsequently focussed down with a standard lens. Behind the lens, the beam profile is determined in different planes along the propagation direction throughout the focus, as it is indicated schematically in fig. 4.2. Beam radii $w_{x,y}(z)$, see eqs. (2.4) and (2.8), in the direction parallel and orthogonal to the optical table's surface, named x- and y-direction in the following, are recorded. The resulting values are displayed in fig. 4.1 b) with black boxes indicating the x-direction and blue ones representing the y-direction. The abscissa positioning corresponds to a centring around the focal plane of the beam. In order to obtain the M^2-number, the datapoints are fitted with the relevant expression for the beam waist divergence in the multimode beam case (eq. (2.8))

$$\tilde{w}_{x,y}(z) = w_{0,x,y}^2 \left(1 + \left(\frac{\lambda \cdot M^2 \cdot (z - z_0)}{\pi w_{0,x,y}^2} \right)^2 \right),$$

indicated in fig. 4.1 b) by a red line for the x- and a blue line for the y-direction. From the fitting routine, we yield numbers for the parameter M^2 of:

$$M_x = 1.07 \pm 0.01 \quad ; \quad M_y = 1.07 \pm 0.02 \tag{4.1}$$

These are obviously rather close to $M^2 = 1$, expected for a pure Gaussian beam scenario. We can thus infer, that our cavity is essentially working within the desired transverse mode regime, maintaining approximately a $TEM_{0,0}$ spatial mode, propagating pretty much like a pure Gaussian beam. Also the simplification of setting $M = 1$ during the calculations in subsec. 2.2.1 and 2.2.1 is consequently justified. The minor differences between our experimental situation and an ideal, fundamental mode scenario are also visualised in fig. 4.1 b) by fitting the data with a function according to eq. (2.8) having $M = 1$, i.e. by the ideal Gaussian beam divergence as it has been stated in eq. (2.4). The results are the grey line for the x- and the black line for the y-direction, which hardly deviate from their multimode counterparts. More pronounced are however the different divergence angles of the x- and the y-direction, which indicate the presence of some residual astigmatism in the intra-cavity mode. Finally, due to having $M \approx 1$, the resonator shall furthermore be noted to constitute a good spatial mode filter. Therefore only the $TEM_{0,0}$ parts of the external UV pump field can actually penetrate into the device[2] and we are left with the

[2]Irrespective of any frequency comb matching, outlined in subsec. 2.1.4.

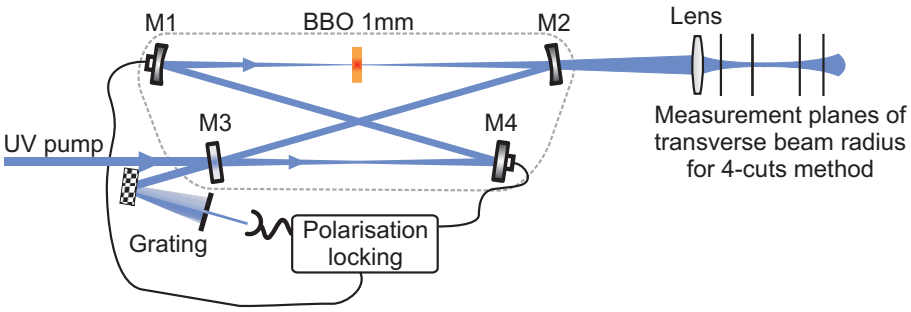

Figure 4.2: Measurement set-up for determining the M^2-factor. The leaking UV signal through cavity mirror $M2$ gets focussed down with an additional lens, and the beam radius is determined at several planes in front and behind the focal plane.

degraded efficiency of $\approx 50\,\%$ coupling, mentioned in subsec. 3.1.2.

4.2 Power Enhancement

4.2.1 Introduction

We will now move on towards discussing the power enhancement, achievable by the resonator, and also look at the implications regarding dispersion in it, which are retrievable thereof. As the name already suggests, the power enhancement represents the available magnification properties for the UV power. It is thus also one of the most important features of the apparatus, since increasing the UV pump strength for the non-linear process has been the underlying reason for setting-up the device in the first place. The desired SPDC interaction also defines the most important feature to be comprised by the power enhancement: In order to yield sufficient multi photon pair emission rates, it is necessary to operate the down-conversion with ultra-short pulses, which in turn translates into a required constancy of the achieved power enhancement over the spectrum of the external UV pump, so that the intensities of as many frequency components as possible experience amplification and as little spectral content as possible is cut off, which would lead to an enlargement in pulse duration. Hence a spectrally resolved analysis of the power enhancement is necessary, performed by a comparison between the UV pulse spectra in front and inside of the cavity. From the overlap of both spectra, additional conclusion on the dispersion, imparted on round-tripping pulses in the system, can be attained. Furthermore sufficient long term time stability of the power enhancement is indispensible to allow for appropriate counting statistics of the multi-partite entangled quantum states, which are to be produced with this photon-source later on. All of these features will be investigated in the following, whereby the assessment shall start with statements regarding the experimental recording method and the obtained outcomes.

4.2.2 Experimental set-up, measured UV spectra and power levels

Experiment The arrangement, applied for carrying-out the measurement, is shown in fig. 4.3. Since the internal UV spectrum and the internal UV power level, present during the enhancement process, are desired, the transmitted light leaking through one of the cavity mirrors can be utilised for recording. In doing so, we have positioned an additional mirror behind the resonator mirror $M4$, redirecting the out-coupled intensity onto a beam splitter (BS). This component splits it up into one fraction directly impinging onto a photodiode and another, coupled into a spectrum analyser by the aid of a SM fibre. The spectrum is now recorded by the analyser and entire internal UV power, integrated over all frequency contributions within the pulses, is observed by the photodiode. The internal parameters, i.e. power and spectrum, are gained by locking the cavity at the highest possible power level, as the maximally achievable enhancement is to be investigated here. Clearly lower levels are feasible as well, yet we would like to infer what our system is capable of at the high end. The external counterparts are recorded separately: For the spectrum, the propagation of pulses inside the resonator is prevented by placing a beam block in between mirror $M1$ and $M2$ in fig. 2.2. The entire spectrum of the external pulses is accordingly just transmitted through the input coupler (mirror $M3$ with transmittance T_{IC}) and the cavity mirror $M4$ (with transmittance T_{M4}), being readily measurable with the spectrum analyser as well. In contrast the overall external UV power gets determined by positioning a power meter in front of the input coupler, due to our applied definition for the power enhancement (see subsec. 4.2.3 below).

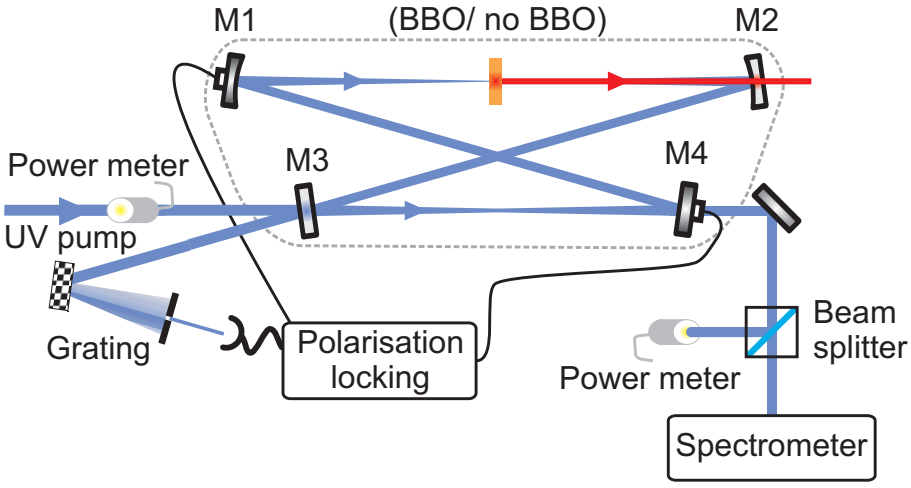

Figure 4.3: Apparatus to measure the internal and external UV spectra and the power levels inside and in front of the resonator, needed for power enhancement evaluation.

It shall furthermore be mentioned, that for dispersion assessment by comparison between the internal and external UV spectra, it is absolutely necessary to have no varying offset along the frequency axis in both datasets. That is because we would later on like to determine the spectral overlap between the internal and external spectra for this manner, which would be altered by such a shift in positioning. Offsets in frequency, or in other words, artificial displacements along the frequency axis between both spectra, would change this quantity and therefore imply a different influence of dispersion effects on frequency comb matching. In the experimental implementation the spatial propagation directions of the external beam and the cavity mode are however slightly deviating. To certify equality of the coupling conditions into the spectrometer during recording the external and internal spectra, the free-space coupling, depicted in fig. 3.1, has thus been substituted by the aforementioned SM fibre.
Datasets have furthermore been recorded for two experimental scenarios: One with the cavity containing the BBO crystal, as it is used for photon pair generation in chapter 6, and another arrangement without the non-linear medium, just resembling a high repetition rate enhancement system.

UV power levels and locking stability Since we measure the intra-cavity power with a photodiode behind mirror $M4$, the received voltage signal has to be set in relation to the power level, actually present inside the resonator. The required conversion constant, which is applied whenever the internal UV power level is spoken about, is derived in appendix B.1.
For the internal spectra, the cavity has to be locked in order to maintain its maximum enhancement level over the duration of the measurement. It is therefore essential, that the UV power, initially set by locking, is kept equal for all spectra contributing to the power enhancement computation. If the level changes remarkably during the experiment, this would correspond to modifications in the input-coupling condition and to associated alterations in the spectrum. In other words, if the level is for instance decreasing, less intensity is coupled into the resonator as some external frequency comb modes loose their matching with cavity resonances, which in turn narrows the internal spectrum and diminishes the spectrally resolved power enhancement for these frequencies. Thus prove of constancy in the cavity level is required. For the situation with BBO this is rather easy to achieve. The internal UV spectra have been measured for a period of $30\,min$ and the UV power level inside the resonator over that time is shown exemplarily in fig. 4.4. Note here, that each black datapoint in this graph corresponds to an averaged value over all power levels apparent during a time period of $1\,min$ previous to it. An overall mean internal UV power with BBO of

$$P_{\text{int}}^{\text{BBO}} = 7.19 \pm 0.15\,W \tag{4.2}$$

is received. The light intensity can thus be regarded to be rather stable on average and this has allowed to measure internal spectra with rather long integration times approximately on the order of $1\,min$. However having no non-linear medium inside the resonator renders stable locking harder, since the losses are diminished in such a situation. In turn the finesse will be increased, as we will see in the next section 4.3, and the cavity resonances get narrower, making it tougher to fulfill the frequency comb matching over

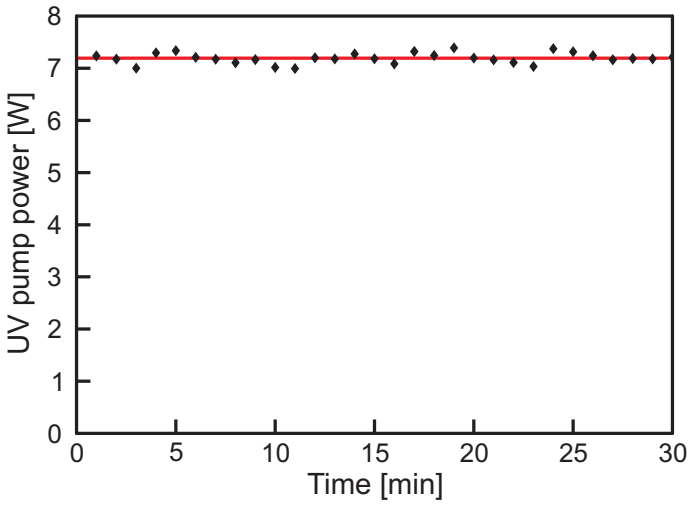

Figure 4.4: UV power level inside the resonator over the measurement time for the internal UV spectra. Black points represent level averages taken over 1 min, the horizontal red line corresponds to the averaged power of $P_{\text{int}}^{\text{BBO}} = 7.19 \pm 0.15\, W$.

the entirety of the external spectrum[3]. Additionally, no polarisation selecting element is present inside the cavity which would allow a stable locking with the Hänsch-Coulliaud method. Thus the cavity is only stable on shorter time scales, allowing for less integration time in recording the spectrum, consequently leading to greater fluctuations in the spectral intensity and greater statistical uncertainties in the spectral amplitude for this situation. Yet the internal power level is[4]

$$P_{\text{int}}^{\text{noBBO}} = 20.65 \pm 0.97\, W. \tag{4.3}$$

The external pumping power is equal for both set-up arrangements. The straight forward power meter measurement yielded

$$P_{\text{ext}} = 0.54 \pm 0.01\, W, \tag{4.4}$$

which is the amount of second harmonic light in front of the cavity to be gained from frequency doubling of the Ti:Sa laser.

UV spectra The measured internal and external UV spectra for the cavity with and without the BBO crystal shall now be presented. In order to gain some statistics, several spectra have been recorded for each arrangement. Each individual spectrum has been normalised with its intensity maximum corresponding to unity. For the future discussion the mean spectra, averaged over all individual datasets, have been computed for all of the four possible cases[5]. The statistical errors on these are given by the standard deviation between all intensity values to be averaged over at a certain wavelength. The spectra are presented in fig. 4.5 -4.8, whereby the left hand side always shows the individual recordings plotted in a different colour for each dataset and on the right hand side the averaged spectra are depicted.
As already indicated, the internal spectra without the crystal show a rougher structure due to shorter integration times, which also translates into greater uncertainties. For the external spectra, no big a difference can of course be seen, as these should be approximately equal for both situations. It shall nevertheless be noted, that the second measurement, without BBO, has been performed a few weeks after the first one and the spectral output of the Ti:Sa laser has slightly changed over such a time scale. This has especially to be accounted for, if the reader attempts to compare the spectra presented here with those to those stated in chapter 5. Both datasets are not comparable with one another, since half a year time difference has passed between performing both measurements.

[3] For more details see the discussions in subsec. 2.1.4 and the implications of the finesse in subsec. 4.3.2

[4] It shall be noted, that in the power uncertainties $\Delta P^{\text{BBO/noBBO}}\text{int/ext}$ the errors on the observed photodiode voltage reading, defined as their standard deviation ΔV^j, as well as the uncertainty in the conversion factors, eqs. (B.2) and (B.3) in the appendix B.1, are included according to: $\Delta P_{\text{int}}^j = \sqrt{(\Delta\alpha^j)^2 \cdot (V_{\text{int}}^j)^2 + (\alpha^j)^2 \cdot (\Delta V^j)^2}$.

[5] which are external and internal UV spectrum with and without BBO

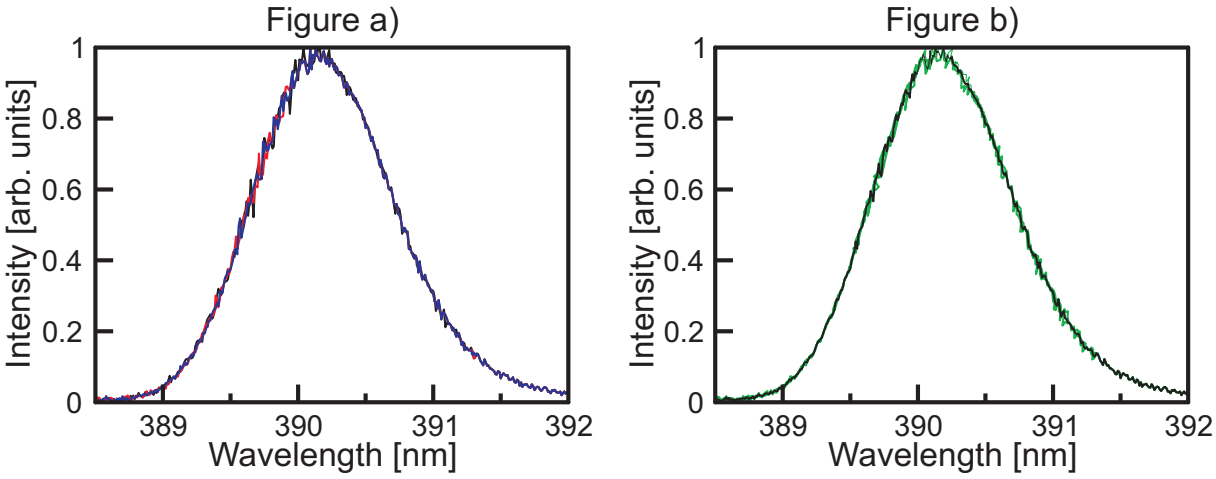

Figure 4.5: External UV spectra with BBO: The curves on the left hand side are individual recordings of the spectrum entering the average spectrum. The latter is drawn on the right hand side as a black line, whereby the green lines indicate the upper and lower error boundaries.

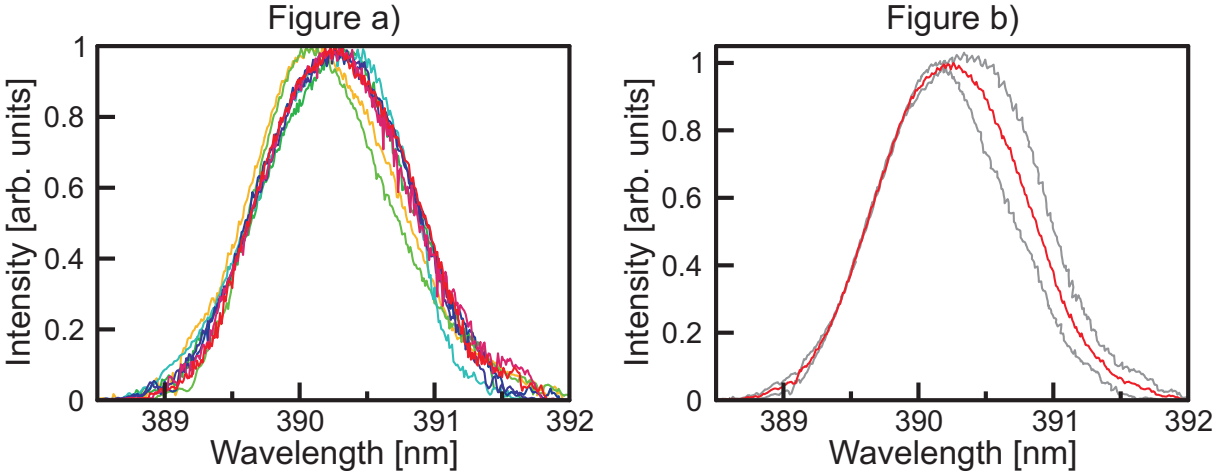

Figure 4.6: Internal UV spectra with BBO: The curves on the left hand side are individual recordings of the spectrum entering the average spectrum. The latter is drawn on the right hand side as a red line, whereby the grey lines indicate the upper and lower error boundaries.

4.2.3 Computation of power enhancement

The power enhancement, as we refer to it, is defined by the power inside the cavity with respect to the power in front of the cavity, i.e. the power impinging onto the input coupler prior to propagation through it. There are furthermore two different quantities going along under the same name.
The first is the integrated, or respectively overall power enhancement. It does neither take the spectral structure of the pulses nor dispersive effects into account, thus it does not differentiate between the difference in power amplification individual frequency comb modes are subject to. Instead its magnitude is determined by the entire, i.e. spectrally integrated, pulse power inside and outside of the cavity, given by eqs. (4.2), (4.3) and (4.4). So the relevant numbers for this parameter can easily be stated as[6]:

$$\bar{PE}^{\mathrm{BBO}} = \frac{P_{\mathrm{int}}^{\mathrm{BBO}}}{P_{\mathrm{ext}}^{\mathrm{BBO}}} = 13.3 \pm 0.4 \tag{4.5}$$

$$\bar{PE}^{\mathrm{noBBO}} = \frac{P_{\mathrm{int}}^{\mathrm{noBBO}}}{P_{\mathrm{ext}}^{\mathrm{noBBO}}} = 38.2 \pm 1.9 \tag{4.6}$$

Since it neglects any spectral and hence temporal information, necessary to know about for checking the

[6] With the errors given by: $\Delta\bar{PE}^{j} = \sqrt{\left(\frac{\Delta P_{\mathrm{int}}^{j}}{P_{\mathrm{ext}}^{j}}\right)^{2} + \left(\frac{P_{\mathrm{int}}^{j}}{P_{\mathrm{ext}}^{j}}\right)^{2} \cdot \left(\Delta P_{\mathrm{ext}}^{j}\right)^{2}}$

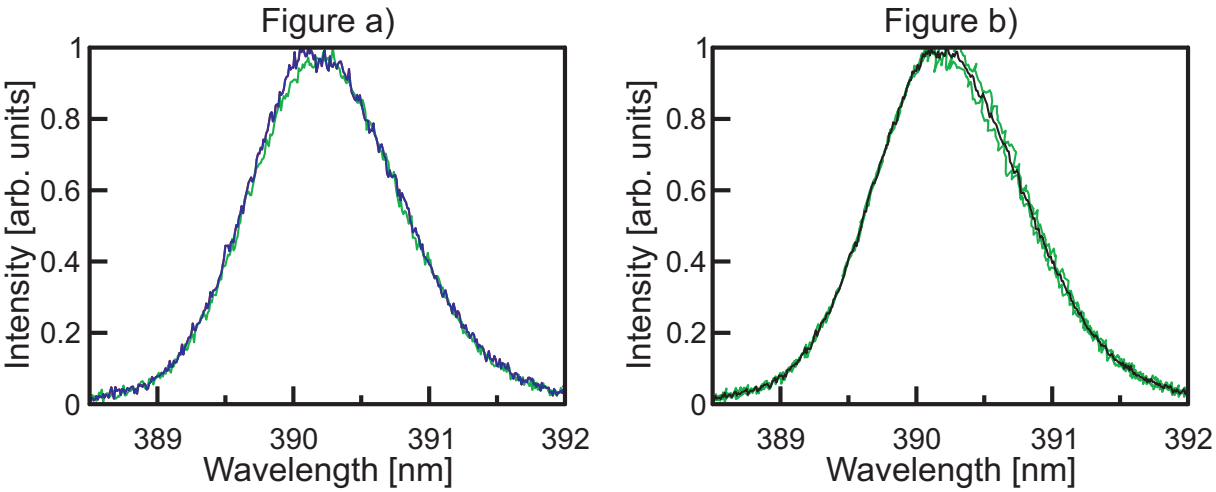

Figure 4.7: External UV spectra without BBO: The curves on the left hand side are individual recordings of the spectrum entering the average. The latter is drawn on the right hand side as a black line, whereby the green lines indicate the upper and lower error boundaries.

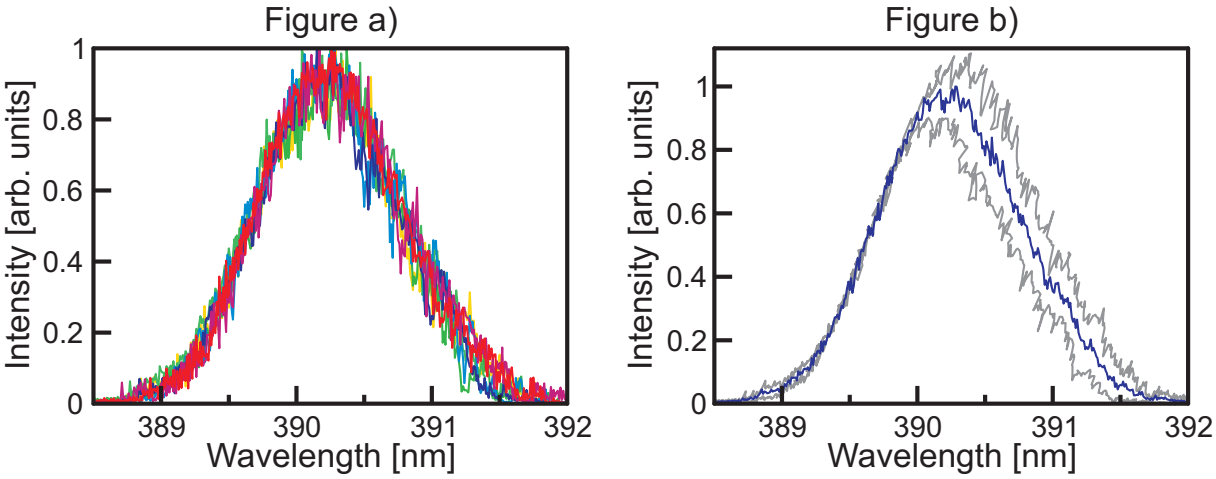

Figure 4.8: Internal UV spectra without BBO: The curves on the left hand side are individual recordings of the spectrum entering the average. The latter is drawn on the right hand side as a blue line, whereby the grey lines indicate the upper and lower error boundaries.

suitability of the amplification process to pump the SPDC process, all it tells is a rough ballpark figure about how good the cavity's amplification is.
For our purposes, we will require the spectrally resolved power enhancement, which represents the second possible quantity involved here. For its investigation the spectrum measurements have been made. It includes the full information about how much each frequency comb tooth of the external pulse is enhanced by the resonator. The relevant definition can accordingly be written as

$$PE^j(\lambda) = \frac{P^j_{\text{int}}(\lambda)}{P^j_{\text{ext}}(\lambda)} \tag{4.7}$$

whereby $P^j_{\text{int}}(\lambda)$ is the internal power as a function of wavelength and $P^j_{\text{ext}}(\lambda)$ is the analogue counterpart in front of the resonator, with $j \in \{\text{BBO}, \text{noBBO}\}$. From the definition it is clear, that this quantity contains information about the frequency comb matching, as modes which are not transmitted through the input coupler do not appear in $P^j_{\text{int}}(\lambda)$ and do not contribute to $PE^j(\lambda)$. To evaluate this expression, the values for $P^j_i(\lambda)$, with $i \in \{\text{int}, \text{ext}\}$, will be required. Yet all we have so far are the normalised internal, $S^j_{\text{int}}(\lambda)$, and external, $S^j_{\text{int}}(\lambda)$, spectra as well as the overall powers in eqs. (4.2)-(4.4). Hence, a proper scaling between these two sets of data has to be developed in the first place.
As already mentioned, we are aware that integration over the spectral power yields the total power:

$$\int P_i^j(\lambda)d\lambda = P_i^j \tag{4.8}$$

Furthermore the constant scaling factors, defined as γ_i^j, have to connect power with spectrum, or in other words:

$$\gamma_i^j \cdot S_i(\lambda) = P_i^j(\lambda) \tag{4.9}$$

Putting both equations together returns the correct formula for γ_i^j:

$$\int P_i^j(\lambda)d\lambda = \int \gamma_i^j \cdot S_i^j(\lambda)d\lambda = \gamma_i^j \underbrace{\int S_i^j(\lambda)d\lambda}_{=:A_i^j} = P_i^j \Longleftrightarrow \gamma_i^j = \frac{P_i^j}{A_i^j} \tag{4.10}$$

whereby the A_i^j are the areas covered by the normalised spectra. By numerical integration of the datasets for all four average spectra, shown in figs. 4.5-4.8, we acquire numbers of:

$$\begin{aligned} A_{\text{int}}^{\text{BBO}} &= 1.34 \pm 0.14 \quad ; \quad A_{\text{ext}}^{\text{BBO}} = 1.29 \pm 0.03 \\ A_{\text{int}}^{\text{noBBO}} &= 1.3 \pm 0.17 \quad ; \quad A_{\text{ext}}^{\text{noBBO}} = 1.42 \pm 0.02 \end{aligned}$$

The errors ΔA_i onto these are computed by the mean difference in area coverage between the maximum and minimum error bound of each spectrum[7]. The difference between $A_{\text{ext}}^{\text{BBO}}$ and $A_{\text{ext}}^{\text{noBBO}}$ stems from taking the data at different days, as mentioned before. Plugging these figures, together with those from eqs. (4.2)-(4.4), into eq. (4.10) gives the scaling parameters[8]:

$$\begin{aligned} \gamma_{\text{int}}^{\text{BBO}} &= 5.37 \pm 0.55 \quad ; \quad \gamma_{\text{ext}}^{\text{BBO}} = 0.42 \pm 0.01 \\ \gamma_{\text{int}}^{\text{noBBO}} &= 15.87 \pm 0.38 \quad ; \quad \gamma_{\text{ext}}^{\text{noBBO}} = 2.21 \pm 0.01 \end{aligned}$$

Multiplying the normalised spectra with these constants and insertion of the resulting spectral powers into eq. (4.7) gives the desired spectrally resolved power enhancement[9]. The computed data furthermore undergoes low-pass Fourier transform filtering. This operation is applied on the one hand because of the variations on top of the measured average spectra, which are particularly prominent in the internal curves (figs. 4.6 and 4.8). Since these are mainly subject to the integration time choices at the spectrum analyser or resultant from the statistical nature of our experiment, binning them does not destroy information about the desired enhancement of spectral components due to intrinsic properties of our cavity. More important, on the other hand, are the effects due to the convergence between external and internal spectra in their tails, which are thrown out by filtering as well. These can cause large spikes in the power enhancement, which of course are just related to the small amplitudes values, resulting in tiny denominators in eq. (4.7) and hence in large numbers for $PE(\lambda)$. Such high power enhancements in the tails, even if they result from perfect frequency comb mode matching, are irrelevant for our purposes, as the pumping intensities are small in these areas anyway, so they do not significantly contribute to the enhanced pulse inside the cavity.
The smoothed, spectrally resolved power enhancement is shown in fig. 4.9 by blue lines for the presence of the BBO crystal in part a) and its absence in b). To allow an assessment of the power enhancement, additionally the external and internal UV spectra are included as well, whereby the internal ones are already scaled appropriately to their external counterparts as required for estimating the cavity's spectral acceptance.

[7] That is to say by half the difference between the area under the upper and lower green curves in figs. 4.5b), 4.6b) and the respective gray curves in figs. 4.7b), 4.8b).

[8] Their errors are once more retrieved by statistical error propagation following:

$$\Delta\gamma_i^j = \sqrt{\left(\frac{\Delta P_i^j}{A_i^j}\right)^2 + \left(\frac{P_i^j}{(A_i^j)^2}\right)^2 \cdot \left(\Delta A_i^j\right)^2}$$

[9] The associated uncertainties $\Delta PE^j(\lambda)$ are gained from the standard deviations of the normalised spectra $\Delta S_i^j(\lambda)$, indicated by the above mentioned green and grey curves in figs. 4.5 b), 4.6 b) and figs. 4.7 b), 4.8 b), respectively, together with the errors $\Delta\gamma_i^j$ on the scaling factors, according to:

$$\left(\Delta PE^j(\lambda)\right)^2 = \left(\frac{S_{\text{int}}^j(\lambda)\cdot\Delta\gamma_{\text{int}}^j}{S_{\text{ext}}^j(\lambda)\cdot\gamma_{\text{ext}}^j}\right)^2 + \left(\frac{S_{\text{int}}^j(\lambda)\cdot\gamma_{\text{int}}^j}{S_{\text{ext}}^j(\lambda)\cdot(\gamma_{\text{ext}}^j)^2}\right)^2 \cdot \left(\Delta\gamma_{\text{ext}}^j\right)^2 + \left(\frac{\Delta S_{\text{int}}^j(\lambda)\cdot\gamma_{\text{int}}^j}{S_{\text{ext}}^j(\lambda)\cdot\gamma_{\text{ext}}^j}\right)^2 + \left(\frac{S_{\text{int}}^j(\lambda)\cdot\gamma_{\text{int}}^j}{S_{\text{ext}}^j(\lambda)\cdot\gamma_{\text{ext}}^j}\right)^2 \cdot \left(\Delta S_{\text{ext}}^j\right)^2$$

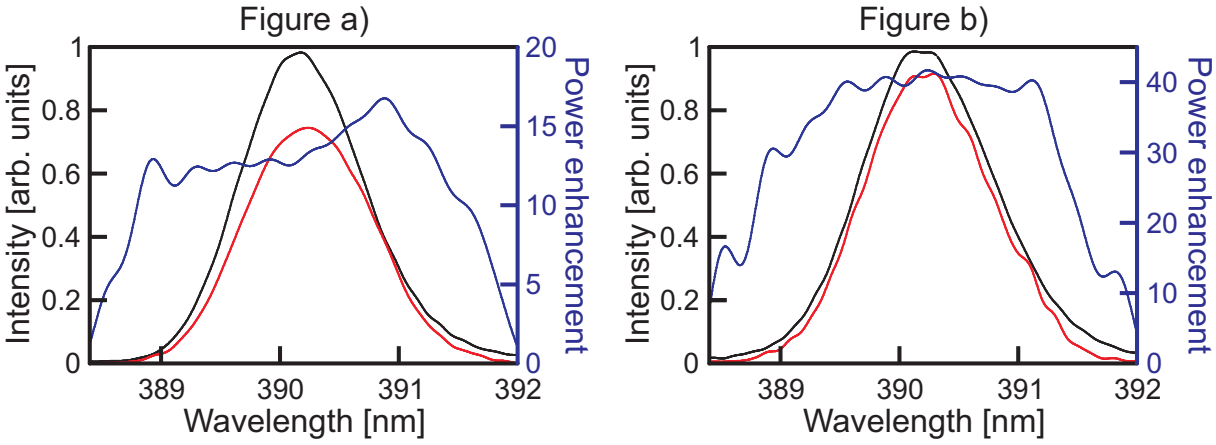

Figure 4.9: Spectrally resolved power enhancement as given by eq. (4.7) after low-pass Fourier filtering. Figure a): The power enhancement curve for the cavity arrangement containing the BBO is drawn in blue, the external UV spectrum is displayed in black and the scaled internal UV spectrum in red. Figure b): The empty resonator scenario with the power enhancement in blue, the external UV spectrum in black and the internal one in red.

Inferring from the graphic, we can acknowledge to have a power enhancement roughly flat and constant over the spectrum of the external UV pulse. The residual structure is expected, due to the remaining GVD in the resonator, see subsec. 2.1.5, which causes the external frequency comb teeth, the cavity is stabilised on, to experience greater enhancement, due to increased overlap with the cavity resonances. Altogether we can however expect the entire frequency content of the external pulses to experience an approximately similar magnification in their intensities during round-tripping. Importantly, no significant portion of the external spectrum is subject to a largely diminished or even no amplification. First, this means that no major parts of the pulse spectra are lost during the enhancement process, which would otherwise lead to a smaller spectrum and consequently to a longer pulse duration[10]. Second, we can look at the electric field of the external pulse, which is given by the summation over all individual spectral contributions $E(\lambda) = f(\lambda)\exp(-2\pi i\frac{c}{\lambda}t)$ with a spectral amplitude $f(\lambda)$ and an oscillation term proportional to a plane wave, according to $E_{\text{ext}}^{\text{pulse}} = \sum_\lambda f(\lambda)\exp(-2\pi i\frac{c}{\lambda}t)$: In having a roughly equal power enhancement for all $E(\lambda)$, denoted by $PE(\lambda) \approx const.$, the internal, enhanced pulse can be written in terms of the aforementioned sum as:

$$E_{\text{int}}^{\text{pulse}} = \sum_\lambda PE(\lambda)\cdot f(\lambda)\exp\left(-2\pi i\frac{c}{\lambda}t\right) = PE(\lambda)\cdot\sum_\lambda f(\lambda)\exp\left(-2\pi i\frac{c}{\lambda}t\right) = PE(\lambda)\cdot E_{\text{ext}}^{\text{pulse}}$$

So the intensity amplification inside the resonator should not distort the electric field superposition and thereby the pulse shape. Both are highly desired, since they indicate the ability to use our apparatus for femto-second laser pulses without stretching them. Simultaneously the power enhancement promises the ability to drive the SPDC process with high intensities. However both arguments regarding the power enhancement shall be noted to just deal with intensities. So phase effects due to residual dispersion on the electric fields $E(\lambda)$, whose influences are not large enough to dislocate the cavity resonance positions in frequency space far enough to terminate overlap with an external frequency comb mode (fig. 2.13), are not include, as they drop out in the intensity $I(\lambda) \sim |E(\lambda)|^2$. Hence there is still the possibility to have additional considerable higher order dispersion contributions, like GVD, and associated potential distortions on the internal UV pulses. Investigations of these will be dealt with by direct pulse duration measurements in the next chapter.
The power enhancement is furthermore also situated within the range expected from the overall power enhancement numbers in eqs. (4.5) and (4.6), whereby the maximally achieved enhancements $PE_{max}^{j}(\lambda_k)$, at a certain wavelength λ_k, are yet higher[11]. These turn out to be

[10] The relationship between spectral width and time duration of laser pulses is given by Fourier transform and explained more thoroughly in the next chapter.
[11] This is not surprising, since the $\bar{PE}$s are just averages over the $PE(\lambda)$ and as numbers for the latter tend to get lower towards the tails of the spectra, they have to be higher than the average in the centre.

$$P_{max}^{\mathrm{BBO}}(\lambda = 390.92\,nm) = 17 \pm 3 \tag{4.11}$$

$$P_{max}^{\mathrm{noBBO}}(\lambda = 391.11\,nm) = 45 \pm 10 \tag{4.12}$$

and are achieved at the location where the external frequency comb mode best matches a cavity resonance. In this context it shall be pointed out, that the maximally achieved power enhancements are situated in the flanks of the pulses' spectra (see fig. 4.9) for arrangements with and without BBO. So the frequency on which the Hänsch-Couillaud lock is operating on has been set in a range around $\lambda_{lock} \approx 391\,nm$, which is selected by choosing a particular part of the spectrally resolved back-reflection from the input coupler, see subsec. 3.2.1. In other words, the straight line our dispersion compensation scheme fits onto the proper intra-cavity dispersion $\phi(\lambda)$, as depicted in fig. 2.13, touches the aforementioned curve around $\lambda_{lock} \approx 391\,nm$, so that frequency comb modes here best match the cavity resonances.
We will now investigate the spectral acceptance of the resonator by further looking at the averaged intra-cavity spectra in comparison to the external ones by their respective area coverages.

4.2.4 Overlap between internal and external UV spectra and dispersion estimation

Like already drawn in fig. 4.9 the internal spectrum has first of all to be scaled onto the external for drawing conclusions about spectral acceptance of the cavity. It is clear by energy conservation, that even in the very best scenario, only wavelengths apparent in the pumping spectrum can be enhanced by the resonator. Thus, by retaining the normalised external spectra $S_{\mathrm{ext}}(\lambda)$ from figs. 4.5, 4.7, the internal spectra from fig. 4.6, 4.8 can maximally show amplitudes equal to the external values for the upcoming analysis. This is because if the internal spectrum was allowed to exceed the external one for some wavelength positions, the former could in principle be scaled up in such a manner to have finite spectral intensity even within its tails, where the latter has decreased to zero intensity already. Hence the energy conservation would be violated due to these additional contributions in the internal spectrum. To fulfill the requirement, the internal spectrum has to be scaled by a factor σ^j in order to touch but not intersect the external in one point[12], yielding the curves presented in fig. 4.9[13]. We can therefrom qualitatively acknowledge a great part of the external UV spectrum to be covered by the internal one, i.e. a large fraction of the former is coupled in and enhanced. In number terms, spectral coverages, defined by

$$\Gamma^j = 100\,\% \cdot \frac{\int \sigma^j S_{\mathrm{int}}^j(\lambda)d\lambda}{\int S_{\mathrm{ext}}^j(\lambda)d\lambda},$$

of

$$\Gamma^{\mathrm{BBO}} = 78 \pm 8\,\% \quad ; \quad \Gamma^{\mathrm{noBBO}} = 86 \pm 13\,\% \tag{4.13}$$

are obtained. The uncertainties hereon stem once more from the standard deviation error bounds in the spectral intensities[14], depicted in figs. 4.5-4.8. It shall be noted here, that these figures for the fractional coverages in principle include a combination of effects stemming on the one hand from the spectral acceptance and on the other hand from the spectral power enhancement of the cavity. That is to say, the former property determines, which frequencies are resonant and therefore coupled into the apparatus in the first place. The latter subsequently defines how big the losses for each mode are and by how much it can thus be amplified. To illustrate the last effect it is intriguing to anticipate equal input coupling efficiencies for all wavelengths. For a non perfect coverage, i.e. $\Gamma^j < 100\,\%$, some wavelengths would hence have to suffer greater losses than others, thereby exhibit smaller intensity amplitudes. To thoroughly infer the strength in influence of both effects with respect to one another, a spectrally resolved loss assessment

[12] In principle also more than one point would be possible, if the straight line for dispersion compensation in fig. 2.13 is chosen to have multiple intersection with $\phi(\lambda)$ instead of just touching it.

[13] It shall be noted that these spectra do not correspond to the power levels in eqs. (4.4)-(4.6).

[14] With an error of $\Delta\left(\int S_i^j(\lambda)d\lambda\right)$ on the individual spectra, these are given by:

$$\Delta\Gamma^j = 100 \cdot \sigma^j \sqrt{\frac{\left(\Delta\left(\int S_{\mathrm{int}}^j(\lambda)d\lambda\right)\right)^2}{\left(\int S_{\mathrm{ext}}^j(\lambda)d\lambda\right)^2} + \frac{\left(\int S_{\mathrm{int}}^j(\lambda)d\lambda\right)^2 \cdot \left(\Delta\left(\int S_{\mathrm{ext}}^j(\lambda)d\lambda\right)\right)^2}{\left(\int S_{\mathrm{ext}}^j(\lambda)d\lambda\right)^2}}$$

of the cavity over all relevant wavelengths would be necessary. In order to do so, the finesse F of the apparatus would have to be determined for all contributing frequencies in the external comb separately. Since for a particular wavelength one gets $PE = \frac{F}{\pi}$, the optimally achievable power enhancement without spectral acceptance effects would be obtained. In order for this formula to be valid, impedence matching has to be fulfilled as well, i.e. the mode under study has to be resonant with the cavity in its wavelength as well as its spatial mode structure, demanding pumping with a $TEM_{0,0}$ mode, and the input coupler has to have a transmission as high as the losses for that wavelength. Yet, as outlined in section 4.1, we do not have such an ideal situation at hand and have furthermore only measured a finesse, averaged over all wavelengths, as will be explained in the next section 4.3. However an evaluation of the mirror reflectivities and the losses of BBO and air over the relevant spectral range reveal constancy in the expected losses, i.e. the finesse should stay roughly the same. Major influence on the difference in the spectral coverages Γ^j can thus be attributed to the spectral acceptance of the cavity. Equally the spectrally resolved power enhancement $PE(\lambda)$ in fig. 4.9 is also mainly governed by the aforementioned feature. This depencence allows us to gain some information about the quality of frequency comb matching in input coupling. For the wavelengths λ_k, at whose positions the internal and external spectra coincide in their amplitude, dispersion compensation is perfect, since these represent the points where the straight line in fig. 2.13 resembles the cavity dispersion curve $\phi(\lambda)$. The external frequency comb modes hence optimally match cavity resonances for these λ_k. For that very reason the power enhancement $PE(\lambda)$ also comprises its maximal values here, given in eqs. (4.11), (4.12). Departing from these positions, an examination of figs. 4.9 a) and b) reveals a worsening in matching, since the differences between internal spectral amplitudes and their external counterparts rise, which mean less external modes, or respectively a smaller fraction of these, overlap with cavity resonances, like it is drawn schematically in fig. 2.13. The deviation is larger for an arrangement with BBO than for an empty resonator, which is to be expected due to the doubling in dispersion introduced by the crystal. So although the finesse of the resonator becomes lower with the dielectric medium and the cavity resonances accordingly become broader by an approximate factor of 3.5 (see eqs. (4.28) and (4.29) in the next section about finesse), rendering it easier to hit them, the displacement of the resonances by the additionally introduced crystal dispersion exceeds that and causes less overlap with external comb modes. Hence there are fewer modes coupled into the cavity, the associated spectral amplitude $\sigma \cdot S_{\mathrm{int}}(\lambda)$ shrinks and the areal coverage of Γ becomes smaller than for the empty apparatus, like stated in eq. (4.13).
For the power enhancement $PE(\lambda)$ this reasoning implies, that the differences in its maximal values (eqs. (4.11), (4.12)) are only determined by the different losses or respectively by the different finesse between both scenarios, which is further examined later in subsec. 4.3.2. The difference in the overall power enhancements $\bar{PE}^j = \int PE^j(\lambda) d\lambda$ in eqs. (4.2), (4.3) is however influenced by the varying spectral acceptance as well. Summarising, the influences of dispersion on the intra-cavity pulses are visible and not negligible, however still the major parts of the UV pulses are coupled into the resonator and get enhanced to an appropriate level for our purposes, as we will see in the next two chapters.

4.2.5 Time stability of power enhancement

The aforementioned cavity locking time scale shall now be presented in this last step of the discussion. Due to the requirements regarding counting statistics of linear optics based quantum computing with multi-partite entangled photonic qubits, it is highly desirable to have a photon source comprising constant production rates over long time scales, which are commonly on the order of hours up to days. In turn constant pumping powers are needed to operate the underlying SPDC process. Since we would ultimately like to use our resonator system as such a device, a stable power enhancement and cavity locking is indispensible. While in fig. 4.4 the stability of the internal UV power has already been shown over the time duration of the spectra measurements, which only have been on the order of approximately $30\,min$, we can proof the ability to reach far longer periods of solid pumping power level with our apparatus. For the high-end region of possible intensities within the cavity, an exemplary measurement is shown in fig. 4.10. It has been recorded during the characterisation of our resonator set-up as a source for multi-photon states, as further described in chapter 6.
We have been able to acquire a pumping power as high as $P_{UV}^{max} = 7.2 \pm 0.2\,W$ for more than $3.5\,h$ during this run. It shall be stressed that the stability of the cavity level is normally not spoiled by termination of input coupling and associated loss of locking, but by a bleaching of the BBO crystal's anti-reflection coating, which can only sustain such high peak intensities for a limited period of time. Destruction of the coating increases cavity losses and deteriorates the power enhancement. At the time when the dataset of fig. 4.10 was measured, the crystal always had to be moved by hand to have the cavity mode impinging onto another spot of its surface after these problems occurred. In the meantime, a computer-operated driving procedure has been implemented, which offers the possibility to slowly move the crystal during

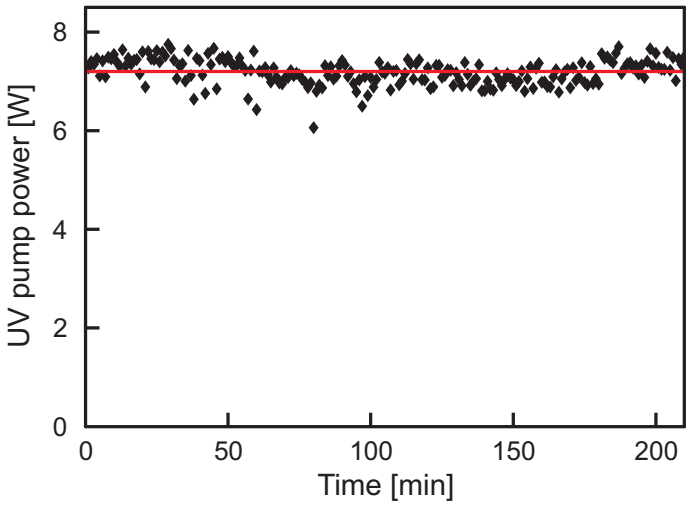

Figure 4.10: UV pumping level in resonator as used for the measurement of multi-photon count rates, presented in subsec. 6.3.2. A mean power of $\bar{P}_{UV}^{max} = 7.2 \pm 0.2\,W$ has been achieved over a time scale of more than $3.5\,h$ and is indicated by the straight red line in the figure. Black points correspond to measured values averaged over a time period of $1\,min$.

the measurements, thereby circumventing negative influences of the pumping beam. It has furthermore turned out, that such a continuous motion does neither affect the cavity locking nor trouble the collection of the generated photon pairs by the single mode fibre beyond the cavity's output coupler (mirror $M2$ in fig. 2.2), at least not if the dislocation range is chosen narrow enough.

4.3 Finesse

The measurement of the finesse and the associated light storage qualities of an optical cavity can in principle be performed in many different ways, which are more or less applicable to our situation. In the following we will choose a method in order to conclude onto the cavity's finesse F, known as ring-down spectroscopy. It was originally developed to measure absorption rates of objects positioned inside cavities for pulsed laser light ([90]) with much higher accuracy than attainable in direct observation of the absorption magnitude of cw lasers. For instance an application has been the direct measurement of energy level splittings in molecules ([90]). For our purpose, we will follow an approach devised in reference ([91]), using it with a bare cavity only in order to figure out the latter's energy decay rate.

4.3.1 Principles of ring down spectroscopy

Connections between ring down signal, decay rate and finesse The general idea behind the ring down technique is to deposit some light into an optical resonator and subsequently observe its leakage through one of the mirrors. Having an optical pulse with a certain amount of energy inside a resonator to start with, transmission through the mirrors and any additional source of loss will step by step diminish the stored intensity during round-tripping of the pulse. Thus the observed out-coupled signal will decay as well. Obviously the lower the resonator's losses, i.e. the higher its quality and finesse, the longer the extinction time of circulating light. Energy deposition is achieved by having a light source for an instant of time in resonance with the cavity and, once light is coupled in, quickly switching off the external pumping by termination of the resonance condition. That is either achieved by modulating the external laser frequency[15] or by changing the cavity's FSR. We will choose the second option and sweep the fast piezo-electric transduzer (attached to mirror $M1$, see 2.2), normally used for stabilising the repetition rate, over a fraction of its entire travel range $\Delta L_{\text{piezo}}^{tot} = 2.2\,\mu m$ with a frequency f_{piezo}. Hence for some mirror position the cavity comes into resonance with the external UV pulses and light is coupled in, but as ω_{FSR} is continuously changed the cavity repetition rate moves out of resonance again and the light inside is decoupled from the external pump. From this hand-waving explanation it is clear, that the travel range of the piezo has to be small enough not to scan over adjacent cavity resonances, as otherwise

[15] For instance by aid of an AOM.

additional light could penetrate in again, while the piezo frequency has to be high enough to allow for a quick switch-off of the external pump, but still lower than the inverse decay time of the stored energy. In order to develop a quantitative understanding of the intensity decrease, an easy argumentation, following reference ([51]), shall be presented.
Consider light just coupled into the cavity to comprise an electric field given by $E'(t) = t_{IC}E(t)$, whereby t_{IC} is the transmittivity of the input-coupler. After one round-trip, with a time duration $T_R = \frac{L_{cav}}{c}$, the resulting field will be

$$E'(t + T_R) = r \cdot E'(t) \cdot \exp(i\Phi) \tag{4.14}$$

The reflectivities of all cavity components have here been combined into the total cavity reflectivity $r = r_{M1} \cdot r_{M2} \cdot r_{M3} \cdot r_{M4} \cdot t_{\text{BBO}} \cdot t_{\text{air}}$ and all temporal phases picked up are accounted for by $\Phi = \Phi_{M1} \cdot \Phi_{M2} \cdot \Phi_{M3} \cdot \Phi_{M4} \cdot \Phi_{\text{BBO}} \cdot \Phi_{\text{air}}$. Accordingly, after n roundtrips, an electric field of

$$E'(t + n \cdot T_R) = r^n \cdot E'(t) \cdot \exp(in\Phi) \tag{4.15}$$

is obtained, resulting in an intra-cavity intensity given by

$$I_{cav}(t + nT_R) \sim r^{2n} \cdot |E'(t)|^2 = R^n \cdot |E'(t)|^2 := |E'(t)|^2 \cdot \exp\left(-\frac{nT_R}{\tau}\right) \tag{4.16}$$

with a total cavity reflectance defined as[16]

$$R = r^2 := \exp\left(-\frac{T_R}{\tau}\right) = \exp\left(-\frac{1}{f_{rep}\tau}\right). \tag{4.17}$$

In the above expression, $f_{rep} = \frac{1}{T_R}$ symbolises the cavity repetition rate and τ stands for the cavity ring down time. Observation of the transmitted signal through one cavity mirror thus yields an intensity $I_{\text{leak}}(t) = |t_{\text{Mirror}}|^2 \cdot I_{cav} \sim \exp\left(-\frac{t}{\tau}\right)$ showing an exponential decrease. Determination of the constant τ from this recording allows, by knowledge of the cavity's free-spectral range $\nu_{FSR} = \frac{\omega_{FSR}}{2\pi} = f_{rep}$, the computation of the entire reflectivity r and therefrom the cavity finesse by aid of ([51])

$$F = \frac{\pi\sqrt{r}}{1 - r} \tag{4.18}$$

It shall be mentioned, that this method only works, if f_{rep} is approximately constant during the cavity length sweep in order to obtain the last term in eq. (4.16). With a cavity length of $L_{cav} = 3.71\,m$ and a maximally possible sweep range of only $\Delta L^{tot}_{\text{piezo}} = 2.2\,\mu m$, the aforementioned condition is very well satisfied and the cavity repetition rate can be regarded as equal to the Ti:Sa pulse repetition rate of $f_{rep} \approx 80\,MHz$.

Shape of the ring down signal The above picture is yet a little too simple in order to account for the real experimental findings, as these comprise some additional oscillations with increasing frequency and an exponentially decaying amplitude (eq. (4.16)), e.g. depicted in figs. 4.11 and 4.12. For brevity, only a qualitative reasoning for this behaviour will be presented in the following. For a detailed mathematical treatment, the reader might consult reference ([91]), containing an argumentation based on classical physics, and reference ([51]), taking the full relativistic nature of the electromagnetic light field into account. For what is required to understand the measurements evaluated later on, it is sufficient to acknowledge the oscillating feature to stem from interference between the round-tripping pulses, which are shifted in frequency by the Doppler effect, encountered during each reflection off the moving mirror $M1$. While so far we anticipated to have a strict cut-off of any pulse penetration into the cavity once its length is swept out of resonance, in reality there is still some residual transmittance of the external pulses through the input coupler, due to the finite transmittance of this component ([91]). For the intra-cavity field an interference between a number of n already stored copies of the pulse inside the resonator, each with a number of 1 up to n accomplished roundtrips, with a newly input-coupled pulse occurs. As the intra-cavity field experiences a relativistic Doppler shift of $u_{DS} = \frac{1-\frac{V}{c}}{\sqrt{1-(\frac{V}{c})^2}}$ during each reflection off the mirror $M1$, moving with a velocity V, we have an interference of the electric fields, that have been subject of 0 up to n shifts in their frequency and hence a superposition of $E_{cav} \sim \sum_{j=0}^{n} r^j \cdot \exp\left(i\omega(u_{DS})^{2j}t\right)$ ([51]). So depending on the exact phase relationships between all pulses as a function of time, oscillations

[16] For high cavity finesse, this expression can be Taylor expanded to $R = \exp\left(-\frac{nT_R}{\tau}\right) \approx 1 - \frac{T_R}{\tau}$, which coincides with the result derived by approximation in reference ([91]).

between constructive and destructive interference are obtained[17]. It shall particularly be noted, that this interference happens inside the resonator already and is therefore observable on every signal leaking through any mirror. Under the approximation of each Doppler shift causing a phase variation much smaller than 2π, an exact calculation yields an intra-cavity field of ([51])

$$E'_{cav}(t_m+t') = E'(t_m+t')\sqrt{\frac{ic}{8Vm}}\exp\left(g(t')^2\right)\left(1+\operatorname{erf}\left(g(t')\right)\right) \tag{4.19}$$

with

$$g(t') = \sqrt{\frac{-ic}{8\pi Vm}}\left(2\pi\frac{\omega V t'}{\pi c} + i\ln(r)\right), \tag{4.20}$$

whereby ω is the instantaneous frequency of the round-tripping light and the time t has been split up into $t = t_m + t'$. The variable t_m is the time at which the m^{th} resonance in the cavity occurs for the Doppler shifted light, in other words $\exp\left(i\omega(u_{DS})^{2m}t_m\right) = \exp\left(i2\pi m\right) = 1$. Hence t' is a time offset between two of these constructive resonances. The error function $\operatorname{erf}(x)$ in eq. (4.19) is defined by:

$$\operatorname{erf}(x) = \frac{2}{\sqrt{\pi}}\int_0^\infty \exp\left(-x'^2\right)dx'$$

In order to retrieve the decaying intensity I_{cav}, one has to take the absolute square of eq. (4.19) ([51])

$$\begin{aligned} I_{cav}(t_m+t') &\sim \exp\left(\frac{\operatorname{Im}\left(\frac{c\left(2t'\omega V/c + i\ln(r)\right)^2}{mV}\right)}{4\pi}\right) \\ &= \exp\left(\frac{c}{m\pi V}\operatorname{Im}\left(4t'^2\omega^2\frac{V^2}{c^2} - \ln^2(r) + 4it'\omega\ln(r)\frac{V}{c}\right)\right) \\ &= \exp\left(2\cdot\underbrace{\frac{\omega_0}{m}}_{=1/T_R}\cdot\ln(r)t'\right) = \exp\left(\frac{2\ln(r)}{T_R}t'\right) = \exp\left(-\frac{t'}{\tau}\right) \end{aligned} \tag{4.21}$$

showing also an exponentially decreasing amplitude. Examining the last substitution in closer detail, we can infer

$$\tau = -\frac{T_R}{2\ln(r)} \Longleftrightarrow \ln(r) = -\frac{T_R}{2\tau} \Longleftrightarrow r = \exp\left(-\frac{T_R}{2\tau}\right) \Longleftrightarrow R = r^2 = \exp\left(-\frac{T_R}{\tau}\right) \tag{4.22}$$

which resembles the result obtained from the simple picture of leakage during round-tripping, expressed by eq. (4.16). So for figuring out the finesse of the cavity, it is sufficient to just use the oscillation maxima at times t_m from the ring down signal, fit these datapoints by a simple exponential decay function $y(t) = \alpha\cdot\exp\left(-\frac{t}{\tau}\right)$ and extract τ with subsequent calculation of F under consideration of eqs. (4.17) and (4.18).

Ring down signal observed in reflection In the measurement, we will record the transmitted signal through the input coupler (mirror $M3$ in fig. 2.2), which is superposed with the uncoupled electric field $r_{IC}E(t)$ directly reflected thereof. Thus an additional interference between these two contributions in principle occur and the resulting intensity can be expressed as ([51]):

$$\begin{aligned} I_{RD}(t_m+t') &= |-r_{IC}E(t_m+t') + t_{IC}E'_{cav}(t_m+t')|^2 \\ &= R_{IC}I(t_m+t') + T_{IC}I_{cav}(t_m+t') \\ &\quad +2I(t_m+t')\underbrace{\operatorname{Re}\left(r_{IC}t_{IC}^2\sqrt{\frac{ic}{8Vm}}\exp\left(g(t')^2\right)\left(1+\operatorname{erf}\left(g(t')\right)\right)\right)}_{=:f(t')} \\ &= \underbrace{R_{IC}I(t_m+t')}_{\text{term 1}} + \underbrace{T_{IC}I_{cav}(t_m+t')}_{\text{term 2}} + \underbrace{2I(t_m+t')f(t')}_{\text{term 3}} \end{aligned} \tag{4.23}$$

[17] The same argumentation applies to cw pumping of the resonator. One only has to think about interference of electric field strengths at times $t + jT_R$ instead of distinct pulses.

Term 1 assigns the directly reflected intensity of the external pump, so no ring down fingerprint is to be expected here. Term 2 is the transmitted intensity of the ring down signal, given by eq. (4.21), as it also observable in leakage through mirrors $M1$, $M2$ and $M4$. The last term 3 represents the interference between the external pumping field and the electric field of the ring-down signal, only present at the input-coupler. Calculating $\exp\left(g(t')^2\right)$ in $f(t')$, one is left with

$$\begin{aligned}
\exp\left(g(t')^2\right) &= \exp\left(\sqrt{\frac{-ic}{8\pi Vm}}\left(2\omega_0\frac{V}{c}t' + i\ln(r)\right)\right)^2 \\
&= \exp\left(\frac{\omega_0\ln(r)t'}{2\pi m} + \frac{ic\ln^2(r)}{8\pi Vm} - \frac{i\omega_0^2 Vt'^2}{2\pi mc}\right) \\
&= \exp\left(\frac{\ln(r)t'}{T_R}\right)\cdot\exp\left(-i\left(\frac{\omega_0^2 Vt'^2}{2\pi mc} - \frac{c\ln^2(r)}{8\pi mV}\right)\right) \\
&= \exp\left(\frac{t'}{\tau'}\right)\cdot\exp\left(-i\left(\frac{\omega_0^2 Vt'^2}{2\pi mc} - \frac{c\ln^2(r)}{8\pi mV}\right)\right) \qquad (4.24)
\end{aligned}$$

By further analysis of the exponentially decaying term and comparison with the decrease in ring down signal strength, described by eqs. (4.16) and (4.21), we get:

$$\tau' = -\frac{T_R}{\ln(r)} \Longleftrightarrow \ln(r) = -\frac{T_R}{\tau'} \Longleftrightarrow R = r^2 = \exp\left(-\frac{2T_R}{\tau'}\right) \Longrightarrow \tau' = 2\tau \qquad (4.25)$$

So the interference term comprises a decay constant of twice the ring down time τ and the entire signal reflected off the input coupler contains two contributions, one decaying with τ (term 2 $\sim I_{cav}(t_m + t')$) and one with 2τ. For examination of our measurement results, we will however only account for term 2 in eq. (4.23) and neglect the additional interference with the longer extinction time. The reason for that will be described at the end of this part regarding finesse evaluation, where flaws in the experimental implementation are to be discussed.

4.3.2 Data analysis

Experimental ring down signals The ring down signal has been recorded by positioning a fast photodiode into the reflected beam off the cavity input coupler in front of the Hänsch-Couillaud polarisaton analysis apparatus (see fig. 3.1), since the latter is not required during the measurement procedure. Ring down signals have been taken for the situation with a BBO crystal, utilising an input coupler of $R_{IC} = 97.36\%$ reflectance, and for an empty cavity with a mirror $M3$ of $R_{IC} = 98.72\%$ reflectance. The mirror $M1$[18] has been moved by driving the fast piezo electric crystal with different frequency and voltage parameter sets of

$$(f_{\text{piezo}}, V_{\text{piezo}}) \in \{(7\,kHz, 75.2\,V), (20\,kHz, 37.6\,V), (25\,kHz, 37.6\,V)\}$$

for the case with the non-linear crystal and

$$(f_{\text{piezo}}, V_{\text{piezo}}) \in \{(7\,kHz, 75.2\,V), (10\,kHz, 37.6\,V), (15\,kHz\,37.6\,V), (20\,kHz, 37.6\,V), (25\,kHz, 37.6\,V)\}$$

for its absence. The datapoint for $(f_{\text{piezo}}, V_{\text{piezo}}) = (20\,kHz, 37.6\,V)$ has been measured twice in both runs. An exemplary graph for the results with the BBO is provided in fig. 4.11 and outcomes without the BBO are shown in fig. 4.12, both for a parameter choice of $(f_{\text{piezo}}, V_{\text{piezo}}) = (20\,kHz, 37.6\,V)$. Application of a detector with a fast response time enables to observe the repetition frequency of the pumping laser on top of the ring down signal, which can be seen as fast oscillations in the parts denoted by a) in figs. 4.11 and 4.12. To precisely infer the oscillation maxima of the ring down curve, it is however necessary to get rid of these additional fluctuations in the data. Therefore a Fourier analysis has been pursued. A pronounced peak is visible therein at a frequency of $f_{rep} \approx 80\,MHz$, which corresponds to the laser's repetition rate and in turn also to the FSR of the resonator. For further analysis, f_{rep} is determined in each dataset and subsequently low-pass Fourier filtering is performed with a cut-off frequency of $f_{cut-off} = 30\,MHz$. The evaluated laser repetition rates for the various measurements can be found in the appendix B.2. Such an operation delivers a smoothed ring down signal, from which the relevant maxima are readily spotted, as exemplarily drawn in figs. 4.11 b) and 4.12 b). Furthermore one can also

[18] see fig. 2.2

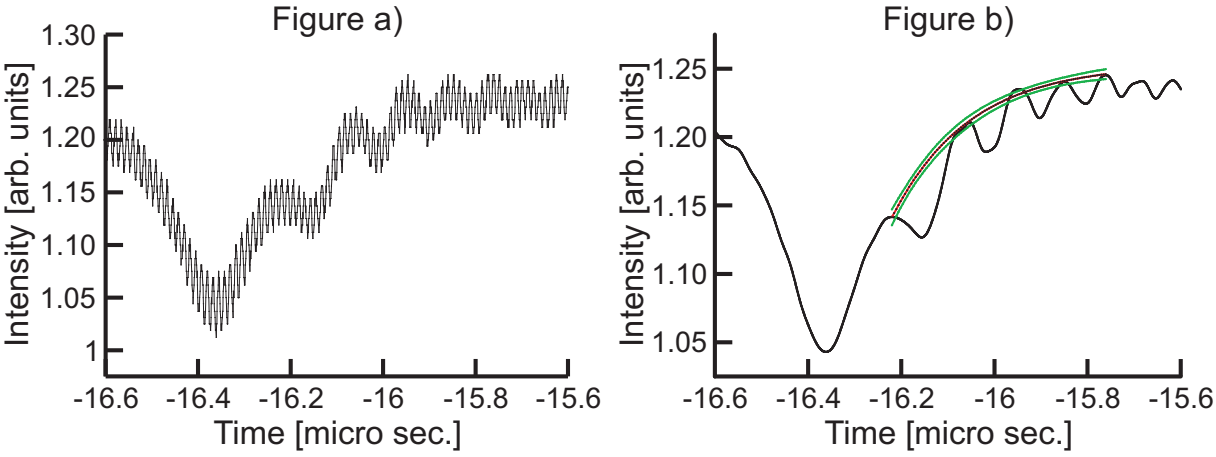

Figure 4.11: Ring down signal with the BBO crystal at a piezo frequency of $f_{\text{piezo}} = 20\,kHz$ and an applied voltage of $V_{\text{piezo}} = 37.6\,V$. Figure a) shows the raw ring down data with fast oscillations on top, stemming from the driving laser's repetition rate. Figure b) represents the smoothed signal after low-pass Fourier filtering with a cut-off frequency of $f_{cut-off} = 30\,MHz$. The red line indicates a fit according to eq. (4.26) to the ring down maxima. The green lines are the error boundaries of twice the standard deviation on the fit.

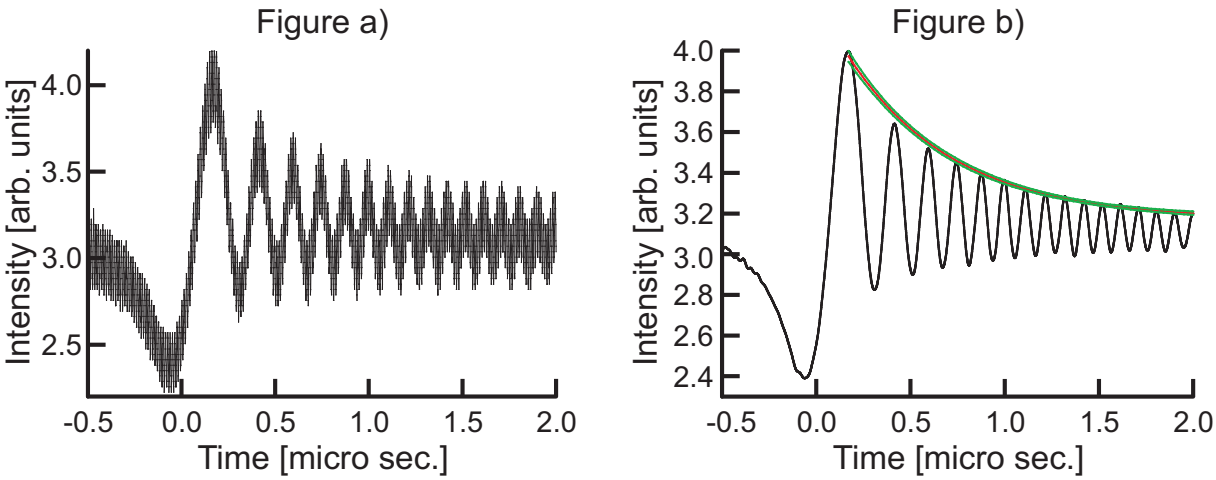

Figure 4.12: Ring down signal without the BBO crystal at a piezo frequency of $f_{\text{piezo}} = 20\,kHz$ and an applied voltage of $V_{\text{piezo}} = 37.6\,V$. Figure a) shows the raw ring down data with fast oscillations on top, stemming from the driving laser's repetition rate. Figure b) represents the smoothed signal after low-pass Fourier filtering with a cut-off frequency of $f_{cut-off} = 30\,MHz$. The red line indicates a fit according to eq. (4.26) to the ring down maxima. The green lines are the error boundaries of twice the standard deviation on the fit.

acknowledge both signals to be rather different compared to each other. While the ring down oscillations without the BBO inside the cavity show nice modulations with exponentially decreasing maxima and exponentially increasing minima, as expected from eq. (4.21), the situation with the crystal present is different and no full modulation can be observed, resulting in the maxima in the ring down signal to exhibit an exponential increase as well. The most likely explanation for such a behaviour is found in an interplay between the multi-mode nature of our measurement, caused by the application of a pulsed laser, in combination with altered dispersion by the BBO; it will be illuminated in more detail later on.

Ring down time τ Now all oscillation maxima in the ring down signals are selected and fitted by the decaying exponential[19]

$$I(t) = I_0 \exp\left(\pm\frac{t}{\tau}\right) + I_{offset} \tag{4.26}$$

The resulting data is plotted in fig. 4.11 b) for the cavity containing the BBO and fig. 4.12 b) for its absence, exemplarily again for $f_{\text{piezo}} = 20\,kHz$ and $V_{\text{piezo}} = 37.6\,V$, comprising the fitted functions indicated by red lines. Altogether the ring down times τ, as stated in table 4.1, are obtained by the fitting procedure. The errors therein originate from the fitting uncertainties and are thus statistical in their nature.

Piezo freq. [kHz]	τ with BBO [ns]	τ without BBO [ns]
7	422 ± 99	495 ± 17
10	–	461 ± 13
15	–	735 ± 23
20	167 ± 11	561 ± 19
20	158 ± 8	510 ± 16
25	99 ± 1	411 ± 14

Table 4.1: Ring down times obtained from fitting the oscillation maxima in the ring down signals by exponentially decaying functions according to eq. (4.26).

The confidence level of the fit is also included into figs. 4.11 b) and 4.12 b) by the green lines enclosing an area of twice the standard deviation above and below the fitted behaviour. Looking at the number for τ with BBO at $f_{\text{piezo}} = 7\,kHz$, as well as the one without BBO at $f_{\text{piezo}} = 15\,kHz$, one can see that these numbers deviate considerably, since they do not match with the magnitude range implied by their counterparts at the other sweeping frequencies. So one has to check whether their underlying signals make sense in terms of what is expected from a ring down measurement. Furthermore an analysis of the suitability of all measured data in this experiment is generally necessary just for the very reason that we attempt to measure the ring down signal with a broadband light source, which could lead to a wash out of the oscillations in the intensity as it will be outlined later. A possible means to do so is offered by the oscillation frequency of the round-tripping light intensity inside the cavity. It is shown in reference ([91]), that the time separation between the first two minima in the ring down curves must be approximately given by[20]

$$T_{12} = (\sqrt{2} - 1)\sqrt{\frac{L_{cav}}{c}\frac{\lambda}{v}} \tag{4.27}$$

whereby $v = \Delta L_{\text{piezo}} \cdot f_{\text{piezo}}$ equals the velocity of the mirror displacement during cavity length sweeping. The dislocation of the mirror is expressed by the one of the PZT, ΔL_{piezo}, which is proportional to the applied voltage, V_{piezo}, according to[21] $\Delta L_{\text{piezo}} = \Delta L^{tot}_{\text{piezo}} \cdot V_{\text{piezo}}/(100\,V)$. One should note in this context the first minimum to be the one adjacent to the right hand side of the first maximum (i.e. at times $t > t_{1^{st}max}$) and not the global minimum to its left hand side in figs. 4.11 b), 4.12 b). This relationship approximately describes every ring down signal leaking out of any resonator mirror except the input

[19] Due to the aforementioned modifications in the ring down oscillations with BBO, a positive sign has to be chosen for this scenario.

[20] The missing factor of 2 under the square root in eq. (4.27) with respect to the formula, stated in ([91]), is due to our set-up being a ring cavity, in which the entire round-trip length is L_{cav}, whereas An et. al. ([91]) have been considering a linear, two mirror arrangement with a mirror separation of $L^{[91]}_{cav}$ and consequently a round-trip length of $2 \cdot L^{[91]}_{cav}$, entering their expression for the interference minima distance.

[21] The extension of the PZT crystal is specified as $2.2\,\mu m/100\,V$ with an uncertainty of $\pm 20\,\%$.

coupler. Here the interference between $E'_{cav}(t_m + t')$ and the external field $E(t_m + t')$, expressed by eq. (4.23), could potentially modify the oscillation periods. However as we neglect the interference term 3 in eq. (4.23) it shall be applied here. Plugging the cavity length of $L_{cav} = 3.71\,m$, the piezo travelling ranges ΔL_{piezo} and frequencies f_{piezo} into eq. (4.27) yields the theoretically expected times T_{12}^{theo}, which are stated together with the durations from the measurements in table 4.2.

Piezo freq. [kHz]	T_{12}^{theo} expected [ns]	T_{12}^{exp} with BBO [ns]	T_{12} without BBO [ns]
7	267	169	325
10	316	–	287
15	258	–	432
20	224	146	186
20	224	183	200
25	200	138	169

Table 4.2: Time separation of the first two minima in oscillation of the ring down signal. Theoretical numbers are calculated by eq. (4.27).

Indeed the value for $f_{\text{piezo}} = 15\,kHz$ without BBO reveals severe deviations in this parameter from the theoretical expectations. Also the value for $f_{\text{piezo}} = 7\,kHz$ with BBO differs from the trend set by the other data, which roughly resembles T_{12}^{theo}. The ring down times for both measurements are furthermore considerably off the averaged outcome among all the other ones, whereby the former digresses by more than 4 standard deviations from their mean value and the latter is off by as much as 7.6 standard deviations. Thus the datasets at $f_{\text{piezo}} = 7\,kHz$ with BBO and the one at $f_{\text{piezo}} = 15\,kHz$ without BBO will be neglected in the following analysis, which is justified, since τ is directly proportional to the finesse and we expect F to be equal for all datasets. Regarding the deviations of all other measurements from their theoretical expectation in table 4.2, one should keep in mind, that first of all eq. (4.27) only provides an approximate quality measure for the data[22]. Second, the extension length of the PZT is only specified within an error boundary of 20 % around the calculated value. Finally, a possible reason for such a mismatch could of course also be the already mentioned blurring of the oscillations, due to the multimode nature of our ring down signal. Nevertheless we continue the finesse evaluation with the residual data in table 4.2.

Resonator reflectivity and reflectance We can conclude onto the mirror reflectivities r^j, respectively their reflectances R^j, by the aid of eq. (4.17). The errors on both can be computed from the uncertainties of the ring down time $\Delta\tau$ and the repetition rate Δf_{rep}. However because the error Δr cannot be gained from ΔR simply by taking the square root and since the cavity reflectivity as well as the reflectance will be needed shortly, their resulting numbers are stated separately in table 4.3 for both experimental arrangements[23].

Piezo freq. [kHz]	r with BBO	R with BBO [%]	r without BBO	R without BBO [%]
7	–	–	0.9876 ± 0.0004	97.53 ± 0.08
10	–	–	0.9867 ± 0.0004	97.35 ± 0.08
20	0.963 ± 0.002	92.9 ± 0.5	0.989 ± 0.0004	97.82 ± 0.07
20	0.961 ± 0.002	92.4 ± 0.4	0.9879 ± 0.0004	97.6 ± 0.07
25	0.9395 ± 0.0007	88.3 ± 0.1	0.985 ± 0.0005	97 ± 0.1

Table 4.3: Reflectivities r and reflectances R for the entire cavity apparatus with and without the BBO crystal inside, gained from eq. (4.17).

Before moving on to calculating the finesse, one can briefly check the cavity losses associated with these

[22] Therefore the $f_{\text{piezo}}^{\text{noBBO}} = 15\,kHz$ and $f_{\text{piezo}}^{\text{BBO}} = 7\,kHz$ values are not solely disregarded on the basis of their deviation from T_{12}^{theo}, but also by their huge deviation from the mean, set by the other data.

[23] The respective formulae for the two errors are:

$$\Delta r = \sqrt{\left(\frac{1}{2f_{rep}^2\tau}\exp\left(-\frac{1}{2f_{rep}\tau}\right)\right)^2(\Delta f_{rep})^2 + \left(\frac{1}{2f_{rep}\tau^2}\exp\left(-\frac{1}{2f_{rep}\tau}\right)\right)^2(\Delta\tau)^2}$$

$$\Delta R = \sqrt{\left(\frac{1}{f_{rep}^2\tau}\exp\left(-\frac{1}{f_{rep}\tau}\right)\right)^2(\Delta f_{rep})^2 + \left(\frac{1}{f_{rep}\tau^2}\exp\left(-\frac{1}{f_{rep}\tau}\right)\right)^2(\Delta\tau)^2}$$

reflectances. We know that the reflectance of the entire cavity is proportional to the cavity loss L. In other words, each bit of light intensity that does not get reflected, gets transmitted or absorbed, so $R = 1 - L$. During designing the cavity, an input coupler reflectance for a resonator with BBO of $R^{\mathrm{IC,BBO}} = 97.36\,\%$ and one of $R^{\mathrm{IC,noBBO}} = 98.72\,\%$ has been figured out to be appropriate (see subsec. 2.1.3). Since R represents the entire cavity reflectance, division by R^{IC} yields the one of apparatus without the input coupler, still containing all other three mirrors as well as the losses due to air and the non-linear crystal (if it is included), whereby the reflectances of mirrors $M1$, $M2$ and $M4$ are $\geq 99.9\,\%$. So by calculating $R^{\mathrm{noIC,BB0}} = \frac{R^{\mathrm{BBO}}}{R^{\mathrm{IC,BB0}}}$ and $R^{\mathrm{noIC,noBB0}} = \frac{R^{\mathrm{noBBO}}}{R^{\mathrm{IC,noBB0}}}$, the losses, the intensity in the ring down signal experiences, can be assessed and compared with the values for the combination of the BBO crystal, air and the mirrors $M1$, $M2$, $M4$. The relevant numbers are:

Piezo freq. [kHz]	$R^{\mathrm{noIC,BBO}}$ [%]	L^{BBO} [%]	$R^{\mathrm{noIC,noBBO}}$ [%]	L^{noBBO} [%]
7	–	–	98.79 ± 0.08	1.21 ± 0.08
10	–	–	98.62 ± 0.08	1.38 ± 0.08
20	95.4 ± 0.5	4.6 ± 0.5	99.08 ± 0.07	0.92 ± 0.07
20	94.9 ± 0.4	5.1 ± 0.4	98.86 ± 0.08	1.14 ± 0.08
25	90.7 ± 0.1	9.3 ± 0.1	98.3 ± 0.1	1.7 ± 0.1

As average loss values, $\bar{L}^{\mathrm{noBBO}} = 1.3 \pm 0.3\%$ is recieved without BBO and $\bar{L}^{\mathrm{BBO}} = 6.3 \pm 2.6\%$ with BBO, whereby the errors represent the standard deviation. Both are larger than the expectations based on calculations of the optical components' properties. From the discussion in subsec. 2.1.2, we receive a loss estimate for the cavity without BBO of $L^{\mathrm{noBBO}} \approx 0.16\,\%$ and for the presence of the crystal we approximate $L^{\mathrm{BBO}} \approx 1.5\,\%$. However the best choices of input couplers, see eqs. (2.55) and (2.57), considering the entire spectrum, would indicate a loss rate of $\tilde{L}^{\mathrm{noBBO}} \approx 2.64\,\%$ and $\tilde{L}^{\mathrm{BBO}} = 1.28\,\%$. These values are nevertheless also a function of the external and internal mode overlap, as outlined in subsec. 2.1.4, so they do not only account for losses in the cavity but also include contributions due to dispersion. The latter terminates coupling of certain modes into the cavity, causing an overestimation of the losses these modes would experience with respect to a situation, where dispersion would be absent and they would actually be resonant. As we have measured the ring down signal with the full spectrum of the pumping pulse, these spectrally averaged loss values are therefore the more appropriate ones to compare $\bar{L}^{\mathrm{noBBO}}$, $\bar{L}^{\mathrm{BBO}}$ to. The first number $\bar{L}^{\mathrm{noBBO}} = 1.3 \pm 0.3\%$ from the ring down measurement thus accords at least with the figure retrieved by input coupler optimisation. The second value of $\bar{L}^{\mathrm{BBO}} = 6.3 \pm 2.6\%$ does not correspond to any of the appraisals though[24]. A possibility for such a mismatch might again be due to in employing a broadband spectrum to investigate the ring down time, washing out the oscialltions and hence preventing one from retrieving the proper mirror reflectances. But this is just one potential reasoning and a proper verification of the deviations' origin is not clear yet. This leaves us with the notion, that quantities infered from this measurement, especially for the arrangement with BBO, are an estimation only.

Finesse Nevertheless the conclusion onto the resonator's finesse[25] shall be accomplished by eq. (4.18) with the overall reflectivities stated in table 4.3. The results are provided in table 4.4.

Piezo freq. [kHz]	Finesse with BBO	Finesse without BBO
7	–	251 ± 9
10	–	234 ± 7
20	85 ± 6	285 ± 10
20	80 ± 4	258 ± 8
25	50 ± 1	209 ± 7

Table 4.4: Finesse of resonator obtained from datasets at different piezo sweeping frequencies, calculated by eq. (4.18).

For a mean value of the finesse, we thus achieve

$$\bar{F}^{\mathrm{BBO}} \approx 72 \pm 19 \tag{4.28}$$

with the BBO crystal and

[24] Even if the differing datapoint for $f_{rep} = 25\,kHz$ is neglected, still an attenuation of $\bar{L'}^{\mathrm{BBO}} = 4.8 \pm 0.3\,\%$ would be implied by the ring down method, exceeding the real resonator losses.

[25] Errors on the individual datasets are computed according to $\Delta F = \left(\frac{\sqrt{r}}{(1-r)^2} + \frac{1}{2\sqrt{r}(1-r)}\right)\pi\Delta r$.

$$\bar{F}^{\mathrm{noBBO}} \approx 247 \pm 28 \tag{4.29}$$

without it. The errors on these averages are the standard deviations between all contributing data, since those are larger than the propagated individual errors and account more appropriately for the discrepancies between the numbers at different piezo frequencies. The presence of the non-linear medium obviously deteriorates the quality of the resonator by approximately a factor of 3.5. In turn, by maintaining the same FSR, the cavity resonances widen by an equal amount due to $F \sim \frac{1}{\Delta\omega_{FWHM}}$. So matching external frequency comb modes to these, or in other words coupling light into the resonator, should be much easier. Indeed that has been observed experimentally during recording of internal UV spectra for measuring the spectrally resolved power enhancement. While the cavity offers stable enhancement over a time scale of days up to a week, if the crystal is included, it is otherwise challenging to have it stabilised even for a couple of minutes. However this does not only result from a higher sensitivity to dispersive displacements between external comb teeth and cavity resonances, but also from the higher susceptibility to any source of noise, for instance caused by vibrations, which dislocate the latter modes with respect to the former, thereby terminating the input coupling.

Comparison with power enhancement As initially mentioned, it is not sensible to extract the finesse from a power enhancement measurement for broadband resonators, accommodating ultra-short laser pulses. Contrary, it is nonetheless feasible to gain a gross idea about significance of the separately yielded finesse by comparing the power enhancement it suggests, denoted by PE', with the value really apparent, assigned as PE. We will do so using the connection between power enhancement and finesse, given by

$$PE' = \frac{F}{\pi}, \tag{4.30}$$

i.e. dividing eqs. (4.28) and (4.29) by π leaves us with a power enhancement of $\bar{PE'}^{\mathrm{BBO}} = 23 \pm 6$ and $\bar{PE'}^{\mathrm{noBBO}} = 79 \pm 9$. These numbers are best to be compared to the maximum of the spectrally resolved power enhancement $PE(\lambda)$. That is because we expect the finesse to be rather constant over the pulse spectrum due to the approximate constancy in the mirror reflectances as well as BBO and air absorption. In contrast, the power enhancement strongly depends on the input coupling condition, set by frequency comb matching, and does therefore only accord to eq. (4.30) for perfect dispersion compensation, fulfilled best at the maximum of the power enhancement spectrum $PE(\lambda)$. This is not a contradiction to what has just been said in the course of the cavity loss estimation. A finesse value, retrieved from the power enhancement, is only sensible for impedance matched coupling, when eq. 4.30) is solely valid. A comparison with a finesse value, derived from the spectrally integrated power enhancements $\bar{PE}^j$ (eqs. (4.5), (4.6)), is hence not sensible, since the connection between both quantities is not well defined. Referring to the previous discussion in subsec. 4.2.3, figures turned out to $PE_{max}^{\mathrm{BBO}}(\lambda = 390.92\,nm) = 17 \pm 3$ with the crystal and $PE_{max}^{\mathrm{noBBO}}(\lambda = 391.11) = 45 \pm 10$ without it. Before establishing a connection with the $\bar{PE'}$s, it is necessary to become aware of the difference in the way of their determination: PE' values solely account for features intrinsic to the resonator, i.e. enhancement experienced by light already transmitted through the input coupler, whereas the PE ones also include the effects of reflection off the input coupler. That is to say, the latter quantity has been scaled to the total[26] amount of stored internal to the total external UV power and hence includes a reduction in power enhancement by a factor of 2, which is due to transverse mode mismatch at the input coupler as outlined in subsec. 3.1.2. Spoken more precisely: Since $\approx 50\,\%$ of the external UV light of $P_{UV}^{ext} \approx 0.54\,mW$, impinging onto the input coupler, are reflected by that component, only $t_{IC}P_{UV}^{ext} \approx 0.27\,mW$ make it into the resonator and can be enhanced. The power enhancement values PE are normalised to $P_{UV}^{ext} \approx 0.54\,mW$ though and are thus artificially diminished, due to our definition of PE as "power within the cavity divided by power outside the cavity". So the values for PE' have to be halved in order to accound for this inequality in definition. We consequently yield with the BBO $\bar{PE''}^{\mathrm{BBO}} = \frac{\bar{PE'}^{\mathrm{BBO}}}{2} \approx 12 \pm 3$, which is to be compared with $PE_{max}^{\mathrm{BBO}}(\lambda = 390.92\,nm) = 17 \pm 3$, and without it $\bar{PE}^{\mathrm{noBBO}} \approx 40 \pm 5$, to be contrasted with $PE_{max}^{\mathrm{noBBO}}(\lambda = 391.11) = 45 \pm 10$. Both sets of values coincide within their error boundaries, although they still deviate and the uncertainty ranges are rather large[27]. The figures for the finesse are hence to be regarded sensible in terms of their correspondence with results obtained from independent measurements. Nevertheless the non perfect resemblance underlines, that the finesse evaluation, presented here, just provides an estimation about the precise number for this parameter. This has to be kept in mind,

[26] i.e. spectrally integrated over all frequencies within the laser pulses

[27] Especially for $PE_{max}^{\mathrm{noBBO}}$, due to the low statistics on the spectra, caused by the problematic cavity locking.

particulary since the power enhancement $PE(\lambda)$ is a rather precisely, flawlessly and, above all, directely measured value, which puts the numbers of $PE_{max}(\lambda)$ on solid footings. The finesse and its associated implications (like PE' and R^{noIC}) are opposingly acquired indirectly and are subject to approximations and uncertainties, which are stated in the appendix B.3.

Chapter 5

Characterisation of pulse duration within resonator

5.1 Introduction into autocorrelation with SPDC

5.1.1 Determination of pulse duration with autocorrelation

Within this chapter, the duration of the intra-cavity UV pumping pulses will be measured. Since laser pulses with durations on the order of femtoseconds are far too short to be measured by electronic means, self-referencing techniques in the optical domain are commonly utilised instead. These are based on the idea of measuring the pulse under study with a time delayed copy of itself by the aid of a generated signal, which is sensitive to the overlap, respectively the convolution between both pulses. Varying the time separation and thus moving one pulse over the other, produces a signal, whose width is proportional to the pulse duration and therefore allows sampling of the pulse's electric field amplitude. It is obvious, that an optical process, generating the desired signal, cannot be linear in the electric field, since it has to be sensitive to the overlap between the fields and not just to their superposition. In other words, the signal s has to comprise terms proportional to $E_1 \cdot E_2$, whereby E_i represents the electric field of the i^{th} pulse. So non-linear optical processes have to be utilised, which result for two pulse copies in $s \sim (E_1 + E_2)^n$ for a process on the order of n. Commonly, non-linearities scaling with second order in the electric field, i.e. $n = 2$, are used for such measurements, whereby especially second harmonic generation ([96]) became the workhorse in this field. Nevertheless we will employ SPDC as the process of choice. The easiest and oldest approach to infer the pulse duration from such a generated non-linear signal is to just measure its strength as a function of pulse separation τ and set the width of the resulting function in relation to the duration of the expected underlying pulse. Such a measurement is termed autocorrelation and will also be the method of our choice to gather information about the intra-cavity pulse length. Although there are more advanced schemes at hand, which allow retrieval of addition information (see references [115]-[124]), the aforementioned method will suffice for our needs. Furthermore one can distinguish between two different types of autocorrelation. The first one is incorporating the intensities of the overlapping pulses and is therefore termed intensity autocorrelation, see references ([97], [98]). The second one in contrast is sensitive to the pulses' electric fields, consequently named interferometric autocorrelation, first considered in reference ([95]). We will focus on the latter version for reasons to be outlined within the following section and start the discussion by evaluation of the autocorrelation function for the down-conversion process. More general information about autocorrelation can be found in ([79], [111]) and references therein.

5.1.2 Autocorrelation by the SPDC process

Although the fundamental requirement to obtain an autocorrelation type signal is to just have a non-linear process available for its generation[1], taking a closer look at our specific effect of SPDC will be fruitful. Since SPDC is not a standard means for this kind of measurement, indeed to our knowledge no previous attempt has been published so far, evidence about the applicability of autocorrelation theory shall be provided in the first place.

[1] See reference ([92]) for general discussions about this manner. Particular examples of implementing an autocorrelation without using frequency conversion can e.g. be found in reference ([93]) employing two photon absorption, or reference ([94]), relying on the non-linear electron emission from a tungsten needle tip.

Before examining the down-conversion effect in more detail, the reader shall be made aware of the terminology used within this chapter, referring to an expression given by the superposition of two electric fields, according to ([110])

$$g_n(\tau) = \frac{\int_{-\infty}^{\infty} |(E_1(t) + E_2(t-\tau))^n|^2 dt}{\int_{-\infty}^{\infty} |(E_1(t))^n|^2 dt + \int_{-\infty}^{\infty} |(E_2(t))^n|^2 dt}, \tag{5.1}$$

as the correlation function of n^{th} order ([110]). This stands in contrast to the nomenclature commonly used in the field of quantum information science, where a correlation is represented by the expectation value of a tensor product of projectors instead of the expectation value of a linear combination of operators[2] to the power of n (see also section 6.2). However it is commonplace when dealing with measurements on ultra-short laser pulses and shall therefore be used here as well.
The second order ($n = 2$) of the g_n-functions is generally adopted when measuring autocorrelation, which relies on effects involving two pump photons. While it is thus sufficient for an SHG-based system to just record one signal photon, for SPDC four photons have to be measured, since each pumping photon splits up into a signal and idler photon. Since the BBO crystal inside the optical resonator is orientated for collinear type-II down-conversion (see subsec. 6.1.2), two horizontally and two vertically polarised photons are required to be measured for g_2. In contrast only one horizontally and one vertically polarised photon is needed to yield the first order correlation $g_1(\tau)$. For the following discussion a single mode description for SPDC shall be considered in the first place and subsequently extended towards the inclusion of multi mode effects, which result from a finite phase matching bandwidth and a pulsed pumping beam ([114], [126]). Doing so is justified, as we are only interested in the terms regarding the pump pulses, unlike e.g. the autocorrelation measurement on the down-converted photons stated in reference ([100]). Any implications by phase matching as well as the spectral features of the SPDC photons are thus of no concern at the moment as these will all be integrated over in detection, resulting just in a scaling factor for the number of measured photon pairs. The interaction Hamiltonian for type-II SPDC is introduced in subsec. 6.1.2, whereby the resulting output state of the conversion process is given by[3] (eq. (6.13)):

$$|\Psi(t)\rangle = \sqrt{1 - \tanh^2 |g'|} \sum_{n=0}^{\infty} \frac{\tanh^n |g'|}{n!} \left(\hat{a}_H^\dagger \hat{a}_V^\dagger\right)^n |\text{vac}\rangle \tag{5.2}$$

The variable g' represents an interaction parameter in this expression, which is proportional the nonlinearity and the length of the BBO crystal as well as the phase matching and the pumping power P_{UV}. Further the annihilation and creation operators for SPDC fields at a particular frequency with horizontal or vertical polarisation are assigned by $\hat{a}_H^\dagger$, $\hat{a}_H$, $\hat{a}_V^\dagger$, $\hat{a}_V$. Considering the pump power values we will have available during the actual autocorrelation experiment, these will be situated within an interval of $P_{UV} \in [1.97\,W, 3.47\,W]$. From a simulation of our set-up, carried out in reference ([139]), the parameter g' can in turn be figured out to lie within an interval of $g' \in [0.21, 0.28]$. Such a parameter range is suitable for the small pumping power approximation $g' \ll 1$, leading to $\tanh |g'| \approx |g'|$ and $\sqrt{1 - |g'|^2} \approx 1$, under which eq. (5.2) simplifies to (see eq. (6.17)):

$$|\Psi(t)\rangle \approx \sum_{n=0}^{\infty} \frac{|g'|^n}{n!} \left(a_H^\dagger a_V^\dagger\right)^n |0\rangle = \sum_{n=0}^{\infty} \frac{|g|^n}{n!} \left(a_H^\dagger a_V^\dagger \hat{b}_p\right)^n |0, p\rangle \tag{5.3}$$

Here also the quantisation of the pump field has been taken into account by splitting up g' into a crystal parameter dependent constant g and the destruction operator $\hat{b}_p$, operating on the pump field $|p\rangle$. Now the particular situation for an autocorrelation set-up has to be taken into account. Since there are two pumping pulses of which one is delayed with respect to the other by a variable time separation τ, there has to be some ambiguity in the origin of the down-converting pump photon. In other words, to be sensitive to the pulses' overlap, the conversion must be able to occur with equal probability either at time t or $t-\tau$. We include this pump pulse structure into the interaction model by assuming equal electric field amplitudes between both pulses and rewriting the pump field annihilation operator as $\hat{b}_p = \frac{1}{\sqrt{2}} \left(\hat{b}_p(t) + \hat{b}_p(t-\tau)\right)$, acting on a photon from the pulse at time t or $t-\tau$, respectively. Eq. (5.3) modifies to:

$$|\Psi(t)\rangle = \sum_{n=0}^{\infty} \frac{|g|^n}{n!} \left(a_H^\dagger a_V^\dagger\right)^n |0\rangle \left(\frac{1}{\sqrt{2}} \left(\hat{b}_p(t) + \hat{b}_p(t-\tau)\right)\right)^n |p\rangle \tag{5.4}$$

[2] Here in the classical limit electric field amplitudes

[3] Here the interaction parameter τ from eq. (6.13) has been substituted by the symbol g' in order to avoid confusion with the time separation between pumping pulses, also referred to as τ.

Further simplification is achieved by utilising the process strength once more: Since the efficiency of the down-conversion process is rather small, scaling with $\approx 10^{-12} \cdot I_{\text{pump}}$, the depletion of the pumping beam can be neglected. With a total average pumping power during this measurement of $\approx 2.3\,W$ at a repetition rate of $\approx 80\,MHz$, a pulse energy of $E_{\text{pulse}} = \frac{1}{2} \cdot \frac{2.3\,W}{80\,MHz} \approx 29\,nJ$ is obtained, corresponding to an approximate number of $n_{\text{pulse}} = \frac{E_{\text{pulse}}\lambda}{hc} \approx 57 \cdot 10^{10}$ pump photons per pulse of which about[4] $57 \cdot 10^{10} \cdot 10^{-12} = 0.057$ are converted, so roughly only a small portion of the pulses, propagating through the crystal, takes part in the frequency conversion. Therefore the pump field can comfortably be treated classically, resulting in $b_p(t)|p\rangle = E_0(t)$ and $b_p(t-\tau)|p\rangle = E_0(t-\tau)$, whereby $E_0(t')$ is the complex valued electric field amplitude functions of a classical ultra-short laser pulse at time t'. Hence eq. (5.4) reduces to:

$$|\Psi(t)\rangle = \sum_{n=0}^{\infty} |g|^n |n_H, n_V\rangle_{SPDC} \left(\frac{1}{\sqrt{2}} \left(E_0(t) + E_0(t-\tau) \right) \right)^n \tag{5.5}$$

In the experiment, the $2n$-photon coincidence count rate gets measured by the aid of the linear optical set-up (see section 3.3), applied as a photon counting unit. The language of quantum mechanics translates this into the expectation value of the photon number within the SPDC state $|n_H, n_V\rangle_{\text{SPDC}}$, evaluated by the conditional number operator, which for a four photon coincidence has the form ([101]) $\langle : \hat{a}_H^\dagger \hat{a}_V^\dagger \hat{a}_V \hat{a}_H : \rangle$. For detecting n signal and idler photons, we obtain the expression

$$\begin{aligned}
\langle : \hat{n}_H, \hat{n}_V : \rangle &= \langle \Psi_n(t) | \hat{a}_H^\dagger \hat{a}_V^\dagger \hat{a}_V \hat{a}_H | \Psi_n(t) \rangle \\
&= |\alpha'|^2 \underbrace{\langle n_H, n_V | \hat{a}_H^\dagger \hat{a}_V^\dagger \hat{a}_V \hat{a}_H | n_V, n_H \rangle}_{= n_{\text{SPDC pairs}}} \left(E_0^*(t) + E_0^*(t-\tau) \right)^n \cdot \left(E_0(t) + E_0(t-\tau) \right)^n \\
&= |\alpha'|^2 n_{\text{SPDC pairs}} | \left(E_0(t) + E_0(t-\tau) \right)^n |^2
\end{aligned} \tag{5.6}$$

whereby α' is a proportionality constant, including g and factors of $\frac{1}{\sqrt{2}}$, $n_{\text{SPDC pairs}}$ represents the number of photon pairs and $|\Psi_n(t)\rangle$ is state resulting from the n^{th} order SPDC emission, given by

$$|\Psi_n(t)\rangle = |g|^n |n_H, n_V\rangle_{SPDC} \left(\frac{1}{\sqrt{2}} \left(E_0(t) + E_0(t-\tau) \right) \right)^n$$

So far, all down-conversion photons have been assumed within the same frequency mode. This is clearly oversimplified as, due to the phase matching condition[5], in SPDC an entire continuum of down-converted photons is generated, which is also highly correlated in its wavelength and momentum degree of freedom (see [101], [102]). Including now all SPDC wavelengths possible, the annihilation and creation operators for signal and idler have to be rewritten as[6] ([101])

$$\hat{a}_{H,V}^{(\dagger)} \to \sum_{\omega_{H,V}} \hat{a}_{H,V}^{(\dagger)}(\omega_{H,V}) \underset{\text{continuum}}{\longrightarrow} \int_{\omega_{H,V}} d\omega_{H,V} \hat{a}_{H,V}^{(\dagger)}(\omega_{H,V}).$$

Furthermore we have only allowed for pump photons at a certain point in time within the pumping pulses. Since these have a certain duration, referred to as τ_p, all times $t' \in \left[\frac{-\tau_p}{2}, \frac{+\tau_p}{2} \right]$ have to be included as well, resulting in an integration over t'. In our model for the autocorrelation, we will only treat isolated optical pulses, that is to say no pulse trains of $80\,MHz$ repetition rate are considered. Therefore the integration boundaries of t' can be extended to $\pm\infty$. All these changes plugged into eq. (5.6) yield the following expression[7]:

[4] Assuming a non-linear conversion efficiency of $\chi^{(2)} \sim 10^{-12}$.

[5] See the discussion in subsec. 5.3.3 later on in this chapter.

[6] Different pump and emission directions are neglected here, as the former are relevant for phase matching, which we considered as fulfilled here for all contributing wavelengths $\omega_{H,V}$, and the latter determine the spatial distribution of SPDC photons, which is of no concern due to its fixation be the SM fibre coupling (see section 3.3).

[7] The double integral stems from the presence of $a_{H,V}$ and $a_{HV}^\dagger$ in eq. (5.6).

$$\begin{aligned}\langle :\hat{n}_H,\hat{n}_V: \rangle &\sim \underbrace{\int_{\omega_H}\int_{\omega_H}\langle n_H(\omega_H)\rangle d\omega_H\, d\omega_H}_{S(\omega_H)} \cdot \underbrace{\int_{\omega_V}\int_{\omega_V}\langle n_V(\omega_V)\rangle d\omega_V\, d\omega_V}_{S(\omega_V)} \cdot \int_{-\infty}^{+\infty} |\left(E_0(t')+E_0(t'-\tau)\right)^n|^2 dt' \\ &= \underbrace{\int_{\omega_H} S(\omega_H)d\omega_H \cdot \int_{\omega_V} S(\omega_V)d\omega_V}_{\sim n^{\text{total}}_{\text{order n SPDC}}} \cdot \int_{-\infty}^{+\infty} |\left(E_0(t')+E_0(t'-\tau)\right)^n|^2 dt' \\ &= n^{\text{total}}_{\text{order n SPDC}} \cdot \int_{-\infty}^{+\infty} |\left(E_0(t')+E_0(t'-\tau)\right)^n|^2 dt' \end{aligned} \tag{5.7}$$

whereby $S(\omega_s)$ and $S(\omega_i)$ represent the respective spectra of the signal and idler photons, and $n^{\text{total}}_{\text{order n SPDC}}$ is the total number of down-conversion pairs in the n^{th} order emission, including all signal and idler wavelengths possible[8].
The only relevant term for us here is the second one in the above expression, which results from the pulsed temporal structure of the pump. We can infer by comparison with eq. (5.1) that it constitutes the numerator of the n^{th} order autocorrelation signal. If one now normalises eq. (5.7) by the sum of the background signals, either at time t and $t-\tau$, obtained for a single pulse only, i.e. $\langle :\hat{n}_H,\hat{n}_V: \rangle(t) \sim n^{\text{total}}_{\text{order n SPDC}} \cdot \int_{-\infty}^{+\infty} |E_0^n(t)|^2 dt'$ and $\langle :\hat{n}_H,\hat{n}_V: \rangle(t-\tau) \sim n^{\text{total}}_{\text{order n SPDC}} \cdot \int_{-\infty}^{+\infty} |E_0^n(t-\tau)|^2 dt'$, an expression equal to eq. (5.1) is obtained

$$\begin{aligned}\frac{\langle :\hat{n}_H,\hat{n}_V: \rangle(t,t-\tau)}{\langle :\hat{n}_H,\hat{n}_V: \rangle(t)+\langle :\hat{n}_H,\hat{n}_V: \rangle(t-\tau)} &= \frac{\zeta \cdot n^{\text{total}}_{\text{order n SPDC}} \cdot \int_{-\infty}^{+\infty} |\left(E_0(t)+E_0(t-\tau)\right)^n|^2 dt'}{\zeta \cdot n^{\text{total}}_{\text{order n SPDC}} \cdot \left(\int_{-\infty}^{+\infty} |\left(E_0(t)\right)^n|^2 dt' + \int_{-\infty}^{+\infty} |\left(E_0(t-\tau)\right)^n|^2 dt'\right)} \\ &= \frac{\int_{-\infty}^{+\infty} |\left(E_0(t)+E_0(t-\tau)\right)^n|^2 dt'}{\int_{-\infty}^{+\infty} |\left(E_0(t)\right)^n|^2 dt' + \int_{-\infty}^{+\infty} |\left(E_0(t-\tau)\right)^n|^2 dt'} \\ &= g_n(\tau), \end{aligned} \tag{5.8}$$

where the "=" sign can be used as the additional proportionality factors ζ, the photon count rate is also subject to[9], drop out. If we now furthermore consider, that the count rates

$$\langle :\hat{n}_H,\hat{n}_V: \rangle(t) + \langle :\hat{n}_H,\hat{n}_V: \rangle(t-\tau) = 2 \cdot \langle :\hat{n}_H,\hat{n}_V: \rangle(t)$$

are contained in an autocorrelation measurement already for pulse separation values $t \gg \tau_{\text{pulse}}$, i.e. outwith the pulses' interference region, our ability to record an autocorrelation curve is certified by eq. (5.8). The last expression (5.8) tells us how to evaluate the recorded data. This is done by normalisation of all data points to the average value of count rates at positions far outside the pulses interference region.
Importantly, we can infer from eq. (5.8) the unique ability, to infer all different orders n in the interferometric autocorrelation signal[10] from the down-conversion process simultaneously, with the specific order defined by the chosen number of observed photon pair coincidences. This feature is to be contrasted with the commonly applied SHG autocorrelation measurements, which only enables access to the second order g_2-function in their standard set-up. However, since expression (5.8) is only valid in the low pumping power limit with $g' \ll 1$, the strength of higher order SPDC pair emissions is rather weak as we will see in the course of subsec. 6.3.2.

5.2 Theory on correlation functions of first and second order

Within the following part of this chapter the necessary correlation functions and related expressions will be derived. It will be dealt with first and second order autocorrelation, whereby focus is placed on our particular experimental situation. Furthermore the information retrievable in both cases shall be examined in a little bit more detail, especially with respect to the correspondence between first order

[8] Since the aforementioned spectra have been introduced artificially into the discussion, the reader might want to refer to a more thorough analysis of these contributions in reference ([101]).
[9] Such are e.g. the collection and coupling efficiency into the SM fibre (see section 3.3 and fig. 5.6) and the distribution probability of four photons into four distinct spatial modes in the linear optical set-up (see fig. 3.3).
[10] See subsec. 5.2.3 for details.

correlation and pulse spectra as well as regarding the difference between intensity and interferometric autocorrelations.

5.2.1 First order correlations

General form of first order correlation The first order correlation function is proportional to the intensity yielded by the linear superposition of the electric fields from two optical pulses, separated in time by τ with respect to one another. Mathematically spoken, $g_1(\tau)$ is:

$$g_1(\tau) = \frac{\int_{-\infty}^{\infty} |E_1(t) + E_2(t-\tau)|^2 dt}{\int_{-\infty}^{\infty} |E_1(t)|^2 dt + \int_{-\infty}^{\infty} |E_2(t-\tau)|^2 dt}. \tag{5.9}$$

This expression is very well known to represent interference of first order ([84]), thus no non-linear effect is needed in the context of its measurement and it can e.g. just be recorded by observing the output of a standard interferometer with a linear detector[11].
It is now important to consider the situation of having two electrical fields differing in their respective amplitude, i.e. $|E_1(t)| \neq |E_2(t)|$. As it will turn out, during discussing the implementation of the pulse length measurement (section 5.3), we will be dealing with a non ideal interference visibility of $V \leq 1$. This degradation leads to non perfect interference. Hence it is advantageous to rewrite the electric field amplitudes of the overlapping pulses according to

$$E_1(t) = a \cdot E'(t) \tag{5.10}$$
$$E_2(t-\tau) = b \cdot E'(t-\tau), \tag{5.11}$$

with $a, b \in \mathbb{R}$. Herein $E'(t)$ and $E'(t-\tau)$ represent the same arbitrary pulse amplitude centred at two different times t, $t-\tau$. Furthermore real electric fields shall be assumed here, i.e. $E_1(t) = E_1^*(t)$ and $E_2(t-\tau) = E_2^*(t-\tau)$, since they are the appropriate quantities for future comparisons with experimental data. The $g_1(\tau)$-function can thus be expressed as:

$$\begin{aligned} g_1(\tau) &= \frac{\int_{-\infty}^{\infty} |E_1(t) + E_2(t-\tau)|^2 dt}{\int_{-\infty}^{\infty} |E_1(t)|^2 dt + \int_{-\infty}^{\infty} |E_2(t-\tau)|^2 dt} \\ &= 1 + \frac{2\int_{-\infty}^{\infty} E_1(t)E_2(t-\tau)dt}{\int_{-\infty}^{\infty} E_1(t)^2 dt + \int_{-\infty}^{\infty} E_2(t-\tau)^2 dt} \\ &= 1 + \frac{2ab\int_{-\infty}^{\infty} E'(t)E'(t-\tau)dt}{a^2\int_{-\infty}^{\infty} E'(t)^2 dt + b^2\int_{-\infty}^{\infty} E'(t-\tau)^2 dt} \\ &\overset{(*)}{=} 1 + \frac{2ab}{a^2+b^2} \cdot \underbrace{\frac{\int_{-\infty}^{\infty} E'(t)E'(t-\tau)dt}{\int_{-\infty}^{\infty} E'(t)^2 dt}}_{=:(**)} \end{aligned} \tag{5.12}$$

For computing the denominator, the equality between $\int_{-\infty}^{\infty} E'(t)^n dt$ and $\int_{-\infty}^{\infty} E'(t-\tau)^n dt$ has been used, which becomes obvious by substitution:

$$\underbrace{\int_{-\infty}^{\infty} E'(t-\tau)^n dt}_{\text{Subs:}t'\to t-\tau;dt\to dt'=\frac{dt'}{dt}dt=dt'} = \int_{-\infty}^{\infty} E'(t')^n dt'. \tag{5.13}$$

Indeed, in the case of equal pulse amplitudes $a = b$, the prefactor in front of the term $(**)$ in eq. (5.12) reduces to unity and the commonly stated expression for normed first order interference is obtained ([110], [113]). For recording the $g_1(\tau)$-function in our experiment, there are several opportunities offered by placing an interferometer in front of the enhancement resonator[12]: On the one hand, the intensity can be measured directly, e.g. by monitoring the signal with a photodiode or by logging the power level inside the resonator. On the other hand the SPDC process also provides an appropriate means, since down-conversion of a single UV pumping photon generates two infra-red photons. These single photon

[11] which is also done in our measurement, see fig. 5.6
[12] see fig. 5.6

pair processes are linear in the pump field amplitude (see eqs. (5.5) and (5.8)), and can therefore be associated with a certain pulse, providing a first order interference signal as well. In the course of the experiment all three possible methods have been applied to gain the $g_1(\tau)$-function.
Its evaluation however demands the assumption of a particular underlying pulse shape, whereby we choose in this respect to follow the most widespread approach and presume our laser pulses to be either Sech- or Gauss-like. The $g_1(\tau)$-functions for both pulse models shall consequently be calculated in the following.

$g_1(\tau)$ for Gaussian pulses In the case of Gaussian pulses, the electric field distribution for both interfering pulses is given by:

$$E^{\text{Gauss}}(t) = E_{1,2} \cdot \exp\left(\frac{-t^2}{2\left(\Delta t\right)^2}\right) \cdot \cos\left(\omega_0 t\right) \tag{5.14}$$

Within this function the pulse envelope has conveniently been centred around zero pulse delay and any additional temporal phase has been neglected since it does not influence the first order correlation function, as will be shown later in subsec. 5.2.2. Plugging the pulse model (5.14) into eq. (5.12), the Gaussian $g_1(\tau)$-correlation function can be gained by integration of the term $(**)$. The result can e.g. be found in ref. ([110]), leaving us with a first order correlation for Gauss-pulses of:

$$g_1^{\text{Gauss}}(\tau) = 1 + \frac{2ab}{a^2+b^2} \cdot \exp\left(\frac{-\tau^2}{4\left(\Delta t\right)^2}\right) \cdot \cos\left(\omega_0 \tau\right). \tag{5.15}$$

As we will see during the discussion about the circumstances for the actual measurement in section 5.3, only the values at constructive and destructive interference will be important for data evaluation, wherefore the oscillating term $\cos\left(\omega_0\tau\right)$ can be taken at its extrema and set to ± 1, reducing eq. (5.15) to the proper $g_1(\tau)$ fitting functions

$$g_1^{\text{Gauss}}(\tau) = 1 \pm \frac{2ab}{a^2+b^2} \cdot \exp\left(\frac{-\tau^2}{4\left(\Delta t\right)^2}\right), \tag{5.16}$$

whereby the minus sign applies for interference minima and the plus sign has to be taken for fitting interference maxima. A graphical representation of first order interference (eq. (5.15)) and its envelopes (eq. (5.16)) is given in fig. 5.1, which depicts perfect interference, i.e. $a = b \Rightarrow \frac{2ab}{a^2+b^2} = 1$, on its left hand side. On the right hand side a situation for a reduced interference with parameters $a = 1, b = 0.477$ is displayed, which corresponds to the average value of all b parameters, received during the actual measurement. The interference visibility, defined by

$$V = \frac{(a+b)^2 - (a-b)^2}{(a+b)^2 + (a-b)^2} = \frac{2ab}{a^2+b^2} \tag{5.17}$$

and discussed more thoroughly in terms of its physical implications within the experimental part of this chapter, is $V = 0.777$ for this set of electric field amplitude parameters.

$g_1(\tau)$ for Sech pulses Assuming a Sech-shape for the underlying UV pulses requires an electric field model of:

$$E_1^{\text{Sech}}(t) = E_{1,2} \cdot \operatorname{sech}\left(\frac{t}{\Delta t}\right) \cdot \cos\left(\omega_0 t\right) \tag{5.18}$$

The expression can be inserted into eq. (5.12) as well, and by solving the relevant interference integral $(**)$, one ends up with the $g_1(\tau)$-function for Sech-pulses ([110]):

$$g_1^{\text{Sech}}(\tau) = 1 + \frac{2ab}{a^2+b^2} \cdot \frac{\frac{\tau}{\Delta t}}{\sinh\left(\frac{\tau}{\Delta t}\right)} \cdot \cos\left(\omega_0 \tau\right) \tag{5.19}$$

Once more, only the points at constructive and destructive interference will become important, simplifying eq. (5.19) to:

$$g_1^{\text{Sech}}(\tau) = 1 \pm \frac{2ab}{a^2+b^2} \cdot \frac{\frac{\tau}{\Delta t}}{\sinh\left(\frac{\tau}{\Delta t}\right)} \tag{5.20}$$

Both, the Sech-first order interference function (eq. (5.19)) and its envelope (eq. (5.20)), have also been plotted in fig. 5.1, again for perfect interference on the left and conditioned to the parameters $a = 1$

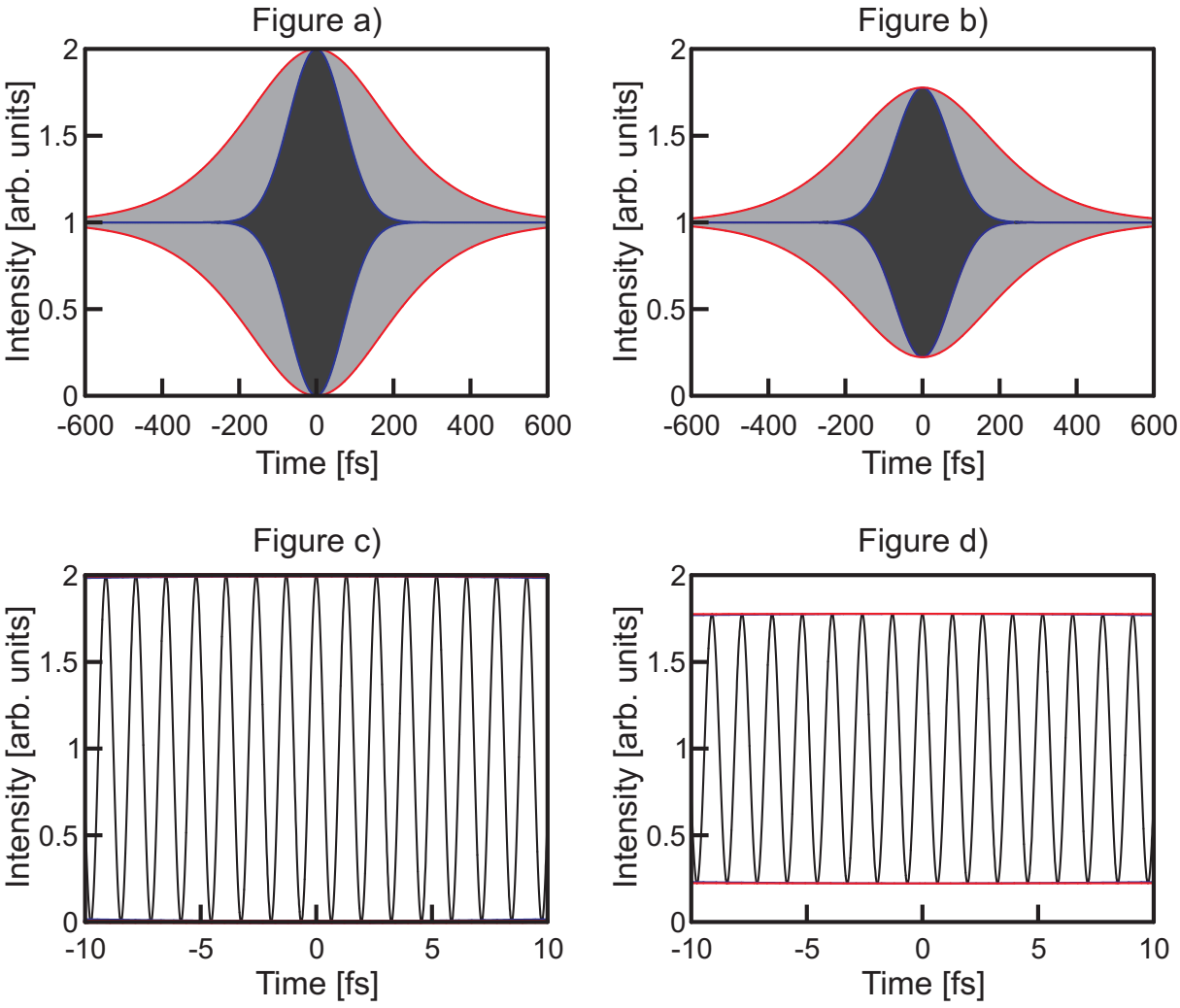

Figure 5.1: $g_1(\tau)$-correlation function (black curve) with envelopes for Gaussian pulses (blue curve) together with the full $g_1(\tau)$-function for Sech-pulses (grey curve) and its envelopes (red curve) for a value of $\Delta t = 100\,fs$. The left picture shows the situation of complete interference, the right one reduced interference. The upper row includes the entire interference region, whereas in the lower row an interval between $-10\,fs \leq \tau \leq +10\,fs$ has been cut out for the Gaussian $g_1(\tau)$-function, to allow spotting of the interference fringes.

and $b = 0.477$ on the right. We can observe from fig. 5.1 a peak-to background ratio of $2:1$ in the case of perfect interference between both pulses, deminishing to a lower value of $1+b:1 \Rightarrow 1.477:1$ for the degraded situation ($a = 1$, $b = 0.477$). It can furthermore be inferred that the interference pattern in both first order correlation functions (5.15) and (5.19) oscillates at the carrier frequency ω_0 of the electromagnetic fields involved (eqs. (5.14), (5.18)). Thus one can in principle yield the latter by measuring the width of the individual interference fringes, if a complete interferogram is available.

FWHM of the correlation functions and minimal pulse duration It is interesting to evaluate the full width at half maximum (FWHM) values for the $g_1^l(\tau)$-functions ($l \in \text{Sech}, \text{Gauss}$) and set them into a relation with the FWHM of the actual optical pulses in the time domain. This is because the FWHM pulse durations obtained from the $g_1^l(\tau)$-functions via the aforementioned connection constitute a measure for the minimum possible pulse duration allowed by the spectral content of the underlying pulses, as we will see in the upcoming discussion about the spectral information inherent in the first order interference.
To establish this relation, it has to be defined what exactly is meant by pulse duration in the first place: This work will follow the convention to name the FWHM of the envelope of the pulse's intensity distribution its pulse duration[13]. The pulse duration is therefore strictly defined by the value $\tau^{FT,l}$, which satisfies the following conditions:

$$I_{\text{env}}^{\text{Gauss}}(\pm\frac{\tau^{FT,\text{Gauss}}}{2}) = a^2 \exp\left(-\frac{(\pm\tau^{FT,\text{Gauss}}/2)^2}{(\Delta t)^2}\right) \stackrel{!}{=} \frac{a^2}{2} \tag{5.21}$$

and

$$I_{\text{env}}^{\text{Sech}}(\pm\frac{\tau^{FT,\text{Sech}}}{2}) = a^2 \text{sech}^2\left(\frac{\pm\tau^{FT,\text{Sech}}}{2\Delta t}\right) \stackrel{!}{=} \frac{a^2}{2} \tag{5.22}$$

Solving the above equations for $\tau^{FT,l}$ yields the dependence between pulse duration and width parameter Δt for the respective pulse model:

$$\tau^{FT,\text{Gauss}} = 2\sqrt{\ln 2}\cdot\Delta t \tag{5.23}$$

$$\tau^{FT,\text{Sech}} = 2\text{arcsech}\left(\frac{1}{\sqrt{2}}\right)\cdot\Delta t. \tag{5.24}$$

In an analog fashion, the FWHM values $\Delta\tau_{g1}^{FWHM,l}$ for the $g_1^l(\tau)$-correlation functions (eqs. (5.16) and (5.20)) can be figured out as a function of Δt ,defined by the conditions:

$$g_1^{\text{Gauss}}\left(\pm\frac{\Delta\tau_{g1}^{FWHM,\text{Gauss}}}{2}\right) = 1+\frac{2ab}{a^2+b^2}\cdot\exp\left(\frac{-(\pm\Delta\tau_{g1}^{FWHM,\text{Gauss}}/2)^2}{4\,(\Delta t)^2}\right) \stackrel{!}{=} 1+\frac{1}{2}\cdot\frac{2ab}{a^2+b^2} \tag{5.25}$$

$$g_1^{\text{Sech}}\left(\pm\frac{\Delta\tau_{g1}^{FWHM,\text{Sech}}}{2}\right) = 1+\frac{2ab}{a^2+b^2}\cdot\frac{\frac{\pm(\Delta\tau_{g1}^{FWHM,\text{Sech}})}{2\Delta t}}{\sinh\left(\frac{\pm(\Delta\tau_{g1}^{FWHM,\text{Sech}})}{2\Delta t}\right)} \stackrel{!}{=} 1+\frac{1}{2}\cdot\frac{2ab}{a^2+b^2}, \tag{5.26}$$

in which only the functions for interference maxima have been considered as the minima conditions are redundant. Since these expressions are analytically solvable with all parameters a and b dropping out, the values for $\Delta\tau_{g1}^{FWHM,l}$ are independent of the choices for $\{a,b\}$ and hence of the interference visibility. One yields constants $\alpha_{g1}^l = \frac{\Delta\tau_{g1}^{FWHM,l}}{\Delta t}$ with numbers of:

[13] Although there are other definitions in use, the chosen one is most suitable for our experimental situation and furthermore allows to compare results with standard textbooks, such as ([57], [58]). However this FWHM definition is particularly poor for a situation with a lot of third order dispersion, TOD, on top of the pulses to be measured. Since TOD causes pulses to be split up into a major (mother-) pulse and some adjacent "sidepulses" at the leading or trailing edge, successively decreasing in their intensity, the FWHM is not unambiguously defined anymore. That is to say, it depends whether such a sidepulse exceeds half the intensity of the motherpulse for it to be considered for the FWHM of the pulse as well (see ([111]) for a more thorough discussion). Obviously it makes a major difference in the numerical outcome if such an additional pulse is included or not, spoiling the applicability of the FHWM pulse duration definition. Since TOD and all higher order dispersion contributions are negligible for our set-up, as we have seen in section 2.1.5, the FWHM definition is sensible.

$$\alpha_{g1}^{\text{Gauss}} = 4 \cdot \sqrt{\ln 2} \tag{5.27}$$

$$\alpha_{g1}^{\text{Sech}} = 4.35464 \tag{5.28}$$

Combining both sets of factors (eqs. (5.23), (5.24) and (5.27), (5.28)) provides us with the desired conversion factors $\gamma_{g1}^{l} = \frac{\tau^{FT,l}}{\Delta\tau_{g1}^{FWHM,l}}$ between FWHM of the first order correlation functions $g_1^l(\tau)$, $\Delta\tau_{g1}^{FWHM,l}$, and the minimal possible pulse duration $\tau^{FT,l}$, which are both consequently independent of the interference visibility as well[14]:

$$\gamma_{g1}^{\text{Gauss}} = \frac{1}{2} \tag{5.29}$$

$$\gamma_{g1}^{\text{Sech}} = 0.4048 \tag{5.30}$$

One can recognise the Sech-shaped pulses to be generally shorter in time duration than their Gaussian counterparts, a property which solely stems from the different weighting between wing and central peak parts in both functions. The Gaussian has lower values for the former and is broader in the latter region, rendering its FWHM larger and accordingly the pulse duration computed thereof longer.
At this point, a potentially misleading nomenclature shall be pointed out. One might tend to refer to $\tau^{FT,l}$ as the coherence time of the pumping beam. This terminology will also be used in this work when dealing with the temporal indistinguishibility of SPDC photon pairs in subsection 6.2.2. Therefore usually the minimal pulse duration $\tau^{FT,l}$ of the SPDC photons is chosen as a decisive quantity, whereby the "coherence length" $\Delta x_{SPDC} = c \cdot \tau^{FT,l}$ has to be greater than the spacings between individually emitted pairs. However for mode locked laser pulses, the coherence time is defined by the inverse spectral width of each individual frequency comb mode within the pulse spectrum. These are on the order of time scales expected for conventional single mode cw lasers, e.g. $\tau_{\text{Coh}}^{CW} \approx 1\,ms \gg \tau^{FT,l}$, and by far longer than the pulse duration. As the phrase "coherence time" is therefore rather ambiguous, it will not be used during the determination of the UV pulse lengths and only taken up for the SPDC photon pairs to examine their indistinguishibility in chapter 6 later on.

5.2.2 Pulse spectra in connection with $g_1(\tau)$-functions

To receive the well known time-bandwidth products for short laser pulses and to furthermore shown the insensitivity of first order correlation functions to any phase terms, the linkage between $g_1(\tau)$ and the pulse spectra shall be investigated. Therefore we have to consider the Fourier transform connection between the time and frequency domain. By examination of eq. (5.12), it becomes clear that only the numerator in term $(**)$ results in a non-constant contribution under Fourier transformation[15]. All constant parts are neglected from now on, since the spectral data will be normalised for its analysis anyway. Focussing on the relevant part we get:

$$FT\{\underbrace{\int_{-\infty}^{\infty} E(t) \cdot E^*(t-\tau)dt}_{\text{Convolution}}\} = FT\{(E \otimes E^*)(t)\} = FT\{E(t)\} \cdot FT\{E^*(t)\}, \tag{5.31}$$

where use was made of the interference integral being the convolution between $E(t)$ and its complex conjugate as well as the Fourier transform (FT) of a convolution of two functions being equal to the product of the Fourier transforms of each individual function ([103]).
The FT of the electric field in the time domain results in the spectral amplitude $FT\{E(t)\} = E(\omega)$ and $FT\{E^*(t)\} = E^*(\omega)$ reducing eq. (5.31) to the spectral intensity[16] of the pulse:

$$S(\omega) = |E(\omega)|^2 = E(\omega) \cdot E^*(\omega) = FT\{E(t)\} \cdot FT\{E^*(t)\} \tag{5.32}$$

We can now see, that any phase contributions, resulting e.g. from GVD or TOD effects, cannot affect the pulse spectrum, as they show up by an additional spectral phase factor $E(\omega) = E_0(\omega) \cdot \exp(-i\phi(\omega))$ in the frequency domain, cancelling out in eq. (5.32). Moreover they do not enter the $g_1(\tau)$-function either, since there is a strict Fourier transform connection between $S(\omega)$ and $g_1(\tau)$. We can now use eq. (5.32) to calculate the expected theoretical spectral functions for both of our pulse models (eq. (5.14) and (5.18)). This will enable us to later compare the spectral information in the first order correlation measurements with the directly recorded UV spectra inside the cavity.

[14] This feature will turn out to be different for the second order correlation function
[15] Assigned as FT in the following.
[16] i.e. the spectrum measured by any spectrometer

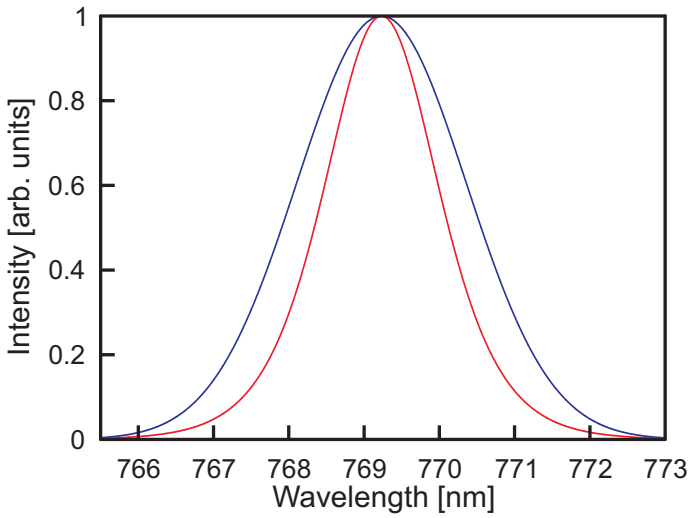

Figure 5.2: Theoretical spectral functions for Gaussian pulses (blue lines) and Sech pulses (red lines) with a value of $\Delta t = 100\,fs$. The spectral functions, given by eqs. (5.34) and (C.3), which correspond to eqs. (5.35) and (5.37) within the plot range, are shown for positive frequencies, relevant for the subsequent comparison with measured spectra.

Spectra for Gauss-pulses For the Gaussian pulse spectrum, $E^{\text{Gauss}}(t) = a \cdot \exp\left(\frac{-t^2}{2(\Delta t)^2}\right) \cdot \cos(\omega_0 t)$ is Fourier transformed as stated in the appendix C.1.1, yielding:

$$FT\{E(t)\} = \sqrt{\frac{\pi}{2}} a\Delta t \left(\exp\left(-\frac{1}{2}(\Delta t)^2(\omega+\omega_0)^2\right) + \exp\left(-\frac{1}{2}(\Delta t)^2(\omega-\omega_0)^2\right)\right). \tag{5.33}$$

Due to having real field amplitudes, i.e. $E(t) = E^*(t)$, the FT of the complex conjugate field in eq. (5.32) results in the same expression as eq. (C.1), only swapping the parameter a for b. However, in the following we will always be dealing with normalised spectra, wherefore the scaling factor, $\sqrt{\frac{\pi}{2}} a\Delta t$ or $\sqrt{\frac{\pi}{2}} b\Delta t$, will be dropped and angular frequencies shall be transformed into proper frequencies by $\omega = 2\pi\nu$. With these replacements the Gaussian pulse spectrum turns out to be

$$\begin{aligned} S(\nu)^{\text{Gauss}} &= \left(\exp\left(-2\pi(\Delta t)^2(\nu+\nu_0)^2\right) + \exp\left(-2\pi(\Delta t)^2(\nu-\nu_0)^2\right)\right)^2 \\ &= \exp\left(-4\pi^2(\Delta t)^2(\nu+\nu_0)^2\right) + \exp\left(-4\pi^2(\Delta t)^2(\nu-\nu_0)^2\right) + 2\exp\left(-4\pi^2(\Delta t)^2(\nu^2+\nu_0^2)^2\right) \end{aligned} \tag{5.34}$$

which has been plotted for positive frequencies only in fig. 5.2. Eq. (5.34) comprises three contributions, whereby the first term is centred around the negative and the second term around the positive value of the carrier frequency ν_0. The former' appearance is not surprising as real functions for the electric fields have been utilised in the calculation ([103]); nevertheless in the measurement only the positive frequency parts are recorded, rendering the first term negligible for later comparison with experimental spectra. The third term is proportional to a sum of optical frequencies to the power of four times the $1/e$ pulse duration squared. With optical frequencies relevant for our experiment of $\nu \approx \nu_0 \pm 3\,THz$, $\nu_0 \sim 770\,THz$ (corresponding to a UV pumping pulse centred at $\lambda_0 = 390\,nm$) and a $1/e$ width of $\Delta t \approx 100\,fs$, this term results in a number $\exp(-9 \cdot 10^5) \approx 0$ and can hence be neglected as well. So the Gaussian spectral function for the decisive positive frequency part simplifies to

$$S(\nu)^{\text{Gauss}} = \exp\left(-4\pi^2(\Delta t)^2(\nu-\nu_0)^2\right), \tag{5.35}$$

providing the functional dependence shown in blue in fig. 5.2. It shall be regarded as the appropriate theoretical spectrum for future discussions.

Spectra for Sech-pulses The analogous computation for the Sech-pulse model $E^{\text{Sech}}(t) = a \cdot \text{sech}\left(\frac{t}{\Delta t}\right) \cdot \cos(\omega_0 t)$ can be found in the appendix C.1.1 and solely the result shall be stated here, which provides a spectral function of:

$$S(\nu)^{\mathrm{Sech}} = \frac{1}{\cosh^2\left(\pi^2\Delta t(\nu+\nu_0)\right)} + \frac{1}{\cosh^2\left(\pi^2\Delta t(\nu-\nu_0)\right)} + \frac{2}{\cosh^2\left(\pi^2\Delta t\nu\right)+\cosh^2\left(\pi^2\Delta t\nu_0\right)} \tag{5.36}$$

The first term in eq. (C.3) is centred around negative carrier frequencies and is therefore unimportant. The third term carries a denominator containing a sum of two cosh functions. Their arguments can once more be estimated by assuming the adequate variable values $\nu \approx \nu_0 \approx 770\,THz$ and $\Delta t \approx 80\,fs$, which lead to numbers around $2\pi^2\Delta t\nu \approx 1200$. Consequently $\frac{1}{\cosh(2\pi^2\Delta t\nu)} \approx \frac{1}{\cosh(2\pi^2\Delta t\nu_0)} \to 0$ and we can forget about the contribution from the third term, ending up with a normalised theoretical spectral function for Sech-pulses of

$$S(\nu)^{\mathrm{Sech}} = \mathrm{sech}^2\big(\pi^2\Delta t(\nu-\nu_0)\big) \tag{5.37}$$

shown as the red curve in fig. 5.2. A very nice feature for both pulse models is consequently the equivalence between the pulse shapes in the time domain, eqs. (5.14), (5.18), and the spectral shapes in frequency domain, eqs. (5.35), (5.37). While this is commonly known to be true for Gaussian pulses it does hold for Sech pulses as well.

FWHM of spectra and time-bandwidth-products As a last step in the analysis of the first order correlation function, the conversion factors connecting the FWHM values of the spectra with the width parameter Δt for each pulse form can be worked out. Referring to the spectral FWHM as $\Delta\nu_l$, these are computed in an analogous fashion to the numbers for the pulse duration (eqs. (5.29), (5.30)) and are defined by the conditions:

$$S^{\mathrm{Gauss}}\left(\frac{\pm\Delta\nu_{\mathrm{Gauss}}}{2}\right) = \exp\left(-4\pi^2\left(\Delta t\right)^2\left(\pm\Delta\nu_{\mathrm{Gauss}}/2\right)^2\right) \stackrel{!}{=} \frac{1}{2}$$

$$S^{\mathrm{Sech}}\left(\frac{\pm\Delta\nu_{\mathrm{Sech}}}{2}\right) = \mathrm{sech}^2\big(\pi^2\Delta t(\pm\Delta\nu_{\mathrm{Sech}}/2)\big) \stackrel{!}{=} \frac{1}{2}$$

Evaluation provides the desired expressions:

$$\Delta\nu_{\mathrm{Gauss}} = \frac{\sqrt{\ln 2}}{\pi\Delta t} \tag{5.38}$$

$$\Delta\nu_{\mathrm{Sech}} = \frac{2\cdot\mathrm{arcsech}(1/\sqrt{2})}{\pi^2\Delta t} \tag{5.39}$$

If the constants connecting the minimal pulse duration $\tau^{FT,l}$ with Δt (eqs. (5.23), (5.24)) are utilised, we can derive the well known time-bandwidth-products of short laser pulses, connecting the FT limited pulse duration with the spectral width for a particular pulse shape ([58]):

$$\Delta\nu_{\mathrm{Gauss}}\cdot\tau^{FT,\mathrm{Gauss}} = \frac{2\ln 2}{\pi} = 0.441 \tag{5.40}$$

$$\Delta\nu_{\mathrm{Sech}}\cdot\tau^{FT,\mathrm{Sech}} = \frac{4\cdot\mathrm{arcsech}^2(\frac{1}{\sqrt{2}})}{\pi^2} = 0.315 \tag{5.41}$$

It is therefrom also clear, why the time period $\tau^{FT,l}$ defines the minimum possible duration of a pulse. By the Fourier transform connection and the time-bandwidth products one can directly infer that $\tau^{FT,l}$ is the length of the pulse, built up by coherent superposition of all frequency modes contained within the pulse spectrum. Any phases added onto certain frequency comb teeth, e.g. due to dispersion, disturbs this constructive interference and can consequently only temporally broaden the pulse ([57]). However by aid of eq. (5.31) it has been proven that these phases do not contribute to the spectral function for the pulse and thus do not affect $\Delta\nu_l$. Obeying the time-bandwidth products (eqs. (5.40), (5.41)), the FT limited pulse duration $\tau^{FT,l}$ is just stipulated by a pulse shape dependent constant times $\Delta\nu_l$ and therefore also uninfluenced by any elongation.
Nonetheless this argumentation quickly exemplifies the limitations of the information regarding the pulse duration extractable from the $g_1(\tau)$-function: We can certainly not rule out the presence of dispersion. So another means for determining the proper pulse duration, which includes effects originating from phase contributions, has to be applied to investigate the UV pumping pulses inside the enhancement resonator. It can be found in higher order correlation functions, i.e. $n > 1$ in eq. (5.1), whereby the interferometric autocorrelation function $g_2(\tau)$ will be of particular interest for us.

5.2.3 Second order correlation functions

We will now discuss the appropriate way to estimate the real duration of our UV intra-cavity pulses, which in principle includes all broadening effects from higher order dispersion[17]. However the down-side of all autocorrelation measurements is the impracticality to extract the apparent pulse shape from the experimental findings. Autocorrelation is thus only a useful method for determining the pulse duration, but cannot be applied for full pulse reconstruction, as proven in reference ([104]). Furthermore the reader shall be made aware of the existence of two rather different second order autocorrelation functions, namely the intensity and interferometric autocorrelation. While the former is easier to implement, it suffers the great disadvantage of the impossibility to determine pulse broadening due to temporal phases added onto the pulses. This serious downside renders it just as impractical for our purposes as the $g_1(\tau)$-function. Nevertheless it shall quickly be introduced at the beginning, especially to grasp a more thorough demonstration of the phase information loss during the cross-over between interferometric and intensity autocorrelation.

Intensity autocorrelation function The intensity autocorrelation function with background is defined as ([113])

$$G_2(\tau) = 1 + 2 \cdot \frac{\int_{-\infty}^{\infty} I(t) \cdot I(t-\tau) dt}{\int_{-\infty}^{\infty} (I(t))^2 dt}. \tag{5.42}$$

With background refers in this context to the simultaneous measurement of the autocorrelation signal produced by each individual beam itself together with the combined signal generated by the overlap of the pulses. From this definition one could be led to think that the insensitivity of $G_2(\tau)$ to any phase effects is already spotable, since these show up in the electric fields according to $E(t) = E_0(t) \exp(i\phi(t))$ and hence cancel out in the intensities $I(t) \sim E(t) \cdot E^*(t)$. However considering real fields, whose amplitudes can be written according to $E(t) = const. \cdot f(t) \cdot \cos(\omega_0 t + \phi(t))$, with $f(t) \in \mathbb{R}$, the entire situation is not as clear cut anymore and a proper prove is given later. Nevertheless the message remains, that $G_2(\tau)$-functions cannot detect dispersion effects.
For the two pulse models assumed for our experimental situation (eqs. (5.14) and (5.18)) the intensity autocorrelation function $G_2(\tau)$ for Gauss pulses turns out to be ([113])

$$G_2^{\text{Gauss}}(\tau) = 1 + 2 \cdot \exp\left(-\frac{\tau^2}{2 \cdot (\Delta t)^2}\right) \tag{5.43}$$

and for Sech pulse shapes one gets:

$$G_2^{\text{Sech}}(\tau) = 1 + 2 \cdot \frac{3\left(\frac{\tau}{\Delta t}\cosh\left(\frac{\tau}{\Delta t}\right) - \sinh\left(\frac{\tau}{\Delta t}\right)\right)}{\sinh^3\left(\frac{\tau}{\Delta t}\right)} \tag{5.44}$$

Both functions have been plotted in fig. 5.3 for a parameter value $\Delta t = 120\, fs$ with the Gaussian pulse case being drawn in blue and the Sech pulse case in red. The peak to background ratios for the $G_2(\tau)$ functions amounts to a maximum of $3:1$ for perfect overlap between both pulses in the non-linear medium. Less well adjusted pulse intersection only diminishes this number. It can thus be compared to the ratio from the interferometric autocorrelation, deduced subsequently, which yields for perfect pulse interference a value of $8:1$. For our experimental situation, we reach a degraded ratio of approximately $4.1:1$, which is mostly due to residual mode mismatch (see subsec. 5.3.4). Nevertheless it is clearly still larger than the maximum ratio achievable for intensity autocorrelations, which indicates interferometric stability. Furthermore the intensity autocorrelation does not show any interference oscillations as they are present in the $g_1(\tau)$- or $g_2(\tau)$-correlation functions (see figs. 5.1, 5.4). That stems from the requirement to particularly not have any stable interference during measurements of $G_2(\tau)$ and contributes to the major advantage of this type of autocorrelation, namely its simple experimental implementation. As it is extractable from eq. (5.42), just two delayable copies of the pulse to be measured have to be generated. Subsequently these have to impinge onto a non-linear medium, generating a signal proportional to their mutual intensity overlap, i.e. their convolution given by the integral in eq. (5.42). It must be assured though, that it is the intensity of both pulses the autocorrelation signal is subject to and not their electric field amplitudes. That is to say, the electric fields must not interfere with one another to enable

[17] For instance GVD. Since this dispersive effect results in varying propagation velocities for the different frequency parts of the pulse spectrum, leading to a divergence of these, it modifies the pulse carrier wavelength to increase or respectively decrease in its oscillation frequency (see ([111]) for detail). Such an alteration can be viewed as an imparted overtone, wherefore GVD is also referred to as chirp.

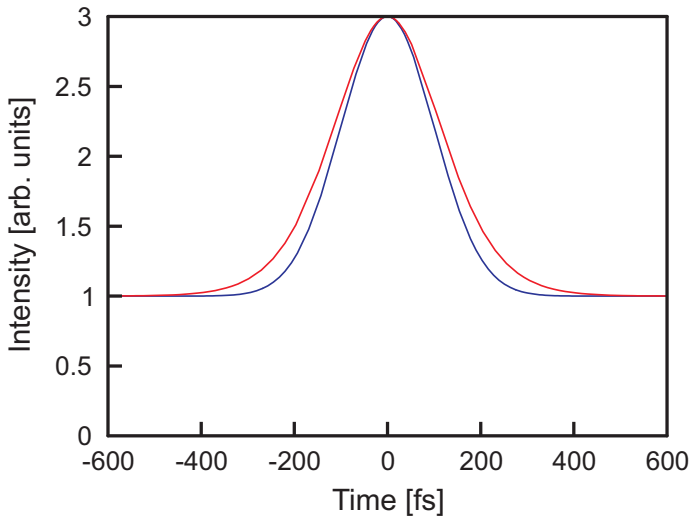

Figure 5.3: Theoretical intensity autocorrelation function with background for Gaussian pulses (blue curve) and Sech pulses (red curve). The width parameter Δt has been set to 120 fs for both cases and perfect pulse overlap has been assumed, providing a peak to background ratio of 3 : 1.

the measurement of the intensity autocorrelation. Possible experimental set-ups to measure the quantity $G_2(\tau)$ are presented in reference ([111]).

General form of the interferometric autocorrelation function In the course of the future discussion about the experimental set-up for the autocorrelation (see 5.3.1) we will realise a collinear geometry, with both pumping pulse copies $E(t)$ and $E(t-\tau)$ impinging onto the BBO crystal under the same angle, as required to observe the $g_2(\tau)$ correlation ([79]). Therefore the relevant quantity to be used is the interferometric autocorrelation with background, defined as ([110]):

$$g_2(\tau) = \frac{\int_{-\infty}^{\infty} |(E_1(t) + E_2(t-\tau))^2|^2 dt}{\int_{-\infty}^{\infty} |(E_1(t))^2|^2 dt + \int_{-\infty}^{\infty} |(E_2(t-\tau))^2|^2} \tag{5.45}$$

In order to determine it for Gaussian and Sech pulses, the expression above shall be simplified in the first place. Likewise to the derivation of the $g_1^I(\tau)$-functions, real electric field distributions are assumed and unequal amplitudes between both pulses, resulting in a degraded interference, are taken into account as well. Therefore the electric fields are:

$$E_1(t) = a \cdot E_0^{\text{Gauss/Sech}}(t) \cdot \cos(\omega_0 t + \phi_1(t)) = a \cdot E'(t) \tag{5.46}$$

$$E_2(t-\tau) = b \cdot E_0^{\text{Gauss/Sech}}(t-\tau) \cdot \cos(\omega_0 (t-\tau) + \phi_1(t-\tau)) = b \cdot E'(t-\tau) \tag{5.47}$$

whereby $t = 0$ has been set to the centre of pulse $E_1(t)$, the functions $E_0^{\text{Gauss/Sech}}(t')$ represent Gaussian or Sech pulse envelopes given by $E_0^{\text{Gauss}}(t') = \exp\left(-\frac{t'^2}{2(\Delta t)^2}\right)$ or $E_0^{\text{Sech}}(t') = \text{sech}\left(\frac{t'}{\Delta t}\right)$, respectively, and possible spectral phases $\phi(t')$ have been included this time as well. Inserting both expressions into eq. (5.45), the $g_2(\tau)$ function can be simplified. The detailed calculations are stated in the appendix C.1.2 and as a result

$$g_2(\tau) \overset{(*)}{=} 1 + 6 \cdot \frac{a^2 b^2}{a^4 + b^4} \cdot \underbrace{\frac{\int_{-\infty}^{\infty} E'(t)^2 E'(t-\tau)^2 dt}{2\int_{-\infty}^{\infty} E'(t)^4 dt}}_{=:(***)} + 4 \cdot \frac{ab^3 + a^3 b}{a^4 + b^4} \cdot \underbrace{\frac{\int_{-\infty}^{\infty} \left(E'(t)E'(t-\tau)^3 + E'(t)^3 E'(t-\tau)\right) dt}{2\int_{-\infty}^{\infty} E'(t)^4 dt}}_{=:(****)} \tag{5.48}$$

is yielded. Before proceeding on to compute the interferometric autocorrelation function for both pulse models, another assumption shall be made concerning the variable for the pulse width: Although $g_2(\tau)$ is sensitive to dispersive broadening, it is not possible to extract the underlying pulse form from the $g_2(\tau)$ measurement results ([104]). It is e.g. possible to multiply our chosen pulse shapes by Blaschke prod-

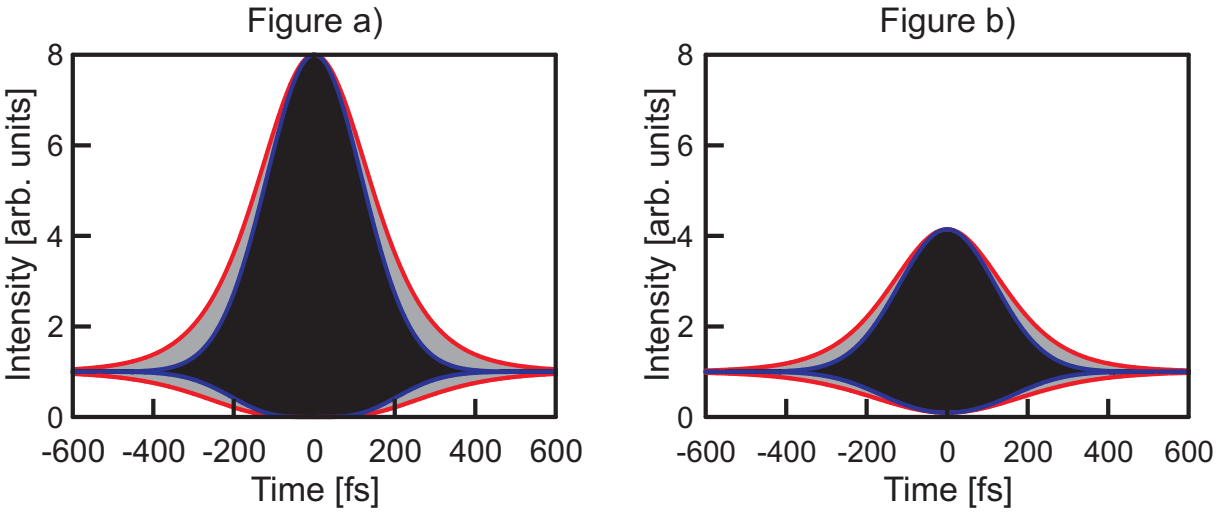

Figure 5.4: $g_2(\tau)$ correlation function for Gauss pulses (black line), with its envelopes (blue lines), and Sech pulses (grey line), with its envelopes (red lines), for a width parameter of $\Delta t = 110\,fs$. The left column represents a situation of perfect interference, $V = 1$, whereas the right column shows degraded interference, $V = 0.777$. The FWHM values $\Delta\tau_{g2}^{\text{Gauss}}$ and $\Delta\tau_{g2}^{\text{Sech}}$ are also included in green.

ucts[18]([108], [109]) and still retain the same $g_2(\tau)$-function. In terms of the pulse duration τ^l, retrieved from interferometric autocorrelation, will thus not distinguish between the contributions stemming from underlying pulse itself and others introduced by dispersive broadening. The phase elongation $\Delta\tau_{\text{dis}}(\phi(t))$ will therefore be included implicitly into the width parameter Δt in the pulse models, which of course now does not connect to the FT limited pulse duration anymore, resulting in the phase factors in eqs. (5.46) and (5.47) to be dropped.
It shall also be mentioned in this respect, that chirp effects deform the flanks of the interferometric autocorrelation signal, which is further discussed in reference ([79]). However our experiment is not sensitive enough to reveal these modifications.

$g_2(\tau)$ correlation function for Gauss pulses Using our model for real Gaussian field amplitudes (eq. (5.14)) the integrals indicated by $(***)$ and $(****)$ can be calculated ([110], [111], [113]), yielding the following interferometric autocorrelation function of second order:

$$g_2(\tau) = 1 + 4\cdot\frac{a^2b^2}{a^4+b^4}\cdot\exp\left(-\frac{\tau^2}{2\,(\Delta t)^2}\right) + 2\cdot\frac{a^2b^2}{a^4+b^4}\cdot\exp\left(-\frac{\tau^2}{2\,(\Delta t)^2}\right)\cdot\cos\left(2\omega_0\tau\right)$$
$$+4\cdot\frac{ab^3+a^3b}{a^4+b^4}\cdot\exp\left(-\frac{3\tau^2}{8\,(\Delta t)^2}\right)\cdot\cos\left(\omega_0\tau\right) \tag{5.49}$$

The above expression has been plotted for a pulse width parameter value of $\Delta t = 110\,fs$ in fig. 5.4. In the graph to the left hand side, the situation for equal pulse intensities of $I_1 \sim |E_1(t)|^2$ and $I_2 \sim |E_2(t-\tau)|^2$ as well as perfect interference, i.e. $a = b = 1$, has been depicted, whereas on the right hand side the actual experimental situation has been accounted for. In the latter a first order interference visibility of $V = 0.777$ and thus a b-parameter of $b = 0.477$ have been achieved (see table 5.2). We also acknowledge the peak-to-background ratio for $g_2(\tau)$ with $a = b = 1$ to yield $8:1$, whereas in the degraded interference case a ratio of just $4.13:1$ is observed. As autocorrelation set-ups, particularly the ones relying on interferometric autocorrelation, are commonly aligned to achieve the maximal peak-to-background ratio possible, which should normally at least be situated in the proximity of $8:1$ ([104]), it will have to be explained why such a degradation is present and does not influence the accuracy of our measurement. A justification for this will be provided in the experimental section (see subsec. 5.3.4). For the moment, focus shall be placed on the properties of the $g_2(\tau)$-function.
Further inspection of eq. (5.49) reveals the interferometric autocorrelation function to consist of three

[18]Specifically, i.e. multiplying the electric field's spectral amplitudes by factors of $B(\omega) = \prod_{m=1}^{N}\frac{\omega-\omega_m^*}{\omega-\omega_m}$, whereby the constants ω_m are complex zeros of an analytic continuation of the pulse spectrum, see ([104], [108], [109]) for details.

differently oscillating contributions and hence to comprise three Fourier components: One constant part, one oscillating at the carrier frequency ω_0 and another one at twice the carrier frequency $2\omega_0$. Additionally the non-oscillating part $1+4\cdot\frac{a^2b^2}{a^4+b^4}\cdot\exp\left(-\frac{\tau^2}{2(\Delta t)^2}\right)$ shall be noted to reduce to the intensity autocorrelation function $G_2(\tau)$ (eq. (5.43)) in the case of $a=b$. This is a direct consequence of the requirement to have no interferometric stability in order to measure the intensity autocorrelation. If one takes the time average of eq. (5.49), i.e.

$$\begin{aligned}
\langle g_2(\tau)\rangle_T &= \lim_{\Delta T\to\infty}\frac{1}{2\Delta T}\int_{-\Delta T}^{\Delta T} g_2(\tau)d\tau \\
&= \lim_{\Delta T\to\infty}\frac{1}{2\Delta T}\int_{-\Delta T}^{\Delta T}\left(1+4\cdot\frac{a^2b^2}{a^4+b^4}\cdot\exp\left(-\frac{\tau^2}{2(\Delta t)^2}\right)\right)d\tau \\
&\quad+\underbrace{\lim_{\Delta T\to\infty}\frac{1}{2\Delta T}\int_{-\Delta T}^{\Delta T}\left(2\cdot\frac{a^2b^2}{a^4+b^4}\cdot\exp\left(-\frac{\tau^2}{2(\Delta t)^2}\right)\cdot\cos(2\omega_0\tau)\right)d\tau}_{\to 0} \\
&\quad+\underbrace{\lim_{\Delta T\to\infty}\frac{1}{2\Delta T}\int_{-\Delta T}^{\Delta T}\left(4\cdot\frac{ab^3+a^3b}{a^4+b^4}\cdot\exp\left(-\frac{3\tau^2}{8(\Delta t)^2}\right)\cdot\cos(\omega_0\tau)\right)d\tau}_{\to 0} \\
&= 1+4\cdot\frac{a^2b^2}{a^4+b^4}\cdot\exp\left(-\frac{\tau^2}{2(\Delta t)^2}\right) \\
\langle g_2(\tau)\rangle_T &= G_2^{a\neq b}(\tau)
\end{aligned} \tag{5.50}$$

it can be directly seen that the oscillating terms average out to zero and one is left with the intensity autocorrelation function for unequal pulse intensities and non perfect interference $G_2^{a\neq b}(\tau)$. Although $G_2^{a\neq b}(\tau)$ has not been explicitly stated here, it follows from eq. (5.42) in exactly the same manner as eqs. (5.15), (5.19) and (5.49), (5.51) do from the first and second order correlation functions eqs. (5.12) and (5.48). This cross-over between interferometric and intensity autocorrelation will also turn out to be the appropriate tool to prove the phase information loss by going from the former to the latter function.
Since we are only capable of recording data at the oscillation maxima of eq. (5.49), for reasons to be described in subsec. 5.3.1, we can set $\cos(\omega_0\tau)=\pm1$ and $\cos(2\omega_0\tau)=\pm1$, leaving us with maximum and minimum envelope functions for $g_2(\tau)$. Their functional dependence is consequently determined by

$$g_2(\tau)=1+6\cdot\frac{a^2b^2}{a^4+b^4}\cdot\exp\left(-\frac{\tau^2}{2(\Delta t)^2}\right)\pm4\cdot\frac{ab^3+a^3b}{a^4+b^4}\cdot\exp\left(-\frac{3\tau^2}{8(\Delta t)^2}\right), \tag{5.51}$$

whereby the positive sign provides the envelope for oscillation maxima and the minus sign for minima. Both functions are included in fig. 5.4 by blue lines, indicating Gaussian pulses.

$g_2(\tau)$ correlation function for Sech pulses The very analogue of what has been said regarding the electric field distributions in the context of Gaussian pulses applies to Sech shapes as well. Using the electric field function, as stated in eq. (5.18), followed by insertion into eq. (5.48) and calculation of the integrals $(***)$ and $(****)$ ([110], [111], [113]) yields:

$$\begin{aligned}
g_2(\tau) = 1 &+12\cdot\frac{a^2b^2}{a^4+b^4}\cdot\frac{\frac{\tau}{\Delta t}\cosh\left(\frac{\tau}{\Delta t}\right)-\sinh\left(\frac{\tau}{\Delta t}\right)}{\sinh^3\left(\frac{\tau}{\Delta t}\right)} \\
&+6\cdot\frac{a^2b^2}{a^4+b^4}\cdot\frac{\frac{\tau}{\Delta t}\cosh\left(\frac{\tau}{\Delta t}\right)-\sinh\left(\frac{\tau}{\Delta t}\right)}{\sinh^3\left(\frac{\tau}{\Delta t}\right)}\cdot\cos(2\omega_0\tau) \\
&+3\cdot\frac{ab^3+a^3b}{a^4+b^4}\cdot\frac{\sinh\left(\frac{2\tau}{\Delta t}\right)-\frac{2\tau}{\Delta t}}{\sinh^3\left(\frac{\tau}{\Delta t}\right)}\cdot\cos(\omega_0\tau)
\end{aligned} \tag{5.52}$$

This autocorrelation function is also displayed in fig. 5.4 by the grey curve for the same pulse amplitude parameters as in the Gaussian case, i.e. $V=1$ and $b=1$ for the plot on the left hand side and $V=0.777$

and $b = 0.477$ for the one to the right hand side[19]. Likewise to the aforementioned scenario, eq. (5.52) does not surprisingly contain three Fourier components and reduces to the intensity autocorrelation for Sech pulses (eq. (5.44)) by time averaging, which is due to an intrinsic property of all $g_2(\tau)$ functions as derived shortly. The calculation is absolutely analogous to the Gaussian case and thus skipped here. However what is important is to also extract the envelope functions for constructive and destructive interference from eq. (5.52), being given by

$$g_2(\tau) = 1 + 18 \cdot \frac{a^2b^2}{a^4+b^4} \cdot \frac{\frac{\tau}{\Delta t}\cosh\left(\frac{\tau}{\Delta t}\right) - \sinh\left(\frac{\tau}{\Delta t}\right)}{\sinh^3\left(\frac{\tau}{\Delta t}\right)} \pm 3 \cdot \frac{ab^3+a^3b}{a^4+b^4} \cdot \frac{\sinh\left(\frac{2\tau}{\Delta t}\right) - \frac{2\tau}{\Delta t}}{\sinh^3\left(\frac{\tau}{\Delta t}\right)} \tag{5.53}$$

and represented graphically in fig. 5.4 by the red curves. The ultimate fitting function for interferometric autocorrelation maxima for the Sech pulse model is consequently defined by implementing eq. (5.53) with plus signs between the individual terms.

FWHM of the $g_2(\tau)$ correlation function and real pulse duration Having the explicit second order correlation functions for Gauss and Sech pulses at hand, we can now establish the connection between these and the real FWHM pulse duration τ^l, with $l \in \{\text{Gauss}, \text{Sech}\}$. Since dispersive broadening has been included into the parameter Δt and the pulses have been assumed to be undistorted Gaussian or Sech functions, the conversion factors between the parameters Δt in the pulse models (eqs. (5.14), (5.18)) and the FWHM durations of the pulse intensity envelopes (eqs. (5.21), (5.22)) are equal to the ones derived for the $g_1(\tau)$-correlation function (eqs. (5.23) and (5.24)):

$$\begin{aligned}\tau^{\text{Gauss}} &= \alpha_{g2}^{\text{Gauss}} \cdot \Delta t = 2\sqrt{\ln 2} \cdot \Delta t \\ \tau^{\text{Sech}} &= \alpha_{g2}^{\text{Sech}} \cdot \Delta t = 2 \cdot \operatorname{arcsech}\left(\frac{1}{\sqrt{2}}\right) \cdot \Delta t\end{aligned}$$

To gain the pulse length from the interferometric autocorrelation functions, the FWHM values of these, referred to as $\Delta\tau_{g2}$, have to be expressed in terms of the parameters Δt, determined by the following condition:

$$g_2(\Delta\tau_{g2}) = \frac{1}{2}\left(\lim_{\tau\to 0} g_2(\tau) - 1\right) + 1 \tag{5.54}$$

By substituting in the appropriate correlation function (eq. (5.51)), we obtain for Gaussian pulses:

$$1 + 6 \cdot \frac{a^2b^2}{a^4+b^4} \cdot \exp\left(-\frac{\Delta\tau_{g2}^2}{2\left(\Delta t\right)^2}\right) + 4 \cdot \frac{ab^3+a^3b}{a^4+b^4} \cdot \exp\left(-\frac{3\Delta\tau_{g2}^2}{8\left(\Delta t\right)^2}\right) = 1 + 3 \cdot \frac{a^2b^2}{a^4+b^4} + 2 \cdot \frac{a^3b+b^3a}{a^4+b^4} \tag{5.55}$$

For the Sech-case, it is useful to examine the individual terms of eq. (5.53) in the limit of $\tau \to 0$ first. Using the behaviour of $\lim\limits_{\tau\to 0} \frac{\frac{\tau}{\Delta t}\cosh\left(\frac{\tau}{\Delta t}\right) - \sinh\left(\frac{\tau}{\Delta t}\right)}{\sinh^3\left(\frac{\tau}{\Delta t}\right)} \to \frac{1}{3}$ and $\lim\limits_{\tau\to 0} \frac{\sinh\left(\frac{2\tau}{\Delta t}\right) - \frac{2\tau}{\Delta t}}{\sinh^3\left(\frac{\tau}{\Delta t}\right)} \to \frac{4}{3}$, the condition eq. (5.54) can be evaluated for this pulse shape as well, yielding:

$$\begin{aligned}1 + 18 \cdot \frac{a^2b^2}{a^4+b^4} \cdot \frac{\frac{\Delta\tau_{g2}}{\Delta t}\cosh\left(\frac{\Delta\tau_{g2}}{\Delta t}\right) - \sinh\left(\frac{\Delta\tau_{g2}}{\Delta t}\right)}{\sinh^3\left(\frac{\Delta\tau_{g2}}{\Delta t}\right)} \\ + 3 \cdot \frac{a^3b+ab^3}{a^4+b^4} \cdot \frac{\sinh\left(\frac{2\Delta\tau_{g2}}{\Delta t}\right) - \frac{2\Delta\tau_{g2}}{\Delta t}}{\sinh^3\frac{\Delta\tau_{g2}}{\Delta t}} = 1 + 3 \cdot \frac{a^2b^2}{a^4+b^4} + 2 \cdot \frac{a^3b+ab^3}{a^4+b^4}\end{aligned} \tag{5.56}$$

In contrast to the equations for $\Delta\tau_{g1}^{FWHM,l}$ (eqs. (5.25) and (5.26)), both expressions above are not analytically solvable anymore in terms of Δt, therefore a numerical solution is pursued. Furthermore the factors containing the electric field parameters a and b are not separable from the remainders in eqs. (5.55) and (5.56). This is rather important as it means that the solutions of both equations are functions of a and b: $\Delta\tau_{g2} = \Delta\tau_{g2}(a, b)$. In turn it implies the conversion factors to be dependent on

[19] Although the experimental parameters, recieved particularly for the HHVV coincidences deviate slightly from the b parameter and the visibility used here, see table 5.2, $V = 0.777$ and $b = 0.477$ shall nevertheless be used, as they represent the averaged values over all intra-cavity datasets and have also been applied during discussing the $g_1(\tau)$ function.

the interference visibility of the pulses to be measured. There are two specific situations for which the solution of the above equations and the conversion factors calculated thereof shall explicitly be stated. The first one is the situation for perfect interference and equal pulse intensities, given by the parameter set of $a = b = 1$. Eqs. (5.55) and (5.56) return:

$$\Delta\tau_{g2}^{\mathrm{Gauss}}\left(a=1,b=1\right)=\beta_{g2}^{\mathrm{Gauss}}\cdot\Delta t=2.553\cdot\Delta t \tag{5.57}$$

$$\Delta\tau_{g2}^{\mathrm{Sech}}\left(a=1,b=1\right)=\beta_{g2}^{\mathrm{Sech}}\cdot\Delta t=2.9901\cdot\Delta t \tag{5.58}$$

Further application of the constants $\tau^l = \alpha_{g2}^l \cdot \Delta t$ allows to gain the relation between pulse duration and FHWM of the $g_2(\tau)$-functions according to

$$\tau^l=\frac{\alpha_{g2}^l}{\beta_{g2}^l}\cdot\Delta\tau_{g2}^l:=\gamma_{g2}^l\cdot\Delta\tau_{g2}^l, \tag{5.59}$$

with the final set of conversion factors to be:

$$\tau^{\mathrm{Gauss}}\left(a=1,b=1\right)=0.6523\cdot\Delta t_{g2}^{\mathrm{Gauss}}\left(a=1,b=1\right) \tag{5.60}$$

$$\tau^{\mathrm{Sech}}\left(a=1,b=1\right)=0.5895\cdot\Delta t_{g2}^{\mathrm{Sech}}\left(a=1,b=1\right) \tag{5.61}$$

These values are the commonly applied ones when dealing with interferometric autocorrelation. It shall be particularly stressed, that they are different to the set of parameters obtained if considering intensity autocorrelation (given by $\gamma_{G2}^{\mathrm{Gauss}}\left(a=1,b=1\right)=1/\sqrt{2}$ and $\gamma_{G2}^{\mathrm{Sech}}\left(a=1,b=1\right)=0.6481$). Although the latter numbers are often the factors stated in the literature ([104], [111], [113]), one should not fall for the trap of using them with respect to interferometric autocorrelations, since they overestimate the pulse length.
With the precise experimentally determined b-parameter from the measurement of HHVV coincidences, $b_{HHVV} = 0.4383$ (see table (5.2)), we get from eqs. (5.55) and (5.56) the relevant constants for our situation of reduced visibility. The constants β_{g2}^l are

$$\Delta\tau_{g2}^{\mathrm{Gauss}}\left(a=1,b=b_0\right)=2.58\cdot\Delta t \tag{5.62}$$

$$\Delta\tau_{g2}^{\mathrm{Sech}}\left(a=1,b=b_0\right)=3.0289\cdot\Delta t, \tag{5.63}$$

which translate via eq. (5.59) into conversion factors $\gamma_{g2}^l(a=1,b=b_0)$ of:

$$\tau^{\mathrm{Gauss}}\left(a=1,b=b_0\right)=0.6454\cdot\Delta\tau_{g2}^{\mathrm{Gauss}}\left(a=1,b=b_0\right) \tag{5.64}$$

$$\tau^{\mathrm{Sech}}\left(a=1,b=b_0\right)=0.582\cdot\Delta\tau_{g2}^{\mathrm{Sech}}\left(a=1,b=b_0\right) \tag{5.65}$$

Those will be the correct values for the future evaluation of our experimental findings. However the difference to the optimal situation is not tremendously severe, as deviations only start to make a difference from second leading order onwards.
Due to our particular realisation of our experimental set-up, subsec. 5.3.1, so far our model had to take degraded interference and different intensities between the pulses at time t and $t-\tau$ into account, due to the cavity acting as a spatial mode filter. If a free space set-up is considered, only degraded interference will be important to obey, as both pulses have equal intensities. In this case the denominators of the $g_2(\tau)$ correlation functions transform into $I_1 = const. \cdot a^2 = I_2 = const. \cdot b^2$, while the numerators still have to account for the imperfect electric field interference, consequently comprising products of $a \cdot b$ with $a \neq b$. Thereby eqs. (5.51) and (5.53) change into:

$$g_2'^{\mathrm{Gauss}}(\tau)=1+6\cdot\frac{a^2b^2}{2a^4}\cdot\exp\left(-\frac{\tau^2}{2\left(\Delta t\right)^2}\right)+4\cdot\frac{ab^3+a^3b}{2a^4}\cdot\exp\left(-\frac{3\tau^2}{8\left(\Delta t\right)^2}\right) \tag{5.66}$$

$$g_2'^{\mathrm{Sech}}(\tau)=1+18\cdot\frac{a^2b^2}{2a^4}\cdot\frac{\frac{\tau}{\Delta t}\cosh\left(\frac{\tau}{\Delta t}\right)-\sinh\left(\frac{\tau}{\Delta t}\right)}{\sinh^3\left(\frac{\tau}{\Delta t}\right)}+3\cdot\frac{ab^3+a^3b}{2a^4}\cdot\frac{\sinh\left(\frac{2\tau}{\Delta t}\right)-\frac{2\tau}{\Delta t}}{\sinh^3\left(\frac{\tau}{\Delta t}\right)} \tag{5.67}$$

We can now compute the conversion factors for both cases, $g_2(\tau)$ and $g_2'(\tau)$, by the aid of eqs. (5.55) and (5.56) evaluated according to the appropriate situation with the correct denominators. For both pulse

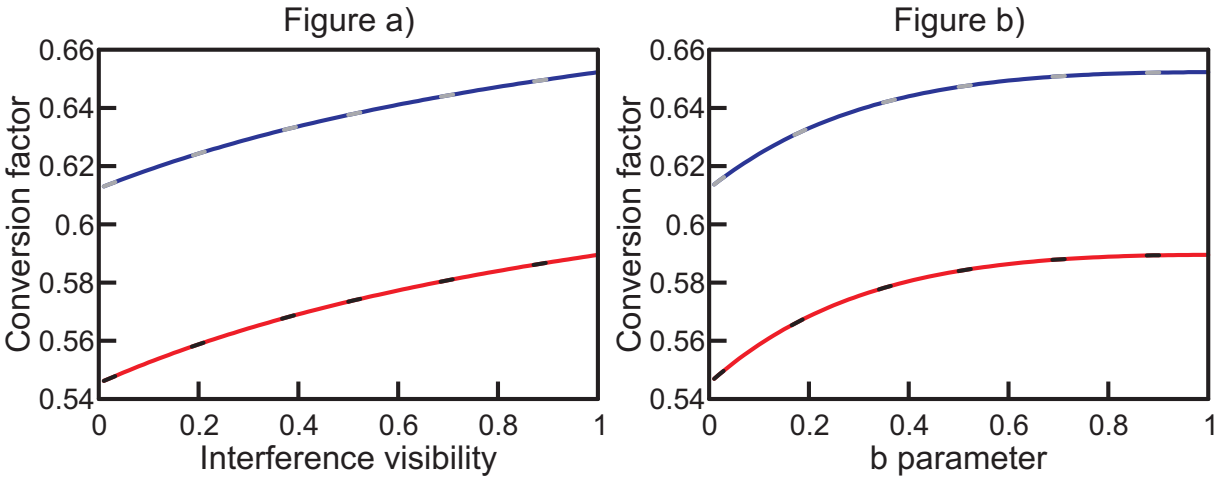

Figure 5.5: Conversion factor between the FWHM of the interferometric autocorrelation function $g_2(\tau)$ and the FWHM pulse duration, displayed as a function of interference visibility in plot a) and the b-parameter in plot b). Gaussian pulses with degraded interference and different pulse intensities are indicated as solid blue curves, whereby their Sech counterparts are indicated as solid red curves. Situations with equal pulse intensities, yet still having a degraded interference as described by eqs. (5.66) and (5.67), are drawn as a dashed grey curve for the Gaussian and a dashed black curve for the Sech scenario.

models the conversion factors are shown in fig. 5.5 as a function of visibility on the left hand side and the b-parameter on the right hand side, each evaluated numerically within a range of $0.01 \leq (V, b) \leq 1$ and with stepsize of $\Delta b = \Delta V = 0.01$. The dependencies on both parameters have been depicted since from a measured autocorrelation curve, the b-parameter can be determined very easily, whereby in terms of an interference measure, the visibility is generally considered. Gaussian pulses with unequal intensities, given by eq. (5.51), are displayed by solid blue curves and with equal intensities, given by eq. (5.66), by dashed grey curves. Sech pulses are draw in solid red lines for a situation with unequal intensities, eq. (5.53), and by dashed black lines for a situation with equal intensities in both pulses, eq. (5.67). From the computation and fig. 5.5 it is inferred that regardless of the intensity distribution between the two pulses, both of the aforementioned situations[20] yield the same conversion constants. Thus γ_{g2}^{l} only depends on the interference visibility. In other words: Attention only has to been paid to the interferometric interaction between the pulses but one does not have to worry about intensity modifications on individual pulses, if their respective interfering fraction remains constant.

5.2.4 Phases in the second order autocorrelation function

In the last part of the theoretical investigations regarding autocorrelation the appearance of phase terms, generated by dispersive processes, are to be discussed in the context of second order correlation functions. As we have already seen, such effects are invisible for first order interference experiments, due to their cancellation (eq. (5.32)). It has already been mentioned, that interferometric autocorrelation functions of second order in contrast show influences from dispersion, whereby these alterations vanish again in the observed signal when interferometric stability is lost and the cross-over to the intensity autocorrelation function is pursued. In order to give accurate evidence for this behaviour, we will analyse the $g_2(\tau)$-function in its most general form (eq. (5.45)) once more under the assumption of arbitrary pulses, which have been subject to some temporal phase addition. By considering real fields, our electric field model is now:

$$E(t) = \mathrm{Re}\left(A(t)\exp\left(i\phi(t)\right)\exp\left(i\omega_0 t\right)\right) = \frac{1}{2}\left(A(t)\exp\left(i\phi(t)\right)\exp\left(i\omega_0 t\right) + A^*(t)\exp\left(-i\phi(t)\right)\exp\left(-i\omega_0 t\right)\right) \tag{5.68}$$

with the pulse envelope to be taken as a real function in the following[21], i.e. $A(t) = A^*(t)$. Plugging it into the general expression for the $g_2(\tau)$-function (eq. (5.45)) results in a lengthy calculation, which is skipped here for brevity and the final outcome is taken over from reference ([111]), given by:

[20] eq. pair (5.51) and (5.53), compared with (5.66) and (5.67)

[21] The situation of unequal pulse intensities and/or incomplete interference between both pulses is dropped here for the sake of simplicity, since only general properties of the autocorrelation are examined and an additional constant factor does not change these.

$$g_2(\tau) = \frac{1}{\int_{-\infty}^{\infty} A^4(\tau)dt} \cdot \underbrace{\left(\int_{-\infty}^{\infty} \left(A^4(t) + 2A^2(t)A^2(t-\tau) \right) dt \right)}_{\text{constant in } \tau =: \text{term 1}}$$
$$+ \frac{2}{\int_{-\infty}^{\infty} A^4(\tau)dt} \cdot \underbrace{\mathrm{Re}\left(e^{(i\omega_0\tau)} \int_{-\infty}^{\infty} A(t)A(t-\tau) \left(A^2(t) + A^2(t-\tau) \right) e^{(i(\phi(t-\tau)-\phi(t)))} dt \right)}_{\text{oscillation} \sim \cos(\omega_0\tau) =: \text{term 2}}$$
$$+ \frac{1}{\int_{-\infty}^{\infty} A^4(\tau)dt} \cdot \underbrace{\mathrm{Re}\left(e^{(i2\omega_0 t)} \int_{-\infty}^{\infty} A^2(t)A^2(t-\tau) e^{(i2(\phi(t-\tau)-\phi(t)))} dt \right)}_{\text{oscillation} \sim \cos(2\omega_0\tau) =: \text{term 3}} \tag{5.69}$$

For deriving the above expression, the equality stated in eq. (5.13) has been used again. It can thus be seen, that any second order interferometric autocorrelation for an arbitrary pulse shape accommodates three different contributions, one being constant, one oscillation at the carrier frequency as a function of pulse separation and another one oscillating at twice that frequency. The temporal phases $\exp(i\phi(t'))$, which carry the information about any pulse elongation, are furthermore only found in the oscillating terms. Therefrom the susceptibility of the $g_2(\tau)$ autocorrelation function to dispersion is revealed. The last point is the important message here in terms of the difference between $g_2(\tau)$ and $G_2(\tau)$: We have already acknowledged the ability to extract the intensity autocorrelation from its interferometric counterpart by time averaging during the discussions regarding eq. (5.50), corresponding to a loss in interferometric stability. So application of this kind of operation shall be incorporated here as well, whereupon one should note τ to constitute the correct variable to average over[22]. By further substituting $\kappa := \int_{-\infty}^{\infty} A^4(\tau)dt$, $f_1 := \int_{-\infty}^{\infty} \left(A^4(t) + 2A^2(t)A^2(t-\tau) \right) dt$, $f_2 := \int_{-\infty}^{\infty} A(t)A(t-\tau) \left(A^2(t) + A^2(t-\tau) \right) e^{(i(\phi(t-\tau)-\phi(t)))} dt$ and $f_3 := \int_{-\infty}^{\infty} A^2(t)A^2(t-\tau) e^{(i2(\phi(t-\tau)-\phi(t)))} dt$ we compute:

$$\begin{aligned}
\langle g_2(\tau) \rangle_{\Delta t_{\text{det.}}} &= \frac{1}{\kappa} \cdot \underbrace{\lim_{\Delta t_{\text{det.}} \to \infty} \int_{-\Delta t_{\text{det.}}/2}^{\Delta t_{\text{det.}}/2} f_1 d\tau'}_{\to f_1} \\
&\quad + \frac{2}{\kappa} \cdot \underbrace{\lim_{\Delta t_{\text{det.}} \to \infty} \int_{-\Delta t_{\text{det.}}/2}^{\Delta t_{\text{det.}}/2} \frac{1}{2} \left(f_2 \cdot e^{(i\omega_0\tau)} + f_2^* \cdot e^{(-i\omega_0\tau)} \right) d\tau'}_{\to 0} \\
&\quad + \frac{1}{\kappa} \cdot \underbrace{\lim_{\Delta t_{\text{det.}} \to \infty} \int_{-\Delta t_{\text{det.}}/2}^{\Delta t_{\text{det.}}/2} \frac{1}{2} \left(f_3 \cdot e^{(i2\omega_0 t)} + f_3^* \cdot e^{(-i2\omega_0 t)} \right) d\tau'}_{\to 0} \\
&= \frac{\int_{-\infty}^{\infty} \left(A^4(t) + 2A^2(t)A^2(t-\tau) \right) dt}{\int_{-\infty}^{\infty} A^4(t)dt} \\
&= 1 + \frac{2 \cdot \int_{-\infty}^{\infty} A^2(t)A^2(t-\tau)dt}{\int_{-\infty}^{\infty} A^4(t)dt}
\end{aligned} \tag{5.70}$$

Hence all the terms sensitive to temporal phases vanish in the course of time averaging and soleley the first term remains. Consulting the assumption of having real field amplitudes $A(t)$ only in the derivation of eq. (5.69), which consequently implies the pulse intensity to be $I(t) = \frac{1}{2}\epsilon_0 c|E(t)E^*(t)|^2 = \frac{1}{2}\epsilon_0 c A(t)^2$, the above expression changes, by usage of eq. (5.42), into

$$\langle g_2(\tau) \rangle_{\Delta t_{\text{det.}}} = 1 + \frac{\int_{-\infty}^{\infty} 2I(t)I(t-\tau)dt}{\int_{-\infty}^{\infty} I^2(t)dt} = G_2(\tau), \tag{5.71}$$

proving the equivalence of the time averaged interferometric and the intensity autocorrelation function. For the reason of all temporal phase information having dropped out on the way from eq. (5.69) to

[22] If the interferometer, which creates both pulses for the autocorrelation, is not stable, its arm lengths fluctuate, leading to a non-stable pulse separation $\Delta x_{\text{int}} = \frac{\tau}{c}$ and therefore to an unsteadiness in the values of τ. The latter translates, by accounting for the finite integration time of the detector used to record the autocorrelation signal, into an averaging over all different values of τ apparent within the time interval $t \in \left[-\frac{\Delta t_{\text{det.}}}{2}, \frac{\Delta t_{\text{det.}}}{2} \right]$. Since $\Delta t_{\text{det.}} \gg \tau$ the extension to infinity of the averaging time scale is justified.

(5.71), the incapability of detecting dispersive pulse elongation with intensity autocorrelation has been demonstrated as well. The equality between $g_2(\tau)$ and $G_2(\tau)$ states the necessary experimental means to swap from measuring one function to the other, namely to deteriorate or respectively improve the interferometric stability. So at the end of the day, we have shown that the intensity autocorrelation cannot detect dispersion effects and therefore just measures the undistorted pulse duration already available in first order correlation. To infer the proper pulse duration, sensitivity to temporal (or respectively spectral) phases like in the case of the interferometric autocorrelation is indispensable.
As a last step it is worth mentioning the contributions from the different Fourier components of the $g_2(\tau)$-function, oscillating at frequencies 0, ω_0 and $2\omega_0$. Referring to fig. 12.27 in reference ([111]) the constant part can be figured out to represent $G_2(\tau)$ with the appropriate peak-to-background ratio of $3:1$. The other two entities are found to interfere constructively with each other in the event of interferometric autocorrelation and amount themselves together with the constant part to a peak-to-background ratio for $g_2(\tau)$ of $8:1$. Effects due to a loss in stability can therefrom easily be imagined to spoil the maximally constructive add-up of the oscillating parts, leading consequently to a degradation in the peak-to-background ratio going from $8:1$ towards $3:1$. For that reason such autocorrelation measurements are generally aligned by maximising this ratio up to a number close to $8:1$, as otherwise experimental outcomes, located somewhere between an intensity and an interferometric autocorrelation, are obtained, recording data which does not fully account for dispersive broadening and thus underestimates the pulse duration. Since we have a ratio of only $4.13:1$, evidence about the interferometric stability of the pulse duration τ in our set-up has to be provided in the first place together with some other essential primary considerations, which will now be discussed in the framework of the experimental findings.

5.3 Measurement of intra-cavity pulse duration

Within this section, the experimental findings concerning the UV pulse duration inside the cavity will be discussed. The particularity of this measurement is its implementation directly within an optical resonator, hence not applying any sort of out-coupling mechanism, which could in itself introduce additional pulse distortion. According to eq. (5.8), we are additionally given the opportunity to observe multiple orders of correlation simultaneously, whereby conveniently use will be made only of the first two.
In the following, the experimental implementation of the autocorrelation measurement is introduced first. Second proof for our ability to measure an accurate autocorrelation function is given, specifically showing that the spectral acceptance of the cavity can be maintained throughout the measurement and proving the sufficiency of the phase-matching bandwidth to allow down-conversion for all spectral components within the pulse. Third, the interference of first order is examined and results therefrom are contrasted with the additionally measured UV spectra inside the cavity. Ultimately the correlation of second order is analysed and an estimate for the actual pulse duration is obtained.

5.3.1 Description of set-up

As mentioned in the theory section regarding the measurement of short laser pulses by autocorrelation, one requires some type of interferometer in order to generate two pulses of variable time delay. To do so, we include a Mach-Zehnder (MZ) interferometer[23] with one fixed and one movable arm into the UV feed beam of the cavity, providing us with the opportunity to scan the delay between the resulting pulses by aid of a translation-stage mounted mirror in the latter arm.
Usually glass retro-reflectors are used for such kind of interferometers, comprising transverse displacement between the forth- and back-reflected beams in the arms, to allow for precise alignment. Operating the set-up with femto-second pulses however prevents us from using these components, as they would add additional dispersion, yielding in a pulse broadening of approximately ([77]) $20\,fs$. Obviously this initial broadening is unacceptable for a method, which is supposed to provide a value for a pulse duration free of additional distortion imparted by the measurement. Therefore two flat mirrors at the end of either arm are used instead. To also avoid additional broadening deriving from a beam splitter cube, a thin beam splitter plate with a transmittance-reflectance ratio of $T = 56.52\,\% : R = 43.48\,\%$ splitting ratio is furthermore used (see fig. 5.6 for a photograph). The down-side of this back-end mirror design is its alignment. Indeed we have not been able to achieve perfect overlap between both beams in the exit arms, resulting in an interference visibility of approximately 77% in the interferometer output.
The optimal positioning of the interferometer requires some attention as well. Clearly one does not want to have the interferometer set up in front of the SHG process as any slight misalignment of the beam overlap in the output would have tremendous impact on the phase-matching in the LBO and in turn on the UV signal strength and the cavity coupling. Locating it in front of the beam pointing stabilisation[24] is not appealing either, as fluctuations on the transverse position of the input beam would deteriorate the entire interferometer alignment and the mode overlap in the output. Accordingly it is placed behind the aforementioned unit but in front of the cavity input-coupling optics, as can be inferred from fig. 5.6. There is however still a residual sensitivity to non-ideal interferometer alignment at this location due to off-axis penetration through optical lenses, which can impart aberations onto the beam profile, deteriorating the coupling efficiency into the enhancement resonator. One output of the interferometer, referred to as output 2 is coupled into the cavity, whereby the other output, named output 1, is monitored directly by a photodiode.
In order to measure the correlation functions within the cavity, we move the back-end mirrors in one arm via the automated translation stage by a distance Δx_{MZ}, providing us with a pulse separation of $\tau_{MZ} = \frac{2\Delta x_{MZ}}{c}$ between both pulses. As we have to lock the resonator to a certain part of the external frequency comb spectrum, see 3.2.1, a non-vanishing amount of light intensity has to be available for the Hänsch-Coulliaud lock. It has thus turned out necessary to have constructive interference between both pulses in the cavity output of the Mach-Zehnder interferometer to have a sufficiently strong error signal for proper stabilising the FSR of the cavity. All measurement points for the correlation functions are therefore measured at translation stage positions providing the appropriate interference condition. These are found by observing an intensity level corresponding to an interference minimum on the photodiode in output 2. At such a stage position, we measure the averaged UV power level inside the cavity as

[23] There are various definitions in use on what exactly to call a Mach-Zehnder interferometer and what to consider as the Michelson version. In this work we will follow the convention that the Mach-Zehnder is an interferometer, which does not reflect the beams in its arms back into themselves. Thus, although comprising only one beam splitter, our device will be regarded as such a type.
[24] See explanation in subsec. 3.1.2 in this unit.

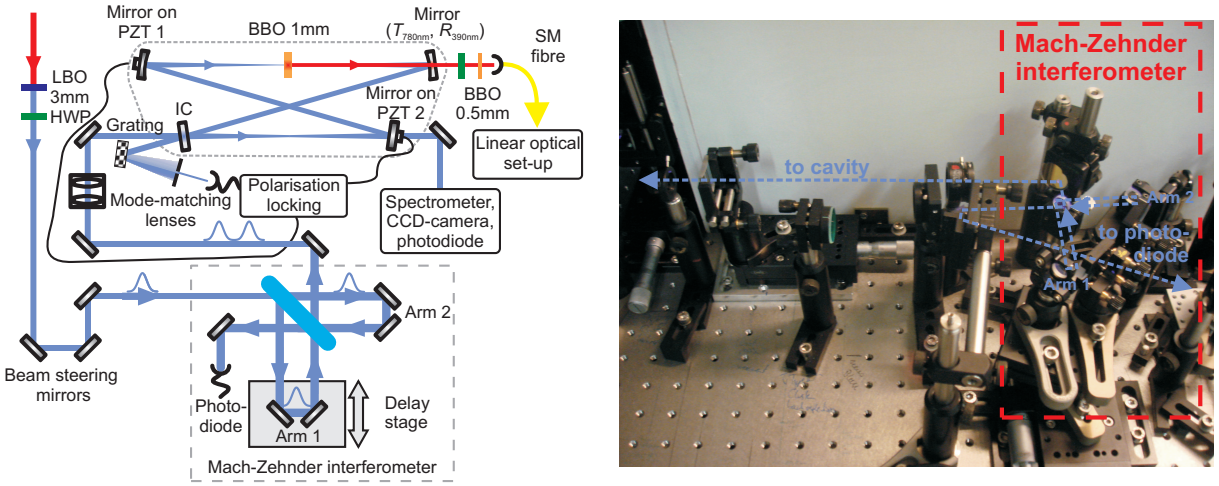

Figure 5.6: Left: Schematic drawing of SPDC autocorrelation set-up: The MZ is positioned in front of the cavity, generating two delayable pulses, which are coupled into the resonator and produce down-converted photon pairs of which four photon coincidences are counted to acquire the autocorrelation function $g_2(\tau)$. Right: Experimental implementation of the MZ interferometer.

well as the amount of two- and four-fold photon coincidences with one horizontally and one vertically polarised photon or with two horizontally and two vertically polarised photons, respectively, in our linear optical set-up[25], which is set for observation in the σ_Z-basis and thus works as a photon counting device[26]. Hence interference fringes can neither be seen in $g_1^{\text{cavity}}(\tau)$, $g_1^{\text{HV}}(\tau)$-correlation functions, nor in the $g_2^{\text{HHVV}}(\tau)$-correlation counterparts. The minima of the fringe patterns were not measurable because the cavity was not lockable on a stable level for a time period long enough to record sufficient data. Leaving the cavity free running was not feasible either for exactly the same reason only with an even shorter time window available for photon detection. However sampling solely interference maxima does not cause any information loss, since the pulse duration is just determined by the FWHM of the fitted $g_1(\tau)$- and $g_2(\tau)$-functions onto the aforementioned datapoints anyway and the visibility is implicitly included too by the overall maximum to background ratio of the resulting curves, as we will see later on. The interference filter in front of the photon counting unit, which is normally applied to gain indistinguishability between different photon pairs, as explained further in subsec. 6.2.2, must be taken out as it would otherwise filter out parts of the SPDC photon spectrum and hence influence the width of the correlation functions and the pulse duration calculated thereof. One possibility to think about this effect is to consider what happens if only photons from the central part of the down-conversion spectrum are impinging onto the photodetectors in the linear optical set-up and the entire rest is filtered out. Accordingly all frequency parts in the UV pump spectrum, which down-convert into photons lying within the filter's spectral pass band, are detected, but all other frequencies are neglected. From Fourier transform (FT) theory this smaller spectrum results in a longer Fourier transform limited pulse duration, scaling reciprocal to the spectral width. However as a laser pulse cannot be shorter than the FT limit, spectral narrowing of the down-conversion photons would result in an artificial elongation of the measured pulse length. This is an analogue effect to the one, which is expected if the phase matching bandwidth of the non-linear process is not sufficiently broad in order to maintain conversion of all spectral components contained in the pump pulse (see subsec. 5.3.3).
In a first measurement run, data has been taken for the average intra-cavity UV level, HV- and HHVV-coincidences by measuring at 17 translation stage positions[27] for a time of approximately 8 s each, while additionally recording the intra-cavity UV spectrum. In a second run, the interference pattern of the $g_1(\tau)$-correlation function has been measured separately by the photodiode in output 1 of the Mach-Zehnder interferometer with a translation stage step size of approximately 19.53 nm, corresponding to the smallest resolution available.
Before discussing the outcomes of these measurements, the essential conditions for conducting a sensible

[25] See section 3.3.
[26] See also discussion in subsec. 6.3.1.
[27] These have been: $-271.54\,\mu m$, $-91.4\,\mu m$, $-66.28\,\mu m$, $-48.14\,\mu m$, $-39.12\,\mu m$, $-35.18\,\mu m$, $-23.04\,\mu m$, $-16.18\,\mu m$,0 μm, $8.84\,\mu m$, $13.82\,\mu m$, $28.92\,\mu m$, $37.48\,\mu m$, $46.54\,\mu m$, $65.36\,\mu m$, $94.58\,\mu m$, $228.8\,\mu m$ with 0 μm corresponding to an equal arm length. These values represent a pulse separation time of: $-1810\,fs$, $-609\,fs$, $-442\,fs$, $-321\,fs$, $-261\,fs$, $-235\,fs$, $-153\,fs$, $-108\,fs$, 0 fs, 59 fs, 92 fs, 193 fs, 250 fs, 310 fs, 436 fs, 631 fs, 1525 fs

autocorrelation experiment will be discussed in the first place.

5.3.2 Discussion of cavity locking condition

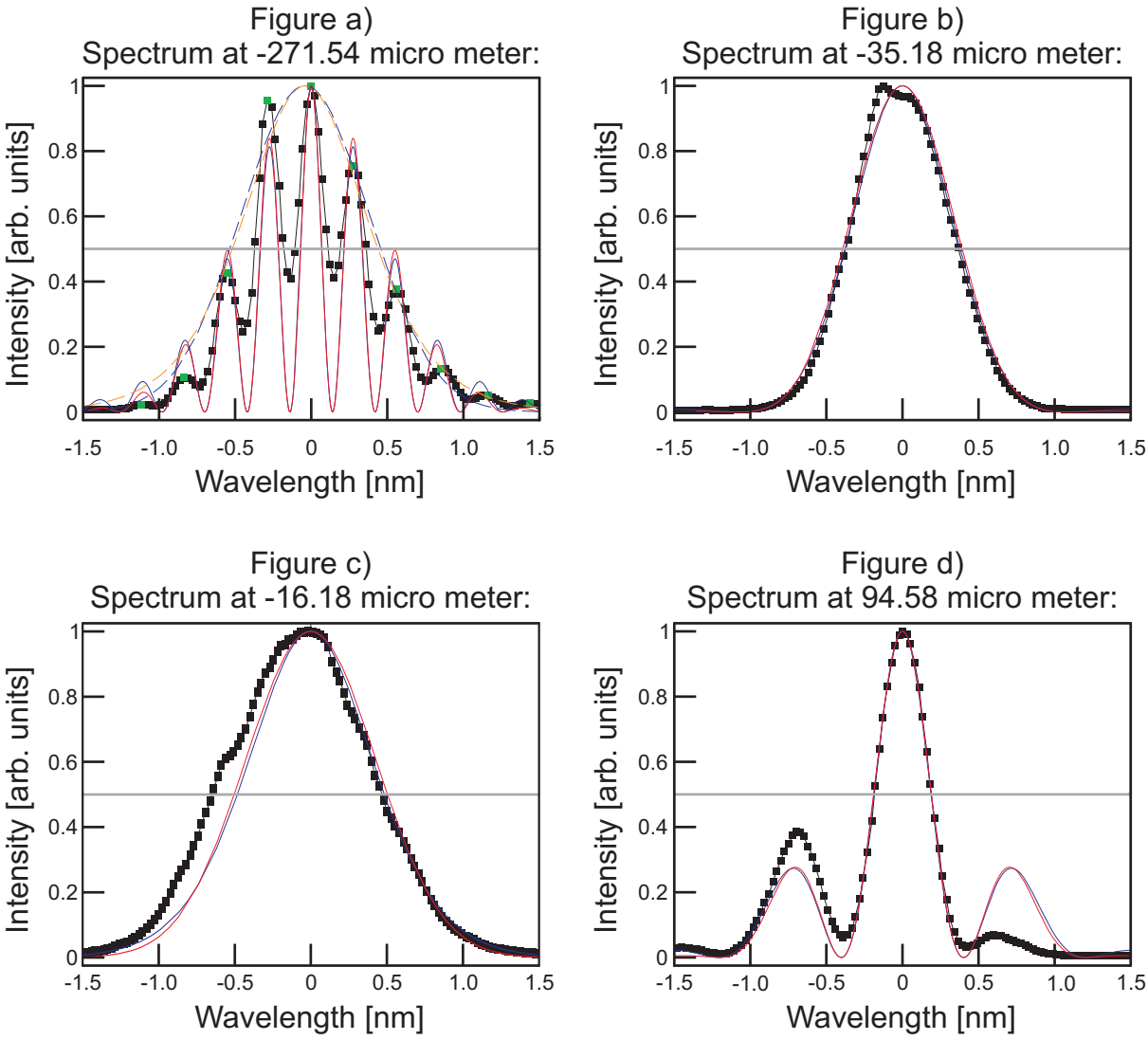

Figure 5.7: Measured oscillations in UV spectra as a function of translation stage displacement together with fits according to the derived model, stated in eq. (5.75). Black points and lines indicate measured data, solid blue lines represent a fit for Gaussian pulses according to eq. (5.78) and solid red lines represent the analogue fit for Sech pulses, eq. (5.79). The dashed lines are fits to the broadest spectrum at $x_{MZ} = -16.18\,\mu m$, with blue standing for a Gaussian and orange for a Sech pulse amplitude. For further details see main text.

Since it is the purpose of this experiment to measure the intra-cavity pulse width, it is absolutely essential to have a similar spectral acceptance range by the cavity for each measurement point in the correlation functions. Spectral acceptance means the amount of external UV frequency comb modes that can couple into the cavity. If that was not fulfilled, one would end up with a different spectral width and, by the FT connection, with a different pulse length at each measurement point. Obviously in such a scenario the $g_2(\tau)$-function would not provide the proper pulse length inside the cavity as it is apparent also without the Mach-Zehnder interferometer. But why should the cavity locking condition change at all during the correlation measurement?
Taking a look at the UV spectra in the interferometer output, measured with the translation stage position away from perfect temporal pulse overlap, one recognises oscillations on these, causing the expected Gaussian shape to evolve into a pattern with fringes of narrowing FWHM widths, as can be seen in fig. 5.7. Since the cavity has to be locked separately at each translation stage position, this could on the one hand lead to a problem, if the same frequency comb tooth is chosen for the locking

signal at each datapoint: As the cavity locking process just works on a small part of the spectrum and the stability of the locking is very susceptible to the Hänsch-Coulliaud error signal, choosing a locking position, through which such a minimum in spectral intensity is dragged, would result in the requirement for a different locking point[28] at positions of too small an error signal intensity. In turn this causes a different dispersion compensation condition, a different external and internal frequency comb matching and thus a different spectrum or respectively pulse length inside the resonator. On the other hand, if different teeth/spectral regions are used for locking the cavity at different stage positions, one has to be certain to establish the same amount of external and internal frequency comb matching each time, ensuring that the spectral width of pulses inside the resonator is maintained for the different dispersion compensation conditions. In order to prove the constance in mode matching, a closer examination of the aforementioned spectral oscillations is necessary.

Modelling the output spectrum of the Mach-Zehnder interferometer Considering the Mach-Zehnder interferometer (fig. 5.6), one can observe its output pulse train to consist of two electric fields

$$E(t) = \frac{E_0}{\sqrt{2}} f(t) \exp(i\omega_0 t) \tag{5.72}$$

$$E(t-\tau) = \frac{E_0}{\sqrt{2}} f(t-\tau) \exp(i\omega_0 (t-\tau)), \tag{5.73}$$

whereby conveniently a 50 : 50 splitting ratio for the beam splitter has been assumed and $f(t)$ represents an arbitrary electric field amplitude function. The Mach Zehnder's output field amounts to

$$E_{tot}(t) = E(t) + E(t-\tau) = \frac{E_0}{\sqrt{2}} f(t) \exp(i\omega_0 t) + \frac{E_0}{\sqrt{2}} f(t-\tau) \exp(i\omega_0 (t-\tau)) \tag{5.74}$$

with the spectrum of this field superposition being obtained by taking the Fourier transform and subsequently calculating the absolute square of the result. The detailed calculation is stated in the appendix C.2.1 with an outcome for the spectrum in terms of wavelength given by

$$S(\lambda, \lambda_0) = S_0(\lambda - \lambda_0) \cos^2\left(\frac{2\pi(\lambda - \lambda_0)}{\lambda_0^2} \Delta x_{MZ}\right) \tag{5.75}$$

with $S_0(\lambda - \lambda_0)$ being the spectrum of the pulse amplitude function $\frac{E_0}{\sqrt{2}} f(t)$. In order to apply our results (eq. (5.75)) to the measurements, a concrete pulse shape has to be considered; therefore the spectra derived for a Gaussian- or a Sech-pulse, given by eqs. (5.35) and (5.37), computed by Fourier transform (see subsec. 5.2.2), are used:

$$\begin{aligned} & S_0^{\text{Gauss}}(\nu, \nu_0) = \exp\left(-4\pi^2 (\Delta t)^2 (\nu - \nu_0)^2\right) \\ \Longleftrightarrow\ & S_0^{\text{Gauss}}(\lambda, \lambda_0) \approx \exp\left(-4\pi^2 (\Delta t)^2 c \left(\frac{(\lambda_0 - \lambda)}{\lambda_0^2}\right)^2\right) =: \exp\left(-\left(\frac{(\lambda - \lambda_0)}{w}\right)^2\right) \end{aligned} \tag{5.76}$$

$$\begin{aligned} & S_0^{\text{Sech}}(\nu, \nu_0) = \operatorname{sech}^2(\pi^2 \Delta t(\nu - \nu_0)) \\ \Longleftrightarrow\ & S_0^{\text{Sech}}(\lambda, \lambda_0) \approx \operatorname{sech}^2(\pi^2 c \Delta t \left(\frac{\lambda_0 - \lambda}{\lambda_0^2}\right)) =: \operatorname{sech}^2\left(\frac{\lambda - \lambda_0}{w}\right) \end{aligned} \tag{5.77}$$

giving the final theoretical formulae for the spectral intensity distribution:

$$S_{\text{Gauss}}(\lambda, \lambda_0) = \exp\left(-\left(\frac{(\lambda - \lambda_0)}{w}\right)^2\right) \cos^2\left(\frac{2\pi(\lambda - \lambda_0)}{\lambda_0^2} \Delta x_{MZ}\right) \tag{5.78}$$

$$S_{\text{Sech}}(\lambda, \lambda_0) = \operatorname{sech}^2\left(\frac{\lambda - \lambda_0}{w}\right) \cos^2\left(\frac{2\pi(\lambda - \lambda_0)}{\lambda_0^2} \Delta x_{MZ}\right) \tag{5.79}$$

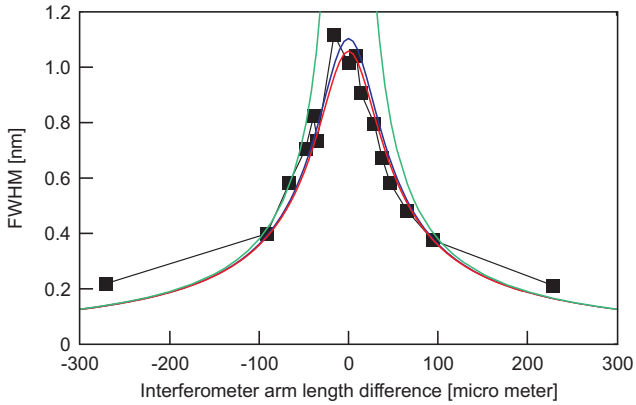

Figure 5.8: FWHM values of the central fringes in all spectra for varying translation stage positions. The black boxes represent the widths extracted from the measured spectra, as they are obtained at the respective positions x_{MZ}, exemplarily shown in fig. 5.7. The blue curve shows the FWHM values of the central fringe in the model function (5.78) for Gaussian pulses, whereby the red one depicts the FWHM for the Sech pulse case, given by eq. (5.79). The green curve displays the width of the central oscillation fringe in the $\cos^2\left(\frac{2\pi(\lambda-\lambda_0)}{\lambda_0^2}\Delta x_{MZ}\right)$ part of the spectrum model for the interferometer output, given by eq. (5.75).

Discussion of the model in comparison to experimental spectra By taking a closer look at eqs. (5.78), (5.79) and their derivation one readily recognises the spectra at each measurement point of the correlation curves to comprise contributions from an undistorted envelope function, depending on the respective pulse form with a constant width, and a modulation function, determined by the relative path length difference between the interferometer arms. Thus the latter can be expected to be negligible once $\Delta x_{MZ} = 0$ and to dominate if $\Delta x_{MZ} > 0$. In order to reveal any information about the cavity's wavelength acceptance range, we can now regard the unmodulated part of the above expressions as a spectrum of the pulse apparent for $\tau_{MZ} \approx 0$, i.e. with only a single pulse to be coupled into the resonator. If the acceptance range remains the same throughout the experiment, all that changes in the spectra at different measurement points is the part proportional to $\cos^2$, adding a modulation, but still showing an envelope which is described by a Gauss- or Sech-pulse spectrum. As can be seen in fig. 5.7, multiple oscillation maxima are only present for displacements of the translation stage lying already outwith the interference region of both pulses (see fig 5.11 in subsec. 5.3.4), causing the spectra within the relevant range for the $g_2(\tau)$-correlation measurement[29] to exhibit not enough such points for reading out the proper FWHM value of the envelope function. Therefore we look instead at the FWHM of the central fringe within all UV spectra, that have been obtained for the different translation stage positions. These widths are determined first from directly reading out the measured data (black points and curves in fig. 5.7) and second from the expected spectra, given by eqs. (5.78) and (5.79) each with the respective value for Δx_{MZ} (red curve for a Sech pulse, blue curve for a Gaussian pulse in fig. 5.7). While in fig. 5.7 four representative datasets are shown, all FWHM values of the central spectral fringe in every measured spectrum are displayed in fig. 5.8 as a function of the translation stage setting. The experimental FWHM values show the greatest width at a position $-16.18\,\mu m$, i.e. $\tau = -108\,fs$ off the perfect pulse overlap. However as it will turn out later on (see table 5.5), this spectrum corresponds more closely to the expected one derived from Fourier transforming the $g_1(\tau)$-function. In the following we will thus treat it as a measure for the unmodulated amplitude function $S_0(\lambda - \lambda_0)$ in eqs. (5.76), (5.77). Fitting it with a Gauss- and Sech-envelope, according to eqs. (5.76), (5.77), yields the values $w_{\mathrm{Gauss}} = 0.663 \pm 0.002\,nm$ and $w_{\mathrm{Sech}} = 0.6 \pm 0.003\,nm$, which are to be plugged into eqs. (5.78) and (5.79). The theoretical spectra are shown in figs. 5.7 and 5.8 as red curves for Sech-pulses and blue curves for Gauss pulses. Within fig. 5.8 the expected central oscillation fringe's FWHM, described solely by the $\cos^2\left(\frac{2\pi(\lambda-\lambda_0)}{\lambda_0^2}\Delta x_{MZ}\right)$ term in eqs. (5.75), (5.78) and (5.79), is provided as well, represented by a green curve. It narrows down the FWHM due to increasing oscillation frequencies with greater stage displacements. The FWHM determined by the envelope functions are of course constant over the entire travel range and thus provide

[28] This means the frequency comb tooth whose dispersion compensation is perfect and onto which the cavity length is stabilised.

[29] i.e. from $-400\,fs \leq \tau_{MZ} \leq 400\,fs$ or $-100\,\mu m \leq \Delta x_{MZ} \leq 100\,\mu m$

an upper boundary for decreasing oscillation periods[30], which are represented by the respective y-axis values for the red (Sech-pulse) and blue (Gauss-pulse) curves at $\Delta x_{MZ} = 0$ in fig 5.8, corresponding by construction to the experimental FWHM at $x_{MZ} = -16.18\,\mu m$. The full model functions (5.78), (5.79) resemble the FWHM from the measured data rather closely, especially for small differences in the interferometer arm lengths. For the outermost stage positions the modelled behaviour does not exactly fit to the observed one, which is mainly due to an incomplete modulation depth of the oscillations on the spectra (see fig. 5.7) providing an underestimate of the central peak's FWHM by the theoretical prediction. This lowered modulation depth might e.g. result from unequal electric field amplitudes of the laser pulses leaving the interferometer. However, these spectra comprise enough oscillation maxima to fit the envelope function directly to them, which is also shown by dashed lines in fig. 5.8 a), for the spectrum at $\Delta x_{MZ} = -271.54\,\mu m$, whereby the orange curve represents a Sech-pulse and the blue curve a Gauss-pulse. The FWHM values of these two fits for the datapoints at $\Delta x_{MZ} = -271.54\,\mu m$ and $\Delta x_{MZ} = 228.8\,\mu m$ can now be compared with the reference spectrum at $\Delta x_{MZ} = -16.18\,\mu m$:

$\Delta x_{MZ}[\mu m]$	FWHM with Gauss pulse $[nm]$	FWHM with Sech pulse $[nm]$
-271.54	0.986 ± 0.037	0.954 ± 0.047
-16.18	1.104 ± 0.003	1.058 ± 0.006
228.8	1.014 ± 0.041	0.982 ± 0.064

These values show a quite good resemblance as well[31]. Consequently spectra at greater pulse separations also constitute an envelope function of constant width.

Conclusion for cavity's spectral acceptance The important message here is that the spectra comprise a Gauss- or Sech-pulse envelope of constant width over the entire relevant pulse delay range, modulated only by an oscillating function according to $\cos^2\left(\frac{2\pi(\lambda-\lambda_0)}{\lambda_0^2}\Delta x_{MZ}\right)$ which results from the Mach-Zehnder interferometer. For that reason, the cavity locking condition does not vary during the alteration of x_{MZ} and always the same spectral portion of the external pulse can couple to cavity resonances. That is to say that the spectral acceptance of resonator is constant throughout scanning the pulse separation, since otherwise some frequencies would be missing at certain stage positions, narrowing down the FWHM of the spectral envelope[32] by an additional mechanism on top of the $\cos^2$ function. We therefore do not artificially alter the pulse spectrum and the pulse duration by relocking the resonator at each measured translation stage position while performing the autocorrelation experiment.

5.3.3 SPDC phase-matching bandwidth

Besides showing the insensitivity of the pulse length measurement to the cavity locking parameters, there is another very important issue to be taken care of before one can regard an autocorrelation measurement to provide accurate information about the underlying pulse duration. It concerns the non-linear process involved in generating the $g_2(\tau)$-signal, i.e. the SPDC leading to the emission of HV-photon pairs.

Phase-matching bandwidth We will have to show the FWHM phase-matching bandwidth of the BBO crystal to be at least as spectrally broad as the pump pulse of $\Delta\lambda_p \approx 1.1\,nm$, centred around $\lambda_{p,0} = 390\,nm$. If that is not the case, the analogue scenario to including an interference filter occurs, and parts of the pumping pulse spectrum are cut off by not being able to participate in the frequency conversion. Hence the retrieved data from the autocorrelation functions would imply having a spectrally narrower and, in turn, temporally elongated pump pulse. For commonly available autocorrelator devices, working with SHG, it is rather easy to get an estimate about the phase-matching bandwidth and it is also straight-forward to fulfil the aforementioned requirement. However for SPDC things are not as clear cut. In that respect, a short derivation of the phase-matching bandwidth in the SHG case shall be given, outlining the unsuitability of this approach for SPDC, and subsequently a possible manner to show its sufficiency for the latter process shall be presented.

[30] i.e. decreasing pulse separation Δx_{MZ}

[31] They do not totally coincide within their error boundaries, which have been calculated only from the statistical error in w by the fitting routine. Yet, as we see later on, there is also some additional systematic error present, not yet included here.

[32] and therefore the FWHM of the central spectral fringe

Phase-matching bandwidth in SHG The derivation for the bandwidth in the SHG case can e.g. be found in ([104]) and commonly follows a single mode description, which is extended to broadband pumping by approximations made upon the single mode phase matching condition. Assuming perfect phase matching at a pump wavelength $\lambda_{p,0}$, the phase mismatch at any other wavelength can be expressed as

$$\Delta k(\lambda_p) = 2k(\lambda_p) - k(\lambda_s) = 2\left(\frac{2\pi n\left(\lambda_p\right)}{\lambda_p}\right) - \left(\frac{2\pi n\left(\frac{\lambda_p}{2}\right)}{\frac{\lambda_p}{2}}\right) = \frac{4\pi}{\lambda_p}\left(n\left(\lambda_p\right) - n\left(\frac{\lambda_p}{2}\right)\right), \tag{5.80}$$

whereby for the signal wavelength $\lambda_s = \frac{\lambda_p}{2}$ has been used. If a Taylor expansion is performed for eq. (5.80) around $\lambda_{p,0}$, assuming a deviation of $\delta\lambda_p = \lambda_p - \lambda_{p,0}$, one receives:

$$\Delta k(\delta\lambda_p) = \frac{4\pi}{\lambda_{p,0}}\left(1 - \frac{\delta\lambda_p}{\lambda_{p,0}}\right)\left(n(\lambda_{p,0}) + \delta\lambda_p\frac{d}{d\lambda}n(\lambda_{p,0}) - n\left(\frac{\lambda_{p,0}}{2}\right) - \frac{\delta\lambda_p}{2}\frac{d}{d\lambda}n\left(\frac{\lambda_{p,0}}{2}\right)\right) \tag{5.81}$$

By considering the pumping bandwidth $\delta\lambda$ to be much smaller than the central wavelength $\lambda_{p,0}$, eq. (5.81) can be further simplified to:

$$\Delta k(\delta\lambda) = \frac{4\pi}{\lambda_{p,0}}\left(n(\lambda_{p,0}) + \delta\lambda_p\frac{d}{d\lambda}n(\lambda_{p,0}) - n\left(\frac{\lambda_{p,0}}{2}\right) - \frac{\delta\lambda_p}{2}\frac{d}{d\lambda}n\left(\frac{\lambda_{p,0}}{2}\right)\right) \tag{5.82}$$

Applying the assumption of perfect phase-matching for $\lambda_{p,0}$, i.e. $n(\frac{\lambda_{p,0}}{2}) = n(\lambda_{p,0})$, eq. (5.82) becomes

$$\Delta k(\delta\lambda) = \frac{4\pi}{\lambda_{p,0}}\left(\delta\lambda_p\frac{d}{d\lambda}n(\lambda_{p,0}) - \frac{\delta\lambda_p}{2}\frac{d}{d\lambda}n\left(\frac{\lambda_{p,0}}{2}\right)\right). \tag{5.83}$$

The intensity dependence of the SHG signal for finite crystal lengths L is given by ([104])

$$I_{SHG} = \text{const.} \cdot \text{sinc}^2\left(\Delta k\frac{L}{2}\right)$$

which decreases by a factor of 2 for argument values of $\Delta k\frac{L}{2} = \pm 1.39 \Leftrightarrow \Delta k = \frac{2.78}{L}$ in the sinc^2-function. The phase-matching bandwidth, defined as the wavelength range at whose boundaries $\text{sinc}^2(\alpha) = 1/2$, can thus be expressed by aid of eq. (5.83) as ([104]):

$$\delta\lambda^{SHG}_{phasematch} = \frac{0.44\frac{\lambda_{p,0}}{L}}{|\frac{d}{d\lambda}n(\lambda_{p,0}) - \frac{1}{2}\frac{d}{d\lambda}n\left(\frac{\lambda_{p,0}}{2}\right)|} \tag{5.84}$$

Within the above equations an intrinsic property of the SHG process has been used, namely the change in signal wavelength by $\frac{\delta\lambda}{2}$ for changing the pumping wavelength by $\delta\lambda$. In the SPDC process this is however not the case, rendering the SHG approach for calculating the phase matching bandwidth unsuitable. The reason for the breakdown is the spectral broadening of the down-converted photons with respect to the pump, which results in $\delta\lambda_{s,i} \gg \delta\lambda_p$ and especially $\delta\lambda_{s,i} \neq \frac{\delta\lambda_p}{2}$. For SPDC eq. (5.82) consequently changes into

$$\Delta k(\delta\lambda) = \frac{4\pi}{\lambda_{p,0}}\left(n(\lambda_{p,0}) + \delta\lambda_p\frac{d}{d\lambda}n(\lambda_{p,0}) - n(\lambda_{s,i}) - \delta\lambda_{s,i}\frac{d}{d\lambda}n(\lambda_{s,i})\right)$$

and cannot be resolved for $\delta\lambda_p$ with simultaneous elimination of $\lambda_{s,i}$ anymore, which is necessary to extract information about the phase-matching bandwidth from this approach.

Phase-matching bandwidth in SPDC Since the most simple approach to calculate the bandwidth is not applicable for the non-linear process of choice, another way of estimating the appropriate value is to take advantage from the multi-mode description of SPDC, specifically the expression for the spectrum of the down-conversion photons. The formulae, applied in the following text, are derived in a thorough manner in reference ([101]), wherefore outlining their origin is skipped here. The relevant expression for the spectra of the signal and idler beams are ([101])

$$S_j(\nu_j) = \text{const.}\int_{\infty}^{\infty} d\nu_p |E_p^+(\nu_p)|^2 L^2 \text{sinc}^2\left(\frac{L}{2}\alpha_j\right) \tag{5.85}$$

whereby $j \in \{s, i\}$ and the abbreviations $\nu_p = \omega_p - \omega_{p,0}$, $\nu_s = \omega_s - \omega_{s,0}$, $\nu_i = \omega_i - \omega_{i,0}$ have been used. $E_p(\nu)$ represents the spectral electric field amplitude of the pumping pulse, derived in eqs. (C.1) and (C.2) of the appendix C.1.1 for both pulse models. The constants α_s and α_i are defined by ([101]):

$$\alpha_s = \frac{\nu_p}{V_p} - \frac{\nu_s}{V_s} - \frac{\nu_p - \nu_s}{V_i} + \frac{D_p\nu_p^2}{2} - \frac{D_s\nu_s^2}{2} - \frac{D_i(\nu_p - \nu_s)^2}{2} \tag{5.86}$$

$$\alpha_i = \frac{\nu_p}{V_p} - \frac{\nu_i}{V_i} - \frac{\nu_p - \nu_i}{V_s} + \frac{D_p\nu_p^2}{2} - \frac{D_i\nu_i^2}{2} - \frac{D_s(\nu_p - \nu_i)^2}{2} \tag{5.87}$$

Within this expression, V_j assigns the group velocity, experienced by the beam $j \in \{p, s, i\}$ inside the BBO crystal, and D_j is the group velocity dispersion parameter of the field j. Both quantities are given by ([101]):

$$\frac{1}{V_j} = \frac{dk_j(\omega_j)}{d\omega_j} = \frac{1}{c}\left(n(\lambda_j) - \lambda_j\frac{dn(\lambda_j)}{d\lambda_j}\right) \quad ; \quad D_j = \frac{d^2k(\omega_j)}{d\omega_j^2} = \frac{d}{d\omega_j}\frac{1}{V_j} = \frac{\lambda_j}{2\pi c^2}\frac{d^2n(\lambda_j)}{d\lambda_j^2} \tag{5.88}$$

The width limiting quantity in eq. (5.85) is the phase-matching bandwidth, the value we would like to figure out, which is present implicitly within the sinc^2 term, in a similar way as in the expression for the second harmonic intensity. One way to extract it is to use the theoretical description (eq. (5.85)) and calculate the spectra for signal and idler. Subsequent comparison with experimentally recorded spectra of the SPDC photons, impinging onto the linear optical set-up, proves the absence of spectral cut-off if both datasets coincide with one another. Such a comparison also takes into account the coupling effects of the down-converted photons into the SM fibre behind the cavity's output coupler (see fig. 3.1). Since the signal and idler photons also posses a certain spatial distribution depending on their respective wavelengths ([101]), the numerical aperture of the fibre could in principle disregard photons with certain frequencies and thereby cut off parts of the down-conversion spectra.
Before beginning with the analysis, the reader should acknowledge the simplification originating from ignoring pump beam focussing on the down-converted spectra. Since differently orientated $\vec{k}$-vectors would be introduced this way, more frequencies could fulfil the phase-matching condition, resulting in a broader down-conversion spectrum ([101]).
In order to calculate $S_s(\nu_s)$ and $S_i(\nu_i)$, one has to decide on what to call signal and idler photons in the following, which will be important for choosing the correct refractive index, group velocity and group velocity dispersion. As BBO is a negative uniaxial crystal and mounted with its effective extraordinary axis in V-direction[33], the pumping photons obviously have to be V-polarised. Conveniently the signal photons will be chosen in V-direction as well, experiencing the effective extraordinary refractive index, which in turn makes the idler photons H-polarised and subject to the ordinary refractive index.
Plugging the appropriate directions into eqs. (5.86), (5.87) and rewriting all values as functions of wavelength[34] leaves one, after some trivial replacement steps, with

$$\begin{aligned}
\alpha_s = {} & \frac{1}{V_{ext}(\lambda_{p,0})}\left(\frac{2\pi c}{\lambda_p} - \frac{2\pi c}{\lambda_{p,0}}\right) - \frac{1}{V_{ext}(\lambda_{s,0})}\left(\frac{2\pi c}{\lambda_s} - \frac{2\pi c}{\lambda_{s,0}}\right) \\
& - \frac{1}{V_{ord}\left(\frac{\lambda_{s,0}\lambda_{p,0}}{\lambda_{s,0}-\lambda_{p,0}}\right)}\left(\frac{2\pi c}{\lambda_p} - \frac{2\pi c}{\lambda_{p,0}} - \frac{2\pi c}{\lambda_s} + \frac{2\pi c}{\lambda_{s,0}}\right) \\
& + \frac{1}{2}D_{ext}(\lambda_{p,0})\left(\frac{2\pi c}{\lambda_p} - \frac{2\pi c}{\lambda_{p,0}}\right)^2 - \frac{1}{2}D_{ext}(\lambda_{s,0})\left(\frac{2\pi c}{\lambda_s} - \frac{2\pi c}{\lambda_{s,0}}\right)^2 \\
& - \frac{1}{2}D_{ord}\left(\frac{\lambda_{s,0}\lambda_{p,0}}{\lambda_{s,0}-\lambda_{p,0}}\right)\left(\frac{2\pi c}{\lambda_p} - \frac{2\pi c}{\lambda_{p,0}} - \frac{2\pi c}{\lambda_s} + \frac{2\pi c}{\lambda_{s,0}}\right)^2
\end{aligned} \tag{5.89}$$

and the according α_i by replacing $s \to i$, $V_{ext}(\lambda_s, 0) \to V_{ord}(\lambda_i, 0)$, $V_{ord}\left(\frac{\lambda_{s,0}\lambda_{p,0}}{\lambda_{s,0}-\lambda_{p,0}}\right) \to V_{ext}\left(\frac{\lambda_{i,0}\lambda_{p,0}}{\lambda_{i,0}-\lambda_{p,0}}\right)$, $D_{ext}(\lambda_s, 0) \to D_{ord}(\lambda_i, 0)$, $D_{ord}\left(\frac{\lambda_{s,0}\lambda_{p,0}}{\lambda_{s,0}-\lambda_{p,0}}\right) \to D_{ext}\left(\frac{\lambda_{i,0}\lambda_{p,0}}{\lambda_{i,0}-\lambda_{p,0}}\right)$. Within these expressions, variables designated *ext* represent quantities for the effective extraordinary refractive index and such identified *ord* stand for the ordinary refractive index. If the correct BBO crystal length of $L_{BBO} = 1\,mm$ is considered, the sinc^2-function part of eq. (5.85) can be calculated for signal and idler. The resulting graphs are

[33] See subsec. 6.1.1 for details on these terms.
[34] That means: $\nu_j = \omega_j - \omega_{j,0} = \frac{2\pi c}{\lambda_j} - \frac{2\pi c}{\lambda_{j,0}}$

Emission direction in BBO	Experimental FWHM $[nm]$	Theoretical FWHM$[nm]$
extraordinary	9.18	10.35
ordinary	8.2	8.48

Table 5.1: Theoretically calculated and measured FWHM values of SPDC photon spectra in signal and idler direction.

show in fig. 5.9 with an appropriate pump and signal/ idler wavelength range of $370\,nm \leq \lambda_p \leq 410\,nm$ and $755\,nm \leq \lambda_s \leq 805\,nm$ as a 3 dimensional plot and, for a better observability of the wavelength dependence, as a contour plot, in which bright regions indicate lower phase mismatch and thus greater SPDC conversion efficiency[35]. It shall be noted here, that the phase-matching curves are not the same for the signal and idler directions, thereby do neither have the same widths nor gradients $\frac{d}{d\lambda_p}\lambda_{s,i}(\lambda_p)$, leading towards two different spectra to be expected for signal and idler. This has furthermore some implications on the quantum mechanical correlations between signal and idler photons as well as their indistinguishibility, which are both described in more detail in reference ([102]). For our way of discussing the phase-matching bandwidth it is however sufficient to just use these sinc^2-functions, inserted into eq. (5.85). The pump envelope function $|E_p(\nu_p)|^2$ is assumed to be a Sech-pulse with a spectral amplitude for the relevant positive frequency part, given by the FT of the electric field in the time domain, of:

$$|E_p(\nu_p)|^2 = \mathrm{sech}^2\left(\pi^2 \Delta t\left(\frac{c}{\lambda_p} - \frac{c}{\lambda_{p,0}}\right)\right) \tag{5.90}$$

Its width parameter Δt is determined from fitting eq. (5.90) to our reference spectrum obtained at the translation stage position $\Delta x_{MZ} = -16.18\,\mu m$, yielding $\Delta t = 85.75\,fs$, and the central wavelength is fixed at $\lambda_{p,0} = 390\,nm$. From the former, a FWHM value for the fitted UV pumping spectrum of $\Delta\lambda_p \approx 1.12\,nm$ can be obtained.
The integrals for the signal and idler spectra are solved by numerical integration within a pump wavelength range of $370\,nm \leq \lambda_p \leq 410\,nm$ and a step size of $\delta\lambda_{p,int} = 0.01\,nm$, reaching well beyond the region of considerable UV intensity. Calculations provide the signal and idler spectrum given by the red and blue curve in fig. 5.10, respectively. The experimentally measured data is displayed in the same plots by the black points and the black curve. In comparing both datasets, particular attention has to be paid to the allocation of the correct experimental spectra with respect to their theoretical counterpart. Since the polarisation of the SPDC photons gets rotated by the $\lambda/2$-waveplate behind the cavity output coupler (see fig. 3.1) to cancel beam walk-off[36], the spectrum for the extraordinary refractive index direction in the BBO, generating V-polarised photons, has to be compared to the spectrum recorded for H-polarised photons, detected in arm a of the linear optical set-up; vice versa for the ordinary spectrum. If one fits the calculated spectra, shown as green curves in fig. 5.10, and the experimental ones, drawn as grey curves in fig. 5.10, with a Sech proportional to eq. (5.90), followed by calculating the FWHM values of all four fitted functions, the values stated in table 5.1 are yielded.
The data-sets show good resemblance between the expected and actually measured values. For a quantitative comparison, the resolution of the single photon spectrometer, used to record the experimental data, has to be taken into account, which is $\Delta\lambda_{spec} \approx 0.5\,nm$ at $\lambda \approx 780\,nm$. Keeping that in mind, the FWHM values for the ordinary refractive index direction in the BBO coincide and the numbers for the extraordinary direction are only slightly deviating from each other. We can therefore regard the calculated SPDC spectra to be in agreement with the ones present during our experiment and accordingly assume phase-matching over the entire pumping pulse bandwidth, indicating the absence of spectral cut-off and associated pulse broadening by the non-linear process.
Nevertheless, for completeness, a quick estimation about the additional error on the pulse width, imparted by the extraordinary spectral mismatch $\delta\lambda$ from the experimental value $\Delta\lambda_{exp}^{FWHM} = 9.18\,nm$, shall be conducted: Conceiving the worst case with the entire $\delta\lambda = 1.17\,nm$ being the spectral cut-off caused by the non-linear process

$$\alpha_{spec-cut-off} = \frac{\delta\lambda}{\Delta\lambda_{exp}^{FWHM}} \cdot 100 \approx 12.7\%$$

of the SPDC spectrum are discarded by phase-mismatch. Simplifying the spectral dependence between pump and signal/ idler as linear, that would mean a non-consideration of $\approx 12.7\%$ of the input spectrum.

[35] The ranges for λ_p and λ_s have been chosen according to the values applied in the numerical integration of eq. (5.85) stated below. Also the curvatures of the phase-matching is better visible for such a broader range.
[36] See discussion in subsec. 6.2.2 for details.

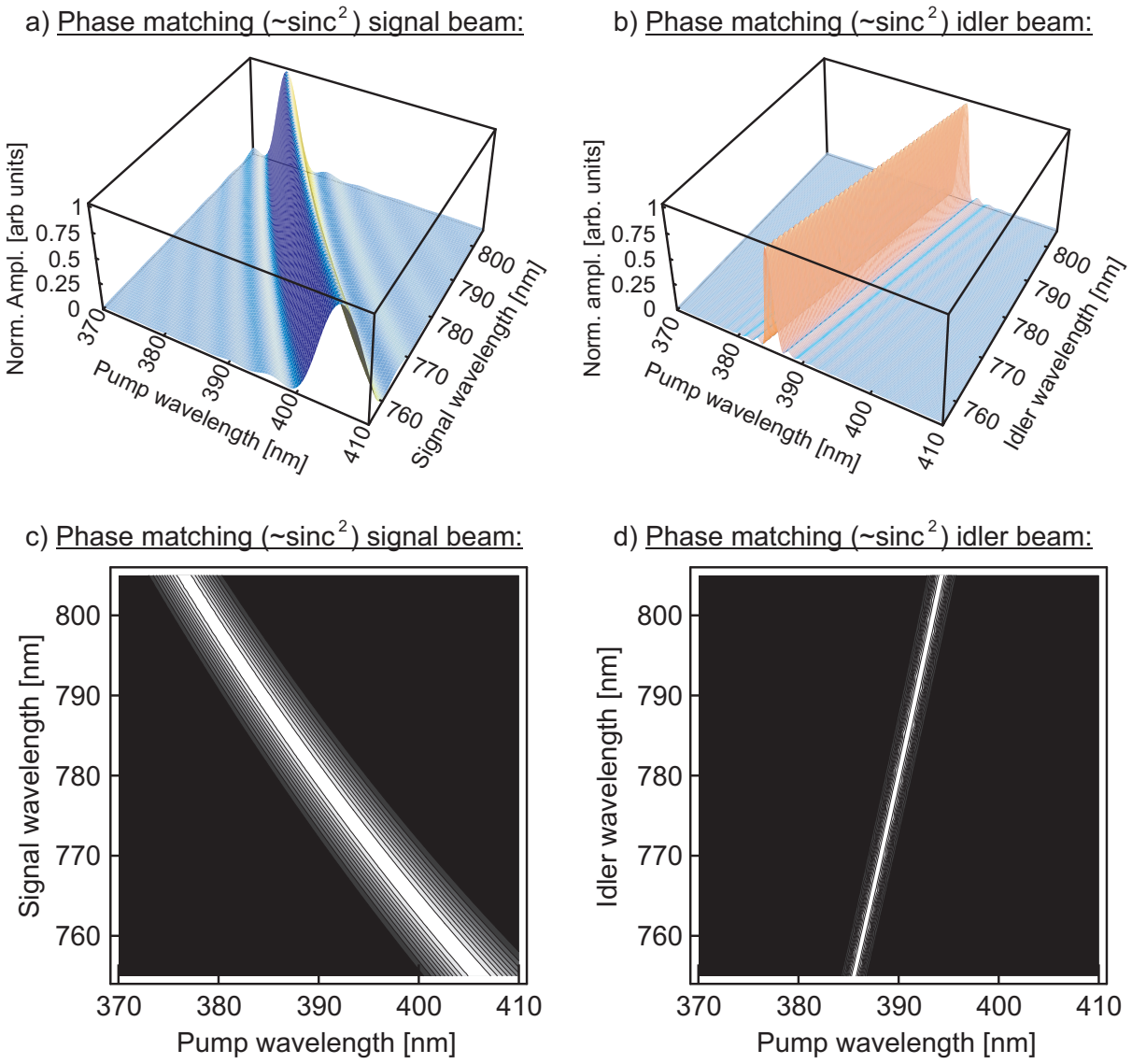

Figure 5.9: Sinc^2 phase matching functions for a $1\,mm$ BBO crystal as incorporated in the expression for the SPDC spectra, eq. (5.85). The left column shows calculations for the signal beam and the right one for the idler beam. The three dimensional plot in the upper row shows the increase of the Sinc^2 term as a function of pump and signal/ idler wavelength, whereby the two dimensional contour plot in the lower row gives better estimation about the bandwidths available for converting the pump to signal/ idler. For further details see main text.

Since the relationship between errors in the expression connecting tbe FT limited pulse duration and the bandwidth is linear as well, i.e. $\delta\tau \sim |\left(\frac{d}{d\nu}\tau(\nu)\right) \cdot \delta\nu|$ and $\delta\nu \sim \left(\frac{d}{d\lambda}\nu(\lambda)\right)\delta\lambda$, giving $\delta\tau \sim \delta\lambda$, a pulse of roughly 12.7% longer duration would result from this mismatch. With the FT limited pulse duration, calculated later on from the $g_1(\tau)$-function, of $\approx 150\,fs$ (see table 5.3), the potential cut-off would result in a pulse elongation of $\delta\tau \sim \alpha_{spec-cut-off} \cdot 150\,fs \approx 19\,fs$. Referring to later results, the pulse duration from the $g_2(\tau)$-function will be shown to have an error boundary of $\approx 20\,fs$ from spectral mismatch and fitting uncertainties (see table 5.8), which implies that even in the worst case of phase-mismatch, the pulse would not be too severely broadened to cause serious deviations in the resulting pulse duration, preventing the applicability of the underlying measurement itself. Ultimately the autocorrelation experiment is only devised to provide an estimation about the pulse length and not to achieve absolute accuracy in the range of a few femto-seconds anyway. From this perspective the spectral resemblance and associated phase-matching is good enough.

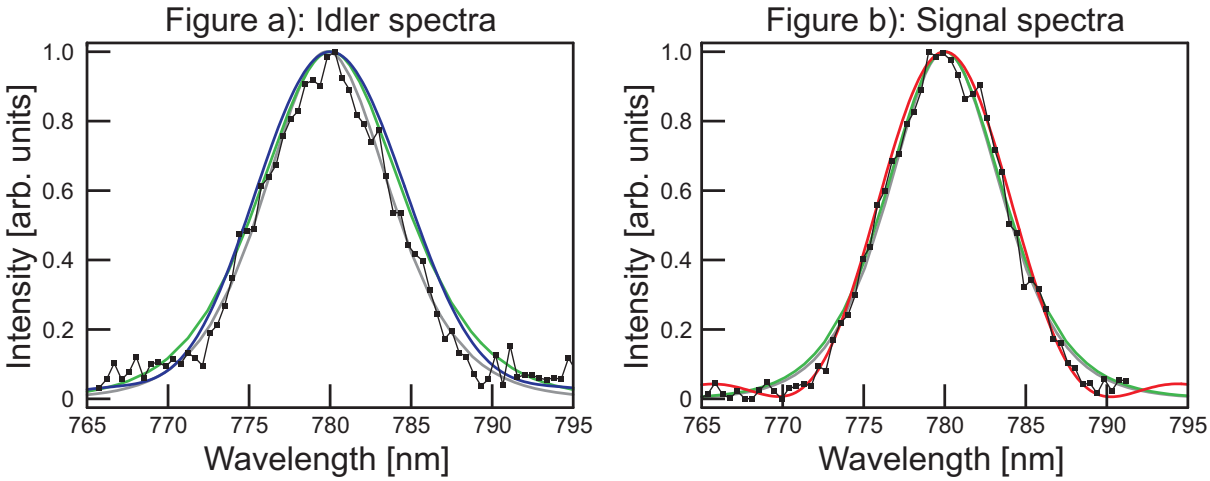

Figure 5.10: Comparison between the calculated SPDC spectra by eq. (5.85) and the experimentally measured spectra for signal and idler photons in our linear optical set-up. Plot a) represents the ordinary and plot b) the extraordinary direction in the crystal, which accord to vertically and horizontally polarised photons, respectively. Black points correspond to the recorded data. The Sech spectrum along the extraordinary direction is shown as a red line, and its counterpart along the ordinary axis is drawn in blue. The green lines represent fitted Sech pulse shapes to the calculated spectra, given by eq. (5.90). The grey lines are analogous Sech fits to the experimental data.

5.3.4 Interference of first order

After showing, that all necessary prerequisites are fulfilled, we can now proceed to the actual experimental findings. These are discussed by first looking at the interference of first order, which does provide a lower boundary for the possible UV pulse length and also carries some information about how well the interferometer is aligned. The data obtained for the $g_1(\tau)$ correlation function (eq. (5.9)), measured by the photodiode in the output arm 1 of the Mach-Zehnder interferometer is presented in fig. 5.11 indicated by black points. The x-axes in these plots represent the femto-second time separation between both pulses $\tau_{MZ} = \frac{2\Delta x_{MZ}}{c}$ with interference taking place inside an interval of roughly $-400\,fs \leq \tau \leq +400\,fs$. As the individual interference fringes are too narrow to be resolved in a plot over the entire interference range, a small portion around $-10\,fs \leq \tau \leq +10\,fs$ pulse delay has been cut out and shown separately in fig. 5.11 b). These fringes will be evaluated first, followed by an analysis of the visibility and the $g_1(\tau)$-function.

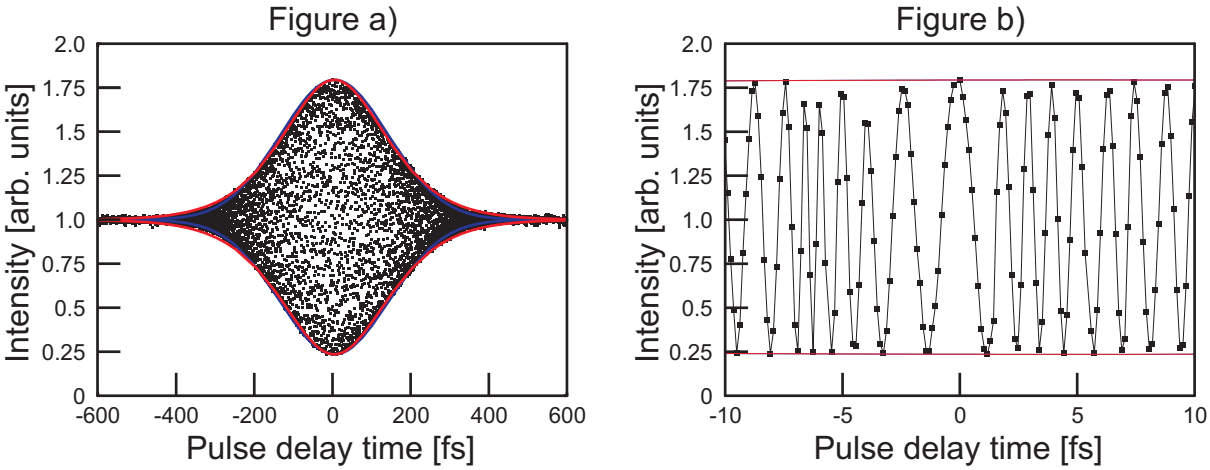

Figure 5.11: Interference function of first order as measured by the photodiode in output arm 1 of the Mach-Zehnder interferometer. Plot a) shows the entire interferogram, which is narrowed down to an interval around $-10\,fs \leq \tau \leq +10\,fs$ pulse delay in plot b). The black points represent experimental data, the blue curve is the fitted $g(\tau)$ function for Gaussian pulses, according to eq. (5.16), whereby the red curve displays its Sech-shaped counterpart following eq. (5.20).

Interference fringes From the interference fringe pattern (fig. 5.11) one can infer the carrier wavelength λ_0 of the optical pulses by aid of the fringe width. The distance between two fringe nodes[37] corresponds to a time separation of $\tau_{MZ} = \frac{\lambda_0}{2}c$ between both pulses. In order to determine this duration, the widths of 51 interference fringes, lying within the range of $-32.1\,fs \leq \tau \leq 32.2\,fs$, has been evaluated for maxima and minima of interference[38] with subsequently calculating their common average value and the standard deviation. For the latter, we obtain

$$\Delta\bar{x}_{fringes} = 189 \pm 54\,nm, \tag{5.91}$$

resulting in a pulse carrier wavelength of

$$\lambda_0 = 2 \cdot \Delta\bar{x}_{fringes} = 378 \pm 107\,nm. \tag{5.92}$$

Not surprisingly the outcome in eq. (5.92) ties in with the expected $\lambda_0 = 390\,nm$ within its error boundaries, since these are quite large rendering this method to conclude back on the carrier wavelength rather unsatisfying. It does not really matter for the determination of λ_0, because the UV spectra have been recorded for the correlation measurement as well (see fig: 5.7) enclosing λ_0 as their respective maximum value.
In terms of the accuracy in translation stage positioning, the error thereon is considered to be on the order of 1 step, which amounts to a distance of approximately $\delta(\Delta x_{MZ}) = 20\,nm$. The resulting uncertainty in pulse separation is $\delta\tau = \frac{2\delta(\Delta x_{MZ})}{c} \approx 0.3\,fs$. Having a FWHM value for the $g_2(\tau)$-function of $FWHM_{g_2}^{\text{Sech}} \approx 305\,fs$ (see fig. 5.16), the precision of the translation stage would add a maximum cumulative error of $\delta\tau_{stage} = 0.6\,fs$, constituting an uncertainty on the order of 0.2%. Since the dependence between $FWHM_{g_2}^{\text{Sech}}$ and the pulse duration $\tau_{pulse}^{\text{Sech}}$ (see table 5.8) is linear, an error of $\delta\tau_{pulse}^{\text{Sech}} \approx 4\,fs$ is to be expected on the latter, which is small compared to the errors of $21\,fs$ from other sources of uncertainty. Hence this systematical error will be neglected.

Interferometer stability Since the Mach-Zehnder interferometer is not actively stabilised, it is furthermore important to certify the constancy of the pulse separation during measuring each datapoint. In other words constancy in pulse interference over time is necessary. For this purpose the optical power level impinging onto the photodiode in output 1 of the Mach-Zehnder interferometer (see fig. 5.13) has been monitored while measuring the correlation curves for the intra-cavity signals. Accordingly, at the maximum of the correlation curves $g_1^{\text{cavity}}(\tau)$, $g_1^{\text{HV coinc.}}(\tau)$, $g_2^{\text{HHVV coinc.}}(\tau)$, the signal on the photodiode reaches its minimal level. To show the constance of the interference condition, the power on the photodiode is displayed in fig. 5.12 as a function of its constituting sampling points, whereby one datapoint in the correlation functions corresponds to 8 sampling points of 1 *sec* duration, for the exemplary pulse separations of $\tau_{MZ} = -1810\,fs$ (red curve) and $\tau_{MZ} = 0\,fs$ (black curve). Additionally the entire interference signal on the photodiode, measured in the second run, has been shown as a function of pulse delay time by a grey curve. The power levels for $\tau_{MZ} = -1810\,fs$ and $\tau_{MZ} = 0\,fs$ must be analysed in their fluctuations, whose amplitudes should be negligible for achieving interferometric stability. Comparing those with certain points on and the height of the $g_1(\tau)$-curve shows that the intensity on the photodiode is rather constant throughout the measurement. Hence the interferometer arm lengths do neither drift away, nor vibrate around the appropriate length for constructive interference considerably. The former effect would reveal itself in a steadily increasing/ decreasing power-level, whereas the latter would result in oscillations about an average value. Both are not apparent to an extend requiring active stabilisation of the Mach-Zehnder interferometer and we can proceed towards the actual measurements of the correlation functions.

Interference visibility and b parameter The interference visibility is commonly defined as:

$$V_{int} = \frac{I_{max} - I_{min}}{I_{max} + I_{min}}, \tag{5.93}$$

whereby I_{max} is the maximal intensity (at constructive interference) achieved within the overall interference region and I_{min} is the corresponding minimal one (at destructive interference); these are in our particular case $I_{max} = 1.794$ and $I_{min} = 0.235$ yielding a visibility of $V = 0.7681$. The visibility is a measure for the fractions of both pulses, that interfere with one another, yielding $V = 1$ for perfect

[37] or anti-nodes as well

[38] Use was made of the nodes in the interference pattern as the precision of the chosen step size of the translation stage is not accurate enough to reliably hit the interference maxima and minima at each instant, whereby the nodes are precisely defined by the background signal level outside the interference region, measured with high statistics.

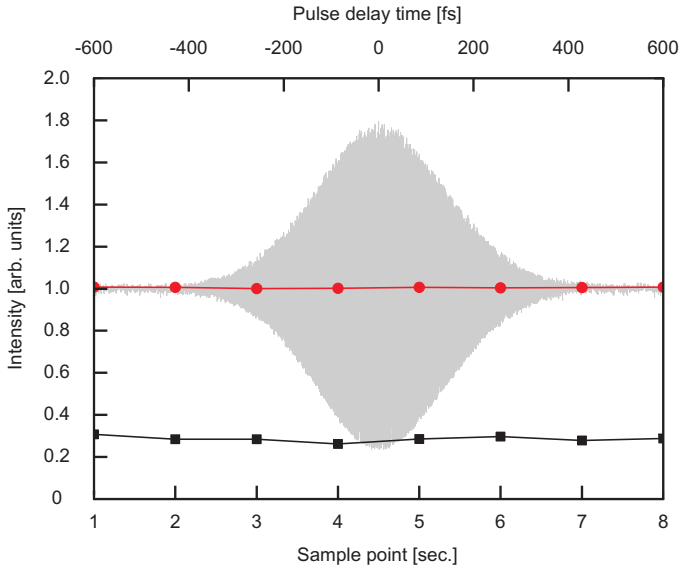

Figure 5.12: Interferometer stability: Power level on photodiode at pulse separations of $\tau_{MZ} = -1810\,fs$ represented by the red curve and $\tau_{MZ} = 0\,fs$ represented by the black curve, normalised to the background signal provided by the average of the combined power level data at pulse separations $\tau_{MZ} = -1810\,fs$ and $\tau_{MZ} = 1525\,fs$. The normalised $g_1(\tau)$-correlation function, depending on pulse delay time, is plotted in grey as well, providing a means for comparison of the variations in the power level.

interference and $V = 0$ for its absence. Having $V < 1$ indicates the interferometer to be not perfectly aligned, which can be due to three reasons:

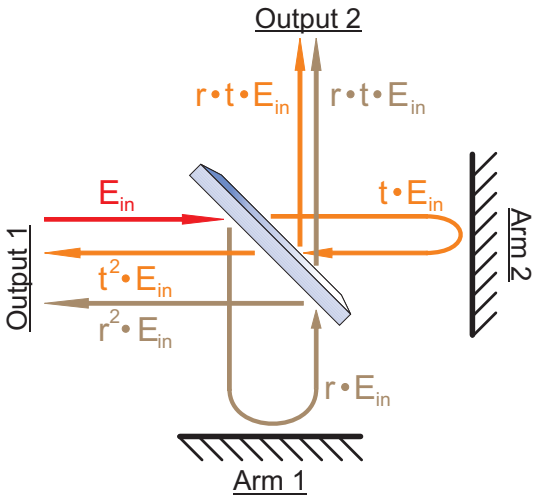

Figure 5.13: The Mach-Zehnder interferometer set-up incorporated in the experiment, including the transmitted and reflected electric fields, which derive from the input field E_{in} by application of the reflectivity r and transmittivity t of the beam splitter.

1. The splitting ratio of the beam splitter within the interferometer might not be 50 : 50, i.e. $R \neq T \neq \frac{1}{2}$. However this flaw would just affects the output arm, which back-reflects the beam (output 1 in the fig. 5.13) into the incoming spatial mode. In order to see that, the visibility for both arms in an arbitrary interferometer shall shortly be calculated. In output 1 it is expected to be

$$V_1' = \frac{((t^2+r^2)^2 - (t^2-r^2)^2)E_{in}^2}{((t^2+r^2)^2 + (t^2-r^2)^2)E_{in}^2} = \frac{1-(T-R)^2}{1+(T-R)^2},$$

therefore having $V < 1$, if $T \neq R$. Yet for output 2, with

$$V_2' = \frac{((rt+tr)^2-(rt-tr)^2)E_{in}^2}{((rt+tr)^2+(rt-tr)^2)E_{in}^2} = 1,$$

it turns out to be independent of r and t. Since in our experiment the photodiode measures V_1 for the apparent beam-splitter reflectivity $r = \sqrt{R} = 0.7518$ and transmittivity $t = \sqrt{T} = 0.6594$, a maximally visibility of still $V_1' = 0.967$ could in principle be expected.

2. The polarisation state of light between both arms might not match. Most likely such a deviation is caused by some residual birefringence in the beam splitter[39], an effect we are already familiar with from the linear optical set-up discussed in section 3.3, where it gets cured by inserting additional pairs of YVO_4 crystals. In order to check for it, a Glan-Thomson prism ([84]) has been placed in output 2, generating a walk-off between the components of the incoming light polarised along the prism's ordinary or extraordinary refractive index axis. The optical power achieved for each polarisation direction is given below, whereby the respective electric field amplitudes have been calculated by $P_k = \alpha \cdot |E_k|^2 = A_{beam} \cdot \frac{1}{2} c\epsilon_0 n_{air} |E_k|^2$, with k representing the polarisation, A_{beam} the beam diameter, ϵ_0 is the permittivity of vacuum, n_{air} the refractive index of air and α the proportionality constant between the time averaged electric field and the time averaged optical power.

MZ Arm	P_{ord} $[mW]$	P_{ext} $[mW]$	E_{ord} $[1/\alpha]$	E_{ext} $[1/\alpha]$
1	53	15	7.3	7
2	49	15	3.9	3.9

Thus the polarisation in the interferometer is only slightly mismatched. Unfortunately it has not been possible to get rid of this misalignment, because inserting another birefringent optical element available to us[40] added absorption and thereby degraded the visibility to an extend exceeding the gain from polarisation compensation contribution. Nevertheless the theoretically achievable visibility can be calculated from the aforementioned polarisations, requiring the treatment of the electric field contributions to the maximal and minimal intensity with respect to their polarisation. With $E_{ord,j} := \gamma_{ord,j}\alpha$ and $E_{ext,j} := \gamma_{ext,j}\alpha$, the intensities at extremal constructive and destructive interference become

$$\begin{aligned}
I_{max}^{output1} &= (t^2E_{ord,2} + r^2E_{ord,1})^2 + (t^2E_{ext,2} + r^2E_{ext,1})^2 \\
&= \alpha^2((t^2\gamma_{ord,2} + r^2\gamma_{ord,1})^2 + (t^2\gamma_{ext,2} + r^2\gamma_{ext,1})^2) \\
&= 66.2\alpha^2 \\
I_{min}^{output1} &= (t^2E_{ord,2} - r^2E_{ord,1})^2 + (t^2E_{ext,2} - r^2E_{ext,1})^2 \\
&= \alpha^2((t^2\gamma_{ord,2} - r^2\gamma_{ord,1})^2 + (t^2\gamma_{ext,2} + r^2\gamma_{ext,1})^2) \\
&= 1.4\alpha^2 \\
I_{max}^{output2} &= (rtE_{ord,2} + trE_{ord,1})^2 + (rtE_{ext,2} + trE_{ext,1})^2 \\
&= RT\alpha^2((\gamma_{ord,2} + \gamma_{ord,1})^2 + (\gamma_{ext,2} + \gamma_{ext,1})^2) \\
&= 263.83RT\alpha^2 \\
I_{min}^{output2} &= (rtE_{ord,2} - trE_{ord,1})^2 + (rtE_{ext,2} - trE_{ext,1})^2 \\
&= RT\alpha^2((\gamma_{ord,2} - \gamma_{ord,1})^2 + (\gamma_{ext,2} - \gamma_{ext,1})^2) \\
&= 0.08RT\alpha^2
\end{aligned}$$

yielding visibility values in both output arms of:

$$V_1' = 0.9585 \quad ; \quad V_2' = 0.9994 \tag{5.94}$$

As expected, the visibility is degraded for unmatched polarisations, however the effect for our set of parameters is rather small and $V_1' = 0.9585$ is still greater than the experimentally determined value of $V_1 = 0.7681$.

[39] Of course under the assumption of having no birefringent media in either interferometer arm.
[40] Which would have either been a YVO_4-crystal or a quartz-glass plate.

3. Incomplete spatial mode matching also reduces the interference and therefore its visibility, due to the absence of interference between non overlapping parts of the respective electric fields from both pulses. We can estimate the non perfect transverse mode overlap in output 2 of the interferometer by the amount of light coupled into the cavity from each interferometer arm: As we have seen in subsec. 3.1.2 the resonator operates as a spatial mode filter. From the signal strengths of the internally excited resonances for the free-running cavity[41] we can infer a difference between the coupling efficiencies for light from both interferometer arms, which leads to an expectation for a degraded interference of $V = 74\,\%$. It shall thus be noticed, that the major contribution, degrading the visibility of the Mach-Zehnder interferometer, stems from a non perfect transverse mode matching. Unfortunately it has not been possible to improve the interference by further alignment.

After understanding where the flaws in the implemented Mach-Zehnder interferometer lie, the $g_1(\tau)$-correlation function shall now be evaluated in output 1 and 2. In the theory part, subsec: 5.2.1, the fitting functions by assumption of Gauss- or Sech-pulses, with a variable electric field amplitude for each pulse, have been calculated. The results for fitting curves derived for intra-cavity quantities, i.e. HV-coincidences and the cavity level, are stated in eqs. (5.16) and (5.20). The fitting functions for the interference pattern on the photodiode are obtained in the same way as computing eqs. (5.66) and (5.67) in subsec. 5.2.3, by setting $a^2 = b^2$ in the denominator of eqs. (5.16) and (5.20). The reason is the absence of spatial mode filtering outside of the resonator, which necessitates to have different background level contributions from both pulses for intra-cavity correlation function. In the following analysis, we furthermore normalise the contributions from both pulses to the $g_i(\tau)$ functions by conveniently setting $a = 1$. For fitting the interference pattern observed on the photodiode (fig. 5.11), the HV coincidence rates as well as the cavity level, both shown in fig. 5.14, the maximum of the fit-function is fixed to the maximum value in the dataset. Since $g_1^{l,\mathrm{output1}}(0) = 1 + b$ and $g_1^{l,\mathrm{output2}}(0) = 1 + \frac{2b}{1+b^2}$. We can extract the respective parameters b from the measured data and conclude from the ones obtained for intra-cavity quantities onto an interference visibility within the resonator. The latter is calculated[42] from the following electric fields

$$\begin{aligned} E_{ord}^{arm1} &= r \cdot b \cdot \gamma_{ord,1}\alpha \quad ; \quad E_{ord}^{arm2} = t \cdot a \cdot \gamma_{ord,2}\alpha \\ E_{ext}^{arm1} &= r \cdot b \cdot \gamma_{ext,1}\alpha \quad ; \quad E_{ext}^{arm2} = t \cdot a \cdot \gamma_{ext,2}\alpha, \end{aligned}$$

providing a visibility in output mode 2 of:

$$V_2 = \frac{((rE_{ord}^{arm2} + tE_{ord}^{arm1})^2 + (rE_{ext}^{arm2} + tE_{ext}^{arm1})^2) - ((rE_{ord}^{arm2} - tE_{ord}^{arm1})^2 + (rE_{ext}^{arm2} - tE_{ext}^{arm1})^2)}{((rE_{ord}^{arm2} + tE_{ord}^{arm1})^2 + (rE_{ext}^{arm2} + tE_{ext}^{arm1})^2) + ((rE_{ord}^{arm2} - tE_{ord}^{arm1})^2 + (rE_{ext}^{arm2} - tE_{ext}^{arm1})^2)}$$

Inserting the relevant expressions for $r = 0.7518$, $t = 0.6594$, $a = 1$, $\gamma_{ord,1} = 7.28$, $\gamma_{ext,1} = 3.87$, $\gamma_{ord,2} = 7$, $\gamma_{ext,2} = 3.87$ gives the visibility inside the cavity as a function of the b parameter:

$$V_2 \approx \frac{1.94 \cdot b}{0.94 + b^2} \tag{5.95}$$

Evaluating the datasets for all measured b parameters as well as visibilities (eq. (5.95)) yields the values shown in table 5.2, in which the b parameter for HHVV coincidences[43] and the first order interference visibility, deduced thereof, have additionally been included in order to allow for a complete discussion of the visibility at this point. The b parameter for output 1 is obviously different to the cases of examining HV coincidences or the cavity level, which is associated with the different denominators in the fitting functions for $g_1(\tau)$ and their underlying experimental situations.
One can deduce from table 5.2 a close resemblance between the visibility values for output 1 and output 2 observing four-fold coincidences. The results for the cavity level lie slightly below and the ones for HV coincidences above the latter; these should however also coincide with b_{HHVV} and $V_2(HHVV)$, since the optical mode inside the cavity is well defined. Unfortunately the reason for this mismatch is still unclear. In the following the values for all three first order interference cases will thus always be provided[44].

[41] i.e. while the FSR of the cavity is scanned by moving the fast PZT over its entire range

[42] taking into account the transmittivity and reflectivity of the beam splitter in the interferometer as well as the polarisation mismatch in terms of $\gamma_{ord,j}$ and $\gamma_{ext,j}$.

[43] Stemming from fitting the HHVV coincidence data by eqs. (5.51) and (5.53) as discussed in subsec. 5.3.5.

[44] i.e. signal on photodiode in output 1, cavity power level and HV coincidences

	Out 1: Int. max.	Out 2: Cavity level	Out 2: HV coinc.	Out 2: HHVV coinc.
b	0.79	0.41	0.58	0.44
V	0.77	0.71	0.88	0.75

Table 5.2: b parameter and visibilities for the interference of first order in both output of the MZ interferometer. The visibility for output 1 is a measured value, whereas the other three are calculated according to eq. (5.95) by aid of their experimentally determined b parameter.

Fourier transform limited pulse duration By fitting the obtained datasets for the HV-coincidences and the intra-cavity power level with the $g_1(\tau)$-functions (5.16) and (5.20), the minimal achievable pulse duration within the cavity, referred to as Fourier transform limited pulse duration, can be obtained. The measured data is shown in fig. 5.14 by black squares, the fitted $g_1^{\text{Sech}}(\tau)$ by a red line and the fitted $g_1^{\text{Gauss}}(\tau)$ by a blue line. Additionally the interference pattern obtained in output 1 has also been fitted[45] with the results displayed in fig. 5.11 by the same colour coding for Sech- and Gauss-pulses.

The results for the width parameters Δt from fitting the $g_1^l(\tau)$-functions to the three datasets can now be used to conclude onto the minimal possible FWHM pulse duration $\tau^{FT,l}$ by application of the conversion factors $\alpha_{g_1}^l$, eqs. (5.27) and (5.28), providing the FWHM of the respective $g_1(\tau)$ function and subsequent multiplication with $\gamma_{g_1}^l$, stated in eqs. (5.29) and (5.30), to yield $\tau^{FT,l}$, whereby $l \in \{\text{Sech}, \text{Gauss}\}$. The resulting values for Δt and τ_{pulse}^{FT} are displayed in table 5.3, itemised according to the various pulse shapes and datasets.

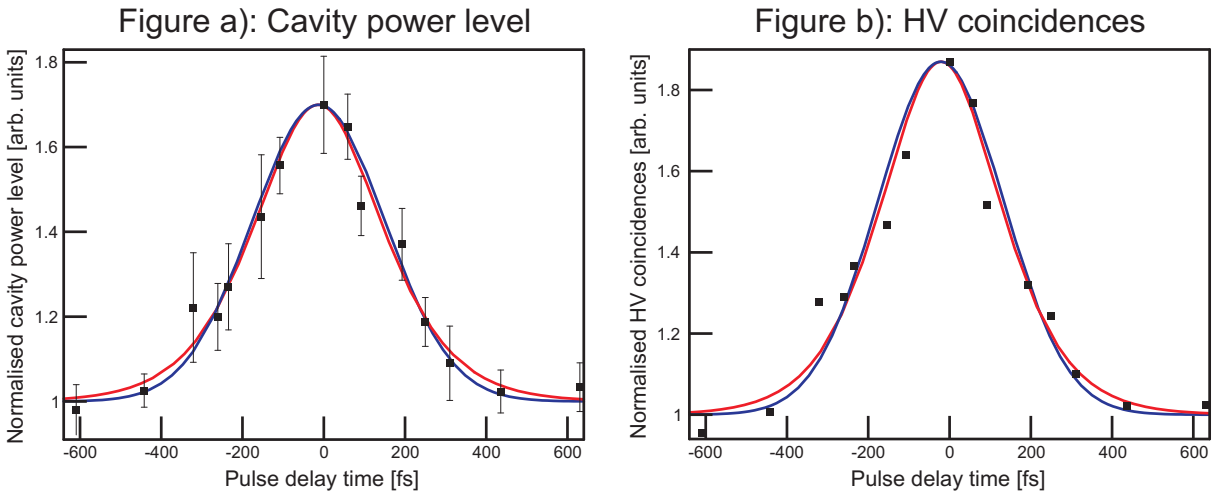

Figure 5.14: Intra-cavity $g_1(\tau)$ correlation functions. Plot a) shows the outcomes for the cavity level and plot b) the ones for HV coincidences. Black boxes indicate measured data, red lined the fitted $g_1(\tau)$ function for Sech pulses and blue lines the fitted $g_1(\tau)$ function for Gaussian pulses.

	Photodiode [fs]	Cavity level [fs]	HV coinc. [fs]
τ^{Sech}	126.3 ± 5.6	149.8 ± 10.9	140.06 ± 11.68
τ^{Gauss}	162.4 ± 10.2	192.8 ± 16.8	182.09 ± 18.36
Δt^{Sech}	71.7 ± 3.2	85 ± 6.2	79.5 ± 6.6
Δt^{Gauss}	97.5 ± 6.1	115.8 ± 10.1	109.4 ± 11

Table 5.3: Fourier transform limited pulse durations.

Regarding first the interference pattern sampled by the photodiode in output 1, the quantities in table 5.3 shall be noted to represent the maxima of interference only. The minima have also been evaluated, as shown in fig. 5.11, delivering approximately the same numbers ($\tau^{\text{Sech}} = 129.05 \pm 5.61\, fs$ and $\tau^{\text{Gauss}} = 163.59 \pm 10\, fs$) as expected and are therefore neglected in the further discussion. The errors for both quantities comprise two contributions, one statistical and one systematic in nature. The former is received simply from the fitting error of the $g_1^l(\tau)$-functions to the respective measurement curves. It provides

[45] With functions analogue to (5.16) and (5.20) with $a^2 = b^2$ in their denominator, as outlined in the last paragraph.

an uncertainty in the parameter $\delta_{\text{stat}}(\Delta t)$, which is further taken care of by Gaussian error propagation, leading to an error in the minimal pulse duration $\delta_{\text{stat}}\tau^{FT}_{\text{pulse}}$ of:

$$\delta_{\text{stat}}\tau^{FT}_{\text{pulse}} = \sqrt{\left(\frac{\partial}{\partial(\Delta t)}\gamma^l_{g1}\alpha^l_{g1}\Delta t\right)^2 \delta_{\text{stat}}(\Delta t)^2} = \gamma^l_{g1}\alpha^l_{g1}\delta_{\text{stat}}(\Delta t) \tag{5.96}$$

As this error is different for each measurement, the individual values are as follows:

	Photodiode [fs]	Cavity level [fs]	HV coinc. [fs]
$\delta_{\text{stat}}(\Delta t^{\text{Sech}})$	0.16	3.17	3.6
$\delta_{\text{stat}}\tau^{\text{Sech}}$	0.28	5.6	6.35
$\delta_{\text{stat}}(\Delta t^{\text{Gauss}})$	0.34	4.31	5.25
$\delta_{\text{stat}}\tau^{\text{Gauss}}$	0.57	7.18	8.74

The much smaller numbers for the measurement by the photodiode compared to the intra-cavity quantities are due to the larger number of recorded interference maxima, yielding better statistics and less uncertainty (see fig. 5.11 and 5.14).
The systematic error adds another uncertainty $\delta_{\text{sys}}(\Delta t^{\text{Sech}}) = 3.06\,fs$ and $\delta_{\text{sys}}(\Delta t^{\text{Gauss}}) = 5.78\,fs$, leading to $\delta_{sys}\tau^{\text{Sech}} = 5.33\,fs$ and $\delta_{\text{sys}}\tau^{\text{Gauss}} = 9.62\,fs$ via systematic error propagation given by:

$$\delta_{\text{sys}}\tau^{FT}_{\text{pulse}} = \left|\left(\frac{\partial}{\partial(\Delta t)}\gamma^l_{g1}\alpha^l_{g1}\Delta t\right)\cdot\delta_{\text{sys}}(\Delta t)\right| = \gamma^l_{g1}\alpha^l_{g1}\delta_{\text{sys}}(\Delta t) \tag{5.97}$$

The derivation of this type of uncertainty is not as straight forward as the statistical one and stems from the spectral information inherent in the correlation functions for first order interference. It will be worked out in the next paragraph. For the moment however only its value will be important, which is the same for all datasets. To yield the entire error the minimal pulse length is subject to, given in table 5.3, the systematic and statistical contributions have to be added up linearly, i.e.

$$\delta_{\text{tot}}\tau^l = \delta_{\text{stat}}\tau^l + \delta_{\text{sys}}\tau^l \tag{5.98}$$

If we now compare the results for the minimal pulse lengths with one another, the difference between Sech- and Gaussian-pulses becomes obvious. It is well understood by the different conversion factors in eqs. (5.29) and (5.30) or more generally known by the time-bandwidth-product[46], just telling us that pulses with equal spectral width are shorter in the time domain if they are Sech-shaped. By far more interesting is the difference for τ_{pulse} within and outwith the resonator showing a pulse broadening of approximately $20\,fs$ being picked up during input coupling. This is a direct result of the frequency comb matching requirement, discussed in subsec. 2.1.4. The difference between $\tau^{\text{photodiode}}_{\text{pulse}}$ and $\tau^{\text{cavity}}_{\text{pulse}}$ / $\tau^{\text{HV coinc.}}_{\text{pulse}}$ implies that several frequencies in the external pulse are not in resonance with the resonators longitudinal modes, getting reflected and thereby shortening the spectral width of the internal pulses. In turn, a longer pulse in the time domain is to be expected. This ties in with the results for the spectral coverage Γ^{BBO} (eq. (4.13)) of the intra-cavity UV spectrum with respect to the external pumping spectrum, as discussed in 4.2.4.

Spectral information from $g_1(\tau)$ in comparison with the UV spectra Before proceeding towards the autocorrelation measurement, there is still the spectral information contained in the first order correlation function $g_1(\tau)$ which is worthwhile being examined. In subsec. 5.2.2 the Fourier transform connection between $g_1(\tau)$ and the underlying pulse spectrum has already been described. The normalised spectra for Sech- and Gauss-pulses, eqs. (5.35) and (5.37), consequently are:

$$S(\nu)^{\text{Gauss}} = \exp\left(-4\pi^2\left(\Delta t\right)^2(\nu-\nu_0)^2\right) \tag{5.99}$$

$$S(\nu)^{\text{Sech}} = \text{sech}^2\left(\pi^2\Delta t(\nu-\nu_0)^2\right) \tag{5.100}$$

Since the widths of these spectral functions only depend on the parameter Δt, which has been obtained from fitting the $g_1(\tau)$-functions to the first order correlation measurements, we can plug the previous outcomes for Δt (table 5.3) into eqs. (5.99) and (5.100) in order to compare them with the directly measured UV spectra inside the cavity. In doing so, we receive the spectra shown in fig. 5.15. Therein the three experimental spectra around zero pulse delay, namely at $\tau = -108\,fs$, $\tau = 0\,fs$ and $\tau = 59\,fs$, are presented as black squares. The spectral functions for the cavity level, with Δt_{Cavity}, are shown

[46] See subsection 5.2.2.

as red lines, the ones for the HV coincidences, Δt_{HV}, as blue lines and the functions resulting from the interference maxima in output 1, $\Delta t_{\text{Int. max.}}$, are displayed as green lines. In order to once more compared FWHM values of these, the measured datapoints have therefore also been fitted by a Gauss- or respectively a Sech-spectrum, according to eqs. (5.99) and (5.100) with Δt as a free fitting parameter. Furthermore fig. 5.15 is split up according to the underlying pulse shape assumed, with the left column enclosing fits for Sech-pulses and the right for Gauss-pulses.

	Spec. $\tau = -108\,fs$	Spec. $\tau = 0\,fs$	Spec. $\tau = 59\,fs$
$\Delta\nu_{exp}$	$2.2\,THz$	$2\,THz$	$2.04\,THz$
$\Delta\lambda_{exp}$	$1.115\,nm$	$0.986\,nm$	$1.034\,THz$
$\Delta\nu_{Sech}$	$2.08 \pm 0.01\,THz$	$1.945 \pm 0.008\,THz$	$1.939 \pm 0.012\,THz$
$\Delta\lambda_{Sech}$	$1.058 \pm 0.005\,nm$	$0.986 \pm 0.004\,nm$	$0.983 \pm 0.006\,nm$
$\Delta\nu_{Gauss}$	$2.174 \pm 0.009\,THz$	$2.023 \pm 0.006\,THz$	$2.02 \pm 0.011\,THz$
$\Delta\lambda_{Gauss}$	$1.102 \pm 0.005\,nm$	$1.026 \pm 0.003\,nm$	$1.023 \pm 0.006\,nm$

Table 5.4: FWHM values for measured intra-cavity UV spectra and fitted Sech-, Gauss-spectra, according to eqs. (5.99), (5.100), around zero pulse delay.

We start evaluating fig. 5.15 by analysing the spectral widths of the UV pulses: The green curves are clearly broader than all the others, which represent intra-cavity pulses. This ties in with the previous discussion about the cavity coupling condition (subsec. 2.1.4), according to which the absence of the reflected modes leads to a spectral shortening of the intra-cavity spectra. Consequently the mismatch between the spectral function for $\Delta t_{\text{Int. max.}}$ in comparison with the other curves is well understood.
Moving on towards a more quantitative discussion, the FWHM values for the measured spectra are read out in the first place. Here, on the one hand, a direct determination from the measured data is performed, while on the other hand the respective widths of Sech- and Gauss-fits to these are evaluated as well. All three sets of quantities are stated in table 5.4, whereby the conversion from frequency to wavelength has been carried out according to $\Delta\lambda = \frac{\lambda_0^2}{c}\Delta\nu$, assuming a carrier wavelength at $\lambda_0 = 390\,nm$. It is justified to use this centre wavelength since the fitted values only slightly deviate from it by not more than the fourth leading order. To gain some information about the accuracy of our correlation and spectra measurements, to figure out, which pulse shape appears to be the most accurate one and to justify the choice of the reference spectrum, made during modelling the Mach-Zehnder output spectra with eqs. (5.78) and (5.79), it is intriguing to compare the values in table 5.4 with the FWHM of the spectral functions derived from the $g_1(\tau)$-fits. The latter are provided in table 5.5, whereby the given errors again present statistical uncertainties from $\delta_{\mathrm{sys}}(\Delta t^{\mathrm{Sech}})$ and $\delta_{\mathrm{sys}}(\Delta t^{\mathrm{Gauss}})$.

	$g_1(\Delta t_{\mathrm{Cavity}})$	$g_1(\Delta t_{\text{HV coinc.}})$	$g_1(\Delta t_{\text{Int. max.}})$
$\Delta\nu_{Sech}$	$2.1 \pm 0.08\,THz$	$2.25 \pm 0.1\,THz$	$2.49 \pm 0.01\,THz$
$\Delta\lambda_{Sech}$	$1.07 \pm 0.04\,nm$	$1.14 \pm 0.05\,nm$	$1.264 \pm 0.003\,nm$
$\Delta\nu_{Gauss}$	$2.29 \pm 0.09\,THz$	$2.42 \pm 0.12\,THz$	$2.72 \pm 0.01\,THz$
$\Delta\lambda_{Gauss}$	$1.16 \pm 0.04\,nm$	$1.23 \pm 0.06\,nm$	$1.378 \pm 0.005\,nm$

Table 5.5: FHWM values of spectral functions derived from $g_1(\tau)$ functions.

We infer from this table the widths between the spectral functions for $\Delta t_{\mathrm{Cavity}}$ and $\Delta t_{\text{HV coinc.}}$ to coincide within their statistical error boundaries. The broader FWHM for $\Delta\nu_l(\Delta t_{\text{Int. max.}})$ is not surprising either. However all FWHM, stemming from the first order correlation measurement, exceed the ones originating from direct determination by the spectrometer (table 5.4). Due to the Fourier transform connection between the $g_1(\tau)$-function and the spectrum, there must nevertheless be a strict resemblance between the measured spectra and the ones derived from the first order correlation. In other words, since these do not match within their statistical error boundaries, there has to be an additional source of uncertainty within the dataset. Unfortunately it is not entirely clear, which part is affected by the aforementioned additional error. In any case, what is important here is the FWHM for the spectrum at $\Delta\tau_{MZ} = -108\,fs$ pulse delay to be still very close to the expected width by the correlation function. For that reason, it has been appointed the spectrum of reference for the previous examination of the cavity's frequency acceptance range as well as for further error considerations. The reason why the spectra at smaller time separation between both pulses are narrower than the one at $\Delta\tau_{MZ} = -108\,fs$ is also not ultimately clear. In the worst case it might be due to a residual variation in the acceptance range of the cavity[47],

[47] It cannot be explained by the spectrometer though, since the impinging beam onto this device is determined by the cavity mode geometry, which has been constant during the experiment.

which would subsequently accumulate to roughly an uncertainty of $\Delta\nu_{\text{cav. acc.}} \approx 0.16\,THz$ equal to $\Delta\lambda_{\text{cav. acc.}} \approx 0.08\,nm$. This is still more than an order of magnitude smaller than the UV pulses' FWHM in frequency space. By application of the same reasoning used to estimate the influence the down-conversion spectra mismatch, during discussing the phase-matching bandwidth, i.e. $\Delta\tau \sim \Delta\nu$, a ball-park figure for the uncertainty in pulse duration of $\approx 10\,fs$ can be inferred. Our measurements are only precise within an interval twice as big as that anyway, so even if the spectral mismatch between $\Delta\tau_{MZ} = -108\,fs$ and $\Delta\tau_{MZ} = 0\,fs$ can be attributed to variations in the cavity's spectral acceptance, it would not seriously spoil the measurement.
To take the mismatch between the experimental and theoretically predicted spectra into account, the standard deviation of all spectral FWHM values for the HV coincidences, the cavity level and the measured as well as the fitted spectrum at $\Delta\tau_{MZ} = -108\,fs$ is calculated and subsequently treated as the systematic error, inherent to the experimental set-up. Due to the way calculating it, this value is obviously equal for all different signals leading to a first order correlation curve (i.e. cavity level etc.), but different for both pulse shapes. It is furthermore expressed in terms of the Δt parameter to allow usage in the error calculations for pulse durations, yielding:

Pulse shape	$\delta_{\text{sys}}(\Delta t)$
Gauss	$5.78\,fs$
Sech	$3.03\,fs$

Since unfortunately an additional external spectrum has not been recorded in the course of the measurements with the photodiode, there is no external reference spectrum to compare the spectral width $\Delta\nu_l(\Delta t_{\text{Int. max.}})$ to. So an individual systematic error for quantities derived from the interference pattern in output 1 of the Mach-Zehnder interferometer cannot be computed and the systematic uncertainties for the intra-cavity measurements will conveniently be taken for these as well. Furthermore the systematic errors just derived will also be applied for the evaluation of the $g_2(\tau)$ measurement and the associated uncertainties in the pulse durations.
Another interesting point are the time-bandwidth products between the FWHM pulse durations, originating from the first order correlation functions, and the FWHM of the experimentally measured reference spectrum[48] in comparison with the expected values from theory, i.e.

$$\Delta\tau_i^l \cdot \Delta\nu_i^l = \beta, \tag{5.101}$$

whereby l stand again for the pulse form ($l \in \{\text{Gauss}, \text{Sech}\}$) and i represents the underlying measured quantity ($i \in \{\text{cavity level}, \text{HV coincidences}\}$). The products are provided in table 5.6, showing rather good resemblance for the cavity level and the HV coincidences with the expected values. The constants for the interference maxima in output 1 (fig. 5.13) are neglected in the following discussion, as there is no measured spectrum for the $g_1(\tau)$ function at hand.

	Gauss-pulses	Sech-pulses
α_{theory}	0.441	0.315
α_{cavity}	0.424	0.3296
$\alpha_{\text{HV coinc.}}$	0.401	0.308

Table 5.6: Time-bandwidth products for the reference spectrum at $\Delta\tau_{MZ} = -108\,fs$ pulse delay with the respective Fourier transform limited pulse durations obtained from the first order correlation measurements.

Finally the analysis of the matching between the measured spectra and the theoretical predictions allows us to conclude, by which pulse shape our experimental situation is described more accurately. It shall be strongly underlined, that the following considerations do definitely not tell us, how the intra-cavity UV pulses look like in reality. It does neither tell us, if we even have pulses of one or the other shape nor whether the assumption of Sech- or Gauss-pulses is justified in the first place. For all these kind of questions a proper analysis of the spectral phases involved would have to be implemented (see reference ([104]) for details). However it is still possible to give a preference towards a certain pulse model. Especially as the conversion factors and thereby the resulting pulse lengths are different for both assumptions (deviating by $\approx 40\,fs$ for the FT minimal pulse lengths and $\approx 30\,fs$ for the real pulse lengths, determined in subsec. 5.3.5), it is fortunate to have a feeling for the number which is more likely to constitute a

[48] For the full spectral widths at half maximum of the spectral functions (5.99) and (5.100), with the Δts from the fitted $g_1(\tau)$-functions and the minimal pulse durations from table 5.3, the time-bandwidth products of course yield the expected theoretical value by construction.

measure for the actual pulses. In order to figure out this preference, the root-mean-square deviation, referred to as RMSD in the following, comes in handy. It is defined as the geometrical mean of the distances between the theoretical spectral functions and the measured data. Representing the former by $[S(\nu_i)]_{\Delta t(g_1^l)}$ and the latter by $y(\nu_i)$, the RMSD can be written as

$$RMSD = \sqrt{\sum_{i=0}^{i=3648} \Big([S(\nu_i)]_{\Delta t(g_1^l)} - y(\nu_i) \Big)^2}, \tag{5.102}$$

whereby the sum runs over all 3648 measurement points within one spectrum dataset. According to this definition a lower value for the RMSD consequently indicates a better resemblance of the theoretical prediction with the experimental spectrum. The matching between both quantities has been calculated for all three considered spectra (with time delays of $\tau = -108\,fs$, $\tau = 0\,fs$, $\tau = 59\,fs$) and all intra-cavity correlation functions. Results are presented in table 5.7.

Spectrum at $\tau = -108\,fs$:	Gauss-pulses:	Sech-pulses:
$RMSD(\Delta t_{\text{Cavity}})$	0.39	0.38
$RMSD(\Delta t_{\text{HV coinc.}})$	0.62	0.53
Spectrum at $\tau = 0\,fs$:	Gauss-pulses:	Sech-pulses
$RMSD(\Delta t_{\text{Cavity}})$	0.66	0.54
$RMSD(\Delta t_{\text{HV coinc.}})$	0.93	0.79
Spectrum at $\tau = 59\,fs$:	Gauss-pulses:	Sech-pulses:
$RMSD(\Delta t_{\text{Cavity}})$	0.74	0.65
$RMSD(\Delta t_{\text{HV coinc.}})$	0.98	0.87

Table 5.7: Root mean square deviations according to eq. (5.102) between the theoretically predicted spectra, with parameters from the first order correlation function $g_1^l(\tau)$, and the experimentally measured spectra, at pulse delays of $\tau = -108\,fs$, $\tau = 0\,fs$ and $\tau = 59\,fs$.

Examining table 5.7 we can directly note the smaller RMSD values for Sech-pulses in each and every measurement. The absence of any ambiguities very nicely ties in with one's expectations, since a certain type of pulse shape should be apparent throughout the entire measurement. We can thus conclude the UV pulses to be more likely Sech-shaped and ultimately apply rather the smaller conversion factors yielding shorter pulses.

5.3.5 Autocorrelation within cavity by SPDC

After all the "preconsiderations" so far, we can now finally move on to the main heart of this pulse length measurement, the interferometric $g_2(\tau)$-autocorrelation, which is given by eq. (5.45) in subsec. 5.2.3. In the following primary focus will be placed on the evaluation of the data and subsequently on the discussion of the implications from the experimental findings. Please note furthermore: Although of a preference for one pulse model has been deduced already, the data is regardlessly going to be examined for Sech- and Gauss-pulses.

Intra-cavity UV pulse length determination The experimentally recorded four-photon HHVV-coincidences are shown as a function of pulse delay in figure 5.16. From this graph we can infer a degraded peak-to-background ration of 4.13 : 1, opposing the normally desired 8 : 1. The latter is required in order to rule out loss in sensitivity to spectral phases and therefore being able to measure the proper pulse duration, not just the Fourier transform limited one, as has been shown in subsec. 5.2.4. However from the aforementioned ratio, a b-parameter in the $g_2(\tau)$-correlation function, stated in eqs. (5.51) and (5.52), of $b = 0.44$ is yielded, which corresponds to a first order interference visibility of $V_2(HHVV) = 0.75$ according to eq. (5.95). Comparison with the numbers received for the evaluation of $g_1(\tau)$ function in table 5.2, proves similarity between $V_1(Int.max.)$ and $V_2(HHVV)$. Thus the deviation from the 8 : 1 ratio can be explained by the incomplete interference between both pulses, caused by a non perfect alignment of the Mach-Zehnder interferometer. In this respect it is also clear that the underlying reasons for imperfect interference between both pulses, namely the transverse beam displacement and slight polarisation mismatch of the pulses, do not cause any pulse elongation. We can therefore certify our ability to measure spectral/temporal phase effects on the intra-cavity pulses and to really perform

an interferometric autocorrelation measurement, although having a lowered peak-to-background ratio in the $g_2(\tau)$-function.
In order to determine the FWHM of HHVV coincidence dataset, which again carries the information about the pulse length, the appropriate theoretical fitting functions for the $g_2(\tau)$-correlation are applied. The relevant function have been derived in subsec. 5.2.3 and are given by the eqs. (5.51) and (5.53). The parameter a is once more conveniently set to unity, $a = 1$. The fits to the measurement by the $g_2(\tau)$-functions, eqs. (5.51) and (5.53), are presented in figure 5.16 by a red curve for Sech-pulses and a blue curve for Gauss-pulses, yielding fit parameters $\Delta t_{g_2}^{\text{Gauss}} = 123.63\, fs$ and $\Delta t_{g_2}^{\text{Sech}} = 99.92\, fs$. To convert the $\Delta t_{g_2}^{l}$s of both functions into a pulse length, the two conversion factors $\beta_{g_2}^{l}$ (eqs. (5.57), (5.58)) and $\gamma_{g_2}^{l}$ (eqs. (5.60), (5.61)) have to be considered for each pulse shape, likewise to the evaluation of the $g_1(\tau)$-function. The first one transforms the value for Δt into $\Delta\tau_{g_2}^{\text{FWHM},l}$, the FWHM of the $g_2(\tau)$-curves, and the second one relates this value further to the FWHM pulse duration τ^l. Please bear in mind here, that in contrast to the factors for first order interference the appropriate numbers for the $g_2(\tau)$-function are dependent on the parameter b or in other words on the interference visibility. The pulse duration is now computed according to

$$\tau_{\text{pulse}}^{l} = \gamma_{g_2}^{l} \cdot \alpha_{g_2}^{l} \cdot \Delta t_{g_2}^{l}. \tag{5.103}$$

The systematic error on it is calculated by consideration of $\delta_{sys}(\Delta t_{g_1})$, identified previously, which is equally employed as an uncertainty on Δt_{g_2}, thus $\delta_{sys}(\Delta t_{g_2}^{\text{Sech}}) = 3.06\, fs$ and $\delta_{sys}(\Delta t_{g_2}^{\text{Gauss}}) = 5.78\, fs$. The statistical contribution is once more given by the fitting error of $\Delta t_{g_2}^{l}$, which is $\Delta t_{g_2}^{\text{Sech}} = 4.78\, fs$ and $\Delta t_{g_2}^{\text{Gauss}} = 6.57\, fs$. All errors are propagated appropriately, according to their source of origin, resulting in identical equations as for the first order interference (eqs. (5.96), (5.97)) by swapping g_1 for g_2.
So we finally end up with the pulse length for the UV light inside the cavity as presented in table 5.8.

Pulse form	Pulse duration [fs]
Sech	176.1 ± 13.7
Gauss	205.8 ± 20.6

Table 5.8: Intra-cavity UV pulse lengths for Sech- and Gauss-pulses as obtained by interferometric autocorrelation.

Discussion of pulse length The minimal pulse length, obtained from the first order interference function and the pulse spectra, is not sensitive to small dispersion effects and sets only a lowest boundary for the pulse duration. Solely larger contributions, which are sufficient to change the input coupling condition of some external frequency comb modes, influence this minimal pulse length in a noticeable fashion. Hence should there be some remaining dispersion apparent, higher order spectral phases, e.g. some chirp or TOD, will still add to the pulse, giving raise to pulse broadening. And indeed by inspection of the findings in table 5.8, a pulse elongation between 20 to 30 fs in comparison to the minimal pulse durations, which have been $\tau_{\text{min}}^{\text{Gauss}} \approx 180 - 190\, fs$ and $\tau_{\text{min}}^{\text{Sech}} \approx 140 - 150\, fs$, becomes evident straight away. What does this now imply for our experiment:
First it proves dispersion effects to be present in the resonator, nonetheless they appear to be not serious enough to distort the pulse completely. Especially since the minimal and actual pulse durations for Gauss-pulses coincide within their uncertainty ranges, $\tau_{\text{HHVV}}^{\text{Gauss}} = 206 \pm 21\, fs \approx 182 \pm 18\, fs = \tau_{\text{min, cavity}}^{\text{Gauss}}$, and the values for Sech-pulses are just short off to do so, $\tau_{\text{HHVV}}^{\text{Sech}} = 176 \pm 14\, fs \gtrapprox 140 \pm 12\, fs = \tau_{\text{min, cavity}}^{\text{Sech}}$, the remaining dispersion will not deform the UV pump to an extend lethal for applications in ultra-short laser physics[49]. Second, it gives a flavour about the limits to the dispersion analysis of the system by the cavity input coupling. The key message here is, yes one can tell something about the pulse maintenance within an ultra-short pulse enhancement resonator by simply comparing the internal to the external spectra, as done in subsec. 4.2.4. However the resolution of such an analysis tool remains quite limited and is by far too poor for being used in the context of shorter UV pulses.
We can thus conclude that the cavity is working nicely for applications using pulses in the range above $100\, fs$. Going to lower pulse lengths in the region of a couple of femto-seconds only, which might be interesting due to the high repetition rates of this enhancement resonator compared to conventional amplifier systems, it will get quite troublesome to operate without further dispersion control (e.g. by using a chirped version of the cavity mirrors).

[49] Such as e.g. the generation of higher harmonics leading to XUV pulses, or as a high repetition rate amplifying system.

Limits of this measurement and possible advancements The last thought of the preceding discussion already leads towards the great downside inherent to any autocorrelation measurement, which is $g_2(\tau)$-interferometric autocorrelation function providing only a measure for the pulse duration but not the pulse shape. This is all related to the fact, that within the width of the interferometric autocorrelation, dispersion effects, such as chirp, and the temporal width of the underlying pulses contribute simultaneously. Furthermore autocorrelation is ambiguous with respect to the underlying pulse shape ([104]), which renders it even impossible to tell how the pulse looks like if dispersion is entirely absent. In order to move on towards operation of the resonator with shorter laser pulses or to understand precisely what is going on inside the cavity in terms of dispersion and pulse distortion, knowledge about the optical pulses' actually appearance is essential.
Within the interferometric autocorrelation frame, there is at least a way to conclude something about the pulse symmetry. Since autocorrelations of higher, odd orders are not symmetric around zero pulse delay for non symmetric pulses, one could use e.g. the third order to measure the pulse duration instead of the second ([104]). In this situation, the correlation would by given by eq. (5.1), taken at $n = 3$. Since utilisation of SPDC as a non-linearity allows simulteaneous generation of multiple orders in the autocorrelation function (5.1), as outlined in subsec. 5.1.2, this third order correlation has implicitly been measured in the course of our experiment as well, since it is simply represented by the six-photon count rates comprising three horizontally and three vertically polarised photons. The measured data for this correlation function is shown in figure 5.17. Unfortunately the count rates for six-photon events are much lower than their four-fold analogues, leading to much greater error bars on each datapoint, due to Poissonian counting statistics. Therefore the third order is not further evaluated here. Nevertheless, one could in principle use the HHHVVV coincidences with a longer measurement time at each translation stage position, which might in turn require an active stabilisation of the Mach-Zehnder interferometer.
Further more sophisticated methods are available, allowing for the determination of the actual electric field function. The two most commonly applied ones are on the one hand a technique termed frequency resolved optical gating (FROG), and on the other hand an approach called spectral phase interferometry for direct electric-field reconstruction (SPIDER). Since there is extensive literature available for both of them, further explanations are skipped here. However the reader shall be pointed out to references ([79], [111]) for an overview over both. More information particularly about FROG can also be found in references ([104],[115]-[120]) and more about SPIDER is provided in references ([121]-[124]).

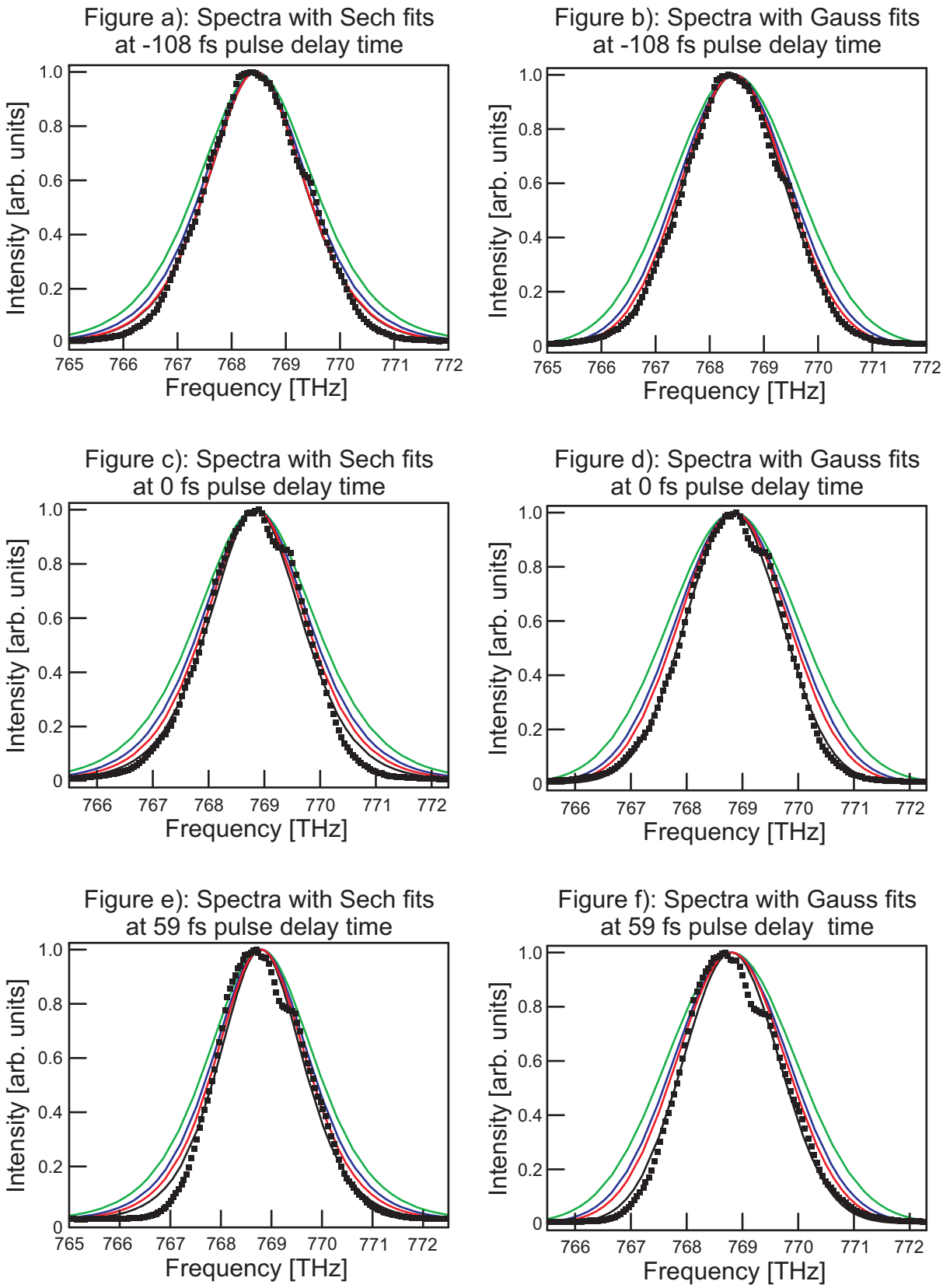

Figure 5.15: Spectra derived from the $g_1(\tau)$-correlation function combined with experimental spectra for pulse delays of $\tau = -108\,fs$, $\tau = 0\,fs$ and $\tau = 59\,fs$. Left column shows curves for Sech-pulse shapes, the right column for Gaussian-pulse shapes. Experimental data is drawn as black squares, fits to the experimental data as black lines, the spectra resulting from the cavity power level ($\Delta t_{\mathrm{Cavity}}$) as red lines, the spectra from the HV coincidences (Δt_{HV}) as blue lines and the spectra from the interference pattern on the photodiode as green lines.

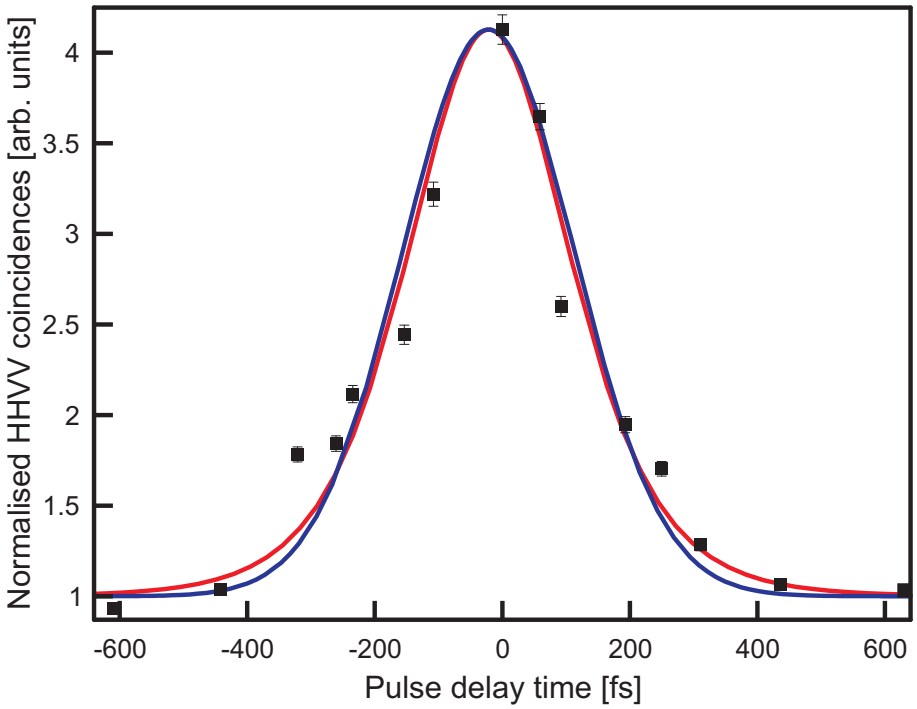

Figure 5.16: HHVV coincidences and $g_2(\tau)$ autocorrelation function. The measured data is shown by black squares while the fit for Sech-pulses is represented by the red curve and the one for Gauss-pulses by the blue curve.

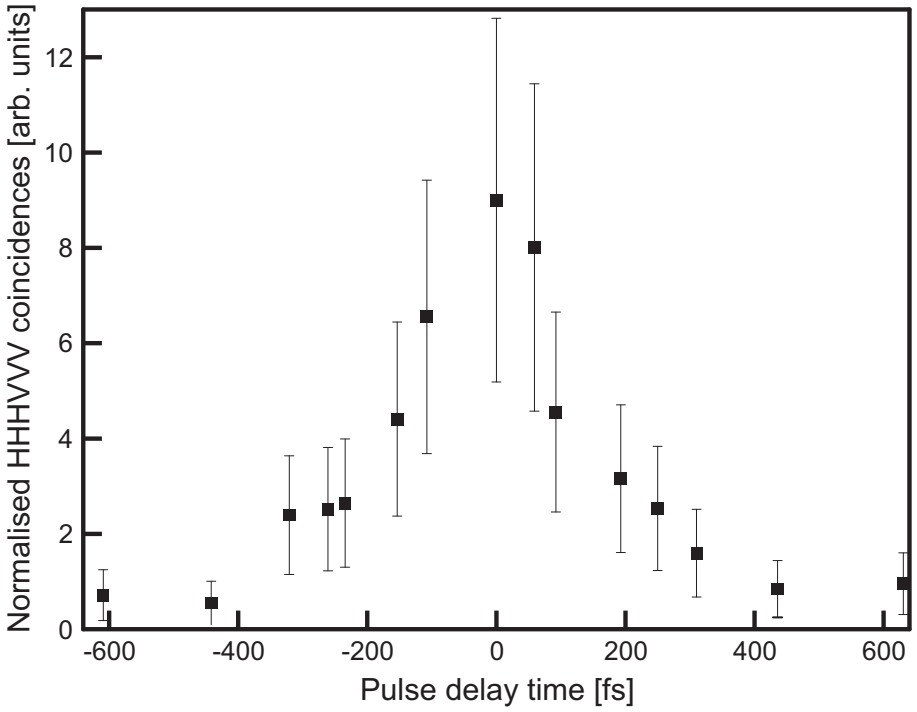

Figure 5.17: Six-fold HHHVVV photon coincidence rates, following a $g_3(\tau)$ autocorrelation function.

Chapter 6

The cavity employed as a photon source

After all important properties of the enhancement resonator have been evaluated, it is time to consider possible applications of the device. Since its purpose is to allow the observation of multi-partite entangled photon states, the main concern in the following chapter will be the investigations of photon production rates depending on the available UV pumping power level established inside the resonator. Therefore a brief summary of the relevant theoretical background regarding SPDC shall be provided in the first place. Additionally, a convenient tool for proving the presence of entanglement, the entanglement witness, will be introduced. Subsequently the features of the cavity, applied as a photon source, will be assessed, whereby focus is not only placed on the bare count rate statistics, but on entanglement observed in the resulting output states as well. Overall the discussion will show the applicability of our apparatus for multi-qubit quantum information logic with unprecedent count rates.

6.1 Theory on SPDC emission

6.1.1 General considerations

As a common feature, all optical processes, whether linear or of arbitrary non-linear order, share their source of origin from a polarisation of a non-linear medium. According to classical electrodynamics ([59]), such a polarisation can be expressed as

$$\vec{P}(t) \sim \epsilon_0 \sum_i \chi^{(i)} \vec{E}(t)^i = \underbrace{\epsilon_0 \chi^{(1)} \vec{E}(t)}_{\text{term 1}} + \underbrace{\epsilon_0 \chi^{(2)} \vec{E}(t)^2}_{\text{term 2}} + \underbrace{\epsilon_0 \chi^{(3)} \vec{E}(t)^3}_{\text{term 3}}, \tag{6.1}$$

whereby $\chi^{(i)}$ represents the medium's susceptibility of i^{th} order[1] and $\vec{E}(t)$ the electric field of the incident light field. While term 1 in eq. (6.1) stands for linear effects like absorption, and the third term for higher order processes, like self-phase modulation or four-wave mixing, it is the second term which concerns us here. Considering a plane wave incidence, given by $E = E_0 \cdot \cos(\omega t)$, we can infer from eq. (6.1) to obtain an expression according to:

$$P(t) \sim \epsilon_0 \chi^{(2)} E_0^2 \cos(\omega_0 t)^2 = \frac{1}{2} \epsilon_0 \chi^{(2)} E_0^2 \left(1 + \cos(2\omega_0 t)\right) \tag{6.2}$$

According to Maxwell's equations, the non-linear polarisation of medium gives rise to a signal field $E_s(t)$ term in the wave equation ([59])

$$\nabla^2 E_s(t) - \frac{1}{c^2} \frac{\partial^2 E_s(t)}{\partial t^2} = -\mu_0 \frac{\partial^2 P(t)}{\partial t^2} \tag{6.3}$$

oscillating at twice the fundamental driving frequency ω. This process is regarded as second harmonic generation (SHG) and consists, quantum mechanically spoken, of the destruction of two pumping photons, fabricating one signal photon of half wavelength. Due to time inversion symmetry of the frequency conversion, described by eqs. (6.2) and (6.3), it can also be expected to observe the reverse process of down-conversion, wherein one pumping photon gets split-up into two light quanta of longer wavelength

[1] It is a tensor, whose structure depends on the specific material properties. For the ease of the argument, we will in the following regard the crystal and the electromagnetic field as appropriately orientated, in order to consider both as scalars.

or respectively lower energy, commonly referred to as signal and idler. In contrast to SHG, a classical description of down-conversion is only possible if a seeding signal or idler field is apparent to start with, i.e. if stimulated bosonic emission into an already occupied light field mode is happening. Otherwise, in the case of spontaneous parametric down-conversion, the initial signal and idler fields are both vacuum states, denoted as $|0\rangle$, and a full quantum treatment has to be carried out, done in the following.
Before getting into more detail, it is clear that, in terms of occurring wavelength values involved in both processes, energy conservation has to be fulfilled. The analogous reasoning applies to the wavevectors associated with the conservation of momentum. Altogether this means for down-conversion

$$\omega_p = \omega_s + \omega_i \tag{6.4}$$

and

$$\vec{k}_p = \vec{k}_s + \vec{k}_i, \tag{6.5}$$

whereby p stands for the pumping beam and s respectively i signify signal and idler modes. Both equations set constraints determining the wavelength spectra and emission characteristics of the conversion process. Eq. (6.4) is easy to comply with, since it does not introduce any limitations on the resulting frequency distributions, however it imposes a strong correlation between signal and idler wavelengths resulting in energy entanglement between both; see e.g. ([128]-[130]) for possible applications. In contrast eq. (6.5) generally cannot be met in normal dispersive material with $n(\omega_1) > n(\omega_2)$ for $\omega_1 > \omega_2$. Utilisation of birefringent non-linear crystalline media[2] can however solve this problem. Such materials comprise either two or three different refractive indices along their Cartesian crystal axes; the former are considered as uniaxial and the latter as biaxial. BBO corresponds to the first category, so only such a scenario shall be investigated further. It leaves us with a different refractive index along the optical axis, here chosen as z-axis, of the substance, named extraordinary direction, with respect to both remaining axes, named x- and y-axis, referred to as ordinary direction. Since the refractive indices along x and y are equal, the whole refractive index profile of the crystal can be modelled as an ellipsoid, depicted in fig. 6.1. In this respect, there are once more two different types of non-linear media available, distinguished by the ratio between ordinary and extraordinary refractive index: if $n_{ext} > n_{ord}$, crystals are said to be positive birefrigent, otherwise they are negative birefringent. BBO falls into the latter category. To infer how to maintain momentum conversion with a BBO crystal, eq. (6.5) can be rewritten to[3]

$$n_p(\lambda_p) \cdot \vec{e}_p \cdot \omega_p = n_s(\lambda_s) \cdot \vec{e}_s \cdot \omega_s + n_i(\lambda_i) \cdot \vec{e}_i \cdot \omega_i, \tag{6.6}$$

indicating the need to have different refractive indices for pump, signal and idler, which are set by the polarisation of either constituent together with the incidence angle of the impinging light beam with respect to the optical axis of the crystal, as illustrated in fig. 6.1 and assigned in eq. (6.6) by the unity vectors $\{\vec{e}_p, \vec{e}_s, \vec{e}_i\}$ pointing into the propagation direction of the pump, signal or idler field, respectively. There are two different schemes how to fulfil eq. (6.6) and establish phase-matching:

1. The pump is polarised orthogonal to signal and idler within the extraordinary refractive index plane under an angle θ to the crystal's optical axis. The latter two are parallel polarised within the ordinary refractive index plane. Eq. (6.5) thus becomes:

$$n_{ext}(\theta, \lambda_p) \cdot \omega_p = n_{ord}(\lambda_s) \cdot \omega_s + n_{ord}(\lambda_i) \cdot \omega_i \tag{6.7}$$

   This orientation is called type-I SPDC.

2. The pump is polarised parallel to either signal or idler and both polarisations are located within the extraordinary refractive index plane under an angle θ to the crystal's optical axis. The remaining SPDC photon is polarised orthogonally, experiencing the ordinary refractive index. Eq. (6.5) thus becomes:

$$n_{ext}(\theta, \lambda_p) \cdot \omega_p = n_{ext}(\theta, \lambda_{s,i}) \cdot \omega_{s,i} + n_{ord}(\lambda_{i,s}) \cdot \omega_{i,s} \tag{6.8}$$

   This arrangement is named type-II SPDC, giving rise to a strong correlation between the polarisations in the signal and idler mode, which can be used for entanglement in the polarisation domain between both particles[4].

[2] Please note: this has to be a non-inversion-symmetric substance, e.g. ionic crystals like BBO or LBO, in order to allow for $\chi^{(2)} \neq 0$, leading directly to $\chi^{(3)} = 0$.

[3] It should be kept in mind, that refractive indices are wavelength dependent, described by the Sellmeier eq. (2.44).

[4] This however requires indistinguishability between signal and idler in all other degrees of freedom in combination with their spatial separation, as outlined later.

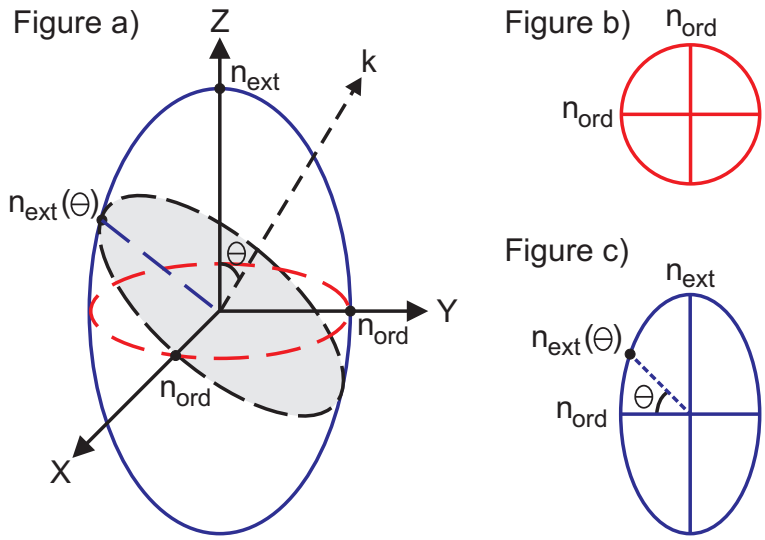

Figure 6.1: Schematic representation of the refractive index profile within a positive birefrigent, uniaxial optical crystal. The extraordinary index n_{ext} is defined along the optical axis (z-axis) and the ordinary one n_{ord} is located in the plane of the x- and y-axes. Light incident with its wavevector $\vec{k}$ under an angle θ with respect to the optical axis and a polarisation within the plane defined by the optical axis and $\vec{k}$ will experience an effective extraordinary refractive index $n_{ext}(\theta)$. Figure a) gives a three dimensional overview, b) is the projection onto the ordinary index plane defined by the x- and y-axes, whereas c) is a projection onto the ordinary-extraordinary refractive index plane, set by the y- and z-axes. Source of graphic: ([101]).

We will apply type-II phase-matching. Meeting the conditions set by eq. (6.8) is here achieved by angle tuning of the non-linear crystal, which modifies the effective extraordinary refractive index according to ([101])

$$\frac{1}{n_{ext}^2(\theta,\lambda_i)} = \frac{\sin(\theta)^2}{n_{ext}^2(\lambda_i)} + \frac{\cos(\theta)^2}{n_{ord}^2(\lambda_i)}, \tag{6.9}$$

whereby $n_{ext}(\lambda_i) = n_{ext}(\theta = 0, \lambda_i)$. It shall be noted, that phase-matching can be yielded not only for a single frequency but for an entire spectral range, as already calculated for our apparatus in subsec. 5.3.3. Thereby type-I commonly produces broader output bandwidths than type-II ([101]). Both methods to phase-match the conversion process also result in different spatial output patterns of signal and idler wavelengths. Type-I generates a single emission cone for each frequency mode involved in the process, whereby signal and idler photons are emitted into spatial directions situated diametrically opposite of either side of the cone, see e.g. ([131], [142]). In contrast, type-II produces two separate cones, one for the signal and one for the idler photons. Again the two constituents of a simultaneously emitted pair are located on diametrically opposite positions of one cone with respect to its orthogonally polarised sibling. Depending on the orientation of the crystal, both cones can on the one hand be made to intersect each other in two points, which corresponds to an emission of say a signal photon into the first intersection, denoted as mode a, and an idler photon into the other spatial mode b. Such an arrangement is called non-collinear type-II SPDC, graphically visualised in fig. 6.2 b). On the other hand, for a certain tilt angle of the BBO crystal, both emission cones can be aligned to just touch one another, defining the common emission mode a in fig. 6.2 a). From the former composition it is clear that, by only further processing photons emitted into modes a and b, a polarisation entangled photon state is obtained straight away[5]. Contrarily, in the latter situation, both photons are located in the same spatial mode, if only the emission direction a is retained. Thus there is no entanglement between these light quanta. Entanglement between the photons is only generated, once both are separated into two distinct spatial modes, as done within our linear optical set-up, described in section 3.3.
Finally, the aforementioned emission characteristics of either down-conversion process also entail correlations in the spatial degree of freedom, represented by the $\vec{k}$-vectors of the signal and idler photons[6]. Regarding the spatial distribution of the SPDC emission, a more rigorous analysis can e.g. be found in

[5] See for instance ([132]) for details.
[6] See for instance ([133]) and ([134]) for experiments taking advantage out of this correlation.

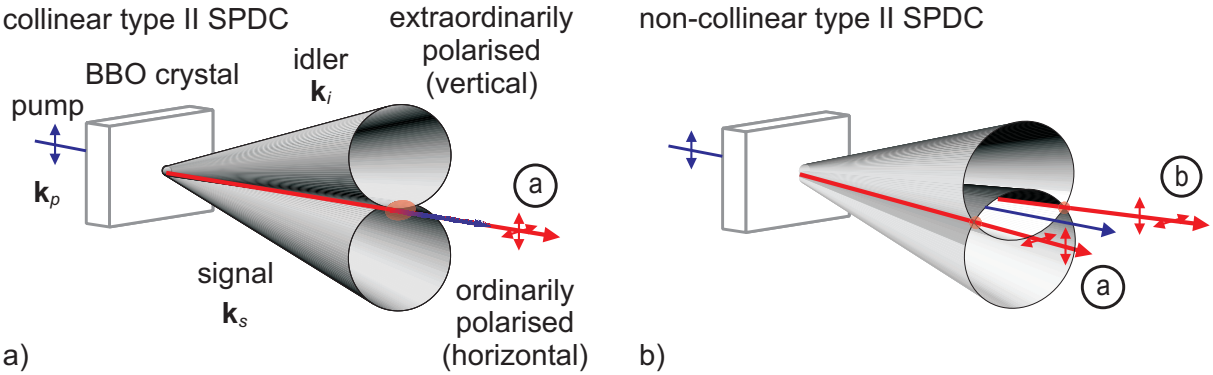

Figure 6.2: Spatial emission characteristics of the type-II SPDC process. Fig. a) represents the collinear scenario, whereas b) shows the non-collinear case.

references ([101], [135], [136]). Pump beam focussing effects, which are ignored throughout this dissertation, have also been considered in this context as well as in terms of the SPDC photon spectra in ([137], [138]). We will now move on to discussing the actual photon emission rates expected from the collinear type-II SPDC source implemented in our experimental set-up.

6.1.2 Single mode description

For the discussions in this thesis, it is sufficient to focus only on a single mode description of the conversion process, i.e. both, the pumping beam as well as the signal and idler beams, will be restricted to a particular wavelength only. Such a simplification is justified, since consideration of the entire frequency spectrum within the ultra-short pulses involved will not change the fundamental functional dependence of the SPDC photon state. As can be inferred from reference ([101]), the extension to a multimode picture introduces an additional time integral over the entire pumping pulse's interaction time with the non-linear crystal. Such an operation corresponds, in the frequency domain, to an integration over all frequency components and therefore just scales up the expected photon pair count rates by the spectral content of the ultra-short pulses. As however the spectral widths remain constant throughout all possible orders of pair emission, which is to say that the signal and idler spectra are equal independent of the number of simultaneously generated pairs, the broadband situation can, in first approximation, be included by a multiplicative factor onto the count rate statistics, expected from the cw scenario, taking the increased spectrum into account. In order to model the observed count rates, proportionality factors are to be experimentally determined anyway, since they are for instance also depending on the detection efficiencies of the produced photons. So only the functional dependencies of multiphoton emission rates on the pumping power will be relevant, which are equal in both situations. In order to establish a suitable expression for modelling the experimentally determined count rates, a single mode description is hence sufficient for our purposes. First, we define the annihilation and creation operators for the signal and idler photon fields of initial photon number n, with $i \in \{\text{signal}, \text{idler}\}$, according to:

$$\begin{array}{lll} \hat{a}_i^\dagger|n\rangle = \sqrt{n+1}|n+1\rangle & \hat{a}_i|n\rangle = \sqrt{n}|n-1\rangle & \left[\hat{a}_i, \hat{a}_j^\dagger\right] = \delta_{i,j} \\ (\hat{a}_i^\dagger)^n|0\rangle = \sqrt{n!}|n\rangle & \hat{a}_i|0\rangle = 0 & [\hat{a}_i, \hat{a}_j] = \left[\hat{a}_i^\dagger, \hat{a}_j^\dagger\right] = 0 \\ (\hat{a}_i^\dagger)^\dagger = \hat{a}_i & \hat{a}_i^\dagger\hat{a}_i|n\rangle = n|n\rangle & \end{array}$$

The analogous equations also apply for the creation and annihilation operators of the pumping field, $(b, b^\dagger)$, as utilised in subsec. 5.1.2. However, having seen therein that the depletion of the strong pump by the SPDC process is negligible in terms of the photon number in the pump mode, these operators are treated as classical fields E_p.
The relevant Hamiltonian for single mode, collinear type-II SPDC is given by[7] ([125], [139])

$$\hat{H} = i\hbar\kappa\left(\hat{a}_H^\dagger\hat{a}_V^\dagger + h.c.\right), \tag{6.10}$$

whereby we have followed the convention introduced in chapter 5, assigning the signal beam as vertically and the idler beam as horizontally polarised. The coupling constant κ is proportional to the susceptibility $\chi^{(2)}$ and the length L_{BBO} of the BBO crystal as well as the electric field strengths of the pump E_p. The

[7] The non-collinear arrangement is for instance treated in references ([139]-[141]).

output state $|\Psi(t)\rangle$ of the down-conversion process can be gained in the Heisenberg picture ([151]) by application of the time evolution operator $\hat{U} = \exp\left(-\frac{i}{\hbar}\hat{H}t\right)$ onto the vacuum state of signal and idler photons, $|\text{vac}\rangle = |0_H, 0_V\rangle$, to be:

$$|\Psi(t)\rangle = \hat{U}|\text{vac}\rangle = \exp\left(-\frac{i}{\hbar}\hat{H}t\right)|\text{vac}\rangle \tag{6.11}$$

If we introduce the ladder operators $\hat{L}^+ = \hat{a}_H^\dagger \hat{a}_V^\dagger = \left(\hat{L}^-\right)^\dagger$, the unitary operator $\hat{U}$ can be rewritten as ([139])

$$\begin{aligned}\hat{U} &= \exp\left(\kappa t\hat{L}^+ - \kappa^* t\hat{L}^-\right) \\ &= \exp\left(\hat{\tau}\tanh\left(|\tau|\right)\hat{L}^+\right)\cdot\exp\left(-2\ln\left(\cosh\left(|\tau|\right)\right)\frac{1}{2}\left[\hat{L}^-,\hat{L}^+\right]\right)\cdot\exp\left(-\hat{\tau}^*\tanh\left(|\tau|\right)\hat{L}^-\right)\end{aligned} \tag{6.12}$$

with a redefined interaction constant $\tau = \kappa t$ and $\hat{\tau} = \frac{\tau}{|\tau|} = \frac{\kappa t}{|\kappa t|} = 1$. Inserting eq. (6.12) into eq. (6.11) yields, after some arithmetics, the final SPDC photon state ([139])

$$|\Psi(t)\rangle = \sqrt{1-\tanh^2|\tau|}\sum_{l=0}^{\infty}\frac{\tanh^l|\tau|}{l!}\left(\hat{a}_H^\dagger\hat{a}_V^\dagger\right)^l|\text{vac}\rangle = \sqrt{1-\tanh^2|\tau|}\sum_{l=0}^{\infty}\tanh^l|\tau||l_H, l_V\rangle \tag{6.13}$$

wherein l assigns the number of signal and idler photon pairs generated during the process[8]. One can readily see from eq. (6.13), that all possible pair numbers are generated simultaneously during the down-conversion process. Yet the probability amplitude $\sim \tanh^l|\tau|$, which is dependent on the pumping strength by $\tau \sim E_p$, yields higher order emission for a fixed small value of E_p, since $\tau \ll 1$. Thus increasing the pumping power in order to gain high emission probabilities for a desired multi-photon pair emission of a certain number l' does not only enhance the production rates for this expected photon state $|l'_H, l'_V\rangle$, but also for higher orders with $l'' > l'$, especially the one with $l'' = l' + 1$. The effect becomes particularly more severe, the greater the electric field strengths of the pump are, since in the limit

$$\lim_{E_p\to\infty}\tau\to\infty \quad\Longrightarrow\quad \tanh|\tau|\to 1,$$

equal emission probabilities for all possible photon pair numbers are achieved. This argument proves clearly, that in order to gain multi-qubit photonic quantum states from SPDC, one cannot just arbitrarily ramp up the pumping power, because, in doing so, simultaneously generated photon states of even higher qubit numbers will cause noise to dominate over the desired state. The noise results on the one hand from photon loss along the way from photon generation to state detection[9]. On the other hand it is also due to the split-up of the photon state into different spatial modes within the linear optical set-up (section 3.3). This can cause two light particles of the higher number state, carrying equal polarisation, to penetrate into the same mode, detected by the same SPAPD. Hence such a coincidence contributes to events associated with a multi-photon state of lower qubit number. Therefore an implementation of a high power based amplifier system, like it is reported in ([75]), is not applicable for our purposes and a compromise between pumping power strength, associated with count rate magnitude, and background noise has to be found.

In the following measurements, likewise to the intra-cavity autocorrelation in chapter 5, correlated multiphoton count rates will be determined, which are evaluated by the conditional, normal ordered number operator ([101]) $:\hat{n}_H\hat{n}_V := a_H^\dagger a_V^\dagger a_V a_H$ by

$$\tilde{n} = \sum_{l=0}^{\infty}\tilde{n}'_l = \langle :\hat{n}_s\hat{n}_i: \rangle = \sum_{l=0}^{\infty}\langle\Psi(t)|\left(\hat{a}_H^\dagger\hat{a}_V^\dagger\hat{a}_V\hat{a}_H\right)^l|\Psi(t)\rangle = \left(1-\tanh^2|\tau|\right)\left(\sum_{l=0}^{\infty}l_H l_V\tanh^{2l}|\tau|\right), \tag{6.14}$$

in which we have assigned the production rates of $2l$ photons by $\tilde{n}'_l$. Since[10] $\tau = \alpha\sqrt{P_{UV}}$, we would expect the detected coincidence events of $2l$ photons in our linear optical set-up (section 3.3), for an emission of l^{th} order, to approximately scale according to[11]

[8] i.e. $l = 1$ gives one H- and V-polarised photon, whereas $l = 2$ returns two H and V polarised quanta within the emittance mode, etc.

[9] For instance by not coupling individual photons of the state into the SM fibre or by photon absorption.

[10] with a proportionality constant α, including the crystal parameters

[11] with yet another proportionality constant β_l, including e.g. l_H, l_V, coupling efficiencies into the SM fibre, laser repetition rate, detection efficiencies, beam splitter ratios in the linear optical set-up, etc.

$$\tilde{n}_l = \beta_l \left(1 - \tanh^2\left(|\alpha| \cdot |\sqrt{P_{UV}}|\right)\right) \tanh^{2l}\left(|\alpha| \cdot |\sqrt{P_{UV}}|\right), \tag{6.15}$$

if higher order contributions are absent or negligible. For low values of E_p, leading to $|\tau| \ll 1$, expression (6.13) can be approximated using $\tanh|\tau| \approx |\tau|$ towards

$$|\Psi(t)\rangle \approx \sqrt{1-|\tau|^2} \cdot \sum_{l=0}^{\infty} |\tau|^l |l_H, l_V\rangle \tag{6.16}$$

and even further considering $\sqrt{1-|\tau|^2} \approx 1$. So we end up with:

$$|\Psi(t)\rangle \approx \sum_{l=0}^{\infty} |\tau|^l |l_H, l_V\rangle. \tag{6.17}$$

This leaves us with expected count rates in the low pump intensity limit of

$$\tilde{n}_l = \beta_l |\tau|^{2l} = \beta_l |\alpha|^{2l} \cdot P_{UV}^l, \tag{6.18}$$

within which the photon generation rate and the associated investigated count rates for the l^{th} order process scale with the UV pumping power to the power of l. The last result has already been used in subsec. 2.2.2 and 5.1.2.

6.2 Indistinguishability and entanglement witnesses

Before moving on to the examination of the experimental findings, one major prerequisite for entanglement and one suitable means to verify the presence of entanglement shall be briefly introduced. The former is the requirement of indistinguishability between photons involved in the quantum state and the latter refers to entanglement witnesses, which can also have a tight relationship to the quantum state's fidelity. However to get into this discussion, a quick reminder about what entanglement actually is, shall be provided in the first place.

6.2.1 Entanglement

In general there is a lot of literature available about entanglement. Some textbooks treat this manner ([28]) and there are also some very nice reviews on the subject available, which also incorporate the multiqubit case, see for instance ([35], [143], [144]) and references therein. Here, a brief summary of entanglement is given sufficient to understand the following experimental results.

Bipartite pure states The proper definition of entanglement can be stated as follows: *Every state that is not separable is entangled.* Mathematically speaking, every bipartite wavefunction, which can be written as

$$|\psi\rangle = |\phi_1\rangle \otimes |\phi_2\rangle \tag{6.19}$$

is separable. If $|\psi\rangle$ does not fall under the category of functions defined by eq. (6.19), it represents an entangled state. In other words, entanglement of a bipartite system is defined as the impossibility to write the wave function as a simple tensor product of the individual subsystems. To illustrate this point, we focus on a two qubit scenario, which is in a pure quantum state. Each contributing particle is considered as a two-level system with the spin as the quantum number, i.e. $|s\rangle_i \in \{|\uparrow\rangle, |\downarrow\rangle\}$, with $i \in \{1,2\}$ representing the respective qubit. For a photon, the qubit is encoded in its polarisation[12] by associating the horizontal state according to $|H\rangle = |\uparrow\rangle$ and the vertical according to $|V\rangle = |\downarrow\rangle$. Considering the wavefunction for the entire bipartite system, there are four possible quantum states, which are entangled and at the same time can form a basis of the state space, called the Bell states ([28],[142]):

$$|\Phi^{\pm}\rangle = \frac{1}{\sqrt{2}}\left(|\uparrow\rangle_1|\uparrow\rangle_2 \pm |\downarrow\rangle_1|\downarrow\rangle_2\right) \quad ; \quad |\Psi^{\pm}\rangle = \frac{1}{\sqrt{2}}\left(|\uparrow\rangle_1|\downarrow\rangle_2 \pm |\downarrow\rangle_1|\uparrow\rangle_2\right) \tag{6.20}$$

From these, we can nicely see what entanglement implies: As soon as a measurement is done on one particle, which collapses the state either into $|\uparrow\rangle$ or $|\downarrow\rangle$, the state of the second particle is instantaneously

[12] It shall be noted, that such a treatment of polarisation by an $SU(2)$ symmetry group is only possible because longitudinal polarisation of light does not occur, at least not in vacuum, due to photons being massless particles.

determined as well. This is often discussed in the context of the Einstein-Podolski-Rosen paradox ([3]) from 1935. A possible way to test this feature has been proposed by Bell ([5], [6]) and a redefinition to the measurable polarisation of correlated photon pairs has been given by Clauser, Horne, Shimony and Holt ([145]). The first experiment carrying out an evaluation of such a CHSH-Bell inequality has been done by Freedman et al. ([7]) in 1972 and lots of successive work has been done since.
For our purposes it is only important to know about the requirement of having this non-classical correlation, because otherwise the state would factorise, as e.g. given by

$$|\tilde{\psi}^{\pm}\rangle = \frac{1}{\sqrt{2}}\left(|\uparrow\rangle_1|\downarrow\rangle_2 \pm |\uparrow\rangle_1|\uparrow\rangle_2\right) = \frac{1}{\sqrt{2}}|\uparrow\rangle_1 \otimes \left(|\downarrow\rangle_2 \pm |\uparrow\rangle_2\right),$$

which is a separable state and consequently not entangled.

Multiqubit pure states So far only two qubits have been considered. In moving to higher numbers, the situation becomes more complex as multiple different types of entanglement appear. For clarity it is intriguing to consider a state consisting of three light quanta with wavefunctions $|\phi_1\rangle$, $|\phi_2\rangle$, $|\phi_3\rangle$ to start with. Here, three forms of entanglement can be distinguished, when considering the criterion of stochastic local operations and classical communication, SLOCC, further discussed in references ([146]-[149]). These are referred to as completely separable, bi-separable and genuine three-partite entangled. Altogether they differentiate further into six classes of states ([146]). The first corresponds to a state, whose wavefunction factorises according to

$$|\psi\rangle^{\text{sep}} = |\phi_1\rangle \otimes |\phi_2\rangle \otimes |\phi_3\rangle. \tag{6.21}$$

The second, third and forth correspond to entanglement either in the qubits 1 and 2, named $|\phi\rangle^{\text{bi}}_{1-2}$, 2 and 3, named $|\phi\rangle^{\text{bi}}_{2-3}$, or 1 and 3, named $|\phi\rangle^{\text{bi}}_{1-3}$, in tensor product with the state of qubit 3, 1 or 2, respectively; thus written as[13]

$$|\psi\rangle^{\text{bi}}_{1-2,3} = |\phi_3\rangle \otimes |\phi\rangle^{\text{bi}}_{1-2} \quad \text{or} \quad |\psi\rangle^{\text{bi}}_{2-3,1} = |\phi_1\rangle \otimes |\phi\rangle^{\text{bi}}_{2-3} \quad \text{or} \quad |\psi\rangle^{\text{bi}}_{1-3,2} = |\phi_2\rangle \otimes |\phi\rangle^{\text{bi}}_{2-3}. \tag{6.22}$$

The fifth and sixth class are not separable at all, hence correlations exist between all three of their entities. Such states are attributed the term genuine multiqubit entangled. The first one is referred to as GHZ-class with states like

$$|GHZ_3\rangle = \frac{1}{\sqrt{2}}\left(|\uparrow_1,\uparrow_2,\uparrow_3\rangle + |\downarrow_1,\downarrow_2,\downarrow_3\rangle\right) \tag{6.23}$$

and the second is labelled W-class, comprising states like

$$|W_3\rangle = \frac{1}{\sqrt{3}}\left(|\uparrow_1,\uparrow_2,\downarrow_3\rangle + |\uparrow_1,\downarrow_2,\uparrow_3\rangle + |\downarrow_1,\uparrow_2,\uparrow_3\rangle\right). \tag{6.24}$$

The former contains the highest degree of entanglement and thus shows the strongest correlation associated with the maximum violation of Bell inequalities among all three-partite entangled states ([35]). The latter is in contrast more robust against qubit loss, i.e. partial tracing over one qubit in the wavefunction. So there is a hierarchy in terms of entanglement between the six classes, shown in fig. 6.3.
For higher qubit numbers than three, infinitely many classes exist ([147], [148]) and quantum states are commonly divided up into different families. A more thorough discussion of this manner can e.g. by found in ([35], [87]). For us, only the family of Dicke states ([150]) is important, which is defined by ([35])

$$|D_{N,k}\rangle = \left(\begin{array}{c} N \\ k \end{array}\right)^{-\frac{1}{2}} \sum_j P_j\{|\uparrow\rangle^{\otimes k} \otimes |\downarrow\rangle^{\otimes(N-k)}\}, \tag{6.25}$$

whereby N assigns the total number of qubits involved in the state and k denotes the number of excitations. As our goal behind building the enhancement resonator apparatus is to generate the $|D_{6,3}\rangle$-state, it now becomes obvious, why we prefer to have a simultaneous emission of three photon pairs, each comprising a horizontally and a vertically polarised photon generated by type-II down-conversion. Furthermore, since one has to be able to achieve the linear superposition of eq. (6.25), all six photons have to be split-up into different, well-defined spatial modes. This motivates the particular implementation of the linear optical set-up, described in section 3.3.

[13] The states $|\phi\rangle^{\text{bi}}_{1-2}$, $|\phi\rangle^{\text{bi}}_{2-3}$, $|\phi\rangle^{\text{bi}}_{1-3}$ correspond to bipartite entangled states, given by the Bell states in eq. (6.20).

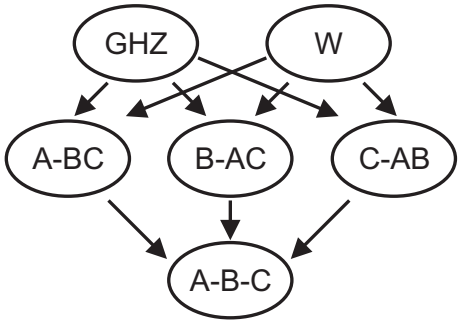

Figure 6.3: Hierarchy of pure, three-partite entangled quantum states. Genuine multi-partite entangled states are located at the top, whereas fully separable states form the bottom. Transformations from higher towards lower levels are feasible by stochastic local operations and classical communication (see [146]-[149] for details). Source: ([87]).

Mixed states As mentioned in subsec. 6.1.2, the SPDC process will produce additional higher orders on top of six-photon emission, which add noise onto the desired quantum state. So the states we really observe in the experiment are not the pure ones considered so far, but a statistical mixture of the desired state with some background noise. Such a situation is described by utilisation of the density matrix formalism[14], whereby the density matrix is given by

$$\rho = \sum_i c_i |\psi_i\rangle\langle\psi_i|, \tag{6.26}$$

with the $|\psi_i\rangle$ representing the different states the system can be in, i.e. either our desired state or states stemming from the noise background. The c_i are probability factors with $\sum_i c_i = 1$. In terms of entanglement, the criterion, eq. (6.19) for a state ρ to be entangled transforms into ([35])

$$\rho \neq \sum_i p_i \rho_i^a \otimes \rho_i^b. \tag{6.27}$$

In contrast, every density matrix, which can be written as a sum of product states $\rho_i^a \otimes \rho_i^b$ is referred to as separable. With this short introduction, we can move on to the necessity of indistinguishability.

6.2.2 Indistinguishability

In order to have the previously mentioned indistingishability needed for entanglement, we must certify not to have another way, i.e. another physical observable available, which allows distinction between the different contributing photons. Such an additional quantity would enable one to figure out in which state the system is without a measurement on the polarization degree of freedom. This would allow to distinguish the photons, described by a separable state. It shall be particularly stressed, that just the mere possibility is already enough to destroy the quantum correlations, independent of an actual measurement being performed or not[15]. Thus, despite the actual polarisation entanglement, all other properties of the photons have either to be equal or smeared out in terms of their quantum uncertainty to an extend preventing distinction between quantum states, i.e. they have to be indistinguishable. We now consider experimental effects that could lead in principle to distinguishability of photons produced by SPDC. Since we are concerned about multi-qubit states, made up of several SPDC photons, there are two subsets to be analysed: first single photon pairs, second different pairs.

Indistinguishability between a signal and idler photon pair Explained in a simplified picture not taking into account the biphoton amplitudes of the down-conversion photons, as e.g. done in references ([101], [153]), the distinguishability between the signal and idler photon arises from the birefringence of the BBO crystal. Due to the difference between extraordinary and ordinary refractive index, photons polarised along either direction will experience walk-off effects between one another. There are two contributions: The first stems from differing spatial propagation angles between the extraordinary polarised

[14] More information about density matrices can e.g. by found in ([28], [151], [152]).

[15] In other words: Quantum mechanical state preparation does not account for how a measurement is performed or if the applied measurement apparatus is accurate enough to gain the required precision for a distinction in this additional parameter.

pump and signal beam with respect to the ordinary polarised idler wave, causing a transverse displacement between both emission modes. The second is a temporal separation imparted by the differing group velocities the signal and idler wavepackets experience, whose magnitude is increasing along the crystal with the greatest time delays occurring for photons generated in the front part of the BBO crystal. More information about both effects can be found in reference ([154]). The resulting effect on the quantum state of the photons is the introduction of an additional mode, or respectively quantum number, denoted for instance t_1 for horizontally ($|\uparrow\rangle$) and t_2 for vertically ($|\downarrow\rangle$) polarised light. In turn the generated two photon Bell state[16] $|\Psi^+\rangle$ in eq. (6.20), would modify to

$$|\Psi'^+\rangle = \frac{1}{\sqrt{2}}\left(|(\uparrow,t_2)_a,(\downarrow,t_1)_b\rangle + |(\downarrow,t_1)_a,(\uparrow,t_2)_b\rangle\right), \tag{6.28}$$

which clearly allows distinction between both terms without a measurement performed on the polarisation degree of freedom, thereby destroying entanglement[17]. The remedy for this problem ([132]) is to include a $\lambda/2$-waveplate and another BBO crystal of half thickness behind the SPDC source, as done within our set-up depicted in fig. 3.1. The waveplate swaps the polarisation of the signal and idler, which hence experience the opposite transverse walk-off directions and group velocity differences in the second crystal. In other words, both wavepackets move together again and the effects of birefringence in the first crystal are compensated for. However things are more subtle than described in this outline and more elaborate discussions can be found in references ([101], [153], [154]).

Indistinguishability between different SPDC pairs For generating a state of higher photon number than two, multiple emissions from the SPDC process have to be indistinguishable from one another. So there must not be an opportunity to distinguish between different emission times of the produced down-conversion pairs. Such a situation has been studied e.g. in references ([155], [156]), whereby it has turned out to be necessary to increase the coherence time of the pairs to exceed the pump pulse duration. The coherence time[18] is regarded here as the FWHM of the temporal intensity profile of the SPDC photons, i.e. the FWHM FT-limited pulse duration. As done previously in subsec. 5.3.3 already, we will again assume a Sech intensity profile for the down-conversion spectrum and achieve, by utilising eqs. (5.24) and (5.39), a relation between the coherence time T_C and the spectral widths $\Delta\nu_{SPDC}$ of

$$T_C = \Delta\tau^{FT}_{FWHM} = \frac{4\cdot \operatorname{arcsech}\left(\frac{1}{\sqrt{2}}\right)}{\pi^2 \Delta\nu_{FWHM}}. \tag{6.29}$$

Using furthermore the relation $\Delta\nu_{FWHM} = \frac{c}{\lambda_0^2}\Delta\lambda_{FWHM}$ with $\lambda_0 = 780\,nm$ and a spectral width for signal and idler as given in table 5.8, we can infer their coherence times to be

$$T_C^H \approx 79\,fs \quad ; \quad T_C^V \approx 88\,fs, \tag{6.30}$$

i.e. much smaller than the temporal width of the pumping beam of $\tau^{\text{Sech}}_{\text{pulse}} \approx 176\,fs$ (table 5.7). Therefore time binning, or, in other words, distinction between pairs, created in the leading edge with respect to ones created in the trailing edge of the pumping pulse, would be possible and indistinguishability between such pairs could not be established. Therefore we spectrally filter the SPDC photons by an interference filter behind the SM fibre output (see fig. 3.4) with a bandwidth of $\Delta\lambda = 2.8\,nm$ and a square-hat transmission profile, leading to a broadened coherence time of the SPDC-photons as large as

$$T_C = 241\,fs > \tau^{\text{Sech}}_{\text{pulse}}. \tag{6.31}$$

Although this picture is a simplification, it provides a good qualitative understanding about what is going on. A detailed analysis is found in references ([155], [156]).

[16] As the SPDC is set-up for collinear emission, the signal and idler photons would consequently have to be spatially separated first in order to obtain an entangled Bell state.

[17] Consider e.g. t_i to represent the arrival time at two ultra-fast detectors, D_a and D_b, in the output modes a and b of a non-polarising beam splitter positioned inserted into the SPDC output mode, in which case always one detector would click before the other. So without retrieving any information about the involved polarisations, if D_a goes first, one would know $|\Psi'^+\rangle$ to be in the state $|\downarrow_{a,t_1},\uparrow_{b,t_2}\rangle$, otherwise its state would be $|\uparrow_{a,t_2},\downarrow_{b,t_1}\rangle$, which are both separable

[18] Note that the SPDC spectrum is continuous and does not have a comb structure like the pumping beam. Therefore defining a coherence time corresponding to the inverse spectral width is sensible and analogous to e.g. the coherence time of atomic excitations. For mode locked laser pulses, the same argument applies for each individual longitudinal mode, whose coherence time is defined by its linewidth. However a coherence time derived from the pulse duration does not make sense because of the pulses' comb structure.

6.2.3 Entanglement witness

As a last point in this theory section, the method of entanglement witnesses shall be introduced. While there are multiple methods to examine entanglement for a bipartite quantum system[19], for higher qubit numbers few are known to detect genuine N qubit entanglement (with N assigning the number of entities involved in the quantum state). Here witness operators come into play, which are versatile tools to detect the presence of entanglement even for multiqubit entangled states. Furthermore they offer the very convenient feature not to require the entire density matrix of the state. Thus a full state tomography can be avoided to test for entanglement, which would otherwise take a considerable amount of measurement time. A nice review regarding entanglement detection can for instance be found in reference ([35]).

Fidelity Before focussing on witnesses, the quantity called quantum state fidelity shall be introduced first. It is generally speaking a measure for the distance between two quantum states ρ_1 and ρ_2 given as ([157])

$$F = \left(Tr\left(\sqrt{\sqrt{\rho_2}\rho_1\sqrt{\rho_2}} \right) \right)^2, \tag{6.32}$$

whereby the operation Tr represents the trace over the resulting matrix. In other words it just indicates, how well the experimentally generated state resembles the theoretically expected one. The last point is evaluate by assigning ρ_1 as the experimental state and $\rho_2 = |\Psi_{theo}\rangle\langle\Psi_{theo}|$ as its theoretical, pure state counterpart. As the latter is a pure state, ρ_2 is a projector onto the desired state and eq. (6.32) simplifies to ([87])

$$F_{\rho_{exp}} = Tr\left(|\Psi_{theo}\rangle\langle\Psi_{theo}|\rho_1\right) = \langle\Psi_{theo}|\rho_1|\Psi_{theo}\rangle. \tag{6.33}$$

If even ρ_1 is pure[20], we obtain

$$F_{\rho_{exp}} = |\langle\Psi_{theo}|\Psi_{exp}\rangle|^2 \tag{6.34}$$

and thus observe the fidelity just to represent the state overlap between these two states.
The experimental determination of the fidelity, as well as the one of entanglement witnesses, can be implemented by a decomposition of the operators. I.e. the measurement operator for the quantity under scrunity is expanded into a linear combination of operators, which are given by the unity matrix and the three Pauli-spin matrices

$$\mathbb{1} = \begin{pmatrix} 1 & 0 \\ 0 & 1 \end{pmatrix}, \quad \sigma_x = \begin{pmatrix} 0 & 1 \\ 1 & 0 \end{pmatrix}, \quad \sigma_y = \begin{pmatrix} 0 & -i \\ i & 0 \end{pmatrix}, \quad \sigma_z = \begin{pmatrix} 1 & 0 \\ 0 & -1 \end{pmatrix}, \tag{6.35}$$

acting on each qubit. To illustrate this method, imagine a term for a four qubit state, e.g. given by

$$\hat{O} = \sigma_x \otimes \sigma_y \otimes \sigma_z \otimes \mathbb{1}. \tag{6.36}$$

In photon polarisation Hilbert space, this operator corresponds to a measurement of the expectation value for the first qubit in the plus-minus basis, with eigenstates $|+/-\rangle = \frac{1}{\sqrt{2}}(|H\rangle \pm |V\rangle)$, for the second qubit in the left-right basis, with eigenstates $|R/L\rangle = \frac{1}{\sqrt{2}}(|H\rangle \pm i|V\rangle)$, for the third qubit in the horizontal-vertical basis, with eigenstates $|H/V\rangle$, and a 1 for the last qubit, whereby 1 represents simply the detection of a photon. Expectation values are evaluated by adjusting the waveplates in linear optical set-up (see section 3.3) to an observation in the correct basis[21]. Since each projection operator in eq. (6.35) has an eigenvalue of either ± 1 within the basis of its two eigenvectors, the expectation values of the operator σ_i can easily be extracted from the measured count rates within each arm of the linear optical set-up. The method to do so is described in detail in reference ([87]) and shall not be repeated here.

[19] See e.g. ([35], [87]) for a good overview.

[20] It shall be noted that purity in ρ_1 is a theoretical simplification and can never be achieved in an experiment, as there is always some noise present.

[21] E.g. this corresponds to waveplate angle settings of $\left(\theta\left(\frac{\lambda}{2}\right) = 22.5°, \phi\left(\frac{\lambda}{4}\right) = 0°\right)$ for the σ_x-basis, angle settings of $\left(\theta\left(\frac{\lambda}{2}\right) = 0°, \phi\left(\frac{\lambda}{4}\right) = 45°\right)$ for the σ_y-basis and angle settings of $\left(\theta\left(\frac{\lambda}{2}\right) = 0°, \phi\left(\frac{\lambda}{4}\right) = 0°\right)$ for both waveplates to observe the σ_z-basis.

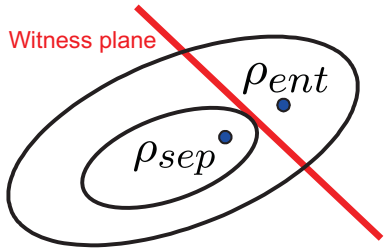

Figure 6.4: Graphical representation of entanglement witness operation. The system's Hilbert space is divided up into a set of separable and entangled states. A witness defines a hyperplane within this Hilbert space, whereby an optimal witness places the plane tangential to the edges of the former subset. The operator evaluates the positioning of the state under consideration with respect to this plane. If it lies towards the side of the plane containing entangled states only, this method concisely proves entanglement. Otherwise no conclusion can be drawn.

Witness operators In order to understand, how entanglement witnesses work, we will rely on a geometrical exemplifications of these tools. The set of all separable states, defined in eq. (6.19), forms a convex set, positioned within the system's entire Hilbert space of separable and entangled states. There is furthermore a sharp boundary between entangled and separable states, as shown in fig. 6.4. A witness operator defines a hyperplane within this Hilbert space, which is tangential to the separable subset ([35]). Furthermore the witness operator, denoted as $\hat{W}$ in the following, assesses the location of a specific state under study, here ρ_{exp}, with respect to the aforementioned plane. Depending on the sign of the outcome, one can tell on which side of the hyperplane ρ_{exp} is located at. So clearly if it lies in the hemisphere only comprising entangled states, ρ_{exp} is also an entangled state. However if it is positioned within the other area, no information about the entanglement of ρ_{exp} can be extracted, since it can in principle be within either subset, as fig. 6.4 indicates. In such a situation, another witness operator has to be used, which is better optimised for the system at hand. In other words the expectation values of witness operators constitute a sufficient, but not a necessary criterion for entanglement.
In terms of their mathematical definition, different types of witnesses exist ([35]). An intriguing species are the generic witnesses, defined as

$$\hat{W}_{gen} = \alpha \cdot \mathbb{1} - |\Psi\rangle\langle\Psi| \tag{6.37}$$

whereby $|\Psi\rangle$ is a pure entangled quantum state. The constant $\alpha = |\langle\Phi_{sep}|\Psi\rangle|^2$ is the distance between the aforementioned state and the closest separable state. States are detected as entangled, if the expectation value of eq. (6.37) with the experimental, mixed state ρ_{exp} obtains a value smaller that 0:

$$\langle\hat{W}_{gen}\rho_{exp}\rangle < 0 \rightarrow \rho_{exp}\,\text{entangled} \tag{6.38}$$

Observing this expression in more detail and using eq. (6.33), provides us with the connection between the generic witness and the fidelity:

$$\langle\hat{W}_{gen}\rho_{exp}\rangle = Tr\left(\hat{W}_{gen}\rho_{exp}\right) = \alpha\underbrace{Tr\left(\mathbb{1}\rho_{exp}\right)}_{=1} - \underbrace{Tr\left(|\Psi\rangle\langle\Psi|\rho_{exp}\right)}_{F_{\rho_{exp}}} = \alpha - F_{\rho_{exp}} \tag{6.39}$$

The witness can consequently be thought of as checking for the minimal fidelity (eq. (6.33)) required to still be able to detect ρ_{exp} as entangled.
For the evaluation of entanglement in the following experimental section regarding photon pair generation rates, we will however utilise a two-setting spin squeezing witness for four qubits ([50], [158]-[160]):

$$\hat{W}^4_{spin} = \hat{J}^2_x + \hat{J}^2_y, \tag{6.40}$$

with $J_k = \frac{1}{2}\sum_{i=1}^{4} P_i\left(\sigma^i_k \otimes \mathbb{1} \otimes \mathbb{1} \otimes \mathbb{1}\right)$ and P_i assigning all symmetric permutations of σ_k over all four qubit locations i, with $k \in \{x, y, z\}$. In contrast to the generic witness (eq. (6.37)), the expectation value of this operator has to be larger than the positive bound of ([50])

$$\langle\hat{W}^4_{spin}\rangle = Tr\left(\hat{W}^4_{spin}\rho_{|D_{4,2}\rangle}\right) = \langle J^2_x\rangle + \langle J^2_y\rangle \overset{!}{>} \frac{7}{2} + \sqrt{3} \approx 5.23 \tag{6.41}$$

with a maximally possible value of $\langle \hat{W}^4_{spin} \rangle = 6$ for the $|D_{4,2}\rangle$ state. Furthermore a lower bound for the fidelity of the $|D_{4,2}\rangle$ can be yielded by utilising yet another, three setting based witness operator, defined as ([47])

$$\hat{W}_{|D_{4,2}\rangle} = 2 \cdot \mathbb{1} + \frac{1}{6}\left(J_x^2 + J_y^2 - J_x^4 - J_y^4\right) + \frac{31}{12}J_z^2 - \frac{7}{12}J_z^4, \tag{6.42}$$

whereby the J_i assign operators as defined above. The fidelity F can consequently be estimated to be greater as ([47])

$$F \geq \frac{2}{9} - \frac{\langle \hat{W}_{|D_{4,2}\rangle} \rangle}{3}. \tag{6.43}$$

6.3 UV cavity as pump source for multi-photon generation

6.3.1 Experimental implementation

In the following we will examine the achievable count rates for different emission orders of the SPDC process as a function of the UV pump power. We are particularly concerned about single, double and triple pair emission rates, wherefore these will be subject of the following investigations. Therefore the resonator is locked at certain cavity levels, and the SPAPDs in the linear optical set-up (see fig. 3.4) are applied as photon counters for registering two-, four- and six-fold coincidence events. Since we would also like to evaluate witness operators in order to detect entanglement and estimate the fidelity of the $|D_{4,2}\rangle$ Dicke state, we investigate every cavity-level setting in all three bases, $\{H/V\}$, $\{+/-\}$ and $\{L/R\}$. Regarding the amount of data taken for a specific cavity level, it has turned out, that particularly the highest and lowest cavity levels tend to be less stable in terms of the intra-cavity UV power, wherefore the acquired data has been registered in a shorter measurement time. This results, especially for the witness analysis, in larger error bars for smaller cavity levels. Besides knowing the integrated intra-cavity UV power level, observed by the photodiode behind mirror $M4$, also the spectral content of the intra-cavity pulses is monitored by the spectrometer positioned behind the same mirror (see fig. 3.1). Before analysing the coincidence data, we will examine these associated UV spectra, as they are important for the relevance of the observed photon count rates.

6.3.2 Multi-photon count rates

UV spectra In terms of the SPDC photon count rate yield provided by our source, one should be aware of its dependence on the properties of the intra-cavity pump spectra. If the spectral width of pumping pulses changes, there are in turn also modifications introduced in the count rate level. The reasons therefor are as follows[22]:

- For a smaller spectral width, less frequency comb modes will couple into the resonator (see discussion in subsec. 2.1.4). While each excited cavity mode still experiences the same power enhancement, which is solely defined by the cavity finesse (see section 4.3), there are altogether less modes. So the intra-cavity pump power will drop as well and correspondingly lower SPDC photon emission rates are achieved, according to eq. (6.15).

- A spectral change of the pump alters the spectral width of the down-conversion photons (see subsec. 5.3.3). As explained in reference ([101]), this will change the spatial distribution of the SPDC photons as well, since their angular positioning is wavelength dependent. Consequently their coupling efficiency into the SM fibre, guiding them to the linear optical set-up, will be modified. Such an alteration becomes the more serious the higher the photon number n of the coincidence event under study is, since the fibre coupling efficiency scales to the power of n for the simultaneous coupling of all n photons.

- Another possible alteration in the observed SPDC photon count rates relates to the applied interference filter at the SM fibre output (see subsec. 5.3.3 and 6.2.2). If the SPDC spectrum is broader due to a broader pumping spectrum, the interference filter will cut-off a higher spectral portion in the spectrum's leading and trailing edge, whereby a greater amount of photons is lost than compared to a situations with a spectrally narrower initial pumping beam.

[22] The wavelength dependence of transmission and reflection properties of optical components as well as that of the SPAPD-detectors are neglected. However these can of course also influence the count rates, if the spectrum of the pump and the SPDC photon spectrum drifts.

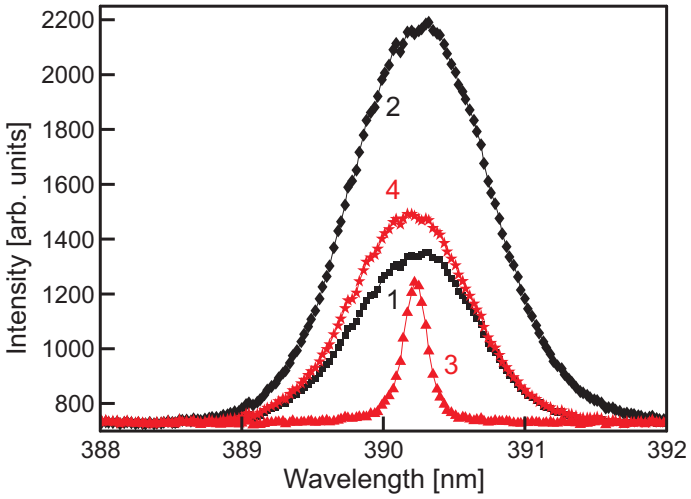

Figure 6.5: Examples of intra-cavity UV pumping spectra. Their numbering $1-4$ and colour coding corresponds to the datapoint labelling in figs. 6.6, 6.8 and 6.9. Spectra 1, 2 and 4 have approximately equal spectral widths, whereby spectrum 3 is a lot narrower than the other three. Spectrum 1 corresponds to the lowest averaged UV pumping power of $P_{UV} \approx 2.8\,W$ still entering the SPDC count rate analysis, whereby spectrum 2 is associated with the second highest pumping power of $P_{UV} \approx 7.2\,W$ applied for this measurement.

In summary, changes in the intra-cavity UV spectrum will lead to variations in the observed correlated SPDC photon count rates. Since we would like to compare count rates for different UV pumping power levels, it is hence vitally important to have a similar spectrum present throughout the entire measurement. To this end, we monitor the UV spectrum as well, recording a dataset with the spectrometer behind mirror $M4$ (see fig. 3.1) at approximately every second. This allows to keep track of changes in the intra-cavity spectrum throughout the count rate measurements. Therefore only count rate measurements coming along with spectra of approximately equal spectral content are considered any further here.
For all spectra, recorded during the count rate measurement for a particular cavity level, an averaged representative has been calculated. The result is shown in fig. 6.5 for the lowest and second highest UV power levels entering the count rate analysis. The spectra are represented by the two black curves, showing the same full width half maximum, although their amplitudes are of course different, due to the gross difference in pulse power. To asses the stability of the UV spectra, all averaged datasets for the cavity level values, used in the following count rate analysis, as well as the ones additionally incorporated later in the discussion concerning entanglement, have been normalised to their maximum value and subsequently fitted by a Sech spectral function according to[23] (eq. (5.37)).

$$S(\nu)^{\text{Sech}} = \text{sech}^2\big(\pi^2 \Delta t(\nu - \nu_0)\big).$$

We calculate the FWHM spectral width $\Delta\nu$ and, by using the relation $\Delta\lambda = \lambda_0^2 \Delta\nu / c$ with $\lambda_0 = 390\,nm$, the spectral width $\Delta\lambda$ in wavelength terms. The resulting values for the latter are shown in fig. 6.6, whereby the black data indicates the spectra corresponding to data used for the following count rate evaluation. The red points are smaller spectra for lower cavity levels, considered later on during discussing the presence of entanglement. We see, that over the relevant UV power range, the black curve is nearly flat with a mean spectral width of $\Delta\lambda \approx 1.03 \pm 0.07\,nm$. Such a behaviour is good enough for our purposes and the recorded count rates relating to them can be utilised to characterise the cavity as a source for SPDC photons.

Count rates and fit by SPDC model To analyse the count-rate statistics of the cavity as a source for SPDC photons, all two-, four-, six-fold coincidences will be considered. In other words, counts resulting from two detectors within the same arm of the linear optical set-up clicking, one detecting an $|H\rangle$- the other one a $|V\rangle$-polarised photon, are taken into account alongside the coincidences between detectors in

[23] It shall be noted, that the values stated here deviate from the ones obtained in the discussion regarding pulse duration (chapter 5). The mismatch is due to the time difference of half a year between both measurements, during which not only the laser system's output spectrum has changed but also the set-up has been realigned several times. So both datasets are not comparable to one another.

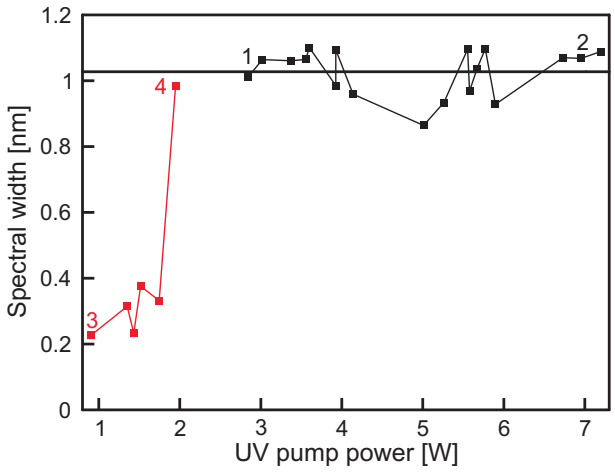

Figure 6.6: Spectral widths of averaged intra-cavity UV spectra recorded during measuring the coincidence count rate levels of the cavity as a function of pumping power. The black points represent spectra, entering the SPDC photon count rate evaluation. Since they are nearly constant in their widths, they enable the simultaneously observed SPDC photon count rates to be used for characterising the emission properties of the photon source. Furthermore they also have appropriate spectral widths to allow for the observation of multi-photon entanglement. The red points correspond to spectrally smaller pulses, which result in gradually increasing distinguishability between photon pairs towards lower UV power levels (see also the discussion in subsec. 6.3.3). The black horizontal line represents the average spectral width of the pump in the SPDC photon count rate measurement. The numbers at individual datapoints correspond to the labelling in figs. 6.5, 6.8 and 6.9, introduced to contrast the pump's spectral width with genuine four photon entanglement and the required coherence length of the SPDC photons, discussed in the main text of subsec. 6.3.3.

different arms. Such data processing is not sensible in terms of detection of entanglement within the multi-photon states, as it is carried out in the next subsec. 6.3.3. However, since we are here only concerned about count rates, all possibilities shall be included to yield as much statistics as possible, particularly as some lower cavity levels have turned out difficult to be maintained over longer time periods. For further evaluation, the total count rates per minute for i-fold coincidences are referred to as c_i. Errors onto these derive from Poissonian counting statistics[24]. All the resulting datapoints with the appropriate spectral width indicated by the black points in fig. 6.6, are shown in fig. 6.7 as a function of the respective UV pump power levels.
Therein we have on the one hand the desired processes with equal numbers of H- and V-polarised photons, represented by boxes and assigned as HV, HHVV, HHHVVV for two-, four- and six-fold coincidences, respectively. On the other hand events deriving from higher order emissions after photon loss, comprising coincidences with the correct number of photons, however with an unequal number of H and V photons, are depicted by diamonds[25]. Plot a) shows all three types of coincidences together in a double logarithmic plot, which enables a comparison between the strengths of the different emission orders. Plots b)-d) focus onto the individual outcomes for a particular number of detected photons, presented with a linear axis scaling. From the latter figures we can nicely infer a behaviour of the count rates with respect to the pumping power as we would expect it from the theoretical model, stated in subsec. 6.1.2: All coincidence rates between equal numbers of H and V polarised photons show different gradients compared to their higher order counterparts. Particularly for the two-fold HV count rates a linear scaling with the pump power can be inferred, whereas the notHV data shows a non-linear behaviour. A comparison between the strengths of the different emission orders in fig. 6.7 a) reveals furthermore a narrowing separation between the desired events of equal H and V polarisation and higher orders. However pumping powers are still low enough to avoid intersections between both sorts of coincidences. This means, that at modest pumping powers, higher orders are still at a sensible level with regard to the desired event rates (HV, HHVV,

[24]The values for c_i are obtained by taking the total amount of counts $C_{i,tot}$, summed over all possibilities to detect the particular coincidence, renormalised by the amount of measurement runs m, the number of measurement settings per run, 9, and the total measurement time t in minutes according to: $c_i = \frac{C_{i,tot}}{9 \cdot m \cdot t}$. Errors are derived by substituting the errors on the total count numbers $\sqrt{C_{i,tot}}$ for $C_{i,tot}$ into the aforementioned expression

[25]Please note, that higher order contributions could in principle also contribute to the count rates considered as desired here, if they are generated by a two orders higher process and have been subject to a loss of two photons, one H and the other V in polarisation. However the probability for these events is low.

HHHVVV), consequently not spoiling the observation of the $|D_{N,k}\rangle$-Dicke states (eq. 6.25) by too much background. Nevertheless by moving towards a high UV power level, the separations, particularly between the third and fourth order (HHHVVV compared to notHHHVVV), but also pronounced for second and third order (HHVV compared to notHHVV), converge together considerably. In such a situation, there will be influences of eight photon emissions apparent on top the six-photon ones or six-photon emission on top of four-photon ones, respectively. Altogether the rise in higher order contributions with respect to the desired emissions for growing pump levels has to be taken into account, when applying the enhancement resonator as a source for multi-partite entangled photon states. Thus to generate quantum states with a high fidelity (eqs. (6.32)-(6.34)), operation at rather intermediate or even lower pump power levels is required ([43]).
We can furthermore compare the measured count rates with the predictions from the theoretical SPDC model, introduced in subsec. 6.1.2. Therefore the data in fig. 6.7 a) has been fitted in two different manners: On the one hand the linearised version for low pumping power levels, eq. (6.18), and on the other hand the full expected behaviour for a particular emission order l, eq. (6.15), have been utilised. The latter is also applied for fitting the linear datasets, shown in the plots 6.7 b)-d). Since we expect from eq. (6.18) the gradient of each dataset in the logarithmic plot 6.7 a) to scale according to the emission order of the underlying event, i.e.[26] $\log_{10}(\tilde{n}_l) = \gamma_l + l \cdot \log_{10}(P_{UV})$, we can check the behaviour of the data by fitting with a fixed l. The results are included in fig. 6.7 a) by solid grey lines for the desired events of equal H- and V-polarised photon numbers and by dashed grey lines for the higher orders. All six fits resemble the data really well, showing that pumping the SPDC process yields emission as expected.
As we however already achieve rather high UV powers, a simulation of our experimental apparatus, presented in ([139]), reveals the approximation $\tanh\tau \approx \tau$, the linear fit is based on, to be at the edge of its applicability. Therefore an investigation with the tanh-behaviour of the SPDC emissions, but still neglecting influences of higher order terms, has been undertaken as well. Truncation of the sum in eq. (6.15) to a single value of l, yields the fit-functions

$$\tilde{n_l} = \beta_l \cdot \left(1 - \tanh^2\left(|\alpha| \cdot |\sqrt{P_{UV}}|\right)\right) \tanh^{2l}\left(|\alpha| \cdot |\sqrt{P_{UV}}|\right) \tag{6.44}$$

for the l-fold coincidence count rates. An analysis also taking into account higher order emission processes on top of the desired order, i.e. a sum over terms with $l' \geq l$, can be found in ([139]). The parameter β_l in the above expression constitutes a free fitting parameter, which changes for different emission orders, due to different SM fibre coupling efficiencies, detector efficiencies, beam splitter parameters, etc. In contrast the parameter α is supposed to be of the same value for all orders, as it is just proportional to the pump pulse and the BBO's crystal parameters, which enter each emission order equally. To work out a sufficient value for the latter, all data has been fitted first by leaving this parameter free as well and subsequently an averaged $\bar{\alpha}$ has been computed, resulting in

$$\bar{\alpha} = 0.03 \pm 0.01,$$

which is used for finally fitting the data once more. The outcomes for fitting the linear datasets are displayed in fig. 6.7 b)-d) by drawing solid black lines for the HV, dotted black lines for the notHV, solid red lines for the HHVV, dotted red lines for the notHHVV, solid blue lines for the HHHVVV and dotted blue lines for the notHHHVVV emissions. Also with this model, we achieve a very nice resemblance with the data. Even more interesting is the outcome of the tanh-fit for the logarithmically plotted data in fig. 6.7 a) indicated by the same colour coding. We see here a close matching between the previous linear fit and the tanh version. Therefrom we can conclude that deviations from the linearised model, due to the tanh behaviour, are still negligible for our pumping power values. In other words, this implies the SPDC emissions to still be situated within the low pump power regime, whereby no levelling-off in the emission rates for increasing pumping powers can be seen yet, i.e. the SPDC process is still far off being driven towards saturation.

6.3.3 Entanglement of four qubit states

For observing entanglement, indistinguishability of photons has to be guaranteed. In the following we will analyse how the pump spectrum in combination with the filtering of the SPDC photons influences the indistinguishability. To this end, we focus on the four photon case (2^{nd} order SPDC emissions), which can lead to the observation of four qubit Dicke states. We will analyse their entanglement for different pump spectral widths. Conveniently four-qubit events are chosen, since count rates for the six-photon state would require longer measurement times resulting in stability issues of the cavity level for certain

[26] γ_l is a free fitting parameter including the constants β_l and $|\alpha|^{2l}$ from eq. (6.18)

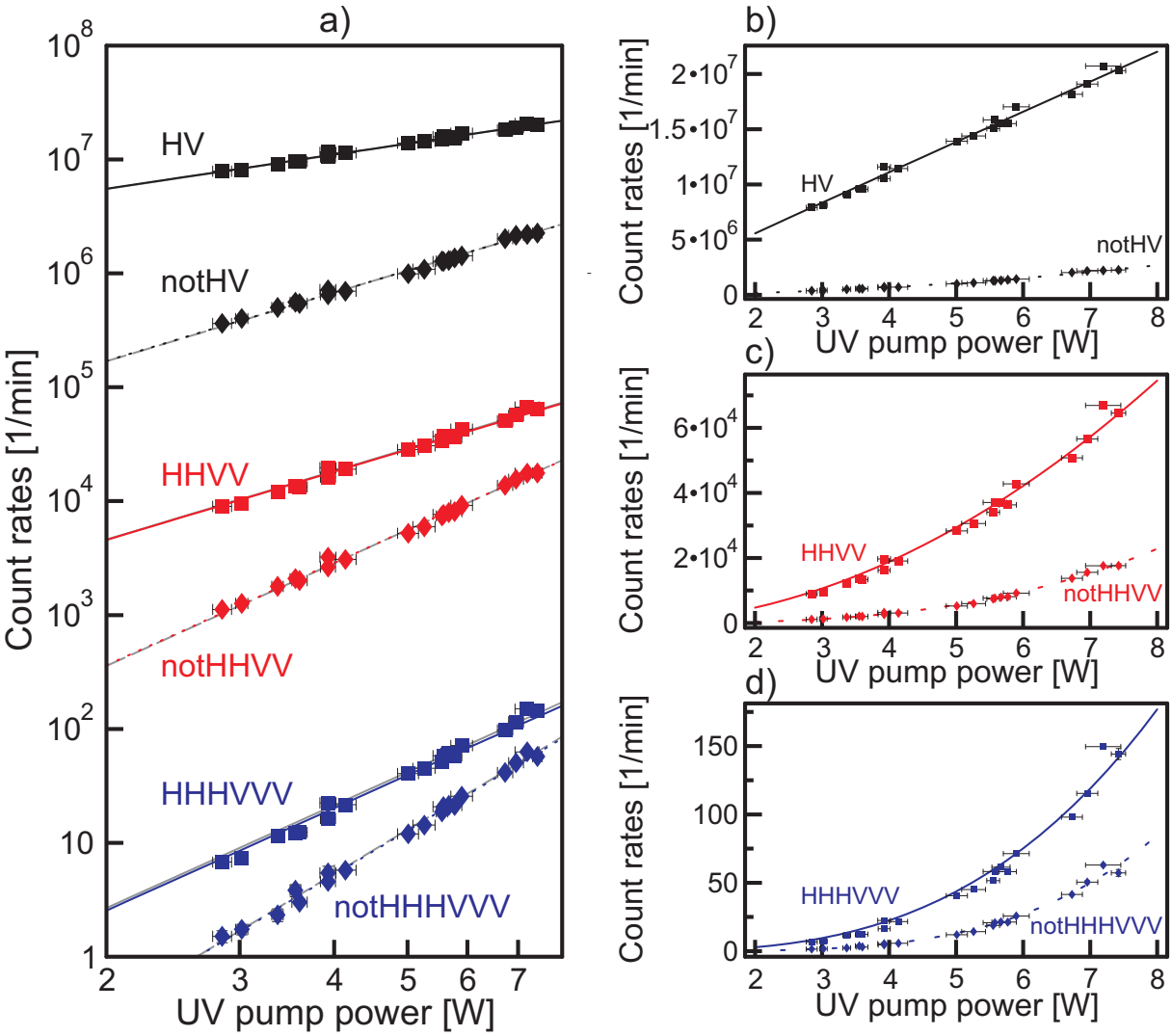

Figure 6.7: Coincidence count rates over UV power level of the SPDC pump. Plot a) shows a logarithmic plot, allowing comparison between all three orders. Plots b)-d) comprise separate linear plots of the individual orders together with counts deriving from higher emissions, depicting the expected tanh behaviour. Within all graphs, the desired coincidences equal in numbers of H- and V-polarised photons are represented by boxes, whereby higher orders with unequal distributions between both polarisation types are indicated by diamonds. The fitted curves to the former are drawn by solid lines and the ones to the latter by dashed lines. Two-fold coincidences are represented in black, four-fold in red and six-fold in blue.

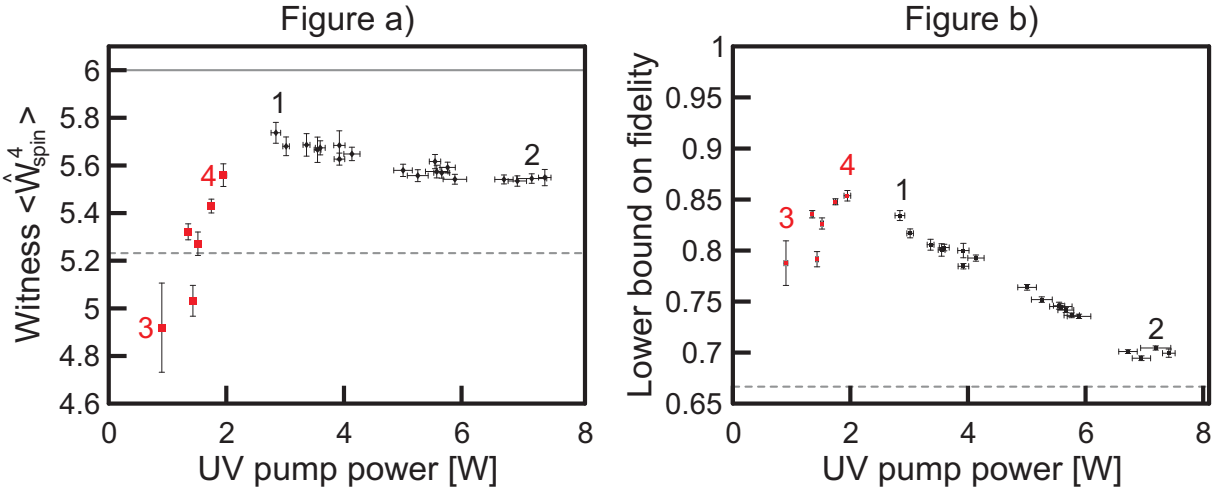

Figure 6.8: Fig. a) provides expectation values of the witness operator (6.40). Black diamonds correspond to the datapoints used for the coincidence rate evaluation presented in fig. 6.7 with spectral widths of the black points in fig. 6.6. The red points correspond to the narrower spectra in the latter plot and indicate the increasing effect of distinguishability for spectral narrowing. The points associated with the numbers $1-4$ correspond to the UV spectra shown in fig. 6.5. The dashed grey line indicates the minimal fidelity required in order to still have four photon entanglement, whereby its solid counterpart provides the maximally possible witness expectation value $\langle \hat{W}^4_{spin} \rangle$, see reference ([50]). Fig. b) shows the lower bounds on the fidelity of the $|D_{4,2}\rangle$ Dicke state, eq. (6.43), as a function of UV pumping power. The black points represent the broad UV spectra in fig. 6.6, appropriate for the count rate analysis displayed in fig. 6.7. The red points are spectra of smaller width, indicated by the red points in fig. 6.6. The datapoints marked with numbers $1-4$ correspond to the analogously labelled UV spectra shown in fig. 6.5. The dashed grey line indicates to the minimal fidelity required in order to still have four photon entanglement, see reference ([50]).

pump powers. It shall be noted, that within these measurements, opposing to the previous analysis, only four-fold coincidences between different arms in the linear optical set-up are considered. Only in this case a $|D_{4,2}\rangle$ Dicke state is observed upon conditional detection.

Fidelity of the four-qubit Dicke state The fidelity of the four photon $|D_{4,2}\rangle$ state can be estimate by evaluating the lower bound values, according to eq. (6.43) for the data recorded in the course of the coincidence rate measurement. The outcomes as a function of pumping powers are presented in fig. 6.8, whereby the black points represent the cavity level values also entering the coincidence rate measurement, being shown in fig. 6.7, and hence comprising a broad spectrum as shown in figs. 6.5, 6.6. The red boxes correspond to measurements for lower UV powers with narrower spectra, as depicted by the same colour coding in figs. 6.5, 6.6. From this plot, we can infer the fidelity to increase for lower pumping levels, whereby after some turning point, it drops down again. Ignoring the last part for a moment, one can readily acknowledge the influences of higher order emissions, which obviously increase for growing pumping powers, adding more noise to our desired state $|D_{4,2}\rangle$. Thereby they cause the fidelity of the pure state $|D_{4,2}\rangle$ to decrease, as can immediately be understood by referring to eq. (6.34). However fig. 6.8 also shows, that for intermediate power levels quite high quantum state fidelities can be obtained. The roll off in quantum state fidelity for low pumping powers, represented by the red points in fig. 6.8, is due to a degradation in entanglement of the quantum state, which results from the narrower UV pumping pulse spectra of the red points in fig. 6.6. These narrower spectra correspond to longer pumping pulses and in turn also narrower SPDC spectra. The interference filter's transmission bandwidth is therefore not tight enough anymore to elongate the coherence times of the SPDC photons by an extent sufficient cover all possible generation times underneath the UV pumping pulse and thus enable indistinguishability between separately emitted pairs. This causes the deterioration of entanglement, as we will see in more detail within next paragraph below, and thus also a degradation in the quantum state's fidelity. The minimum fidelity, required to still detect entanglement according to the generic witness requirement, introduced in eq. (6.39) and outlined for the $|D_{4,2}\rangle$-state in reference ([50]), is included in fig. 6.8 a) by the dashed grey horizontal line.

Entanglement as function of pump power and pump spectral width The aforementioned roll-off in entanglement can be further analysed by looking at the expectation value of the witness operator (6.40). The outcomes for all datapoints shown in figs. 6.6 and 6.8 a), are provided in fig. 6.8 b). The upper horizontal, solid grey line therein indicates the maximally possible value of the witness, indicating the furthest separation between a genuine four-qubit entangled state and the separable subset of states[27]. The lower horizontal, dashed grey line indicates the bound above which the expectation value (eq. (6.41)) has to lie in order to detect entanglement of the state under consideration. Again referring first to the broader UV spectra, indicated by black diamonds in fig. 6.9 a), we can see a slight degradation of the witness, likewise to the fidelity. This is once more caused by higher order contributions arising for larger pump powers. Further the behaviour of the red datapoints in fig. 6.9 a), represents the narrower spectra from fig. 6.6. We can see those decreasing sharply with a loss of entanglement detection for the smallest pump power intensity (datapoint 3 in fig. 6.9 a)) by application of the witness (6.40). However as it can be inferred from fig. 6.8 a), these states are still detected as entangled under the fidelity criterion ([50]). Nevertheless a clear trend towards lowered entanglement and thus less separation between the state under study and the separable subset is observed for spectral narrowing. By looking at the pumping pulses, exemplarily examined at the extreme locations of either set of datapoints, the spectra associated with the datapointes numbered $1-4$ in figs. 6.6 and 6.8 are shown in fig. 6.5 by the already familiar colour coding. The spectral width for the data entering the coincidence rate evaluation (spectra 1 and 2 in fig. 6.5) does of course not change. Also spectrum 4, with the largest pump power of all the red data, possesses a spectrum comparable to the aforementioned black ones. However spectrum 3 at the low pump power end has a much narrower spectral width. This observation explains the rapid degradation of entanglement towards lower cavity powers for the red data in fig. 6.9, which is caused by the narrowing of the pump spectrum, as shown in fig. 6.6. The explanation for this correlation relates to the requirement for indistinguishability between different SPDC pairs and goes as follows: According to chapter 5 narrower spectra translate into longer pumping pulse, meaning that the SPDC photons have a broader time window across which they can be generated. In terms of the requirement regarding their indistinguishablility, explained in subsec. 6.2.2, a broader delocalisation of their wavepackets would hence be needed. However the interference filter within our set-up is not sufficiently narrowband enough to provide such filtering, wherefore the pairs, originating from different emission locations underneath the pump envelope, start to become distinguishable from one another. That of course deteriorates the entanglement between them and leads to the observed drop in the fidelity and witness expectation value in fig. 6.8. A quantitative argument for this explanation is presented in fig. 6.9, where red and black spots correspond to the FT limited pulse duration of the UV pumping pulses, derived from their spectral widths in fig. 6.6 by utilisation of eq. (6.29). These times constitute the required temporal smear-out of the SPDC wavepackets, or in other words the lengthening of their coherence times, in order to render different emission processes throughout the pumping pulse indistinguishable from one another. The maximally achievable coherence time of $T_C = 241\,fs$ (eq. (6.31)), from spectral selection by propagation through the interference filter, is indicated by the horizontal grey line in fig. 6.9. This value is sufficient to achieve SPDC wavepacket overlap for all black datapoints as well as the red one indicated as number 4. For the others however, the overlap between different SPDC pairs is not large enough anymore, leading to the observed decrease in entanglement. It shall in this respect also be noted, that narrower pump spectra in principle results in narrower SPDC spectra (see eq. (5.85)), nevertheless the SPDC spectra are always more broadband than the pump, because of the phase-matching conditions. Even if the pump spectrum is continuously narrowed down towards the cw limit, the SPDC spectrum stops following at some point and levels off to a constant width, determined by the phase-matching function. Thus the coherence time of the down-conversion photons is always shorter than the FT limited pulse duration of the pump, so there will always be an element of distinguishability unless filtering is applied.

[27] Refer to the discussion in context of fig. 6.4 for details.

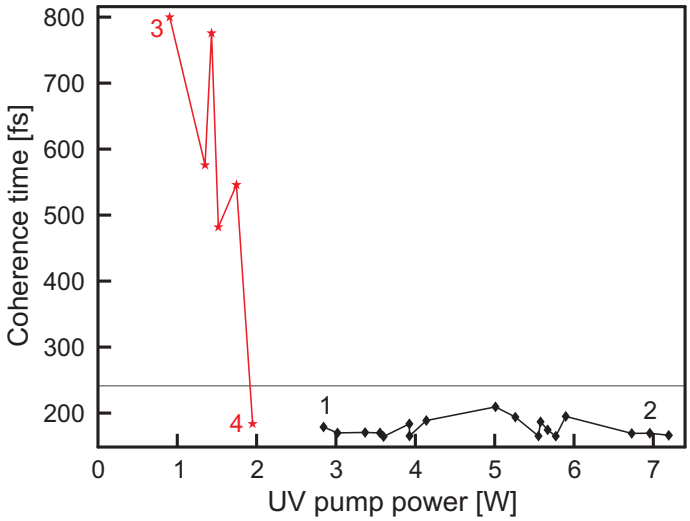

Figure 6.9: Coherence times of SPDC photons necessary to achieve indistinguishability between different pair emissions. The maximum value the interference filter, applied in our set-up, can smear out the SPDC wavepackets is indicated by the grey, horizontal straight line. Thus all black and the red point numbered by 4 should constitute completely indistinguishable photon pairs, whereby this property degrades towards lower pump power levels and hence narrower spectra.

Chapter 7

Summary

In this work, the design and the experimental implementation of a novel pumping source for spontaneous parametric down-conversion has been presented in order to achieve long term stable multi-photon emission with high count rates. The experimental set-up is based on an enhancement cavity for femtosecond mode-locked laser pulses in the ultra-violet regime, operating at a repetition rate of $80\,MHz$. It has been applied for the observation of symmetric Dicke states.
The SPDC pump pulses are coherently superimposed inside the cavity, pumping the non-linear frequency conversion process in a $1\,mm$ thick BBO crystal, positioned therein as well. In a first step, we have laid out the necessary design parameters for the resonator, considering scenarios with and without the BBO crystal. A bow-tie shape is chosen with an entire resonator length of $L_{cav} = 3.71\,m$ and a convenient beam waist for SPDC pumping of $w_0 \approx 100\,\mu m$ is calculated to be present in the focal plane between two curved mirrors. A second waist of $w_1 \approx 330\,\mu m$ lies in the middle between two plane mirrors. A maximally achievable, spectrally integrated power enhancement of 33 has been calculated for the presence of the BBO crystal, while a number of 341 has been yielded for its absence, under the consideration of perfect spatial mode matching in input coupling. The group velocity dispersion inside the cavity has been estimated to approximately $378\,fs^2$ for the former of the aforementioned situations and approximately $190\,fs^2$ for the latter.
In a second step, the resonator has been characterised experimentally. Thereby the spectrally resolved and the integrated power enhancements have been determined by measurements of the internal and external UV power levels as well as the associated internal and external pulse spectra. The outcomes result in an integrated power enhancement of 13 with the non-linear medium and 38 without it. Appropriate scaling of the spectra indicated furthermore a respective coupling fraction of 78 % and 86 % from the frequency comb of the external pulse into the cavity. The deviations from perfect spectral resemblance are caused by dispersion, which deteriorates the matching between the external and internal frequency comb, as has also been described in the course of this thesis. Enhancement stability has been shown to be maintainable at the high end for more than $3.5\,h$ at an average UV power level of approximately $7.2\,W$, whereas even longer time durations on the order of days have been observed for intermediate power levels. Additionally the resonator's finesse has been estimated independently by the ring down technique, which provided values of 72 for a scenario with, and $F^{\mathrm{noBBO}} \approx 250$ for one without the BBO. Although this measurement has been troubled by the utilisation of a spectrally broadband laser beam, the figures for the expected power enhancements, derived from the finesse outcomes under the assumption of impedanced-matched cavity coupling, tie in with the directly investigated numbers. The resonator has also be shown to operate in a regime close to single transverse TEM mode, with a beam quality factor of $M \approx 1.07$, as desired for SPDC pumping. However the low mode quality beam profile of the external pump degrades the coupling efficieny into the enhancement resonator to around 50 % only.
To infer the real duration of the internal UV pulses, we have carried out the first intra-cavity autocorrelation measurement by employing down-conversion as the required non-linear process, which has until now not been considered for this purpose. It offers simultaneous measurability of multiple correlation functions in the small pumping power limit and a pulse duration of $\tau \approx 176\,fs$ has been obtained under the assumption of having Sech-shaped pulses, whose spectral amplitude better resembles the actual internal pulses than their Gaussian counterparts. The time difference of $36\,fs$ in comparison to the Fourier transform limited pulse duration $\tau^{FT} \approx 140\,fs$, extracted from the first order correlation function, reveals the presence of residual dispersion inside the resonator.
Application of the enhancement cavity as a source for multi-photon pair emission has been investigated by registration of two-, four- and six-fold coincidences in a linear optical set-up built for photon state observation. At the high end of averaged pump powers around $7\,W$, detected coincidence count rates on

the order of $2 \cdot 10^7 \frac{\text{counts}}{\text{min}}$ for two-photon, $7 \cdot 10^4 \frac{\text{counts}}{\text{min}}$ for four-photon and $150 \frac{\text{counts}}{\text{min}}$ for six-photon events have been recorded. Here already considerable contributions from higher order noise have been recorded as well. However operating the system at intermediate power levels has been proven to reduce their influences to a level bearable for observation of multi-photon entangled quantum states with sufficient fidelity.
Furthermore, the fidelity of Dicke $|D_{4,2}\rangle$-states, observed with a symmetric distribution of four emitted SPDC photons, has been estimated as a function pumping power and spectral width. Thereby the achievement of high fidelities in an intermediate power regime has been shown. Effects on the quality of the entanglement, stemming from the increase of distinguishability between photon pair emissions from the SPDC process, have been monitored as well. Finally, to improve on the fidelity of the observed Dicke states, a proposal on noise reduction based on higher repetition rate enhancement cavities has been investigated. Such systems have been proven to only provide a sensible alternative, if also the pulse repetition rate of the pumping laser system is scaled up, as otherwise considerable degradation in photon production rates occur.
Despite these operational parameters, which serve well for the desired applications of the resonator, there are nevertheless chances for improvements to be made to the set-up. Immediate advances can be obtained for instance by reshaping the transverse beam profile of the external UV pump mode to achieve $TEM_{0,0}$ quality and in turn to enhance the coupling efficiency into the cavity. By the same token, dispersion compensation can be introduced into the resonator e.g. by substituting some cavity mirrors with chirped versions ([74]). Thereby more external frequencies could couple into the resonator, enhancing the pumping power, and less pulse distortion inside the cavity would be present. On a longer time scale in terms of available technology, of course photon number resolving detectors and increased detection efficiency would improve the experimental apparatus regarding the aforementioned aspect as well.
Concerning applications, the enhancement resonator has in the meantime already been used to study the entanglement properties of the six-photon Dicke state $|D_{6,3}\rangle$, whereby a detailed description of the experimental results is given in reference ([43]). With an average pumping power of $P_{UV} \approx 5.3\,W$, resulting in an event rate of approximately $3.7 \frac{\text{counts}}{\text{min}}$, we have been able to detect genuine multipartite entanglement in the observed state and we have achieved a quantum state fidelity of $F_{|D_{6,3}\rangle} \approx 0.654 \pm 0.024$. This number compares well to the outcomes from other experiments characterising six-photon quantum states, which achieved fidelities of $F^{([44])}_{|D_{6,3}\rangle} \approx 0.56 \pm 0.02$ and $F^{([45])}_{|G_6\rangle} \approx 0.593 \pm 0.025$ at much lower count rates[1].
In the course of the experiment we have also been able to show the usability of the $|D_{6,3}\rangle$-state as a resource for genuine multipartite entangled states of lower qubit numbers, details are given in reference ([43]). Another possibility to incorporate the enhancement resonator in combination with Dicke states is found in phase measurements with a precision below the shot noise limit. This is currently under investigation, and further details can be found in reference ([139]). Also the cavity could be employed as a pump source for other experiments, focussing on multiqubit entangled quantum states, such as for instance an extension of the set-up described in reference ([166]) towards higher qubit numbers. However there are potential applications outside the field of quantum information processing as well, whereby one particular example would be the utilisation as a source for light squeezing. This is especially convenient, since the output of the collinear type-II SPDC is a two mode squeezed state ([167]) already. Commonly known squeezing of the quadrature components in the electromagnetic output field of the down-conversion could be realised by changing the crystal geometry towards a type-I down-conversion source ([167], [168]). An example in yet another area of research would be the generation of ultrashort XUV pulses, by performing up-conversion inside the resonator, as is e.g. described in references ([169], [170]) for the application of infra-red pulses in combination with a gas jet.
Altogether the enhancement resonator presented in this thesis provides a versatile tool for quantum optical experiments, allowing to observe multipartite entangled photon states from down-conversion with very high count rates and also offering potential in other areas of physics. Therefore it constitutes a valuable advance towards the actual implementation of quantum-optical networks and quantum computation, hopefully enabling further research in this regard in the future.

[1] Approximately lower by an order of magnitude than the count rates reported in reference ([43]).

Acknowledgements

As the last and potentially most important part of this dissertation, I would like to express my personal thanks to people, without whom the present work would not have been possible in the first place. In terms of academic support, I would at the foremost like to express my gratitude to my supervisor Prof. Dr. Harald Weinfurter for offering me the opportunity of undertaking the studies for this Diplom project in his research group and supporting me in all sort of ways during my year at the MPQ. A very warm thank-you goes to my colleges Witlef Wieczorek and Roland Krischek for all the advice and assistance they patiently offered me over the last year. Without their experience and afford, the great results, achieved within the last year, would not have had the slightest chance to be realised. In that respect, I would furthermore like to state my deep appreciation for all the time Witlef has put into the correction of drafts for this thesis, despite the shortage of time regarding his own PhD viva. Also many thanks to Nikolei Kiesel, who, although having left the group half way through this project's time, nevertheless shouldered the task to help me finding my path into the world of quantum information science. Likewise many regards to Daniel Lampert-Richard and all the other members of the xqp group, as well as all the MPQ support staff, who helped me within the last 12 months. Finally my thanks also go out to all people in the quantum memories group at Oxford University and Prof. Dr. Ian Walsmley, for all their patience and understanding in giving me the time needed to finish this piece of work.
To express my gratitude concerning non-academic related issues, I would like to switch to my mother tongue, in order to allow comprehensibility for the addressee:
Diesbezüglich möchte ich insbesondere meiner Familie danken, welche mich über all die Jahre meiner Ausbildung stets unterstützt und gefördert hat. Ohne Sie wäre alle dies nicht möglich gewesen. Insbesondere meiner Mutter gebührt hier mein unermesslicher Dank für alle Entbehrungen, welche Sie auf sich genommen hat, um mir meine Ausbildung in dieser Art und Weise zu ermöglichen.
In diesem Sinne bedanke ich mich für ein schönes, lehrreiches, spannendes und sehr erfolgreiches Jahr am Max-Planck-Insitut für Quantenoptik und für mein Studium an der Technischen Universität München.

Appendix A

Cavity design

A.1 Geometrical cavity design parameters for resonator of $80\,MHz$ repetition rate

Summary of all important geometrical design parameters of the UV enhancement resonator, operating at a repetition rate of $f_{rep} = 80\,MHz$:

- Total cavity length: $L_{cav} = 3.71\,m$
- Length of sector 1, i.e. distance between mirrors M1 and M2: $d_{M1,M2} = 0.982\,m$
- Length of sector 2, i.e. distance between mirrors M2 and M1: $d_{M2,M1} = 2.728\,m$
- Distance between M2 and M3 (freely choose): $d_{M2,M3} = 0.872\,m$
- Distance between M3 and M4: $d_{M3,M4} = 0.928\,m$
- Distance between M4 and M1: $d_{M4,M1} = 0.928\,m$
- Radius of curvature mirrors M1 and M2: $R_{M1} = R_{M2} = 0.8\,m$
- Radius of curvature mirrors M3 and M4: $R_{M1} = R_{M2} = \infty\,m$

Furthermore the relevant beam parameters, which are wavefront radius $R(z)$ and spot radius $w(z)$, for the most distinctive locations within the resonator are stated in table A.1 below.

z position	Beam waist $w(z)$	Wavefront radius of curvature $R(z)$
z_{M1}	$610\,\mu m$	$-50.5\,cm$
z_{M2}	$610\,\mu m$	$50.5\,cm$
z_{M3}	$369\,\mu m$	$-2.201\,m$
z_{M4}	$369\,\mu m$	$2.201\,m$
z_0	$101\,\mu m$	$\infty\,cm$
z_1	$330\,\mu m$	$\infty\,cm$

Table A.1: Beam waist $w(z)$ (see eq. (2.4)) and wavefront curvature $R(z)$ (see eq. (2.5)) at the locations of the four cavity mirrors $M1$-$M4$ and the two focal planes z_0 and z_1.

A.2 Geometrical cavity design parameters for resonators of higher repetition rates

A.2.1 $f = 246\,MHz$ repetition rate and $L_{cav} = 1.2195\,m$ length

- Mirror radii of curvature: $R_{M1} = R_{M2} = 0.24\,m$ result in:
  - An excess parameter of $a = 0.044\,m$
  - A sector 1 distance of $d_{M1,M2} = 0.284\,m$

  - A sector 2 distance of $d_{M2,M1} = 0.936\,m$
  - Beam waists and wavefront radii of curvature according to the table below:

z position	Beam waist $w(z)$	Wavefront radius of curvature $R(z)$
z_{M1}	$351.72\,\mu m$	$-14.5\,m$
z_{M2}	$351.72\,\mu m$	$14.5\,m$
z_0	$50.65\,\mu m$	∞
z_1	$201.37\,\mu m$	∞

- Mirror radii of curvature: $R_{M1} = R_{M2} = 0.26\,m$ result in:
  - An excess parameter of $a = 0.057\,m$
  - A sector 1 distance of $d_{M1,M2} = 0.317\,m$
  - A sector 2 distance of $d_{M2,M1} = 0.902\,m$
  - Beam waists and wavefront radii of curvature according to the table below:

z position	Beam waist $w(z)$	Wavefront curvature $R(z)$
z_{M1}	$350\,\mu m$	$-16.3\,m$
z_{M2}	$350\,\mu m$	$16.3\,m$
z_0	$57\,\mu m$	∞
z_1	$191\,\mu m$	∞

- Mirror radii of curvature: $R_{M1} = R_{M2} = 0.28\,m$ result in:
  - An excess parameter of $a = 0.076\,m$
  - A sector 1 distance of $d_{M1,M2} = 0.356\,m$
  - A sector 2 distance of $d_{M2,M1} = 0.864\,m$
  - Beam waists and wavefront radii of curvature according to the table below:

z position	Beam waist $w(z)$	Wavefront radius of curvature $R(z)$
z_{M1}	$350\,\mu m$	$-18.4\,cm$
z_{M2}	$350\,\mu m$	$-18.4\,cm$
z_0	$64\,\mu m$	∞
z_1	$178\,\mu m$	∞

- Mirror radii of curvature: $R_{M1} = R_{M2} = 0.3\,m$ result in:
  - An excess parameter of $a = 0.106\,m$
  - A sector 1 distance of $d_{M1,M2} = 0.406\,m$
  - A sector 2 distance of $d_{M2,M1} = 0.814\,m$
  - Beam waists and wavefront radii of curvature according to the table below:

z position	Beam waist $w(z)$	Wavefront radius of curvature $R(z)$
z_{M1}	$353\,\mu m$	$-21.2\,cm$
z_{M2}	$353\,\mu m$	$21.2\,cm$
z_0	$73\,\mu m$	∞
z_1	$161\,\mu m$	∞

- Mirror radii of curvature: $R_{M1} = R_{M2} = 0.305\,m$ result in:
  - An excess parameter of $a = 0.116\,m$
  - A sector 1 distance of $d_{M1,M2} = 0.421\,m$
  - A sector 2 distance of $d_{M2,M1} = 0.798\,m$
  - Beam waists and wavefront radii of curvature according to the table below:

z position	Beam waist $w(z)$	Wavefront curvature $R(z)$
z_{M1}	$355\,\mu m$	$-22.1\,cm$
z_{M2}	$355\,\mu m$	$22.1\,cm$
z_0	$75\,\mu m$	∞
z_1	$155\,\mu m$	∞

A.2.2 $f = 328\,MHz$ repetition rate and $L_{cav} = 0.915\,m$ length

- Mirror radii of curvature: $R_{M1} = R_{M2} = 0.2\,m$ result in:
  - An excess parameter of $a = 0.047\,m$
  - A sector 1 distance of $d_{M1,M2} = 0.247\,m$
  - A sector 2 distance of $d_{M2,M1} = 0.668\,m$
  - Beam waists and wavefront radii of curvature according to the table below:

z position	Beam waist $w(z)$	Wavefront radius of curvature $R(z)$
z_{M1}	$303\,\mu m$	$-12.7\,cm$
z_{M2}	$303\,\mu m$	$12.7\,cm$
z_0	$51\,\mu m$	∞
z_1	$162\,\mu m$	∞

- Mirror radii of curvature: $R_{M1} = R_{M2} = 0.22\,m$ result in:
  - An excess parameter of $a = 0.07\,m$
  - A sector 1 distance of $d_{M1M2} = 0.29\,m$
  - A sector 2 distance of $d_{M2M1} = 0.624\,m$
  - Beam waists and wavefront radii of curvature according to the table below:

z position	Beam waist $w(z)$	Wavefront radius of curvature $R(z)$
z_{M1}	$304\,\mu m$	$-15.1\,cm$
z_{M2}	$304\,\mu m$	$15.1\,cm$
z_0	$60\,\mu m$	∞
z_1	$145\,\mu m$	∞

- Mirror radii of curvature: $R_{M1} = R_{M2} = 0.229\,m$ result in:
  - An excess parameter of $a = 0.0.087\,m$
  - A sector 1 distance of $d_{M1,M2} = 0.316\,m$
  - A sector 2 distance of $d_{M2,M1} = 0.686\,m$
  - Beam waists and wavefront radii of curvature according to the table below:

z position	Beam waist $w(z)$	Wavefront radius of curvature $R(z)$
z_{M1}	$307\,\mu m$	$-16.5\,cm$
z_{M2}	$307\,\mu m$	$16.5\,cm$
z_0	$65\,\mu m$	∞
z_1	$134\,\mu m$	∞

Appendix B

Characterisation of cavity parameters

B.1 Conversion factor between voltage on photodiode and power in cavity

Here, the correspondence between UV power stored inside the resonator and the voltage on the photodiode behind mirror $M4$ is calculated. As this number will be involved whenever cavity levels are considered in this dissertation, its derivation shall be stated for clarity. We figure it out by blocking the cavity and recording the power at measurement points P1 in front of mirror $M4$, $P_{P1} = 11.575 \pm 0.035\,mW$, and measurement point P2 in front of the photodiode, $P_{P2} = 511 \pm 2.5\,nW$. Therefrom the transmission through the cavity mirror $M4$ and the BS onto the photodiode can be inferred to

$$T_{P1-P2} = \frac{P_{P2}}{P_{P1}} = 4.415 \cdot 10^{-5}$$

with an error of

$$\Delta T_{P1-P2} = \sqrt{(\frac{P_{P2}}{P_{P1}^2})^2 \cdot (\Delta P_{P1})^2 + (\frac{\Delta P_{P2}}{P_{P1}})^2} = 0.025 \cdot 10^{(-5)}$$

Subsequently we observe the voltage generated by the photodiode. Since a lower intensity is transmitted through the cavity mirrors $M3$ and $M4$ for the arrangement without the BBO, due to having an input coupler of higher reflectivity, the resistor in the diode has to be changed. With an input coupler of $R_{IC} = 97.36\,\%$ reflectivity, a $R_{PD}^{\mathrm{BBO}} = 51\,k\Omega$ resistor is used and a voltage reading of $V_{\mathrm{PD,all}}^{\mathrm{BBO}} = 7\,mV$, with a dark voltage of $V_{\mathrm{PD,dark}}^{\mathrm{BBO}} = 2.7\,mV$ and thus a UV light signal of $V_{\mathrm{PD}}^{\mathrm{BBO}} = 4.3\,mV$ is yielded. The UV power incident on the photodiode is furthermore given by the spectral responce of the device, $S_{\lambda,\mathrm{PD}} = 0.17\,\frac{A}{W}$, the utilised resistor R_{PD} and the generated voltage V_{PD} by $P_{\mathrm{PD}} = \frac{V_{\mathrm{PD}}}{S_{\lambda,\mathrm{PD}} \cdot R_{PD}}$. By knowing the transmission T_{P1-P2}, the connection between the power P_{PD} and the intra-cavity level P_{cav} is obviously given by $P_{\mathrm{PD}} = T_{P1-P2} \cdot P_{cav}$, and in terms of voltage

$$P_{cav} = \underbrace{\frac{1}{S_{\lambda,\mathrm{PD}} R_{\mathrm{PD}} T_{P1-P2}}}_{=:\alpha_{\mathrm{PD}}} \cdot V_{\mathrm{PD}} \tag{B.1}$$

whereby α is the desired conversion constant. From the above stated values, the result for $P_{cav} \approx 11.76 \pm 0.07$ can be checked which is in good resemblance with P_{P1}. The appropriate conversion constant for an arrangement with the BBO crystal is hence:

$$\alpha^{\mathrm{BBO}} = \frac{1}{S_{\lambda,\mathrm{PD}} R_{\mathrm{PD}}^{\mathrm{BBO}} T_{P1-P2}} = 2.61 \pm 0.02 \tag{B.2}$$

with the error computed from the transmittance error ΔT_{P1-P2} according to $\Delta\alpha = \frac{\Delta T_{P1-P2}}{S_{\lambda,\mathrm{PD}} \cdot R_{\mathrm{PD}} T_{P1-P2}^2}$.
For the scenario without a BBO crystal hosted by the resonator, with an applied input coupler of $R_{IC} = 98.72\,\%$ reflectivity, a resistive load of $R_{PD}^{\mathrm{noBBO}} = 20\,k\Omega$ is used. We are consequently left with a constant for an empty cavity of:

$$\alpha^{\mathrm{noBBO}} = 6.66 \pm 0.04 \tag{B.3}$$

These conversion factors are always applied, when dealing with UV power levels inside the resonator.

B.2 Laser repetition rates from ring down signal

From the ring down data, the laser repetition rates can be inferred by Fourier analysis of the fast oscillations on top of the slowly varying ring down signal. Since both cavity arrangements, with and without crystal, have been measured at different days, an idea about the stability of f_{rep} can be gathered therefrom and the appropriate numbers can be used in application of eq. (4.17) to the individual datasets. The respective numbers are:

Piezo freq. [kHz]	f_{rep} with BBO [MHz]	f_{rep} without BBO [MHz]
7	80.82 ± 0.21	80.66 ± 0.17
10	–	80.81 ± 0.15
15	–	80.81 ± 0.15
20	80.64 ± 0.35	80.67 ± 0.17
20	80.68 ± 0.32	80.69 ± 0.19
25	80.77 ± 0.52	80.79 ± 0.2

whereby the errors originate from the full widths at half maximum of the laser frequency peaks in the ring down spectra. Comparison of the frequencies clearly proofs their coincidence within their error boundaries. The mean value of the laser repetition rate throughout the ring down time measurements is $\bar{f}_{rep} = 80.73 \pm 0.24\,MHz$. We can hence consider f_{rep} to be stable over a time scales of days, which is relevant all experiments to be discussed in this work.

B.3 Flaws in the finesse measurement

There have been two major simplifications made during recording and evaluating the ring down signal, affecting precision and appearance of itself and all quantities derived thereof:

1. The first one concerns the pumping of the resonator during the experimental runs. We have conveniently applied our Ti:Sa laser for that purpose, although commonly it is advised to utilise a cw light source. This is due to the multimode nature of the pumping beam, which obviously comprises many frequencies matching cavity resonances and thereby exciting multiple ring down signals simultaneously. To get a feeling about the order of magnitude involved here, the mode number N can be estimated by considering the separation between adjacent modes of $\nu_{FSR} = 80\,MHz$ and the overall width of the internal spectrum of $\Delta\nu_{FWHM}^{\text{int. spec.}} \approx 2.5\,THz$, yielding $N \approx 31000$. Yet for ring down spectroscopy, it is generally desired to have just a single frequency contributing to the observed signal, if feasible. So a narrowband pump should be used, which does not necessarily have to have a bandwidth $\Delta\omega_{pump}$ smaller than one resonance, but still less than ω_{FSR}. The underlying physical reason for the requirement stems from the superposition of the individually excited ring down signals. These do not interfere because of their different frequencies, but their intensities are still added up, when measuring a signal transmitted through one of the cavity mirrors. Every signal for each individual frequency however shows a different oscillation period in the ring down signal, which can be seen in the most simple way by eq. (4.27). On top of that come the different phase velocities of the individual ring down signals due to dispersion, which leads to a displacement in the time domain between them. So a superposition of the intensities of all modes can be regarded as an averaging operation over the oscillations in the ring down signals. In other words, the oscillations are expected to wash out for a multimode signal in exactly the way as it is apparent in comparison between the ring down signals shown in figs. 4.11 and 4.12.
   The modifications in the oscillations of the ring down signals are worsened even more by observation of the leakage through the input coupler, as here interference between the transmitted electric fields with the directly reflected pump field might add extra beat frequencies. But as we neglect the interference term (term 3 in eq. (4.23)) for reasons stated in the next point, the data might not be troubled too severely.
   It is now also understandable, why all quantities, derived from the ring down signal, seem to accord better with their counterparts received from other measurements, for an arrangement with an

empty cavity. Since the BBO approximately doubles the dispersion inside the cavity, the blurring of the oscillation maxima is enforced and precision in ring down time determination is sacrificed due to erasement of information about the oscillation extrema (like the comparison between figs. 4.11 and 4.12 reveals).
In implementing the experiment, we unfortunately did not yet know about these troublesome implications, our choice of a pumping source comes along with. So it shall be particularly stressed in this respect, that all numbers, derived from the ring down time, constitute estimations for the proper figures only, whose resemblance with numbers from other approaches proofs them be positioned in the correct magnitude range, but also shows their insufficiency for being treated as a precision measurement.

2. The second approximation has been done in the data analysis by neglecting the interference between the directly reflected pumping field and the ring down signal transmitted through the input coupler (term 3 in eq. (4.23)). The reasoning for that is of absolutely practical nature and based on the additional factor of 2 in the ring down time τ the interference would result in (see eq. (4.25)). Inclusion of this additional factor of two would approximately half all quantities τ has influence on. For instance, the finesse numbers would change to $\bar{F}^{\tau',\mathrm{BBO}} = 36 \pm 9$ and $\bar{F}^{\tau',\mathrm{noBBO}} = 134 \pm 29$. The reflectivity of the cavity without the input coupler would be modified to $\bar{R}^{\mathrm{noIC,BBO}} = 94 \pm 3\%$ and $\bar{R}^{\mathrm{noIC,noBBO}} = 98.7 \pm 0.3\%$, which would even worsen the mismatch between implications by the ring down signal and the expectations from the experimentally optimised input coupler choices or the loss calculations, respectively. Most significant however is the alteration of the power enhancement to $P\bar{E}''^{\tau',\mathrm{BBO}} \approx 6 \pm 1$ and $P\bar{E}'^{\tau'',\mathrm{noBBO}} \approx 21 \pm 5$, whose numbers are in complete disagreement with the previously derived $PE_{max}^{\mathrm{BBO}}(\lambda = 390.92\,nm) = 17 \pm 3$ and $PE_{max}^{\mathrm{noBBO}}(\lambda = 391.11) = 45 \pm 10$. They are exactly too small by the factor of 2, introduced in recognition of the interference term in eq. (4.23). Yet the numbers for PE_{max} are the ones to believe in. So we expect the power enhancement, retrieved from the finesse, to be at least situated in the proximity of the directly measured figures. Since taking into account the interference between the external pump and the ring down signal would precisely counteract such a resemblance, we have concluded the interference to be negligible and utilised the pure ring down signal with its associated ring down time τ, as given by eqs. (4.21) and (4.22), respectively. It shall also be noted in this respect, that all attempts to fit experimental data with eqs. (4.19), (4.20) and (4.23) did not succeed; furthermore the authors of reference ([51]) reckon by themselves the respective equations to be troubled by some yet undiscovered error. However the exponential decay of the ring down signal, as expressed in eq. (4.16), (4.17), (4.21) and (4.22) can be regarded correct, since it has been obtained independently with a different Ansatz ([91]).

Appendix C

Characterisation of pulse duration in resonator

C.1 Theory on correlation functions of first and second order

C.1.1 Fourier transforms of pulses' electric fields

Gaussian pulses By assuming the pulse model for Gaussian pulse, as given in eq. (5.14) by

$$E^{\text{Gauss}}(t) = a \cdot \exp\left(\frac{-t^2}{2\left(\Delta t\right)^2}\right) \cdot \cos\left(\omega_0 t\right)$$

we can calculate its Fourier Transform accordingly to ([112]):

$$\begin{aligned}
FT\{E(t)\} &= \int_{-\infty}^{\infty} a \exp\left(-\frac{t^2}{2\left(\Delta t\right)^2}\right) \cos\left(\omega_0 t\right) \exp\left(i\omega t\right) dt \\
&= \frac{a}{2} \int_{-\infty}^{\infty} \exp\left(-\frac{t^2}{2\left(\Delta t\right)^2}\right) \left(\exp\left(i\omega_0 t\right) + \exp\left(-i\omega_0 t\right)\right) \exp\left(i\omega t\right) dt \\
&= \frac{a}{2} \left(\int_{-\infty}^{\infty} \exp\left(-\frac{t^2}{2\left(\Delta t\right)^2}\right) \exp\left(i(\omega+\omega_0)t\right) dt + \int_{-\infty}^{\infty} \exp\left(-\frac{t^2}{2\left(\Delta t\right)^2}\right) \exp\left(i(\omega+\omega_0)t\right) dt \right) \\
&= \frac{a\sqrt{2\pi\left(\Delta t\right)^2}}{2} \left(\int_{-\infty}^{\infty} \frac{\exp\left(-\frac{t^2}{2(\Delta t)^2}\right)}{\sqrt{2\pi\left(\Delta t\right)^2}} \exp\left(i(\omega+\omega_0)t\right) dt + \int_{-\infty}^{\infty} \frac{\exp\left(-\frac{t^2}{2(\Delta t)^2}\right)}{\sqrt{2\pi\left(\Delta t\right)^2}} \exp\left(i(\omega-\omega_0)t\right) dt \right) \\
&= \sqrt{\frac{\pi}{2}} a \Delta t \left(\exp\left(-\frac{1}{2}\left(\Delta t\right)^2 \left(\omega+\omega_0\right)^2\right) + \exp\left(-\frac{1}{2}\left(\Delta t\right)^2 \left(\omega-\omega_0\right)^2\right) \right)
\end{aligned} \tag{C.1}$$

Sech Pulses Fourier transforming of the Sech pulse model $E^{\text{Sech}}(t) = a \cdot \text{sech}\left(\frac{-t}{\Delta t}\right) \cdot \cos\left(\omega_0 t\right)$ delievers a spectral electric field amplitude of ([112]):

$$
\begin{aligned}
FT\{E(t)\} &= \int_{-\infty}^{\infty} a \cdot \operatorname{sech}\left(\frac{t}{\Delta t}\right) \cos\left(\omega_0 t\right) \exp\left(i\omega t\right) \\
&= \frac{a}{2} \int_{-\infty}^{\infty} \operatorname{sech}\left(\frac{t}{\Delta t}\right) \left(\exp\left(i\omega_0 t\right) + \exp\left(-i\omega_0 t\right)\right) \exp\left(i\omega t\right) \\
&\text{Subst: } t' = \frac{t}{\Delta t};\ dt' = \frac{dt'}{dt} dt = \frac{1}{\Delta t} dt \\
&= \frac{a}{2\Delta t} \left(\int_{-\infty}^{\infty} \frac{\exp\left(-i\Delta t(-\omega - \omega_0)t'\right)}{\cosh\left(t'\right)} dt' + \int_{-\infty}^{\infty} \frac{\exp\left(-i\Delta t(\omega_0 - \omega)t'\right)}{\cosh\left(t'\right)} dt' \right) \\
&= \frac{a}{2\Delta t} \left(\frac{\pi}{\cosh\left(\frac{-\pi\Delta t(\omega+\omega_0)}{2}\right)} + \frac{\pi}{\cosh\left(\frac{-\pi\Delta t(\omega-\omega_0)}{2}\right)} \right) \\
&= \frac{a\pi}{2\Delta t} \left(\frac{1}{\cosh\left(\frac{\pi\Delta t(\omega+\omega_0)}{2}\right)} + \frac{1}{\cosh\left(\frac{\pi\Delta t(\omega-\omega_0)}{2}\right)} \right)
\end{aligned}
\tag{C.2}
$$

The result for the complex conjugate is equal to eq. (C.2), i.e. $FT\{E(t)\} = FT\{E^*(t)\}$ and the constant scaling factor $\frac{a\pi}{2\Delta t}$ can be dropped due to normalisation. By substitution of eq. (C.2) into eq. (5.32) and considering $\omega = 2\pi\nu$, the theoretically expected spectrum for Sech-pulses is:

$$
\begin{aligned}
S(\nu)^{\text{Sech}} &= \left(\frac{1}{\cosh\left(\frac{2\pi^2\Delta t(\nu+\nu_0)}{2}\right)} + \frac{1}{\cosh\left(\frac{2\pi^2\Delta t(\nu-\nu_0)}{2}\right)} \right)^2 \\
S(\nu)^{\text{Sech}} &= \frac{1}{\cosh^2\left(\pi^2\Delta t(\nu+\nu_0)\right)} + \frac{1}{\cosh^2\left(\pi^2\Delta t(\nu-\nu_0)\right)} + \frac{2}{\cosh^2\left(\pi^2\Delta t\nu\right) + \cosh^2\left(\pi^2\Delta t\nu_0\right)}
\end{aligned}
\tag{C.3}
$$

C.1.2 Second order correlation function

Wit the pulses' electric fields, as they are stated in eqs. (5.46) and (5.47), the interferometric autocorrelation function $g_2(\tau)$, eq. (5.45), can be simplified as follows:

$$
\begin{aligned}
g_2(\tau) &= \frac{\int_{-\infty}^{\infty} \left(E_1(t)^2 + E_2(t-\tau)^2 + 2E_1(t)E_2(t-\tau)\right)\left(E_1^*(t)^2 + E_2^*(t-\tau)^2 + 2E_1^*(t)E_2^*(t-\tau)\right) dt}{\int_{-\infty}^{\infty}(E_1(t))^2(E_1^*(t))^2 dt + \int_{-\infty}^{\infty}(E_2(t-\tau))^2(E_2^*(t-\tau))^2 dt} \\
&= \frac{\int_{-\infty}^{\infty} \left(E_1(t)^4 + E_2(t-\tau)^4 + 6E_1(t)^2E_2(t-\tau)^2 + 4E_1(t)^3E_2(t-\tau) + 4E_1(t)E_2(t-\tau)^3\right) dt}{\int_{-\infty}^{\infty} E_1(t)^4 dt + \int_{-\infty}^{\infty} E_2(t-\tau)^4 dt} \\
&= \frac{\int_{-\infty}^{\infty} E_1(t)^4 dt + \int_{-\infty}^{\infty} E_2(t-\tau)^4 dt}{\int_{-\infty}^{\infty} E_1(t)^4 dt + \int_{-\infty}^{\infty} E_2(t-\tau)^4 dt} + \underbrace{6 \cdot \frac{\int_{-\infty}^{\infty} E_1(t)^2 E_2(t-\tau)^2 dt}{\int_{-\infty}^{\infty} E_1(t)^4 dt + \int_{-\infty}^{\infty} E_2(t-\tau)^4 dt}}_{=3\cdot G_2^0(\tau)} \\
&\quad + 4 \cdot \frac{\int_{-\infty}^{\infty} E_1(t)E_2(t-\tau)^3 dt + \int_{-\infty}^{\infty} E_1(t)^3 E_2(t-\tau) dt}{\int_{-\infty}^{\infty} E_1(t)^4 dt + \int_{-\infty}^{\infty} E_2(t-\tau)^4 dt} \\
&\overset{(*)}{=} 1 + 6 \cdot \frac{a^2b^2}{a^4+b^4} \cdot \frac{\int_{-\infty}^{\infty} E'(t)^2 E'(t-\tau)^2 dt}{2\int_{-\infty}^{\infty} E'(t)^4 dt} + 4 \cdot \frac{ab^3 + a^3b}{a^4+b^4} \cdot \frac{\int_{-\infty}^{\infty} \left(E'(t)E'(t-\tau)^3 + E'(t)^3E'(t-\tau)\right) dt}{2\int_{-\infty}^{\infty} E'(t)^4 dt},
\end{aligned}
\tag{C.4}
$$

whereby the equality of $\int_{-\infty}^{\infty} E_1(t)^4 dt = \int_{-\infty}^{\infty} E_2(t-\tau)^4 dt$, proven in eq. (5.13), has been used again to calculate the denominators in step $(*)$

C.2 Measurement of intra-cavity pulse duration

C.2.1 Calculation of output spectra from the Mach-Zehnder interferometer

Considering the two electric fields (5.72), (5.73) and the associated Mach-Zehnder interferometer output (eq. (5.74))

$$E_{ges}(t) = E(t) + E(t-\tau) = \frac{E_0}{\sqrt{2}} f(t)\exp(i\omega_0 t) + \frac{E_0}{\sqrt{2}} f(t-\tau)\exp(i\omega_0(t-\tau))$$

as stated in subsec. 5.3.2, applying a Fourier transform to $E_{ges}(t)$ leads to the following expression:

$$\begin{aligned} FT\{E_{ges}(t)\} &= \int_{-\infty}^{\infty} \left(\frac{E_0}{\sqrt{2}} f(t)\exp(i\omega_0 t) + \frac{E_0}{\sqrt{2}} f(t-\tau)\exp(i\omega_0(t-\tau)) \right) \exp(i\omega t)dt \\ &= \underbrace{\int_{-\infty}^{\infty} \frac{E_0}{\sqrt{2}} f(t)\exp(i\omega_0 t)\exp(i\omega t)dt}_{\text{term 1}} + \underbrace{\int_{-\infty}^{\infty} \frac{E_0}{\sqrt{2}} f(t-\tau)\exp(i\omega_0(t-\tau))\exp(i\omega t)dt}_{\text{term 2}} \end{aligned} \quad \text{(C.5)}$$

Looking at the individual terms 1, 2 and defining $g_1(t) = \frac{E_0}{\sqrt{2}} f(t)$, $g_2(t) = \exp(i\omega_0 t)$, $g_3(t) = \frac{E_0}{\sqrt{2}} f(t-\tau)$, $g_4(t) = \exp(i\omega_0 (t-\tau))$, we can see both terms to be

$$\text{Term 1}: \quad \int_{-\infty}^{\infty} \frac{E_0}{\sqrt{2}} f(t)\exp(i\omega_0 t)\exp(i\omega t)dt = \mathrm{FT}\{g_1(t)g_2(t)\} \quad \text{(C.6)}$$

$$\text{Term 2}: \quad \int_{-\infty}^{\infty} \frac{E_0}{\sqrt{2}} f(t-\tau)\exp(i\omega_0(t-\tau))\exp(i\omega t)dt = \mathrm{FT}\{g_3(t)g_4(t)\}, \quad \text{(C.7)}$$

whereby FT assigns the Fourier transform. The property, that a Fourier transform of the product of two functions is equal to the convolution of the Fourier transforms of each individual function ([171]), i.e. $\mathrm{FT}\{g_i(t)\cdot g_j(t)\} = \mathrm{FT}\{g_i(t)\} \otimes \mathrm{FT}\{g_j(t)\}$ with $\otimes$ standing for the convolution, will now be used. Therewith term 1 simplifies to

$$\begin{aligned} \text{term 1} &= \int_{-\infty}^{\infty} \frac{E_0}{\sqrt{2}} f(t)\exp(i\omega_0 t)\exp(i\omega t)dt \\ &= f(\omega) \otimes \delta(\omega - \omega_0) \\ &= \frac{E_0}{\sqrt{2}} \int_{-\infty}^{\infty} f(\tilde{\omega}) \cdot \delta((\omega - \omega_0) - \tilde{\omega})\, d\tilde{\omega} \\ &= \frac{E_0}{\sqrt{2}} f(\omega - \omega_0) \\ &=: E_0(\omega') \end{aligned} \quad \text{(C.8)}$$

and term 2 results in

$$\begin{aligned} \text{term2} &= \int_{-\infty}^{\infty} \frac{E_0}{\sqrt{2}} f(t-\tau)\exp(i\omega_0(t-\tau))\exp(i\omega t)dt \qquad \text{Subs:} t-\tau = t' \\ &= \int_{-\infty}^{\infty} \frac{E_0}{\sqrt{2}} f(t')\exp(i\omega_0(t'))\exp(i\omega\tau)\exp(i\omega t')dt' \\ &= \frac{E_0}{\sqrt{2}} (\exp(i\omega\tau)\mathrm{FT}\{f(t')\}) \otimes \mathrm{FT}\{\exp(i\omega_0(t'))\} \\ &= \frac{E_0}{\sqrt{2}} (\exp(i\omega\tau) f(\omega) \otimes \delta(\omega - \omega_0)) \\ &= \int_{-\infty}^{\infty} \frac{E_0}{\sqrt{2}} \exp(i\tilde{\omega}\tau) \cdot f(\tilde{\omega}) \cdot \delta((\omega - \omega_0) - \tilde{\omega})\, d\tilde{\omega} \\ &= f(\omega - \omega_0)\exp(i(\omega - \omega_0)\tau) \\ &= f(\omega')\exp(i\omega'\tau), \end{aligned} \quad \text{(C.9)}$$

with the substitution $\omega - \omega_0 = \omega'$ carried out in each last step. Herein $E_0^+(\omega')$ is the Fourier transform of an arbitrary pulse's electric field. The entire expression (C.5) hence simplifies to

$$\begin{aligned} FT\{E_{ges}(t)\} &= E_0(\omega')\,(1+\exp(i\omega'\tau)) \\ &= 2\cdot E_0(\omega')\exp\left(\frac{i\omega'\tau}{2}\right)\cos\left(\frac{\omega'\tau}{2}\right) \\ &= \sqrt{2}E_0 f(\omega-\omega_0)\exp\left(\frac{i(\omega-\omega_0)\tau}{2}\right)\cos\left(\frac{(\omega-\omega_0)\tau}{2}\right) \\ &= E_{ges}\,(\omega-\omega_0) \end{aligned} \tag{C.10}$$

The relevant part of the spectrum is given by the absolute square of eq. (C.10):

$$\begin{aligned} S(\omega-\omega_0) &= \mid E_{ges}(\omega')\mid^2 \\ &= \underbrace{2\mid E_0 f(\omega-\omega_0)\mid^2}_{S_0(\omega-\omega_0)}\cos^2\left((\omega-\omega_0)\frac{\tau}{2}\right)\exp\left(i\frac{(\omega-\omega_0)\tau}{2}\right)\exp\left(-i\frac{(\omega-\omega_0)\tau}{2}\right) \\ &= S_0(\omega-\omega_0)\cos^2\left((\omega-\omega_0)\frac{\tau}{2}\right) \end{aligned} \tag{C.11}$$

As one can see from figure 5.6, the time separation between both pulses can be expresses as $\tau_{MZ} = \frac{2\Delta x_{MZ}}{c}$. Swapping from angular frequencies ω to wavelengths, by $\omega = \frac{2\pi c}{\lambda}$, with $\lambda_0 = 390\,nm$ being the central wavelength of the UV spectra, leaves us with a general expression for the spectral output of the interferometer:

$$\begin{aligned} S(\omega-\omega_0) &= S_0(\omega-\omega_0)\cos^2\left(\left(\frac{2\pi c}{\lambda}-\frac{2\pi c}{\lambda_0}\right)\frac{2\Delta x_{MZ}}{2c}\right) \\ &= S_0(\lambda-\lambda_0)\cos^2\left(\frac{2\pi(\lambda_0-\lambda)}{\lambda\lambda_0}\Delta x_{MZ}\right) \\ &\approx S_0(\lambda-\lambda_0)\cos^2\left(\frac{2\pi(\lambda-\lambda_0)}{\lambda_0^2}\Delta x_{MZ}\right) \\ &= S(\lambda,\lambda_0) \end{aligned} \tag{C.12}$$

The approximation made in the last step shall be explicitly pointed out only to be valid for narrowband spectra, i.e. spectral widths much smaller than central wavelength[1]. If the reader intents to apply any of the above and following outcomes for pulses with durations in the region of a few femto-seconds only, e.g. with an octave spanning spectrum as required for an f-2f interferometer ([73]), these simplifications do not hold anymore.

[1] With our spectral FWHM values of $\Delta\lambda \approx 1\,nm$, and central wavelengths of $\lambda_0 \approx 390\,nm$, the approximation $\lambda \approx \lambda_0$ is fulfilled pretty well.

Bibliography

[1] M. Planck "Über eine Verbesserung der Wieschen Spektralgleichung" Verhandlungen der Deutschen physikalischen Gesellschaft Vol. 2; No. 13; pg. 202-204 1900

[2] A. Einstein "Über einen die Erzeugung und Verwandlung des Lichtes betreffenden heuristischen Gesichtspunkt" Annalen der Physik Vol. 322; No. 6; pg: 132-148 1905

[3] A. Einstein, B. Podolsky, N. Rosen "Can quantum-mechanical description of physical reality be considered complete?" Physical Review Vol. 47 pg. 777-780 1935

[4] E. Schrödinger "Die gegenwärtige Situation der Quantenmechanik" Die Naturwissenschaften Vol. 23 pg. 807 1935

[5] J. S. Bell "On the problem of hidden variables in quantum mechanics" Review of Modern Physics Vol. 38; No. 3; pg: 447-452 1966

[6] J. S. Bell "On the Einstein Podolsky Rosen paradox" Physics Vol. 1; No. 3; pg: 195-200 1964

[7] S. J. Freedman, J. F. Clauser "Experimental test of local hidden-variable theories" Physical Review Letters Vol. 28; No. 14; pg. 938-941 1972

[8] J. F. Clauser, A. Shimony "Bell's theorem. Experimental tests and implications" Reports on Progress in Physics Vol. 41; pg: 1881-1927 1978

[9] A. Aspect, P. Grangier, G. Roger "Experimental realization of Einstein-Podolsky-Rosen-Bohm Gedankenexperiment: A new violation of Bell's inequalities" Phys. Rev. Lett. Vol. 49; No. 2; pg: 91-94 1982

[10] C. H. Bennett, D. P. DiVincenzo "Quantum information and computation" Nature Vol. 404; pg. 247-255 2000

[11] B. Schumacher "Quantum coding" Physical Review A Vol. 51; No. 4; pg: 2738-2747 1995

[12] N. Gisin, G. Ribordy, W. Tittel, H. Zbinden "Quantum crypotgraphy" Reviews of Modern Physics Vol. 74; pg: 145-195 2002

[13] A. K. Ekert "Quantum cryptography based on Bell's theorem" Physical Review Letters Vol. 67; No. 6; pg: 661-663 1991

[14] C. H. Bennett, G. Brassard, C. Crepeau, R. Jozsa, A. Peres, W. K. Wootters "Teleporting an unknown quantum state via dual classical and Einstein-Podolski-Rosen channels" Physical Review Letters Vol. 70; No. 13; pg: 1895-1899 1993

[15] A. Poppe, A. Fedrizzi, R. Ursin, H. R. Böhm, T. Lorünser, O. Maurhardt, M. Peev, M. Suda, T. Jennewein, A. Zeilinger "Practical quantum key distribution with polarization entangled photons" Optics Express Vol. 12; No. 16; pg: 3865-3871 2004

[16] D. Bouwmeester, J. W. Pan, K. Mettle, M. Leibfried, H. Weinfurter, A. Zeilinger "Experimental quantum teleportation" Nature Vol. 390; pg: 575-579 1997

[17] D. Schlingemann, R. F. Werner "Quantum error-correcting codes associated with graphs" Physical Review A Vol. 65; pg: 012308 2001

[18] R. Cleve, H. Buhrmann "Substituting quantum entanglement for communication" Physical Review A Vol. 56; No. 2; pg: 1201-1204 1997

[19] M. Hillery, V. Buzek, A. Berthiaume "Quantum secret sharing" Physical Review A Vol. 59; No. 3; pg: 1829-1834 1999

[20] R. Cleve, D. Gottesman, H.-K. Lo "How to share a quantum secret" Physical Review Letters Vol. 83; No. 3; pg: 648-651 1999

[21] M. Murao, D. Jonathan, M. B. Plenio, V. Vedral "Quantum telecloning and multiparticle entanglement" Physical Review A Vol. 59; No. 1; pg: 156-161 1999

[22] M. Murao, M. B. Plenio, V. Vedral "Quantum-information distribution via entanglement" Physical Review A Vol. 61; pg: 032311 2000

[23] M. Radmark, M. Zukowski, M. Bourennane "Experimental high fidelity six-photon entangled state for telecloning protocols" New Journal of Physics Vol. 11; pg. 103016 2009

[24] P. W. Shor "Polynomial-time algorithms for prime factorization and discrete logarithms on a quantum computer" Society for Industrial and Applied Mathematics Vol. 41; No. 2; pg: 303-332 1999

[25] L. K. Grover "Quantum mechanics helps in searching for a needle in a haystack" Physical Review Letters Vol. 79; No. 2; pg: 325-328 1997

[26] E. Knill, R. Laflamme, G. J. Milburn "A scheme for efficient quantum computation with linear optics" Nature Vol. 409; pg: 46-52 2001

[27] A. Aspect, P. Grangier, G. Roger "Experimental tests of realisitic local theories via Bell's theorem" Physical Review Letters Vol. 47; No. 7; pg: 460-463 1981

[28] M. A. Nielsen, I. L. Chuang "Quantum Computation and Quantum Information" Cambridge University Press 2000

[29] D. Deutsch "Quantum theory, the church-turing principle and the universal quantum computer" Proceedings of the Royal Society of London: Mathematical and Physical Sciences Vol. 400; No. 1818; pg: 97-117 1985

[30] D. Deutsch, R. Jozsa "Rapid solution of problems by quantum computation" Proceedings of the Royal Society of London: Mathematical and Physical Sciences Vol. 439; No. 1907; pg: 553-558 1992

[31] S. L. Braunstein, A. Mann, M. Revzen "Maximal violation of Bell inequalities for mixed states" Physical Review Letters Vol. 68; No. 22; pg: 3259-3261 1992

[32] C. Schmid, N. Kiesel, W. Wieczorek, H. Weinfurter "The entanglement of the four-photon cluster state" New Journal of Physics Vol. 9, No. 236 2007

[33] R. Raussendorf, H. J. Briegel "A one-way quantum computer" Physical Review Letters Vol. 86; No. 22; pg: 5188-5191 2001

[34] M. A. Nielsen "Optical quantum computation using cluster states" Physical Review Letters Vol. 93; No. 4; pg: 040503 2004

[35] G. Toth, O. Gühne "Entanglement detection" Physical Reports Vol. 474; pg: 1-75 2009

[36] J. K. Stockton, J. M. Geremia, A. C. Doherty, H. Mabuchi "Charaterizing the entanglement of symmetric many-particle spin-1/2 systems" Physical Review A Vol. 67; pg: 0221122 2003

[37] D. N. Klyshko, "Coherent decay of photons in a nonlinear medium" Soviet Physics JETP Letters Vol. 6; pg. 23-25 1967

[38] D. C. Burnham, D. L. Weinberg "Observation of simultaneity in parametric production of optical photon pairs" Physical Review Letters Vol. 25; pg. 84-87 1970

[39] B. R. Mollow "Photon correlation in the parametric frequency splitting of light." Physical Review A Vol. 8; pg. 2684 - 2694 1973

[40] M. H. Rubin, D. N. Klyshko, Y. H. Shih, A. V. Sergienko "Theory of two-photon entanglement in type-II optical parametric down conversion" Physical Review A Vol. 50; No. 6; pg: 5123-5133 1994

[41] R. J. Jones, J. Ye "Femtosecond pulse amplification by coherent addition in a passive optical resonator" Optics Letters Vol. 27; No. 20; pg: 1848-1850 2002

[42] R. J. Jones, J. Ye "Precision stabilization of femtosecond lasers to high-finesse optical cavities" Physical Review A Vol. 69; pg: 051803 2004

[43] W. Wieczorek, R. Krischek, N. Kiesel, P. Michelberger, G. Toth, H. Weinfurter "Experimental entanglement of a six-photon symmetric Dicke state" Physical Review Letters Vol. 103; pg: 020504 2009

[44] R. Prevedel, G. Cronenberg, M. S. Tame, M- Paternostro, P. Walther, M. S. Kim, A. Zeilinger "Experimental realization of Dicke states of up to six qubits for multiparty quantum networking" Physical Review Letters Vol. 103; pg. 020503 2009

[45] C. Y. Lu, X.-Q. Zhou, O. Ghne, W.-B. Gao, J. Zhang, Z.-S. Yuan, A. Goebel, T. Yang, J. W. Pan "Experimental entanglement of six photons in graph states" Nature Vol. 3; pg. 91-95 2007

[46] M. Radmark, M. Zukowski, M. Bourennane "'Experimental test of fidelity limits in six-photon interferometry and of rotational invariance properties of the photonic six-qubit entangled singlet state" Physical review letters Vol. 103; pg. 150501 2009

[47] G. Toth, W. Wieczorek, R. Krischek, N. Kiesel, P. Michelberger, H. Weinfurter "Practical methods for witnessing genuine multi-qubit entanglement in the vicinity of symmetric states" New Journal of Physics Vol. 11; pg: 083002 2009

[48] S. Campbell, M. S. Tame, M. Paternostro "Characterizing multipartite symmetric Dicke states under the effects of noise" New Journal of Physics Vol. 11; pg: 073039 2009

[49] P. J. Mosley, J. S. Lundeen, B. J. Smith, P. Wasylczyk, A. B. U'Ren, C. Silberhorn, I. A. Walmsley "Heralded generation of ultrafast single photons in pure quantum states" Physical Review Letters Vol. 100; pg: 133601 2008

[50] N. Kiesel, C. Schmid, G. Toth, E. Solano, H. Weinfurter "Experimental observation of four-photon entangled Dicke state with high fidelity" Physical Review Letters Vol. 98; pg: 063604 2007

[51] C. Gohle "A coherent frequency comb in the extreme ultraviolet" PhD dissertation Ludwig-Maximilians Universität München, Germany 2007

[52] J. Rauschenberger "Phase-stabilized ultrashort laser systems for spectroscopy" PhD dissertation Ludwig-Maximilians Universität München, Germany 2007

[53] E. Peters, S. A. Diddams, P. Fendel, S. Reinhardt, T. W. Hänsch, T. Udem "A deep-UV optical frequency comb at 205 nm" Optics Express Vol. 17; pg. 9183-9190 2009

[54] R. J. Jones, K. D. Moll, M. J. Thorpe, J. Ye "Phase-coherent frequency combs in the vacuum ultraviolet via high-harmonic generation inside a femtosecond enhancement cavity" Physical Review Letters Vol. 94; pg: 193201 2005

[55] V. P. Yanovsky, F. W. Wise Frequency doubling of 100-fs pulses with 50 % efficiency by use of a resonant enhancement cavity" Optics Letters Vol. 19; No. 23 1994

[56] A. Zavatta, V. Parigi, M. Bellini "Toward quantum frequency combs: Boosting the generation of highly nonclassical light states by cavity-enhanced parametric down-conversion at high repetition rates" Physical Review A Vol. 78; pg: 033809 2008

[57] O. Svelto "Principle of lasers" Springer Verlag 1998

[58] A. E. Siegman "Lasers" University Science Books 1986

[59] J.D. Jackson "Classical electro- dynamics" Wiley & Sons 1998

[60] J. T. Verdeyen "Laser electronics" Prentice Hall 1993

[61] H. Kogelnik "On the propagation on Gaussian beams of light through lenslike media including those with a loss or gain variation" Applied Optics Vol. 4; No. 12 1965

[62] S. Feng, H. G. Winful "Physical origin of the Gouy phase shift" Optics Letters Vol. 26; No. 8; pg. 485-487 2001

[63] H. Kogelnik, T. Li "Laser beams and resonators" Applied Optics Vol. 5; No. 10 1966

[64] R. Grimm, M. Weidemüller, Y. B. Ovchinnikov "Optical dipole traps for neutral atoms" Advances in atomic and molecular optical physics arXiv:physics/9902072v1

[65] M. W. Sasnett "Propagation of multimode laser beams- the M^2 factor" in "The physics and technology of laser resonators" Hilger, New York 1989

[66] T. F. Johnston Jr. "Beam propagation (M^2) measurement made as easy as it gets: the four- cuts method" Applied Optics Vol. 37; No. 21 1998

[67] D. N. Nikogosyan "Nonlinear optical crystals: A complete survey" Springer 2005

[68] R. A. McClatchey, R. W. Fenn, J. E. A. Selby, F. E. Volz, J. S. Garing Optical properties of the atmosphere in "Handbook of Optics" by W. G. Driscoll and W. Vaughan McGraw-Hill 1978

[69] W. Sellmeier "Zur Erklärung der abnormen Farbenfolge im Spektrum einiger Substanzen." Annalen der Physik Vol. 143; pg: 272-282 1871

[70] D. R. Lide "Handbook chemistry and physics" Taylor and Francis 2009

[71] K. Birch, M. J. Downs "An updated Edlen equation for the refractive index of air" Metrologia Vol. 30; No. 315; pg: 155-162 1993

[72] V. G. Dmitriev, G. G. Gurzadyan, D. N. Nicogosyan "Handbook of nonlinear optical crystals" Springer Verlag 1999

[73] T. Udem, R. Holzwarth, T. Hänsch "Optical frequency metrology" Nature Vol. 416; pg. 233- 237 2002

[74] R. Szipöcs, K. Ferencz, C. Spielmann, F. Krausz: "Chirped multilayer coatings for broadband dispersion control in femtosecond lasers" Optics Letters Vol. 19; pg. 201-203 2001

[75] H. S. Eisenberg, G. Khoury, G. A. Durkin, C. Simon, D. Bouwmeester "Quantum entanglement of a large number of photons" Physical Review Letters Vol. 93; No. 19; pg: 193901 2004

[76] Internal communication with Thomas Udem

[77] Internal communication with R. Krischek

[78] R. W. Boyd "Nonlinear Optics" Academic Press Inc. 2008

[79] J. C. Diels, W. Rudolph "Ultrashort laser pulse phenomena" Academic Press Inc. 2006

[80] R. W. P. Drever , J. L. Hall, F. V. Kowalski, J. Hough, G. M. Ford, A. J. Munley, H. Ward "Laser phase and frequency stabilization using an optical resonator" Applied Phyiscs B Vol. 31; pg. 97-105 1983

[81] E. D. Black "An introduction to Pound-Drever-Hall laser frequency stabilization" American Journal of Physics Vol. 69; pg. 79-87 2001

[82] T. Hänsch, B. Couillaud "Laser frequency stabilisation by polarisation spectrscopy of a reference cavity" Optical Communications Vol. 35, pg. 441-444 1980

[83] J. M. Boon-Engering, W. E. van der Veer, E. A. J. M. Bente, W. Hogervost "Stabilization of an optical cavity containing a birefringent element" Optics Communications Vol. 140; pg: 285-288 1997

[84] E. Hecht "Optics" Pearson Education 2003

[85] W. Lauterborn, T. Kurz "Coherent Optics-Fundamentals and Applications" Springer Verlag 2002

[86] A. Yariv "Photonics" Oxford University Press 2006

[87] N. Kiesel "Experiments on multiphoton entanglement" PhD thesis Ludwig- Maximilians Universität, München Germany 2007

[88] C. Schmid "Multi-photon entanglement and applications in quantum information" PhD thesis Ludwig- Maximilians Universität, München 2008

[89] D. F. V. James, P. G. Kwiat, W. J. Munro, A. G. White "Measurement of qubits" Physical Review A Vol. 64; pg: 052312 2001

[90] A. O'Keefe, D. A. G. Deacon "Cavity ring- down optical spectrometer for absorption measurements using pulsed laser sources" Review of Scientific Instruments Vol. 59; pg. 2544-2551 1988

[91] K. An, C. Yang, R. Dasari, M. Feld "Cavity ring-down technique and its applications to the measurement of ultraslow velocities" Optics Letters Vol. 29; No. 9; pg. 1068-1070 1995

[92] I. A. Walmsley, C. Dorrer "Characterization of ultrashort electromagnetic pulses" Advances in Optics and Photonics Vol. 1; pg. 308-437 2009

[93] Y. Takagi "Simple autocorrelator for ultraviolet pulse-width measurements based on nonlinear photoelectric effects" Applied Optics Vol. 33; No. 27; pg. 6328-6332 1994

[94] P. Hommelhoff, Y. Sortais, A. Aghajani-Talesh, M. A. Kasevich "Field emission tip as a nanometer source of free electron femtosecond pulses" Physical Review Letters Vol. 96; pg. 077401 2006

[95] T. Mindl, P. Hefferle, S. Schneider, F. Dörr "Characterisation of a train of subpicosecond laser pulses by fringe resoled autocorrelation measurements" Applied Physics B Vol. 31; pg. 201-207 1983

[96] S. L. Shapiro "Second harmonic generation in $LiNbO_3$ by picosecond pulses" Applied Physics Letters Vol. 13; No. 1; pg. 19-21 1968

[97] H. P. Weber "Method for pulsewidth measurement of ultrashort light pulses generated by phase-locked lasers using nonlinear optics" Journal of Applied Physics Vol. 38; No. 5; pg. 2231-2234 1967

[98] D. H. Auston "Measurement of picosecond pulse shape and background level" Applied Physics Letters Vol. 18; No. 6; pg. 249-251 1971

[99] J. A. Giordmaine, P. M. Rentzepis, S. L. Shapiro, K. W. Wecht "Two-photon excitation of fluorescence by picosecond light pulses" Applied Physics Letters Vol. 11; No. 7; pg. 216-218 1967

[100] M. B. Nasr, G. Di Giuseppe, B. E. A. Saleh, A. Sergienko, M. Teich "Generation of high- flux ultra-broadband light by bandwidth amplification in spontaneous parametric down conversion" Optics Communications Vol. 246; pg. 521 - 528 2005

[101] P. Trojek "Efficient generation of photonic entanglement and multiparty quantum communication" PhD thesis Ludwig- Maximilians Universität, München, Germany 2007

[102] P. J. Mosley, J. S. Lundeen, B. J. Smith, I. A. Walmsley "Focusing on factorability:space-time coupling in the generation of purse heralded single photons" Journal of Modern Optics Vol. 56; No. 2-3; pg: 179-189 2009

[103] Arnold Migus: "Femtosecond and subpicosecond ultra- intense lasers"

[104] Rick Trebino "Frequency resolved optical gating: The measurement of ultrashort laser pulses" Kluwer Academic Publishers 2000

[105] L. Cohen "Time-frequency distributions-A review" Proceedings of the IEEE Vol. 77; No. 7; pg: 941-981 1989

[106] S. de Silvestri, P. Laporta, O. Svelto "The role of cavity dispersion in cw mode-locked lasers" IEEE Journal of Quantum Electronics Vol. QE-20; No. 5; pg: 533-539 1984

[107] J. D. McMullen "Chirped-pulse compression in strongly dispersive media" Journal of the Optical Society of America Vol. 67; No. 11; pg: 1575-1578 1977

[108] E. J. Akutowicz "On the Determination of the phase of a Fourier integral 1" Transactions of the American Mathematical Society Vol. 83; Pg: 179-192 1956

[109] E. J. Akutowicz "On the Determination of the phase of a Fourier integral 2" Transactions of the American Mathematical Society Vol. 83; Pg: 179-192 1956

[110] K. Sala et. al. "CW autocorrelation measurements of picosecond laser pulses" IEEE Journal of Quantum Electronics Vol. QE-16; No. 9 1980

[111] F. Träger "Handbook of lasers and optics" Springer Verlag 2007

[112] Bronstein "Taschenbuch der Mathematik" Harri Deutsch 2008

[113] J.-C. Diels et. al. "Control and measurement of ultrashort pulse shapes (in amplitude and phase) with femtosecond accuracy" Applied Optics Vol. 24; No.9 1985

[114] W. H. Louisell, A. Yariv, A. E. Siegman "Quantum fluctuations and noise in parametric processes" Physical Review Vol. 124; pg. 1646 - 1654 1961

[115] R. Trebino, D. J. Kane "Using phase retrieval to measure the intensity and phase of ultrashort pulses: frequency-resolved optical gating" Journal of the Optical Society of America A Vol. 10; No. 5; pg: 1101-1111 1993

[116] D. J. Kane, R. Trebino "Single-shot measurement of the intensity and phase of an arbitrary ultrashort pulse by using frequency-resolved optical gating" Optics Letters Vol. 18; No. 10; pg: 823-825 1993

[117] D. J. Kane, R. Trebino "Characterization of arbitrary femtosecond pulses using frequency-resolved optical gating" IEEE Journal of Quantum Electronics Vol. 29; No. 2; pg: 571-579 1993

[118] K. W. DeLong, R. Trebino, J. Hunter, W. E. White "Frequency-resolved optical gating with the use of second-harmonic generation" Journal of the Optical Society of America B Vol. 11; No. 11; pg: 2206-2215 1994

[119] K. W. DeLong, R. Trebino "Improved ultrashort pulse-retrieval algorithm for frequency-resolved optical gating" Journal of the Optical Society of America A Vol. 11; No. 9; pg: 2429-2437 1994

[120] R. Trebino, K. W. DeLong, D. N. Fittinghoff, J. N. Sweetser, M. A. Krumbüegel, B. A. Richman "Measuring ultrashort laser pulses in the time-frequency domain using frequency-resolved optical gating" Review of Scientific Instruments Vol. 68; No. 9; pg: 3277-3295 1997

[121] I. A. Walmsley, V. Wong "Characterization of the electric field of ultrashort optical pulses" Journal of the Optical Society of America B Vol. 13; No. 11; pg: 2453-2463 1996

[122] C. Iaconis, I. A. Walmsley "Spectral phase interferometry for direct electric-field reconstruction of ultrashort optical pulses" Optics Letters Vol. 23; No. 10; pg: 792-794 1998

[123] L. Gallmann, D.H.Sutter, N. Matuschek, G. Steinmeyer, U. Keller, C. Iaconis, I.A. Walmsley "Characterization of sub-6-fs optical pulses with spectral phase interferometry for direct electric-field reconstruction" Optics Letters Vol. 24; No. 18; pg: 1314-1316 1999

[124] T. M. Shuman, M. E. Anderson, J. Bromage, C. Iaconis, L. Waxer, I. A. Walmsley "Real-time SPIDER: ultrashort pulse characterization at 20 kHz" Optics Express Vol. 5; No. 6; pg: 134-143 1999

[125] L. Mandel, E. Wolf "Optical coherence and quantum optics" Cambridge University Press 1995

[126] B. R. Mollow "Photon correlation in the parametric frequency splitting of light" Physical Review A Vol. 8; pg. 2684-2694 1973

[127] D. Bohm "Quantum Theory" Prentice- Hall 1935

[128] I. A. Khan, J. C. Howell "Experimental demonstration of high two-photon time-energy entanglement" Physical Review A Vol. 73; pg: 0301801 2006

[129] W. Tittel, J. Brendel, H. Zbinden, N. Gisin "Violation of Bell inequalities by photons more than 10 km apart" Physical Review Letters Vol. 81; No. 17; pg: 3563-3566 1998

[130] W. Tittel, J. Brendel, H. Zbinden, N. Gisin "Quantum cryptography using entangled photons in energy-time Bell states" Physical Review Letters Vol. 84; No. 20; pg: 4737-4740 2000

[131] A. Migdall "Polarization directions of noncollinear phase-matched optical parametric downconversion output" Journal of the Optical Society of America B Vol. 15; No. 5; pg: 1093-1098 1997

[132] P. G. Kwiat, K. Mattle, H. Weinfurter, A. Zeilinger "New high-intensity source of polarization-entangled photon pairs" Physical Review Letters Vol. 75; No. 24; pg: 4337-4341 1995

[133] J. C. Howell, R. S. Bennink, S. J. Bentley, R. W. Boyd "Realization of the Einstein-Podolsky-Rosen paradox using momentum- and position-entangled photons from spontaneous parametric down conversion" Physical Review Letters Vol. 91; No. 21; pg:210403 2004

[134] M. N. O'Sullivan-Hale, I. A. Khan, R. W. Boyd, J. C. Howell "Pixel entanglement: experimental realization of optically entangled $d = 3$ and $d = 6$ qudits" Physical Review Letters Vol. 94; pg: 220501 2005

[135] C. Kurtsiefer, M. Oberparleiter, H. Weinfurter "Generation of correlated photon pairs in type-II parametric down conversion-revisited" Journal of Modern Optics Vol. 48 2001

[136] M. H. Rubin "Transverse correlation in optical spontaneous parametric down-conversion" Physical Review A Vol. 54; No. 6; pg: 5349-5360 1996

[137] S. Carrasco, A. V. Sergienko, B. E. A. Saleh, M. C. Teich, J. P. Torres, L. Torner "Spectral engineering of entangled two-photon states" Physical Review A Vol. 73; pg: 063802-(1-6) 2006

[138] R. S. Bennink, Y. Liu, D. D. Earl, W. P. Grice "Spatial distinguishability of photons produced by spontaneous parametric down-conversion with a focused pump" Physical Review A Vol. 74; pg: 023802-(1-7) 2006

[139] W. Wieczorek "Multi-photon entanglement: Experimental observation, characterization, and application of up to six-photon entangled states" PhD dissertation Ludwig-Maximilians Universität München, Germany 2009 *to be published*

[140] P. Kok, S. L. Braunstein "Postselected versus non-postselected quantum teleportation using parametric down-conversion" Physical Review A Vol. 61; pg: 042304 2000

[141] H. Weinfurter, M. Zukowski "Four-photon entanglement from down-conversion" Physical Review A Vol. 64; pg: 010102 2001

[142] D. Bouwmeester, A. Ekert, A. Zeilinger "The Physics of Quantum Information" Springer Verlag 2000

[143] R. Horodecki, P. Horodecki, K. Horodecki "Quantum entanglement" Review of Modern Physics Vol. 81; pg: 865-942 2009

[144] J. W. Pan, Z.-B. Chen, M. Zukowski, H. Weinfurter, A. Zeilinger "Multi-photon entanglement and interferometry" arXiv:0805.2853v1 [quant-ph]

[145] J. F. Clauser, M. A. Horne, A. Shimony, R. A. Holt "Proposed experiment to test local hidden-variable theories" Physical Review Letters Vol. 23; No. 15; pg: 880-884 1969

[146] W. Dür, G. Vidal, J. I. Cirac "Three qubits can be entangled in two inequivalent ways" Physical Review A Vol. 62; pg. 062314 2000

[147] F. Verstraete, J. Dehaene, B.D. Moor, H. Verschelde "Four qubits can be entangled in nine different ways" Physical Review A Vol. 65; pg: 052112 2002

[148] L. Lamata, J. Leon, D. Salgado, E. Solano "Inductive classification of multipartite entanglement under stochasitc local operations and classical communication" Physical Review A Vol. 74; pg: 052336 2006

[149] C. H. Bennett, S. Popescu, D. Rohrlich, J. A. Smolin, A. V. Thapliyal "Exact and asymptotic measures of multipartite pure-state entanglement" Physical Review A Vol. 63; pg: 012307 2000

[150] R. H. Dicke "Coherence in spontaneous radiation processes" Physical Review Vol. 93; No. 1; pg: 99-110 1954

[151] F. Schwabl "Quantenmechanik 1" Springer Verlag 2007

[152] F. Schwabl "Statistische Mechanik" Springer Verlag 2006

[153] Y. Shih "Entangled biphoton source-property and preparation" Reports on progress in physics Vol. 66; pg: 1009-1044 2003

[154] M. Oberparleiter "Effiziente Erzeugung verschränkter Photonenpaare" PhD dissertation Ludwig-Maximilians Universität München, Germany 2002

[155] J. G. Rarity "Interference of single photons from separate sources" Annals of the New York Academy of Sciences Vol. 755; pg: 624-631; Issue: Fundamental problems in quantum theory 1995

[156] M. Zukowski, A. Zeilinger, H. Weinfurter "Entangling photons radiated by independent pulsed sources" Annals of the New York Academy of Sciences Vol. 755; pg: 624-631; Issue: Fundamental problems in quantum theory 1995

[157] A. Uhlmann "The transition probability in the state space of a^*-algebra" Reports on mathematical physics Vol. 9; No. 2; pg: 273-270 1976

[158] G. Toth, O. Gühne "Entanglement detection in the stabilizer formalism" Physical Review A Vol. 72; pg: 022340 2005

[159] G. Toth "Detection of multipartite entanglement in the vicinity of symmetric Dicke states" Journal of the Optical Society of America B Vol. 24; No. 2; pg: 275-282 2007

[160] J. K. Korbicz, J. I. Cirac, M. Lewenstein "Spin squeezing inequalities and entanglement of N Qubit states" Physical Review Letters Vol. 95; pg: 120502 2005

[161] R. Krischek, W. Wieczorek, A. Ozawa, N. Kiesel, P. Michelberger, T. Udem, H. Weinfurter "Ultraviolet enhancement cavity for ultrafast nonlinear optics" Nature Photonics *to be published*

[162] D. Achilles, C. Silberhorn, C. Sliwa, K. Banaszek, I. A. Walmsley "Fiber-assisted detection with photon number resolution" Optics Letters Vol. 23; No. 23; pg. 2387 2003

[163] D. Leibfried, E. Knill, S. Seidelin, J. Britton, R. B. Blakestad, J. Chiaerini, D. B. Hume, W. M. Itano, J. D. Jost, C. Langer, R. Ozeri, R. Reichle, D. J. Wineland "Creation of a six-atom Schrödinger cat state" Nature Vol. 438; pg. 639-642 2005

[164] J. W. Pan, D. Bouwmeester, H. Weinfurter, A. Zeilinger "Experimental entanglement swapping: Entangling photons that never interacted" Physical Review Letters Vol. 80; No. 18; pg: 3891-3894 1998

[165] S. Bose, V. Vedral, P. L. Knight "Multiparticle generalization of entanglement swapping" Physical Review A Vol. 57; No. 2; pg: 822-829 1998

[166] W. Wieczorek, C. Schmid, N. Kiesel, R. Pohlner, O. Gühne, H. Weinfurter "Experimental observation of an entire family of four-photon entangled states" Physical Review Letters Vol. 101; pg: 010503 2008

[167] R. Loudon "The quantum theory of light" Oxford University Press 2000

[168] D. F. Walls "Squeezed states of light" Nature Vol. 306; pg: 141-146 1983

[169] A. Ozawa, J. Rauschenberger, C. Gohle, M. Hermann, D. R. Walker, V. Pervak, A. Fernandez, R. Graf, A. Apolonski, R. Holzwarth, F. Krausz, T. W. Hänsch, T. Udem "High harmonic frequency combs for high resolution spectroscopy" Physical Review Letters Vol. 100; pg: 253901 2008

[170] A. Ozawa, A. Vernaleken, W. Schneider, I. Gotlibovych, T. Udem, T. W. Hänsch "Non-collinear high harmonic generation: a promising outcoupling method for cavity-assisted XUV generation" Optics Express Vol. 16; No. 9; pg: 6233-6239 2008

[171] R. Bracewell "Convolution Theorem: The Fourier Transform and Its Applications" McGraw-Hill 1999.